Spin Dynamics Simulations of Iridium Manganese Alloys

By

Sarah Jenkins

Doctor of Philosophy

The University of York
Physics

May 2020

ABSTRACT

Until the late 1980's, anti-ferromagnets were thought of as theoretically interesting but with no practical application. Since then, this idea has been completely altered, and they are a key element in nearly all magnetic recording devices such as read heads in magnetic hard drives. More recently, the development of antiferromagnetic spintronics has enabled the use of the anti-ferromagnet as the active element and could lead to storage devices with THz speeds, much higher storage densities and a lower power consumption. A current problem in the development of such devices is a lack of understanding of the magnetic properties of antiferromagnets. Atomistic modelling is a powerful tool in understanding these properties as it has the ability to model the materials in atomistic detail on a scale comparable to realistic device sizes. In this thesis, I present an atomistic model of the Iridium Manganese (IrMn) that was created to model the static and dynamic magnetic properties of this complex material. The ground state magnetic structure and thermal stability are calculated including composition effects, disorder effects and finite-size effects. The magnitude and symmetry of the anisotropy in IrMn is calculated, solving a long standing debate between theory and experiment, where the calculations differ orders of magnitude. Finally, an IrMn layer is coupled to a ferromagnet to study the origin of the exchange bias effect, with realistic device sizes, including multiple grains, temperature and interface disorder. The results presented in this thesis determine the properties of IrMn in extraordinary detail, paving the way for a full understanding of this complex and interesting material and its interaction with natural magnets. The work in this thesis has been published in four peer reviewed papers in world leading journals.

CONTENTS

LIST OF TABLES

TABLE

LIST OF FIGURES

FIGURE **Page**

ACKNOWLEDGMENTS

I would like to thank my supervisors, Richard Evans and Roy Chantrell, for there continuing support throughout my PhD and many interesting debates and discussions. I would like to thank them for the many opportunities that they have given to me during my PhD that have made it such an unforgettable experience. Richard, I would like to thank you for your support, friendship and most importantly always encouraging me to grow as a researcher.

I would like to thank my family. Mum, thank you for all of your help and support throughout the years. Dad thank you for your encouragement and support. Pete, thanks for always being a cheerful presence in my life!

I would also like to thank the friends I have made throughout the past 4 years, whether in York, at conferences, or elsewhere, who have provided me with endless laughs, wine and happyiness over the years. To Nikky and Siobhan, thanks for the adventures, infinity girls for life. Harriet, Katie, Claire, Willow, thanks for constantly cheering me up these past few months, you've all really made lock down not just bearable but a nice place to be. I would like to thank the computational physics group at York, old and new, for the endless pub trips and coffee. There are so many more people who have made my time in York so memorable and I give my thanks to you all and I hope that you will all remain in my life forever!

AUTHOR'S DECLARATION

I declare that the work in this thesis was carried out in accordance with the requirements of the University's Regulations and Code of Practice for Research Degree Programmes and that it has not been submitted for any other academic award. Except where indicated by specific reference in the text, the work is the candidate's own work. Work done in collaboration with, or with the assistance of, others, is indicated as such. Any views expressed in the thesis are those of the author.

SIGNED: ..... DATE: .....

List of Publications

Published	**Jenkins, S.**, Evans, R. F. L., *Enhanced Finite size and interface mixing effects in IrMn ultrathin films*, Journal of Applied Physics, **124**, (2018)
Published	**Jenkins, S.**, Chantrell, R. W., Evans, R. F. L ., *Magnetic Anisotropy of the noncolinear anti-ferromagnet $IrMn_3$*, Physical Review B, **100**, (2019)
Published	**Jenkins, S.**, Meo, A., Elliott, L., Piotrowski, S. K., Bapna. M., Chantrell. R. W., Majetich. S. A., Evans. R. F. L. Evans., *Magnetic stray fields in nanoscale magnetic tunnel junctions*, Journal of Physics D , **53**, (2019)
Published	Moreneo, R., *et al*. *The role of faceting and elongation on the magnetic anisotropy of magnetite Fe3O4 nanocrystals*, Scientific Reports, **10**, (2020)
Submitted	**Jenkins, S.**, Evans, R.F.L., *Spin wave excitations in exchange biased IrMn/CoFe bilayers*, **3**, Journal of Applied Physics, (2020)
Submitted	**Jenkins, S.**, Fan, W.J., Gaina, R., Chantrell, R. W., Klemmer, T., Evans, R. F. L., *Uncovering the mystery of delocalised pinned interface spins responsible for exchange bias*, Submitted to Physical Review Letters (2020)
Submitted	Evans, R.F.L., Rozsa, L., **Jenkins, S.**, Atxitia, U., *Temperature scaling of two-ion anisotropy in pure and mixed anisotropy systems*, Submitted to Physics Review Letters, (2020)
Submitted	Augustin, M., **Jenkins, S.**, Evans, R. F. L., Novoselov, K. S., Santos, E. J. G. *Lifetime evolution of meron and antimeron topological spin textures in the two-dimensional magnet CrCl3* Submitted to Science (2020)
Submitted	Augustin, M., *et al*, *The quantum non-Heisenberg nature of two-dimensional CrI3 magnets*, Submitted to Nature Nanotechnology (2020)

1

INTRODUCTION

1.1 Motivation

In his 1970 Nobel lecture, Louis Néel stated that "Antiferromagnetic materials are extremely interesting from the theoretical viewpoint, but do not seem to have any practical application." [1] While this seemed true at the time, anti-ferromagnetic materials have since become a key feature in nearly all magnetic recording devices, such as read heads in magnetic hard drives and magnetic random access memory [2]. The turning point occurred in 1988 when Albert Fert [3] and Peter Grunberg [4] both independently discovered the giant magneto-resistance (GMR) effect. GMR is an observed change in electrical resistance depending on whether the magnetic orientation of two adjacent ferromagnetic (FM) layers are parallel or anti-parallel. To change the relative orientations of the layers independently the magnetisation of one of the FM layers is pinned using an anti-ferromagnet (AFM) [5]. Since then, GMR and hence anti-ferromagnetic materials have become the basis of almost all conventional magnetic recording devices.

Magnetic recording devices are used across the world today in data centres and computers. As the demand for storage is increasing, the demand for computational power is increasing exponentially, the effect of this is described by Moore's law, which states that:"the number of transistors and resistors on a microchip must double every twenty four months [6]." The increase is achieved by reducing the size of processors and increasing the data density, so more processors can fit on every chip. However, processor size cannot be reduced indefinitely. Currently transistors are 5nm in diameter, approaching the physical limit before the electrons can quantum tunnel between the transistors [7]. To increase the data density a new wave of research is developing, in "beyond Moore's law" technology [8]. One

of these technologies is a subfield of spintronics, known as anti-ferromagnetic spintronics. Anti-ferromagnet spintronics uses the AFM as the active element to store, read or write information, contrary to conventional spintronic devices which use FMs as the active element.

Anti-ferromagnetic spintronics has the potential for very high data density as the elements can be tightly packed due to the lack of stray fields eliminating cross-talk between neighbouring devices [9]. The write times could be 1,000 times faster [10] than conventional spintronic devices due the THz timescales of AFMs. The magnetisation is also exceptionally robust, as they are impervious to external magnetic fields. Their robust nature however, comes at a price: the magnetisation is notoriously difficult to manipulate. One possibility comes from coupling the AFM to a FM, as is done in GMR sensors. Usually, in these sensors the AFM is assumed to be approximately fixed. However if the AFM has a weak anisotropy, when the external magnetic field reorients the FM the AFM can be reoriented as well. Controlling the motion of the AFM [11, 12]. The current challenge in the development of anti-ferromagnetic spintronic devices is a full understanding of the AFM properties such as basic characterisation, the exact spin structures and the size and symmetry of the anisotropies [13].

Ferromagnetic materials were first discovered thousands of years ago [14] and have since been extensively investigated both experimentally and theoretically. AFM materials, though naturally much more abundant, were only discovered in the 1930's due to their lack of macroscopic stray fields. In AFM materials the internal magnetic moments spontaneously align themselves anti-parallel causing only minimal detectable fields around the bulk material [15]. The lack of a bulk magnetisation means that some of the magnetic properties such as Néel temperature or magnetic ground state are much harder to measure experimentally, especially in more complex non-collinear AFMs or in thin film devices. The recent interest in AFMs for spintronic applications has led to many novel experimental developments in an attempt to probe the spin structures such as using optical approaches [16] and investigating spin transport effects [17, 18]. However, our knowledge of AFMs still lacks basic understanding and remains a complex and interesting challenge [9].

The computational modelling of FM materials relies heavily on micromagnetic models, where the material is modelled as a continuous medium. This modelling method is unsuitable for AFMs as it uses bulk magnetic properties which in an AFM are zero. Recent developments in computational power have meant that

models can be developed which no longer rely on continuum properties instead the magnetisation can be modelled at an atomistic level where each atom is given a local magnetic moment. These models have been successfully used to model known properties of AFMs such as the thermal stability [19], the magnetic ground states [20], the dynamics of domain walls [21] and the switching frequency [22].

The AFM most widely used in spintronic devices is Iridium Manganese (IrMn). Its main advantage is its high magnetic ordering (Néel) temperature and high magnetic anisotropy, both desirable properties for use in spintronic devices. In these devices IrMn is used in thin film form, and in many compositions has a non-collinear magnetic structure. The magnetic properties, symmetry and size of the anisotropy of these compositions are still being debated, especially on the small scales used in spintronic devices. The focus of this thesis is a full theoretical study of the anti-ferromagnetic material Iridium Manganese using an atomistic spin model and furthers our understanding of these so far unanswered questions.

1.2 Origins of magnetism

To discuss the theory of anti-ferromagnetism it is important to first understand the origin of magnetism. Magnetic materials occur because in an atom, each electron has a magnetic moment defined in Bohr magnetons (μ_B) from its orbital and spin quantum numbers. The orbital contribution is due to the movement of the electronic charge about the nucleus and the spin contribution is due to the electron having an intrinsic spin. In most solid state systems the orbital contribution is weak due to the strong electrostatic interaction with the crystal field. The majority of the observed magnetic moment in bulk materials therefore results from the intrinsic spin of the electrons. The magnetic moment of the atom is the vector sum of all of its magnetic spin moments. Often the number of spin up and spin down electrons is equal, leaving the atom with no net moment, known as a diamagnetic material. Alternatively, they can only partially cancel out, leaving the atom with a net moment (paramagnetic or ferromagnetic materials).

Paramagnetic materials display a net magnetisation under the presence of an applied field but when the field is removed the magnetisation disappears due to thermal fluctuations. Ferromagnetic materials exhibit a spontaneous magnetisation even under no applied field. The effect is largest in $3d$ and $4f$ elements due to the large number of available states in the outer, partially filled orbitals. Hunds rule states that: Every orbital in a sub-level is singly occupied before any orbital is doubly occupied maximising the total spin of the atom. In Iron there

should be 4 unpaired $3d$ electrons per Iron atom, with a moment of $4\mu_B$ per atom. Experimentally, the moment of Iron is found to be $2.21\mu_B$. The reduction is because in metallic systems the electrons are partially delocalised and therefore we cannot easily describe the system in terms of discrete orbitals. The simplest model which takes into account the band structure of such materials is the Stoner model, where the Weiss field from the adjacent atoms in the lattice causes a splitting of the electron band structure. This leads to a difference in the integrated density of states of the spin-up and spin-down states up to the Fermi energy. The difference in these gives the net moment, thus one obtains a moment which is not an integer of multiple of μ_B.

1.3 Exchange Interactions

In ferromagnetic materials a strong internal force is required to align the moments of neighbouring atoms parallel even without the application of an external field. The force responsible is the exchange interaction which is caused by the Pauli exclusion principle. The Pauli exclusion principle forbids two electrons from being in the same quantum state. As spin is a quantum number two electrons can be in the same state if they have different spin quantum numbers. When two atoms are brought close together, there is a probability of an electron jumping from one atom to another. However, as electrons are indistinguishable the systems wavefunction must remain anti-symmetric after the exchange of electrons meaning the interaction probability can indirectly couple the spin moments of the atoms, causing the spin moments to align parallel or anti-parallel. The tendency for the spins to align parallel is ferromagnetic ordering, if the spins align anti-parallel this is anti-ferromagnetic ordering.

1.3.1 Magnetic Ordering

There are four different types of magnetic ordering which can occur within a magnetic material: diamagnetic (as described in section 1.2, ferromagnetic (FM), anti-ferromagnetic (AFM) and paramagnetic. In diamagnetic materials there is no net moment, however, in the other three types, there is a net magnetic moment. These different orderings are shown in Fig. 1.1.

In a ferromagnetic material, the minimum energy occurs when neighbouring atomic moments align parallel to each other. Whereas, in an antiferromagnetic material, the minimum energy occurs when these atomic moments align anti-parallel. Ferrimagnets are very similar to antiferromagnets but instead of having

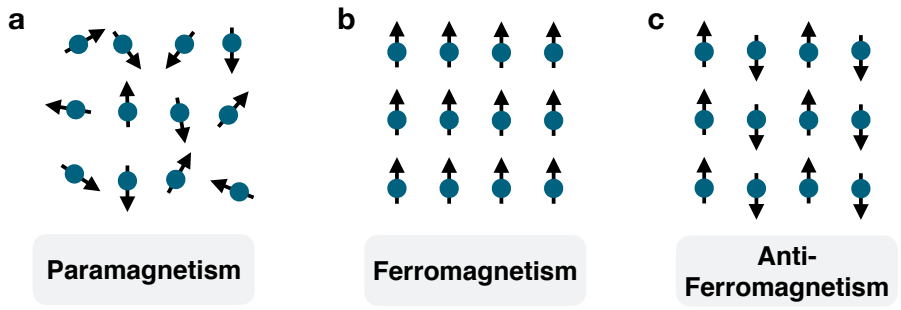

Figure 1.1: **Visualisations of the three different classifications of magnetic material:** (a) Paramagnetism: Under no field the thermal fluctuations are too weak too align the magnetic moments of the atoms. (b) Ferromagnetism: There is a molecular field which acts to align the magnetic moments of the atoms even under no external field. (c) Anti-ferromagnetism: The molecular field acts to align the moments anti-parallel.

two sublattices which cancel out, one sublattice has a higher moment than the other, leaving the material with a low net magnetisation. A paramagnet, has zero net magnetisation as the thermal fields are too high and the atomic moments are randomly oriented. The remainder of this thesis focuses primarily on the modelling of anti-ferromagnetic materials.

1.3.2 Anti-ferromagnetism

In anti-ferromagnetic materials the minimum energy occurs when the magnetic moments of nearest neighbour atoms align anti-parallel. This means the bulk magnetisation of the material is zero as the magnetic moments cancel each other out. This does not mean that the material is not magnetic, as the material still has a strong magnetic ordering. A simple picture of an anti-ferromagnet would be a material which contains two sublattices each with opposite magnetisation, where the magnetisation of these two sublattices compensate each other giving rise to zero net magnetisation. For this reason they do not produce stray magnetic fields and are only weakly coupled to an external magnetic field.

In this thesis, anti-ferromagnetic materials will be computationally modelled. There are different types of model used for simulating magnetic materials depending on the scale of the problem and in the next section we will discuss which is the most appropriate for modelling anti-ferromagnetic materials.

1.4 Modelling methods

The type of magnetic model used depends on the time and length scale of the problem you want to solve. At short time and length scales quantum mechanical first principles methods can be used. For long time and length scales the continuum approach of micromagnetism is typically used. Atomistic models are a classical approach which is used for time and length scales between these two methods.

Quantum mechanical first principles (*ab-initio*) methods use a quantum mechanical formalism to determine the electronic properties starting from the electronic wave functions. The fundamental properties such as exchange energies, magnetic anisotropy and magnetic moments can be calculated. However, *ab-initio* methods are very computationally expensive and can only be used to model very small systems containing at most a couple of hundred atoms.

For larger scale systems between 10^4 and 10^9 atoms atomistic models are most suitable. The first atomistic model was conceived by Ising in 1925 [23], now known as the Ising model and only includes spin up and spin down states. The Ising model is still extensively used but is limited as it cannot be used for dynamic simulations. A natural extension of the Ising model is the classical Heisenberg model [24]. The Heisenberg model allows the atomic spin to vary freely in 3D space whilst neglecting the quantum nature of the atomic spins. Today atomistic simulations of magnetic materials are essential in understanding their complex behaviour.

For even larger systems, from tens of nanometres to micrometres, a continuum (micromagnetic) approach is usually used. This approximation neglects the details at the atomic level and treats the physical quantities as continuous functions. As it is a continuous function the method is unable to fully describe thermal effects or a boundary between two different magnetic materials.

Atomistic and micromagnetic models require input parameters such as the exchange coupling strength and anisotropy constants. In atomistic models these are obtained from experimental measurements or *ab-initio* calculations. In the following thesis, the input parameters are obtained from *ab-initio* calculations [25]. In micromagnetic simulations the input parameters are obtained from either experiments, *ab-initio* or atomistic models. This links the different types of models together and extends the possible time and length scales possible in each type of simulation.

1.4.1 Magnetic modelling of IrMn

Whilst FM materials can be modelled using continuum micromagnetic techniques, the modelling of AFM materials cannot be, due to the lack of bulk magnetic moment described in section 1.3.2. AFMs can be modelled using *ab-initio* methods, and using these methods it is possible to calculate the static properties but they cannot model any dynamic properties and the computational resources required means they are limited to only a few hundred atoms in size. Atomistic modelling is however perfect for modelling AFM materials. The atomistic detail means the complex magnetisation dynamics and magnetic structures can be captured including both dynamic and static calculations. Continual increases in computational power means that currently atomistic calculations are now possible up to billions of atoms in size, corresponding to the size of the components in most spintronic devices. They also have the capability of measuring intricate material details such as composition changes, and disorder effects which are both very important in the thin films used in spintronic devices.

1.5 Thesis Outline

A deeper understanding into the complex magnetisation structures and dynamics in AFM materials is crucial to the creation of novel anti-ferromagnetic spintronic devices which will give faster, lower power consumption, smaller devices to keep up with Moore's law. Atomistic modelling is a vital tool in understanding these properties. In this thesis an atomistic model of the industrially relevant AFM Iridium Manganese is created and the magnetic properties are discussed to an unprecedented level.

The thesis starts with an in-depth discussion of the atomistic spin model of IrMn. The atomistic model is then tested against previous experimental and *ab-initio* results for the static properties of well studied compositions. From this the more interesting, composition dependence and finite size dependence's are studied to investigate the structures which will be used in exchange biased systems. This thesis also answers one of the largest debated topics within the study of IrMn, the magnitude and symmetry of the anisotropy, where previously theoretical and experimental calculations differed by orders of magnitudes. Finally, IrMn will be coupled to a FM to study the origin of the exchange bias effect, initially in a single film and then in a multigranular film as used in spintronic device applications.

2

ATOMISTIC SPIN MODELS

Atomistic modelling has recently emerged as an essential tool in understanding the complex behaviours that govern magnetic materials. Atomistic spin models are based on the principle that each atom possesses a local magnetic moment located on the lattice site. A local magnetic moment assumes that all of the electrons are localised around the atom, the extent to which electrons are localised has always been a heavily debated issue in *3d* metals where the magnetisation originates in the loosely bound outer electrons. However, recent *ab-initio* calculations of the electron density show that even in *3d* ferromagnets the spin polarisation is well localised to the lattice site [26]. The local magnetic moment on each lattice site is known as the spin moment (μ_S), that is dependent on atomic species.

The simulations in this thesis were performed using the vampire software package [27]. VAMPIRE is a software package developed for atomistic spin dynamics simulations. It is open-source and freely available from http://vampire.york.ac.uk. The code was first written 12 years ago by Dr. Richard Evans, since then it has expanded considerably and has contributions from people working across the world, including myself.

In this chapter the fundamentals of atomistic spin models are discussed. Then, the time and temperature dependent system dynamics and finally, an atomistic spin model of IrMn will be presented.

2.1 The Generalised Heisenberg Hamiltonian

The energetics of a system of magnetic spins are described by the spin Hamiltonian. The spin Hamiltonian is formed from a summation of energy terms incorporating all the magnetic interactions into a simple equation. These energy

terms describe the interaction of an atomic spin moment (μ_S) with every other spin moment in the system and an external magnetic field. The spin Hamiltonian ($\mathscr{H}$) has the form:

$$\mathscr{H} = \mathscr{H}_{\text{exchange}} + \mathscr{H}_{\text{anisotropy}} + \mathscr{H}_{\text{applied}} + \mathscr{H}_{\text{dipolar}}. \tag{2.1}$$

In our system the magnetic energy is a sum of four components: the exchange interaction ($\mathscr{H}_{\text{exchange}}$), the magnetic anisotropy ($\mathscr{H}_{\text{anisotropy}}$), the applied magnetic field ($\mathscr{H}_{\text{applied}}$) and the dipolar field ($\mathscr{H}_{\text{dipolar}}$). These are described in more detail in the following sections, and then the specific form used for Iridium Manganese is discussed along with the chosen parameters in section 2.4.

2.1.1 The Exchange Hamiltonian

The largest contribution to the Spin Hamiltonian in most magnetic materials is from the exchange field, which is responsible for long range magnetic order. The exchange interaction can be derived by considering the simplest case of a system of two electrons (a and b). The first electron is in state $\psi_a(\mathbf{r}_1)$ at position $\mathbf{r}_1$ and the second electron is in state $\psi_b(\mathbf{r}_2)$ and position $\mathbf{r}_2$. The joint wavefunction of this system ($\Psi(\mathbf{r}_1,\mathbf{r}_2)$) can be defined as a linear combination of the individual electron wavefunctions ($\Psi(\mathbf{r}_1,\mathbf{r}_2) = \psi_a(\mathbf{r}_1)\psi_b(\mathbf{r}_2)$) which must be a solution to the Schrödinger equation:

$$\Big[-\frac{\hbar^2}{2m}\nabla_1^2 - \frac{\hbar^2}{2m}\nabla_2^2 + V(\mathbf{r}_1) + V(\mathbf{r}_2)\Big]\Psi(\mathbf{r}_1,\mathbf{r}_2) = E\Psi(\mathbf{r}_1,\mathbf{r}_2), \tag{2.2}$$

where E is the energy of the system and is equal to $E_a + E_b$ where E_a is the energy of electron a and E_b is the energy of electron b. $V(\mathbf{r})$ is the potential at point $\mathbf{r}$. As electrons are indistinguishable $\psi_a(\mathbf{r}_2)\psi_b(\mathbf{r}_1)$ must also be a solution to the Schrodinger equation and the observable properties of the system should not change. This means:

$$|\Psi(\mathbf{r}_1,\mathbf{r}_2)|^2 d\mathbf{r}_1 d\mathbf{r}_2 = |\Psi(\mathbf{r}_2,\mathbf{r}_1)|^2 d\mathbf{r}_1 d\mathbf{r}_2, \tag{2.3}$$

must be true. For this to be the case, either $\Psi(\mathbf{r}_1,\mathbf{r}_2) = \Psi(\mathbf{r}_2,\mathbf{r}_1)$ or $\Psi(\mathbf{r}_1,\mathbf{r}_2) = -\Psi(\mathbf{r}_2,\mathbf{r}_1)$ must also be true. The first case is a symmetric wavefunction (Ψ_{sym}) and the second case is an anti-symmetric wavefunction (Ψ_{anti}). The general

solution is a linear combination of these two wavefunctions in either symmetry or anti-symmetric states [28]:

$$\Psi_{sym}(\mathbf{r}_1,\mathbf{r}_2) = \frac{1}{\sqrt{2}}\left[\psi_a(\mathbf{r}_1)\psi_b(\mathbf{r}_2) + \psi_a(\mathbf{r}_2)\psi_b(\mathbf{r}_1)\right] \tag{2.4}$$

and

$$\Psi_{anti}(\mathbf{r}_1,\mathbf{r}_2) = \frac{1}{\sqrt{2}}\left[\psi_a(\mathbf{r}_1)\psi_b(\mathbf{r}_2) - \psi_a(\mathbf{r}_2)\psi_b(\mathbf{r}_1)\right] \tag{2.5}$$

Due to the Pauli exclusion principle (two or more identical electrons cannot occupy the same quantum state within a quantum system simultaneously), the wavefunction describing a two electron system must be anti-symmetric with respect to the exchange of particles. Therefore, the wavefunction must be equation 2.5 ($\Psi = \Psi_{anti}$).

The total energy of the system can be calculated using the Heitler-London approximation, where the system energy is given by:

$$E = \int\int \Psi^*(\mathbf{r}_1,\mathbf{r}_2)\mathscr{H}\Psi(\mathbf{r}_1,\mathbf{r}_2)\delta\mathbf{r}_1\delta\mathbf{r}_2 \tag{2.6}$$

where $\langle\mathscr{H}\rangle$ is the Hamiltonian of the system, which is a sum of the Hamiltonians of each electron and the interaction Hamiltonian $\mathscr{H} = \mathscr{H}_1 + \mathscr{H}_2 + \mathscr{H}_{1,2}$. $\mathscr{H}_1$ produces the energy terms dependent on electron a, $\mathscr{H}_2$ produces the energy terms dependent on electron b and the $\mathscr{H}_{1,2}$ operator produces the energy terms dependent on the interaction between the electrons ($E_{1,2}$).

The energy $E_{1,2}$ is equal to:

$$E_{1,2} = \int\int \Psi^*(\mathbf{r}_1,\mathbf{r}_2)\mathscr{H}_{1,2}\Psi(\mathbf{r}_1,\mathbf{r}_2)\delta\mathbf{r}_1\delta\mathbf{r}_2, \tag{2.7}$$

this has two energy terms, a Coulomb interaction term between the electrons and their respective atoms and an exchange energy that arrises due to the quantum mechanical exchange of electrons. The exchange component is purely quantum mechanical as in the classical picture exchanging electrons gives no change in energy. Now we have shown that the exchange energy exists, we would like to prove that it is the exchange energy which causes the correlation of spins. The electron wave functions ψ can be split up into two components: the radial component ($\phi(\mathbf{r})$) and the spin component (χ) giving $\psi = \phi(\mathbf{r})\chi$. As we know the total wavefunction must be anti-symmetric under the exchange of electrons

following Pauli's exclusion principle, if the spin component is symmetric the radial component must be anti-symmetric and vice versa. The spin component has two possible states: a singlet state and a triplet state. A system in a singlet state is symmetric and has all the electrons paired with total spin S = 0. Whereas, a system in a triplet state is anti-symmetric and has two unpaired electrons with total spin S = 1. This means there are two possibilities for anti-symmetric total wavefunctions:

$$\Psi_S = \frac{1}{\sqrt{2}}[\phi_a(\mathbf{r}_1)\phi_b(\mathbf{r}_2) + \phi_a(\mathbf{r}_2)\phi_b(\mathbf{r}_1)]\chi_S \tag{2.8}$$

$$\Psi_T = \frac{1}{\sqrt{2}}[\phi_a(\mathbf{r}_1)\phi_b(\mathbf{r}_2) - \phi_a(\mathbf{r}_2)\phi_b(\mathbf{r}_1)]\chi_T \tag{2.9}$$

These two states have energies:

$$E_S = \int\int \Psi_S^* \mathscr{H} \Psi_S d\mathbf{r}_1 d\mathbf{r}_2 \tag{2.10}$$

$$E_T = \int\int \Psi_T^* \mathscr{H} \Psi_T d\mathbf{r}_1 d\mathbf{r}_2 \tag{2.11}$$

The exchange energy will be the difference in energy between these two states so if we calculate the difference as:

$$E_S - E_T = 2\int\int \phi_a(\mathbf{r}_1)\phi_b(\mathbf{r}_2)\mathscr{H}\phi_a(\mathbf{r}_2)\phi_b(\mathbf{r}_1)d\mathbf{r}_1 d\mathbf{r}_2 \tag{2.12}$$

If we consider two spin half particles coupled by an exchange interaction, the joint operator $\mathbf{S}_{tot}$ is $\mathbf{S}_1 + \mathbf{S}_2$, so $\mathbf{S}_{tot}^2 = \mathbf{S}_1^2 + \mathbf{S}_2^2 + 2\mathbf{S}_1 \cdot \mathbf{S}_2$. Therefore, the difference between single and triplet states can be parameterised by $A\mathbf{S}_1 \cdot \mathbf{S}_2$. Combining these two particles results in a joint entity with spin quantum number s = 0 (singlet) or s = 1 (triplet) depending on the relative orientation of the two spins. The eignevalues of $\mathbf{S}_{tot}^2$ are S(S+1) so for the singlet case $\mathbf{S}_1 \cdot \mathbf{S}_2 = -\frac{3}{4}$ whereas for the triplet case $\mathbf{S}_1 \cdot \mathbf{S}_2 = \frac{1}{4}$ [29].

As the difference between the singlet and triplet states can be parameterised by $A\mathbf{S}_1 \cdot \mathbf{S}_2$ the Hamiltonian can be written in the form of an effective Hamiltonian:

$$\mathscr{H} = \frac{1}{4}(E_S + 3E_T) - (E_S - E_T)\mathbf{S}_1 \cdot \mathbf{S}_2 \tag{2.13}$$

This Hamiltonian can be split into two terms, the first term is the spin-independent radial term $\mathscr{H}_{\text{rad}}$ and the second spin-dependent $\mathscr{H}_{\text{spin}}$ term.

The second term represents the exchange of the two electrons so $\mathscr{H}_{\text{spin}} = -\frac{1}{2}(E_S - E_T)\mathbf{S}_1 \cdot \mathbf{S}_2$. Here, we define an exchange constant (J_{ex}) where

$$J_{ex} = \frac{1}{2}(E_S - E_T) = \int\int \phi_a(\mathbf{r}_1)\phi_b(\mathbf{r}_2)\mathscr{H}_{spin}\phi_a(\mathbf{r}_2)\phi_b(\mathbf{r}_1)d\mathbf{r}_1 d\mathbf{r}_2 \tag{2.14}$$

From this we can define our spin Hamiltonian:

$$\mathscr{H}_{\text{spin}} = -J_{ex}\mathbf{S}_1 \cdot \mathbf{S}_2, \tag{2.15}$$

The minimum energy occurs for positive values of J_{ex} when the system forms a triplet state (S = 1), whilst the singlet state (S = 0) is the lowest energy configuration if J_{ex} is negative. The spins will align anti-parallel in the singlet case and parallel in the triplet state. Even though we have only considered a two electron system it still shows the origin of the exchange coupling in determining the magnetic ordering in a system.

In real materials, the situation is much more complicated as they are comprised of many atoms all with multiple electrons. Exact calculations of the exchange interactions for multiple atom systems are not possible and we have to use an approximation. An approach that deals with a multi-electron system is an extension of the Heisenberg model which allows interactions between all spins in the system by treating them all as pairs of electrons. The exchange Hamiltonian is:

$$\mathscr{H} = -\sum_{i<j} J_{ij}\mathbf{S}_i \cdot \mathbf{S}_j, \tag{2.16}$$

where $J_{ij}$is the exchange coupling constant for the interaction between spins $\mathbf{S}_i$ and $\mathbf{S}_j$. The exchange coupling constant can be calculated using *ab-initio* methods.

2.1.2 The Magnetocrystalline Anisotropy

Anisotropy is the directional dependence of a material's magnetic properties. The magnetic anisotropy can be classified in different categories, each one characterised by a different origin. In most materials the main source of magnetic anisotropy is the magneto-crystalline anisotropy. Magneto-crystalline anisotropy occurs due to spin-orbit interactions and crystal field interactions. The crystal field reflects the local symmetry of the crystal or surface. Spin-orbit coupling is the relativistic interaction of a particle's spin with its motion inside a potential. In general the orbital moment of magnetic materials is very small compared to the spin moment because the orbital motion is suppressed or *quenched* by the electrostatic crystal field. $3d$ wavefunctions of free atoms have a "circular current" character and yield an orbital moment but in a crystalline environment the electrons are forced to form standing waves with zero orbital moment. These motions are shown in Fig. 2.1 (a) and (b) respectively. However, spin-orbit coupling competes with the crystal field and yields a small amount of residual orbital moment. The size of the magnetocrystalline anisotropy is due to the competition of the quenching from the crystal field and the unquenching from the spin-orbit coupling. This competition changes the shape of the charge density to a partially quenched orbital as shown in Fig. 2.1 (c). Quenched waves have a standing wave character and therefore adapt more easily to the crystal field and have a lower magneto-crystalline anisotropy. Changing the direction of the spins modifies the charge densities and therefore changes the crystal field energy [30, 31].

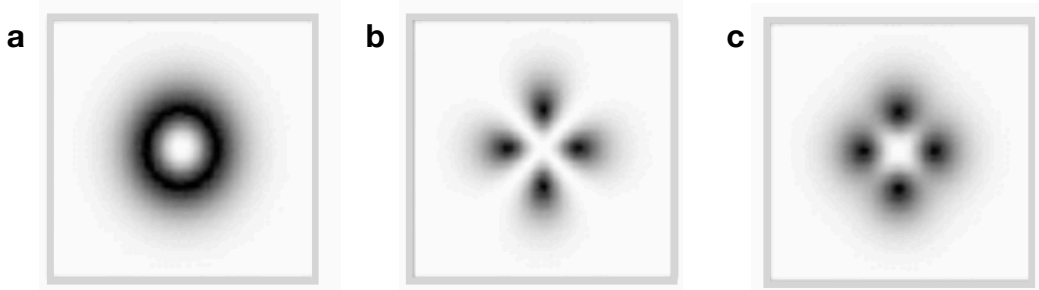

Figure 2.1: **The electron density with different amounts of quenching** (a) unquenched (b) quenched (c) partially quenched. Figure taken from [31]

The simplest form of magneto-crystalline anisotropy is uniaxial anisotropy, where the magnetic moments prefer to align along a single axis. The axis they align along is known as the material's easy axis. The uniaxial anisotropy energy is given by:

$$\mathscr{H}_{\text{anisotropy}} = -k_u \sin^2\theta \tag{2.17}$$

where k_u is the uniaxial anisotropy constant and θ is the angle from the easy axis. Uniaxial anisotropy usually occurs in crystals with a distorted lattice, and is the simplest form of the anisotropy. Materials with a cubic crystal structure have a more complicated form of anisotropy known as cubic anisotropy. Whereas in uniaxial anisotropy there is one easy axis, materials with a cubic symmetry have three. The anisotropy Hamiltonian for a cubic system is given by:

$$\mathscr{H}_{\text{anisotropy}} = d_2(S_x^2 S_y^2 + S_x^2 S_z^2 + S_y^2 S_z^2) \tag{2.18}$$

where d_2 is the cubic anisotropy energy per atom. The form of the magnetocrystalline anisotropy Hamiltonian is dependent on the lattice structure and material properties. The anisotropy in Iridium Manganese, of special interest in this thesis, cannot easily be expressed using a simple equation for the Hamiltonian, and so the specific anisotropies for IrMn are described in section 2.4.4.

2.1.3 The Applied Magnetic Field

A magnetic system will also interact with an externally applied field (B_{app}). The system couples to the magnetic field such that the Hamiltonian is of the form:

$$\mathscr{H}_{\text{app}} = -\sum_i \mu_S(\mathbf{S}_i \cdot \mathbf{B}_{\text{app}}), \tag{2.19}$$

where μ_S is the spin magnetic moment and $\mathbf{S}_i$ is the spin vector on site i. The minimum energy occurs when the spin moment aligns with the applied field. The strength of the coupling is proportional to the magnitude of the magnetic moment

2.1.4 The Dipolar Field Hamiltonian

To obey Maxwell's equations, the magnetic field induced from a magnetisation of a magnet must not diverge ($\nabla \cdot \mathbf{B} = 0$). Therefore, the flux lines must be closed loops causing any magnetised body to have a field surrounding it. The dipole field is generated by the magnetisation of the material and its strength depends on the size, shape and separation of the atomic moments. Atomistically, this can be expressed by the dipole-dipole interaction:

$$\mathbf{B}_{\text{dip}} = \frac{\mu_s \mu_0}{4\pi} \frac{3(\mathbf{S}_i \cdot \hat{\mathbf{e}}_{ij})(\hat{\mathbf{e}}_{ij} \cdot \mathbf{S}_j) - \mathbf{S}_i \cdot \mathbf{S}_j}{r_{ij}^3}, \tag{2.20}$$

where r_{ij} is the distance between spins $\mathbf{S}_i$ and $\mathbf{S}_j$, $\hat{\mathbf{e}}_{ij}$ is the unit vector between $\mathbf{S}_i$ and $\mathbf{S}_j$. The strength of the dipole-dipole interaction is proportional to $1/|\mathbf{r}_{ij}|^3$ making it a very long range interaction. For a system of N atoms each dipole is interacting with $N-1$ dipoles so an atomistic calculation has a computational complexity proportional to $N(N-1) \sim N^2$ which is very computationally expensive and can, in large systems (> 1,000,000 atoms) double the simulation time [15].

2.2 Parameterisation

The atomic parameters in the extended form of the Heisenberg Hamiltonian (J_{ij},k_u,μ_S) can be obtained from either experiments or from *ab-initio* density functional theory (DFT) calculations. For instance, J_{ij} is related to the Curie temperature via the mean field expression: $J_{ij} = 3k_B T_c/(\epsilon z)$ [32] which comes from statistical mechanics and was derived by Garanin in 2004 [32] and comes from the balance of the exchange to the thermal ordering. Here z is the number of nearest neighbours and ϵ is a correction factor depending on the crystal structure which is calculated from spin-wave theory [26]. The parameters I use and where they come from are discussed later in the thesis.

2.3 Integration methods

The spin Hamiltonian calculates the energy of a magnetic system but provides no information regarding its time evolution or the thermal fluctuations. The time dependence and thermal fluctuations give the ability to calculate the equilibrium temperature dependence and the ground state of the system.

In this thesis two integration methods have been used. The dynamic behaviour is calculated using the stochastic Landau-Lifshitz-Gilbert equation with a Heun integrator and the static properties are calculated using Monte Carlo methods.

2.3.1 Landau-Lifshitz equation

The time dependent behaviour of a magnetic body is described by the torque equation first defined by Landau and Lifschitz [33].

$$\frac{\partial \mathbf{M}_i}{\partial t} = -\gamma_e(\mathbf{M}_i \times \mathbf{B}_{\text{eff}}) - \lambda\gamma_e(\mathbf{M} \times \mathbf{M} \times \mathbf{B}_{\text{eff}}) \tag{2.21}$$

The Landau-Lifschitz equation models the motion of a magnetic moment $\mathbf{M}_i$ in the presence of an effective field ($\mathbf{B}_{\text{eff}}$). The effective field causes the atomic moments to precess around the field, where the frequency of precession in this case is determined by the gyromagnetic ratio of an electron ($\gamma_e = 1.76 \times 10^{11}$ rad $\text{s}^{-1}\text{T}^{-1}$) and λ is the damping constant. The first term models the precession of a spin around an applied field, and the second term represents the relaxation of the magnetisation towards the effective field direction. The damping accounts for the energy dissipation from the system. The energy is dissipated in two ways: directly and indirectly. Direct damping is the energy transfer to external degrees of freedom such as phonons, while indirect damping results from energy transfer occurring within the magnetic system. This term represents the energy transfer due to the coupling of the atomic moment to a heat bath (the lattice/other electrons). This causes a damped precessional motion as the magnetic moment relaxes towards the effective field direction. The phenomenological damping constant, determines the rate of relaxation towards the effective field direction. The precession is damped which eventually leads to the spin aligning with the net field.

2.3.2 Landau-Lifshitz Gilbert equation

Gilbert modified the damping parameter in the Landau-Lifshitz equation, deriving his equation from Lagrangian analysis which is more physical than that of Landau and Lifshitz. The main difference is that in Gilbert formalism the size of the damping effects the precession of the magnetisation [34]. This gives a minimum switching time and therefore a more realistic equation. This alters the form of the Landau-Lifshitz equation to form the Landau-Lifshitz-Gilbert equation:

$$\frac{\partial \mathbf{S}_i}{\partial t} = -\frac{\gamma_e}{1+\lambda^2}\left[\mathbf{S}_i \times \mathbf{B}_{eff} + \lambda \mathbf{S}_i \left(\mathbf{S}_i \times \mathbf{B}_{eff}\right)\right] \tag{2.22}$$

This equation was initially derived from the motion of macroscopic spins. The same equation can be used to describe the motion of microscopic (atomistic) spins [35]. For microscopic spins the equation is derived from the quantum mechanical form of the Heisenberg model under an applied field [36]. The effective field, felt by a spin on site i is calculated as:

$$\mathbf{B}_{\text{eff}} = -\frac{1}{\mu_0 \mu_S} \frac{\partial \mathscr{H}}{\partial \mathbf{M}_i}. \tag{2.23}$$

2.3.3 Langevin Dynamics

The LLG equation includes no description of temperature and is therefore strictly only applicable at zero Kelvin. The temperature effects are added using Langevin dynamics. Langevin dynamics was developed by W. F. Brown [37] and introduces a coupling of the system to a heat bath. A stochastic field $\mathbf{B}^i_{\text{Th}}$ is included in the effective field:

$$\mathbf{B}^i_{\text{eff}} = -\frac{1}{\mu_0 \mu_S} \frac{\partial \mathscr{H}}{\partial \mathbf{M}_i} + \mathbf{B}^i_{\text{Th}} \tag{2.24}$$

taking into account both dissipation effects and the exchange of energy between the heat bath and the system. The thermal field can be described as a white noise term. For such an approximation to be valid, the requirement is that the time correlation between the fluctuations induced by the thermal field is shorter than the spin motion. This is generally the case for magnetisation dynamics that occurs on the nanosecond time-scale or slower, as it happens for the phenomena studied in this work. The white noise term is described by a Gaussian distribution (Γ) with a mean of zero. The width of the distribution is proportional to the size of the thermal fluctuations [38]. This assumption is justified by assuming that the time-scale of the electron heat bath is much faster than the spin system. In this case, the bath degrees of freedom can be averaged out and replaced by a stohastic field with a white noise correlation functions [38]. This is incorporated into the LLG equation by including a thermal field into the effective field [39]:

$$\mathbf{B}^i_{\text{Th}} = \Gamma(t) \sqrt{\frac{2\lambda k_B T}{\gamma \mu_S \Delta t}}, \tag{2.25}$$

where k_B is the Boltzmann constant, T the simulation temperature, μ_s is the magnitude of the spin magnetic moment, and Δt is the integration time step.

2.3.4 Time integration using the Heun method

In order to determine the time evolution of the system, the LLG equation must be solved numerically. The solver must conserve the magnitude of the magnetisation of the spin [40]. The simplest solver is the Euler method. The Euler method

assumes a linear change in spin direction in a single time step. In this thesis, I use a improved version of the Euler method, the Heun method [41]. The Heun method uses a predictor-corrector algorithm which allows for larger time steps. In predictor-corrector algorithms however, the energy is not conserved, meaning they can be inaccurate. These inaccuracies are accounted for using a re-normalisation step, which preserves the correct dynamics. There are integrator's which preserve energy however they require significantly smaller time steps, are much more computationally expensive and can also include fictitious damping effects.

This algorithm has two parts, the predictor step and the corrector step. The predictor step calculates a new spin direction using one Euler step:

$$\mathbf{S}_i' = \Big(-\frac{\gamma}{(1+\lambda^2}[\mathbf{S}_i \times \mathbf{B}_{\text{eff}} + \gamma_e \mathbf{S}_i \times (\mathbf{S}_i \times \mathbf{B}_{\text{eff}})]\Big)\Delta t \tag{2.26}$$

After the predictor step the effective field is re-calculated with the new (predicted) spin positions as it is proportional to the spin directions (the thermal field being constant over the step). This is performed on every spin in the system. The corrector step then uses these predicted spin positions and revised fields to calculate the final spin positions using another Euler step and averaging the result. This gives a complete integration step given by:

$$\mathbf{S}_i(t+\Delta t) = \mathbf{S}_i(t) + \frac{1}{2}[\Delta \mathbf{S}_i(\mathbf{S}_i, t) + \mathbf{S}_i(\mathbf{S}_i', t)]\Delta t \tag{2.27}$$

This is repeated many times to simulate the evolution of the system. Spin dynamics is very useful for obtaining dynamic information about a magnetic system. Equilibrium magnetic properties can be found more efficiently using a Monte Carlo simulation [42].

2.3.5 Monte Carlo Methods

The Monte Carlo Metropolis algorithm is a fast, efficient way of finding equilibrium properties when dynamics are not required [43]. One reason for this is that, while the LLG equation can explore the whole phase space, the timescales for this to occur are usually impractically long.

The first step of the Monte Carlo algorithm is to take a spin S_i and change its spin direction from its initial direction $\mathbf{S}_i$ to a new trial direction $\mathbf{S}_i'$. Then, the change in energy between the initial and final states is calculated ($\Delta E = E(\mathbf{S}'_i) - E(\mathbf{S}_i)$. The new trial direction is either accepted or rejected based on an acceptance probability (P):

$$P = \exp\left(\frac{-\Delta E}{k_B T}\right), \tag{2.28}$$

where k_B is the Boltzman constant and T is the absolute temperature. If ($\Delta E < 0$, P > 1) and the spin is automatically accepted. This is repeated N times with N corresponding to the number of atoms in the system. This is known as a Monte Carlo step.

The new random spin positions must obey the principle of detailed balance [44]. This principle is satisfied if the moves are uniformly distributed over the sphere. A computational method for this was devised by Marsaglia [45]. This computational method is efficient at high temperatures, however is inefficient at low temperatures. At low temperatures the exchange energy means only moves with a small change in spin position will be accepted. At low temperatures a tuned step size will be more efficient. This is done using a Gaussian step, which ensures the uniform distribution of points therefore satisfying the principle of detailed balance but allows the displacement to be tuned with temperature. The width of the Gaussian distribution is chosen so the acceptance rate for the Monte Carlo moves is about 50%.

In this thesis, the adaptive method by Alzate-Cardona *et al* [46] is used which is an adaptation of the Hinzke-Nowak method [47] for determining the new spin positions. The Hinzke-Nowak method uses a combination of the uniform and Gaussian methods described above which also includes a probability of the spin flipping. A spin flip reverses the direction of the spin ($\mathbf{S}_i' = -\mathbf{S}_i$). This allows the system to equilibrate quickly at any temperature, the adaptation by Alzate-Cardona *et al* [46] changed the width of the Gaussian distribution so the acceptance rate is always at approximately 50%.

Monte Carlo methods are useful in modelling stationary system states such as the Néel temperature or the ground state spin structure. For these simulations they provide a natural way of simulating temperature effects and quickly converge to equilibrium. However, due to the limited drift process and lack of time quantification it is unsuitable for modelling dynamic systems such as a hysteresis cycles [42].

2.4 Atomic scale parameters of Iridium Manganese

For the atomistic model to represent real materials as closely as possible the parameters for the model are derived from experimental data or *ab-initio* calculations. The atomistic model uses the assumption that each atom possesses a magnetic moment located on the lattice site. The first step is to create an accurate lattice structure for Iridium Manganese then the alloys structure and finally the parameters are chosen.

2.4.1 Crystallographic structure

Iridium Manganese has previously been observed in many crystallographic phases. Most notable, the $L1_0$, $L1_2$ and γ phases. These phases all look very different as the Ir and Mn atoms are in different positions within the unit cell leading to different crystallographic and magnetic structures. However, the majority of these structures have an underlying FCC lattice. The FCC lattice occurs because the Iridium atoms are large and space out the Mn atoms, for all compositions with Mn concentrations less than 95% the structure can be said to be based on an FCC structure. For concentrations of Mn greater than 95% the magnetic structure changes and has a complex allotropic structure with 58 atoms in the unit cell [48]. As the compositions used in spintronic devices have approximately 17 - 25% Ir, we can assume that the IrMn will have a base FCC structure.

The FCC unit cell of Iridium Manganese is comprised of four atoms. In the [001] plane this forms the structure shown in Fig. 2.2(a). The unit cell length (a) for $IrMn_3$ is approximately 0.375 nm but this depends on the composition and order of the crystal.

Iridium Manganese can be grown in many different crystallographic orientations depending on the seed layer used in the sputtering process. Although these all give an observable exchange bias, the largest exchange bias occurs in samples grown with a (111) structure. To maximise the exchange bias and reproduce the thin films used in spintronic devices the crystal structure needs to be reoriented to lie so the (111) direction points out of plane. The (111) oriented crystal structure is shown in Fig. 2.2(b).

Iridium Manganese has a complex magnetic structure containing four magnetic sublattices. The moments of the atoms in different sublattices want to align

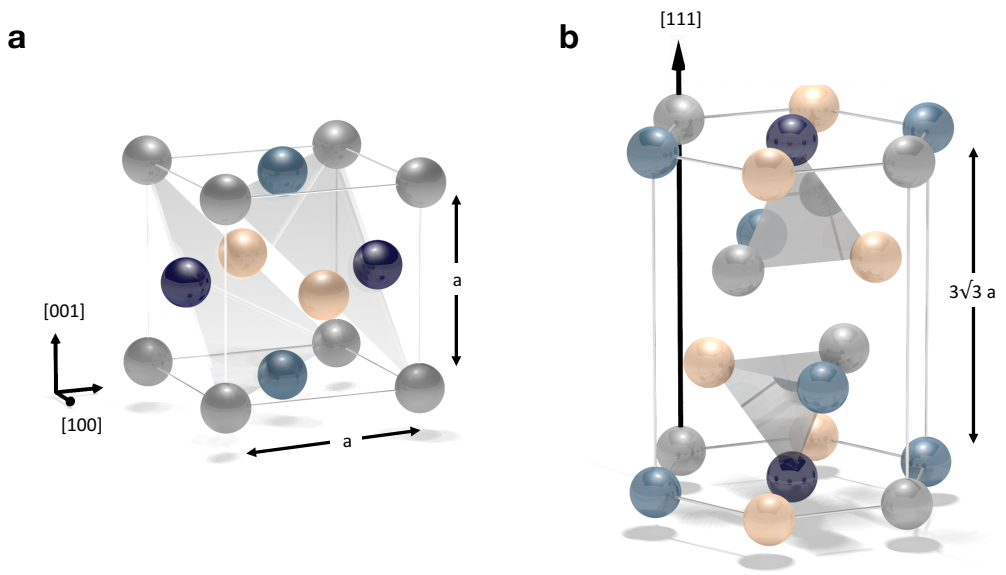

Figure 2.2: **Visualisations of the unit cell structure of Iridium Manganese.** (a) The FCC unit cell structure of Iridium Manganese in the [001] plane orientation. a is the unit cell length. The (111) planes are shaded in grey. (b) The (111) oriented FCC crystal structure. The colours represent the four magnetic sublattices present in Iridium Manganese.

180 degrees apart, due to the Anti-ferromagnetic exchange interactions, but because there are four sublattices this is impossible. Instead the ground states form complex frustrated structures. In Fig. 2.2 the sublattices are highlighted by the different colours and the glass tetrahedron contains one atom from each AFM sublattice, containing all the magnetic information of the crystal.

The magnetic unit cell is the minimum number of atoms which contains all of the magnetic and crystallographic information. The (111) oriented unit cell contains 24 atoms with six atoms from each sublattice and has dimensions $\sqrt{2} \times \sqrt{6} \times \sqrt{3}$ unit cell lengths.

2.4.2 Order and Composition in Iridium Manganese alloys

The ordering of Iridium Manganese depends on the placement of the Ir atoms within the Mn lattice. In ordered Iridium Manganese the Ir atoms are all in the same sublattice and in disordered Iridium Manganese the Ir atoms are equally spread throughout the four sublattices. In disordered Iridium Manganese the random removal of atoms means the crystal has no repeating structure and cannot be simplified to the 24 atom unit cell. This is shown schematically for $IrMn_3$ in Fig. 2.3. In $IrMn_3$ 75% of the atoms are Mn and 25% of the atoms are Ir. In

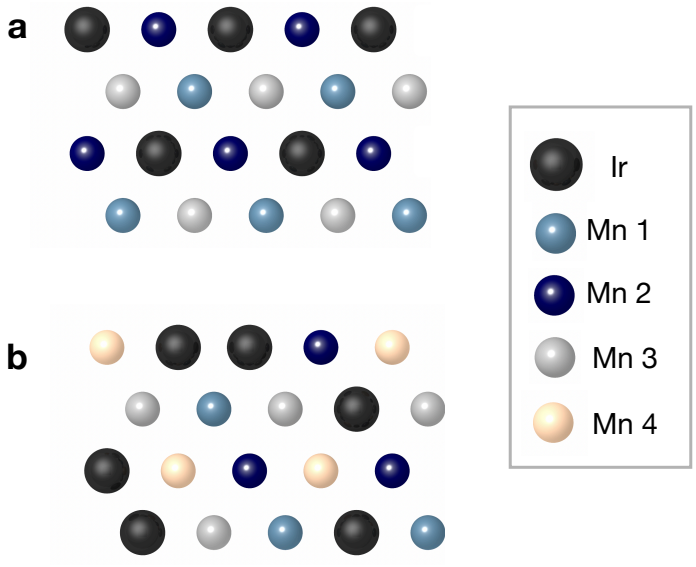

Figure 2.3: **Visualisation of the composition and order of ordered and disordered $IrMn_3$.** The larger black spheres represent Ir atoms and the smaller spheres represent the Mn atoms. The four colours of the Mn atoms represent the different sublattices, as represented by the numbers 1,2,3 and 4 in the key. (a) Ordered $IrMn_3$ where the Ir atoms are all in the same sublattice. (b) Disordered $IrMn_3$ where the Ir atoms are randomly distributed between the four sublattices.

ordered $IrMn_3$ this means one sublattices is completely Ir and three sublattices are completely Mn. In disordered γ - $IrMn_3$ 25% of the atoms in each sublattice are Ir and 75% of the atoms in each sublattice are Mn.

2.4.3 The exchange constants

L. Szunyogh *et al.* calculated the exchange integral for ordered IrMn and $IrMn_3$ using *ab-initio* methods [25]. They found that the exchange coupling varies sinusoidally with interatomic spacing (R_{ij}). The variation is shown in Fig. 2.4 which is taken from reference [25]. The figure shows the exchange coupling switches from positive (FM) to negative (AFM) with each nearest neighbour. The nearest neighbour (NN) interactions are strongly AFM and the next nearest neighbour (NNN) interactions are weaker and FM. The NN interactions occur between atoms in different sublattices whereas the NNN interactions occur between atoms in the same sublattices, which is why atoms in the same sublattice align in the same direction and atoms in different sublattices try to align anti-parallel. The NNN interactions are important because they stabilise the magnetic structure.

The exchange Hamiltonian only has significant values for the first four nearest neighbours. If all four nearest neighbours are included the exchange Hamiltonian

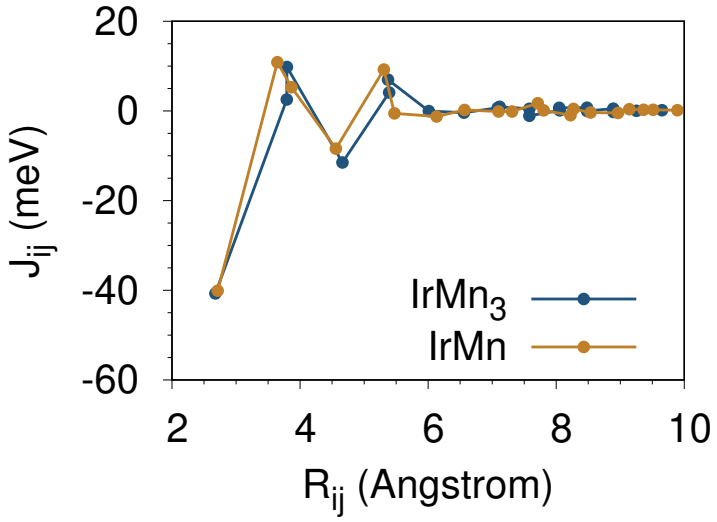

Figure 2.4: ***Ab-initio* data from reference [25] calculating how the exchange constants in IrMn and $IrMn_3$ vary with interatomic spacing (R_{ij}).** The data was calculated using the relativistic torque method. The exchange constants periodically vary between positive (FM) and negative (AFM) with interatomic spacing. The first set of points represents the nearest neighbour (NN) interaction and the second set of points represents the next nearest neighbour (NNN) interaction, this pattern continues.

will include over 30 terms per atom. To calculate all of these terms would be computationally expensive meaning the simulations would be very slow. To decrease the computational power necessary, the Hamiltonian is approximated to only NN and NNN interactions. The approximation used is described in section 3.2 and in 3.3 the approximation will be compared to the full calculation with four nearest neighbours.

Fig. 2.4 shows that the exchange interactions are approximately the same for ordered $L1_0$-IrMn and ordered $L1_2$-$IrMn_3$. These both have very different compositions and structures but this has not greatly affected the exchange constants. As this thesis focuses on compositions close to IrMn and $IrMn_3$ we have assumed that the exchange interactions are the same for all compositions studied.

2.4.4 The magnetocrystalline anisotropy

The size of the magnetocrystalline anisotropy is due to the competition of the quenching from the crystal field and the unquenching from the spin-orbit coupling. Quenched waves, have a standing wave character and therefore adapt more easily to the crystal field and have a lower magneto-crystalline anisotropy. The size of

the crystal field is caused by the symmetry in the crystal, and the Ir atoms will break this symmetry meaning that the Mn orbitals will be more quenched in some directions (next to Mn atoms) than in others (next to Ir atoms). The Ir atoms have a very large spin orbit coupling, which will also reduce the quenching of the electron density in the Mn atoms near them. This means that it is easier for the spin directions to move in some directions (near the Mn atoms) than in others (near other Ir atoms).

In disordered IrMn alloys each atom has a different local environment. The anisotropy is dependent on an atom's environment therefore each atom has a unique anisotropy. The anisotropy surfaces for three different alloys of IrMn are shown in Fig. 2.5, each one shows the Mn atom sitting in a completely different anisotropy environment. If each atom has a unique anisotropy the spin Hamiltonian cannot be expressed numerically. Ideally you would calculate the anisotropy of each individual lattice site using *ab-initio* methods. Unfortunately, using current methods the computational resources necessary would be too large. Instead we express the anisotropy using the Néel pair anisotropy model.

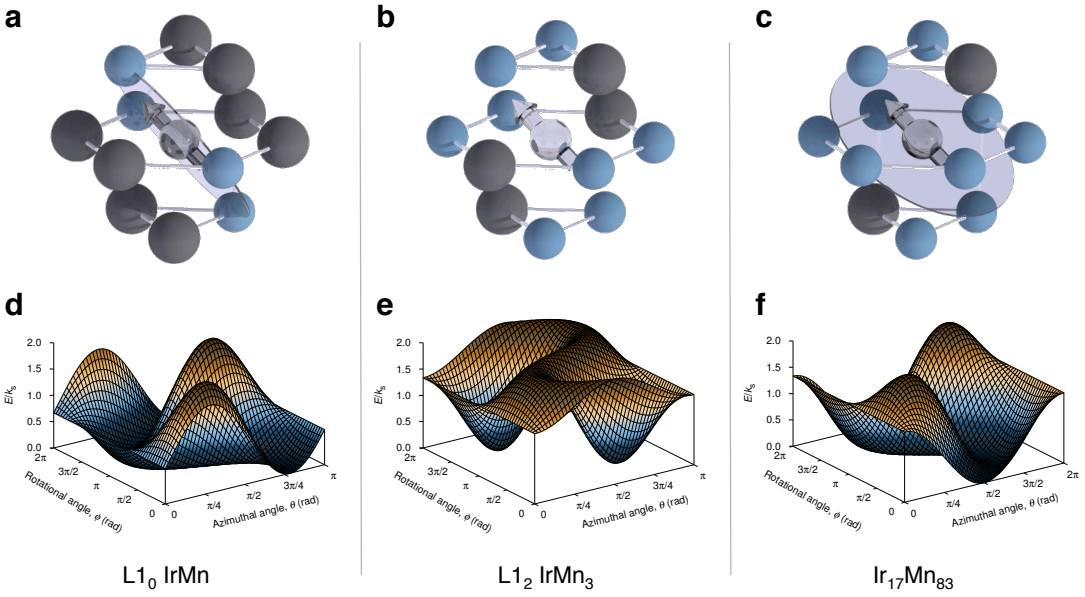

Figure 2.5: **Local atomic configurations and anisotropic energy surfaces for different IrMn compositions calculated with the Néel pair anisotropy model.** The form and anisotropy energy in IrMn is strongly dependent on the local atomic ordering. In disordered crystal structures this leads to a complex energy surface with highly localised variations of the magnetic anisotropy. (a) Spin configuration for ordered $L1_0$ - IrMn, which has an (d) easy plane anisotropy. (b) Spin configuration for ordered $L1_2$ which (e) has a complex energy surface. (c) Spin configuration for disordered γ -$IrMn_3$ which (f) has a complex energy surface.

2.4.4.1 The Néel surface anisotropy model

It has been suggested that a loss of crystal symmetry could result in a reduction in the local anisotropy [49]. Ideally, the loss of anisotropy would be modelled using a completely *ab-initio* approach, but this is only feasible for up to a few 100 atoms, so this is an unrealistic approach to model a realistic size AFM system. Instead, the Néel surface Anisotropy model is used, a model first proposed by Néel in 1954 [49] to model the surface of a crystal. The model assumes that the lack of bonds at surfaces causes an anisotropy. We have extended the Néel pair anisotropy model to model the non magnetic Ir atoms. The Iridium atoms are removed from the simulation because they are non magnetic. These holes create missing bonds and act like the surface in the NSA model. The minimum energy is found when the moments point away from the missing Iridium atoms. This idea has previously been used to model other magnetic materials such as NdFeB [50] but this is the first use of the Néel anisotropy model for use in anti-ferromagnets.

$$\mathscr{H}_{\mathrm{N}}^{i} = -\frac{\mathscr{L}(r_{ij})}{2}\sum_{ij}^{z_i}\left(\mathbf{S}_i \cdot \mathbf{e}_{ij}\right)^2 \tag{2.29}$$

The NSA model calculates the energy of a spin ($\mathbf{S}_i$), by calculating $\mathbf{S_i}\cdot\mathbf{e}_{ij}$ where $\mathbf{e}_{ij}$ is a unit vector connecting spin i with its z nearest neighbours (j). If the atom is missing nearest neighbours (if they are at the surface or the neighbour is Ir) the magnetic moment will have a minimum energy with spins pointing away from the missing bonds. The Hamiltonian (equation 2.29) is calculated by summing over all the atoms in the crystal. $\mathscr{L}(r_{ij})$ is the NSA constant, which varies with distance. In IrMn all the nearest neighbour atoms are at the same distance (r_0) and so the NSA is assumed to be constant $\mathscr{L}(r_{ij}) = \mathscr{L}(r_0)$.

The NSA model was tested by rotating the moment of a Mn atom around the (111) plane of ordered $IrMn_3$. The change in energy was compared to that calculated by L. Szunyogh et al in reference [25]. The change in energy calculated using equation 2.29 exactly matches the *ab-initio* result. This supports the use of the NSA model for modelling IrMn.

The value of the anisotropy constant in IrMn is a widely disputed problem with experimental and theoretical calculations varying by over two orders of magnitude. L. Szunyogh *et al* performed self-consistent calculations using the fully relativistic screened Korringa-Kohn-Rostoker method [25]. They found an extremely large second order magnetic anisotropy for $IrMn_3$, leading to energy barriers of the order of $300 \times 10^5 \mathrm{J/m}^3$ [51]. G. Vallejo-Fernandez *et al* inferred the anisotropy

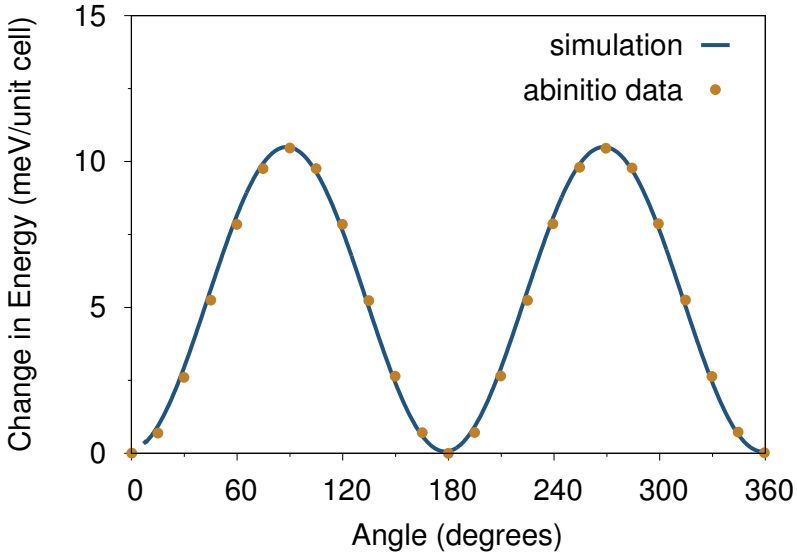

Figure 2.6: **Simulation to calculate the change in energy when a spin is rotated around the 111 plane and compared to the *ab-initio* result by L. Szunyogh *et al* [25].** The points are the *ab-initio* data and the line is the data simulated using equation 2.29. The simulated result and *ab-initio* data both have a $\sin^2(\alpha)$ energy dependence. The $\sin^2(\alpha)$ energy dependence is due to the spin having a high anisotropy energy when it rotates towards the large orbitals of the Ir atoms.

constant of the IrMn experimentally by measuring the mean blocking temperature (T_B) of an IrMn/CoFe bilayer. The blocking temperature is the temperature where the exchange bias shift changes sign, due to thermal activation. They inferred a value of the anisotropy constant of $(5.5\pm 0.5) \times 10^5 J/m^3$ [51] almost two orders of magnitude lower than the theoretical calculation. The symmetry of the anisotropy in $IrMn_3$ is also debated. L. Szunyogh *et al* [25] calculated the anisotropy to be cubic in symmetry and G. Vallejo-Fernandez *et al* [51] calculated the temperature dependence of the anisotropy energy to have a uniaxial symmetry from the Callen-Callen laws [52] (this will be expanded on in Chapter 4) . This difference comes from the problem in defining the bulk anisotropy of an AFM. In this thesis we have used the theoretically calculated value of the anisotropy. This assumption is tested and the disparity between the theoretical and experimental results is resolved in chapter 4.

2.5 Summary

This chapter has discussed the fundamentals of atomistic spins models. The generalised Heisenberg Hamiltonian was described and the Hamiltonian's for

the exchange energy, anisotropy energy, applied field and dipole fields were formalised. Next an atomistic spin model for the industrially relevant AFM Iridium Manganese was created, an approximation for the exchange energy was taken from *ab-initio* results and the anisotropy is calculated using the Néel surface anisotropy model.

3

Properties of Anti-ferromagnetic materials

Calculating the properties of AFM materials is much more complex than FM's as the bulk magnetisation is zero. This means that experimentally the properties cannot be calculated by measuring the macroscopic magnetisation. Instead the magnetisation must be calculated in other more ingenious ways, such as measuring how they affect other materials or by injecting currents/neutrons through the material. The same is true computationally, where the properties cannot be calculated by looking at the bulk magnetic properties. Computationally this problem can be solved in a much simpler way as we can look at the properties of the individual sublattices or even individual atoms instead of looking at the bulk magnetic properties. In the following section we will discuss how the properties of AFMs are calculated computationally from the sublattice properties. Following on from this the bulk magnetic properties of IrMn will be calculated in the most common phases to check a match to previous experimental results. Once the model has been verified more complicated structures and compositions will be studied. The work on finite size effects in IrMn thin films was published in the journal of applied physics [19].

3.1 Calculating the Néel temperature of an AFM

One of the most important properties in an AFM is the Néel temperature (T_{N}), the AFM equivalent of the Curie temperature in FM's. T_{N} describes the stability of an AFM to temperature fluctuations as it is the temperature above which the AFM will become paramagnetic. In paramagnetic systems, as described in section 1.1, the thermal fluctuations are higher than the exchange interactions and the system displays no net magnetisation. Below the Néel temperature the exchange

interactions are higher than the thermal fluctuations and the sublattices tend to align, causing a net sublattice magnetisation. Spintronic devices tend to operate at non-zero temperatures (usually around room temperature) therefore in any spintronic device the Néel temperature is an important factor to consider. In the following section we will attempt to calculate the Néel temperature of ordered $L1_2$- $IrMn_3$ from the sublattice properties using two methods. The first method is from the sublattice magnetisation, the second is from the sublattice magnetic susceptibility. The first method is very quick computationally and accurate for bulk systems. The second is much slower as it takes a long time for the magnetic susceptibility to reach its equilibrium value however it is very accurate even for thin film systems. For both simulations the same 6nm × 6nm × 6nm system of ordered $IrMn_3$ was used. Ordered $IrMn_3$ has 75% Mn and 25% Ir with all of the Ir atoms in the same sublattice, as described in section 2.4.2.

3.1.1 Calculation of the Néel temperature from the sublattice magnetisation

The sublattice magnetisation (n) is the sum of the normalised magnetisation of every atom in that sublattice:

$$n_\alpha = \frac{1}{N_\alpha} \sum_i^{N_\alpha} S_i, \tag{3.1}$$

where N_α is the number of atoms in a sublattice (α) and S_i is the magnetisation of atom i. For example in a saturated two sublattice AFM where the magnetisation's lie 180 degrees apart in the [001] direction the bulk magnetisation would be zero but the sublattice magnetisation's would be [0,0,1] and [0,0,-1] both with a normalised magnetisation length of one as the system is completely saturated.

To calculate the temperature dependence of the sublattice magnetisation the simulated 6nm × 6nm × 6nm system was initialised at zero Kelvin then the temperature was slowly increased to a high temperature (above the predicted Néel temperature of the material). The temperature increase was done in 10K steps. At each temperature step the system was integrated for 100,000 Monte Carlo steps. The resulting mean sublattice magnetisation's at each temperature step are plotted in Fig. 3.1 for each of the three sublattices. The mean sublattice magnetisation is above zero after the Néel temperature because of the finite-size of the system. The Néel temperature was calculated from the sublattice

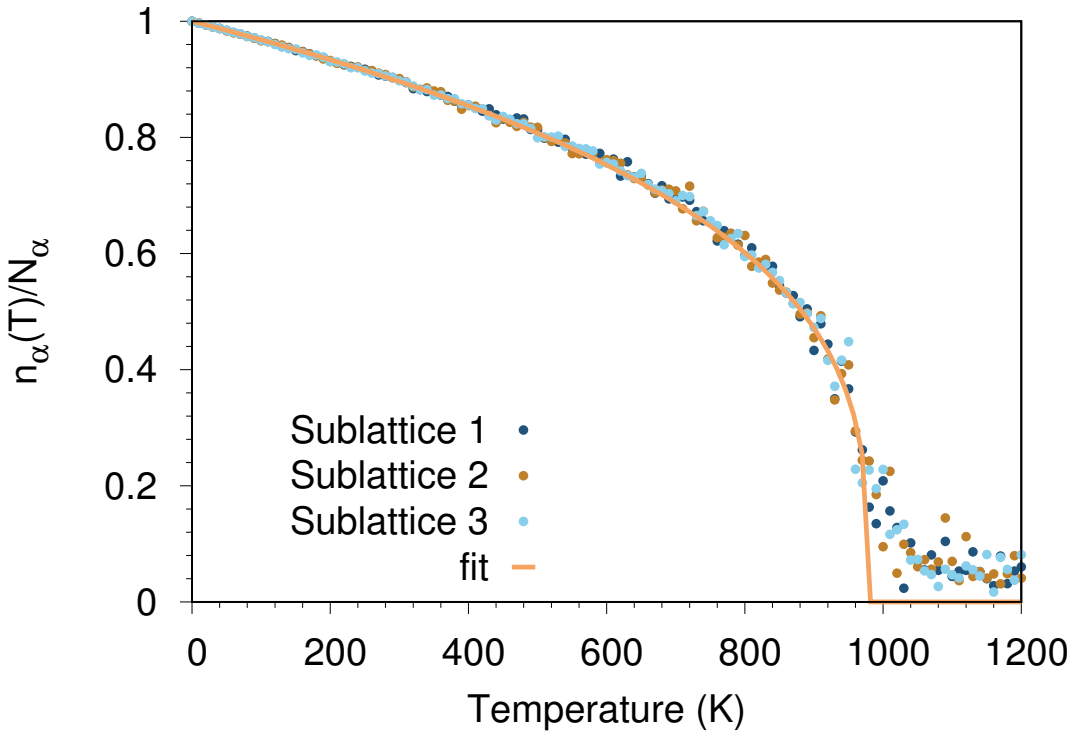

Figure 3.1: **The variation of magnetisation against temperature for each sublattice in ordered $L1_2$ - $IrMn_3$.** The curve was fit to the simulated data using equation 3.2. The Néel temperature for each sublattice was (980 ± 15)K. The error in the Néel temperature is the error in the curve fit. The magnetisation of an AFM can therefore be characterised by looking at the individual sublattice magnetisation.

magnetisation against temperature data by fitting the magnetisation of each sublattice to:

$$n = < n_\alpha > = \left(1 - \frac{T}{T_N}\right)^\beta . \tag{3.2}$$

The Néel temperature for each sublattice was calculated as (980 ± 15)K with a beta value of (0.32 ± 0.03), in both cases the error is the error in the fitting. The three sublattices all have the same Néel temperature so the total sublattice magnetisation of the material is equal to the average sublattice magnetisation. For the rest of the thesis the assumption that the sublattice magnetisation of the bulk material is equal to the average sublattice magnetisation is used. This assumption holds as long as each of the sublattices are in the same composition/order. Later in the thesis, more complex compositions will be investigated where the sublattice magnetisation's are no longer approximately equal, in those sections the sublattice magnetisation will be treated separately, as described in section 2.4.2.

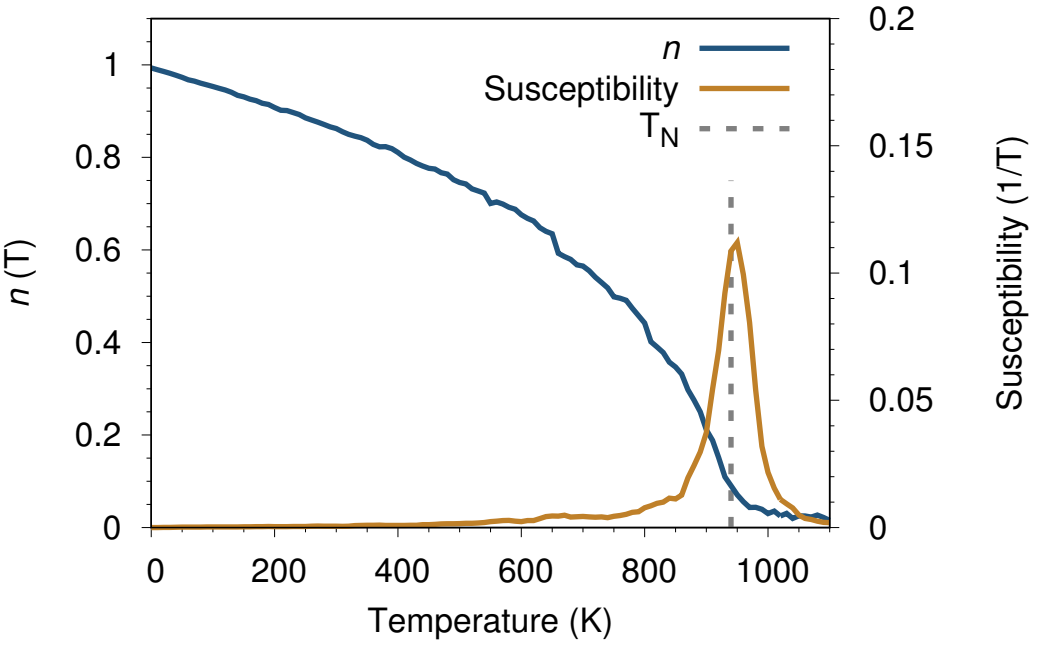

Figure 3.2: **The average sublattice magnetisation n and isotropic longitudinal susceptibility χ_n as a function of temperature for the $L1_2$ phase of $IrMn_3$.** The Néel temperature T_N is extracted from the peak in the susceptibility and is close to the bulk value [53] of 950 K.

3.1.2 Calculation of the Néel temperature from the sublattice susceptibility

A more accurate way of calculating the Néel temperature; especially for small system sizes is from the susceptibility. The susceptibility of a ferromagnet in the paramagnetic region above the Curie point is described by the Curie-Weiss law, the suscebibility of an AFM follows the same trend but the Curie Temperature (T_C) is replaced by the Néel temperature (T_N):

$$\chi_n = \frac{C}{T - T_N}, \tag{3.3}$$

where T is the temperature and χ_n is the susceptibility and C is the Curie constant. From the Curie-Weiss law we can predict a peak in the susceptibility at T = T_C. This is equivalent to the temperature of an AFM and the peak will occur at T = T_N. Whilst the bulk susceptibility is not zero, it can give a small response to a field. The bulk susceptibility is however very weak and does not follow the susceptibility of the sublattices. Therefore we have to use the same technique

as with the sublattice magnetisation and calculate the sublattice susceptibility for each sublattice. We assume that the sublattice susceptibility is equal to the average susceptibility of the sublattices. We calculate the isotropic longitudinal susceptibility for each sublattice as:

$$\chi_n = \frac{\sum_i \mu_i}{k_B T} \left(\langle |n|^2 \rangle - \langle |n| \rangle^2 \right) \tag{3.4}$$

where i are indices of atoms within the same sublattice and μ_i is the magnetic moment of atom i. Fig. 3.2 shows a typical simulation result for a (10 nm)^3 cube of $L1_2$-$IrMn_3$ showing the usual decrease in sublattice spin order with increasing temperature due to spin fluctuations. The sublattice susceptibility diverges at the Néel temperature with a well defined peak from which we extract T_N. The susceptibility measures the ability of a material to orient along different directions (x,y,z) or along the saturation directions, this therefore gives a large peak as the temperature reaches the Curie temperature or the Néel temperature as the material is still aligned but can align along any direction.

3.2 The exchange interactions in IrMn

In the previous section, the simulations were run using all of the non-zero terms in the IrMn exchange energy calculations from Fig. 2.4. The non-zero terms for the first four nearest neighbours have values outlined in the table below:

Neighbour	Energy (J/link)	Number of neighbours
1st	-6.4 × 10^{-21}	12
2nd	+1.12 × 10^{-21}	6
3rd	-1.6 × 10^{-21}	24
4th	+0.9 × 10^{-21}	12

Table 3.1: The non zero exchange interactions in IrMn calculated by L. Szunyogh *et al* [25] and the number of neighbours at each distance.

The values in table 3.1 are in units of Joules per link, the atomistic value of every atom with every nth neighbour interaction. The table also tells you how many atoms of each neighbour type there are. Using all of the non-zero interactions means that each atom interacts with over 50 other atoms, which is computationally expensive. The interactions can all be summarised by AFM (negative) interactions between atoms in different sublattices and FM (positive) interactions between atoms in the same sublattices. The largest contributions to

these are in the first nearest and second next nearest neighbour interactions. The remaining interactions either strengthen or weaken these interactions but don't change the interactions that occur. All the essential information can be surmised from the first two interactions. In the following section an approximation will be created which reduces the number of interactions and speeds up the simulations.

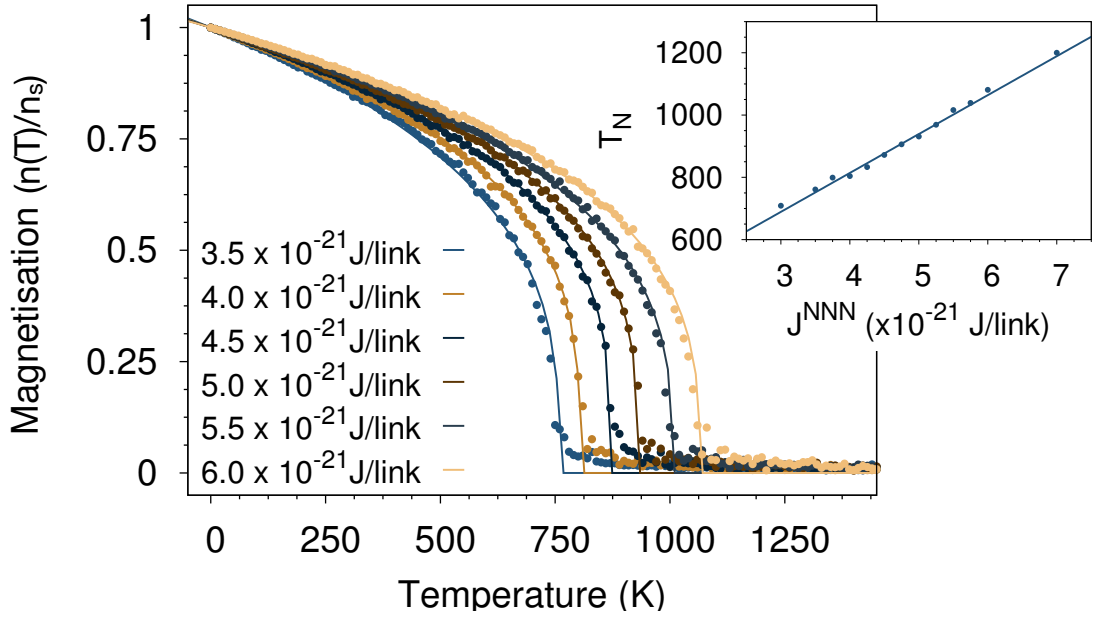

Figure 3.3: **The simulated Néel temperature for different values of J_{ij}^{nnn} for $L1_2$- $IrMn_3$.** To find the value of J_{ij}^{nnn} for IrMn the Néel temperature was calculated for different values of J_{ij}^{nnn} for $L1_2$- $IrMn_3$. This was compared the known value ($\approx$ 1000K) which has been measured via neutron scattering [53]. The value was varied around that found by L. Szunyogh et al. [25]. The T_{N} was calculated by cooling a sample from $T > T_{\text{N}}$ and calculating the magnetisation of the sample at each point when the magnetisation is zero, this is T_{N}. The simulated curves were fit using equation 3.2 as shown. b) The variation of T_{N} with J_{ij}^{nnn}, the points are the calculated T_{N} values, these were fit using a linear function.

The reduction in complexity was achieved by changing the J_{ij}^{nnn} interaction to account for the third and fourth nearest neighbour interactions while keeping J_{ij}^{nn} constant at the calculated *ab-initio* value of 6.4 $\times 10^{-21}$J. This reduces the number of terms in the Hamiltonian to only 18, 12 nearest neighbour interactions and 6 next nearest neighbour interactions. To calculate the new J_{ij}^{nnn} magnetisation vs temperature curves were simulated for varying values of J_{ij}^{nnn} until T_{N} matches the value calculated using all of the non zero interactions. For each value of J_{ij}^{nnn}, T_{N} was calculated from the sublattice magnetisation as in section 3.1.1. The simulated sample was again 6nm $\times$ 6nm $\times$ 6nm and the simulation was run through the same procedure as described in section 3.1.1. The simulated data and

the fit curves are shown in Fig. 3.3. The simulated T_N matches the known value when J_{ij}^{nnn}= 5.61×10^{-21}J. This value was used for all the remaining simulations in this thesis. This value is much larger than the value calculated by L. Szunyogh *et al* [25], however, this makes sense as it now how to account for the neglected neighbours at larger distances. L. Szunyogh *et al* [25] simulated the exchange constants for ordered IrMn and ordered $IrMn_3$ they found that both compositions had approximately the same values for the exchange interactions. Extrapolating from this, the model will assume all compositions and orders of IrMn have the same exchange interactions for all compositions and orders of IrMn. The exchange constants are also assumed to be constant with temperature, whilst an increase in temperature will cause the lattice to expand which will change in the exchange constants, this has been calculated via *ab-initio* methods [54] to be minimal for metallic systems. Even at the very high temperatures of 3000K (approximately three times the Néel temperature of our system) the lattice expansion is still less than 10% so very little change in the exchange constants in expected.

3.3 The bulk magnetic properties of IrMn

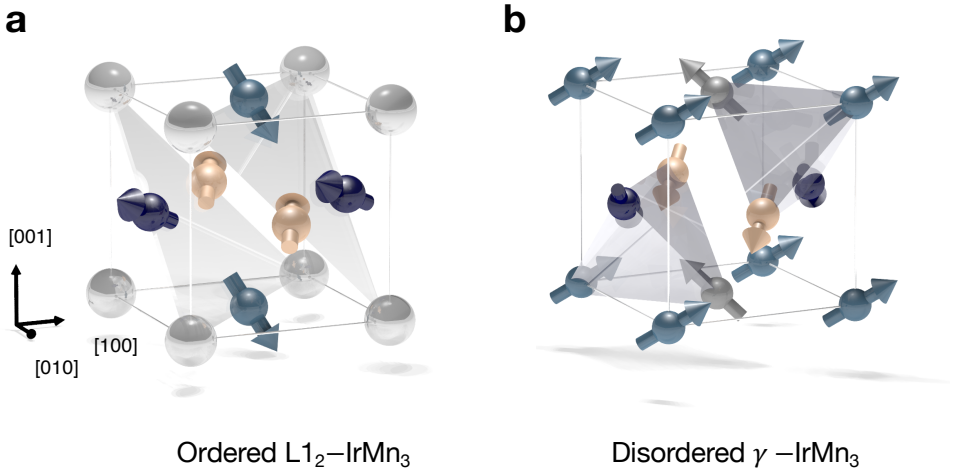

Figure 3.4: **Visualisation of the simulated ground state spin structures of $IrMn_3$ obtained from zero-field cooling.** (a) Simulated spin structures of ordered $L1_2$-$IrMn_3$ and (b) disordered γ - $IrMn_3$. The spins show an average spin direction of each magnetic sublattice direction over the whole sample. In the case of $L1_2$-$IrMn_3$ the corner atoms are all Ir and so have no net magnetic moment and are therefore represented by the spheres.

To validate our model, magnetic ground states and Néel temperatures will be compared to previously known experimental and theoretical results for IrMn.

The validation is done for both the disordered and ordered phase of $IrMn_3$ as there is a lot of previous experimental and theoretical data on these compositions. The Néel temperature is calculated for both compositions using the same method described in section 3.1.1. The ground state spin structure is calculated from the zero Kelvin sublattice magnetisation directions. The ground state spin structures are shown in Fig.3.4 and the Néel temperatures are shown in Fig.3.5. We find that ordered $L1_2$-$IrMn_3$ has a triangular ($T1$) spin structure where the magnetic moments lie in plane along the (111) planes with an angle of 120° degrees between them pointing along the [211] directions and that disordered γ-$IrMn_3$ has a tetrahedral ($Q3$) spin structure [53] analogous to that of CH_4 where the magnetic moments point 109.5° apart. These are both in agreement with previous experimental [53] and *ab-initio* results [25].

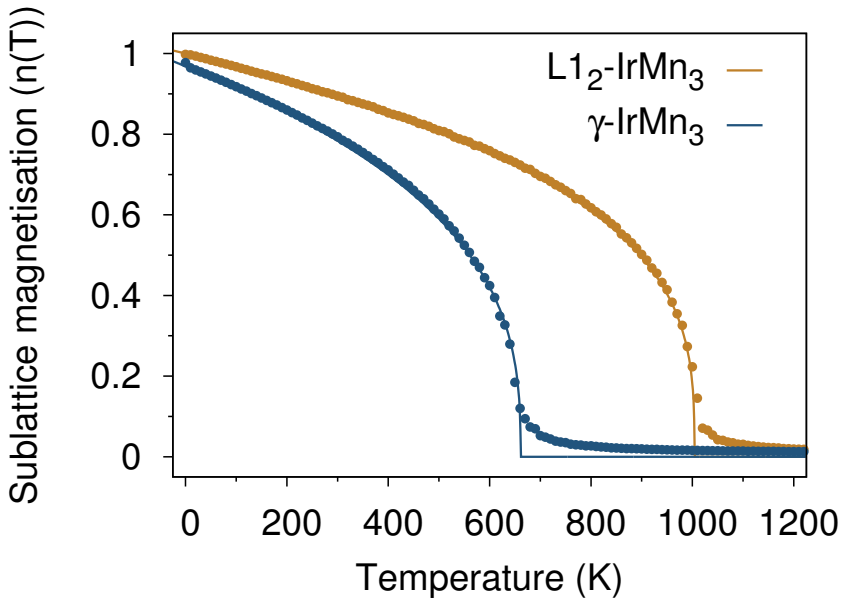

Figure 3.5: **Magnetisation vs temperature curves for ordered and disordered $IrMn_3$**. The Néel temperatures were calculated via Monte Carlo methods. The points represent the average magnetisation of the crystal at each Monte Carlo step, these were fitted using equation 3.2. For ordered $IrMn_3$ the Néel temperature is (1003 ± 7)K. Whereas for disordered $IrMn_3$ the Néel temperature is (688 ± 22)K.

Our simulations reproduce the Néel temperatures for the $L1_2$ ($T_N \sim 1000$ K) and γ ($T_N \sim 700$ K) phases of $IrMn_3$. In FM materials the Curie temperature (T_C) can be calculated as:

$$T_C = \frac{3k_B J_{ij}}{\epsilon z} \tag{3.5}$$

where k_B is the Boltzmann constant, T_C is the Curie temperature z is the number of nearest neighbours and ϵ is a correction factor from the usual mean-field expression. Therefore, if two FM's have the same number of nearest neighbours and exchange constant (J_{ij}) you would expect them to have the same Curie temperature. In our simulations both the ordered $L1_2$-$IrMn_3$ and the disordered γ-$IrMn_3$ phase have the same exchange interactions and the same average number of nearest neighbours. It is therefore a very interesting result that the Néel temperature is so different for the two phases. The difference in Néel temperature arises due to different degrees of geometric frustration in the spin structures. Therefore, in the ground state the spins are already frustrated and so thermal spin fluctuations have a stronger effect on the sublattice ordering in the γ phase compared to the $L1_2$ phase. The geometric frustration occurs because all of the Mn spins in the system energetically prefer full AFM alignment (180°) apart, but due to the geometric arrangement this spin structure is not possible, which lowers the overall energy proportional to $\cos(\theta)$ where θ is the angle between the sublattices. In the γ phase the spins are 109.5° apart, meaning the energy will be reduced to 33% of the Néel temperature in the fully aligned case, whereas in the $L1_2$ phase the sublattices are 120° apart meaning the Néel temperature will only be reduced by 50%. From this we can calculate the difference in Néel temperatures between the compositions should be about 66%, exactly matching our simulated values.

3.4 Temperature dependent antiferromagnetic properties of Ir_xMn_{x-1} alloys

Now we have validated our model of IrMn against previous experimental and theoretical results we can use the model to investigate different orders and compositions. Due to the theoretical complexity of modelling a disordered structure previously only the properties of the ordered states of IrMn and disordered $IrMn_3$ have been extensively investigated. However, using the Néel anisotropy model we can model any order or composition. In the next section a full study of the properties with composition and order will be made. Initially, just $IrMn_3$ will be investigated with a full phase study between the ordered and disordered states. Next a full phase study will be undertaken for all compositions of the completely ordered and completely disordered alloys.

3.4.1 The thermal stability of partially ordered $IrMn_3$ alloys

In this section the Néel temperature of the partially ordered phases of $IrMn_3$ are investigated. The system is partially ordered if the level of order is somewhere between ordered and disordered. I have chosen to investigate $IrMn_3$ because it is the mostly widely studied composition of IrMn.

Order parameter	Sub. 1	Sub. 2	Sub. 3	Sub. 4	D/D_d
1.0	100%	100%	100%	0%	0.0
0.8	95%	95%	95%	15%	0.2
0.6	90%	90%	90%	30%	0.4
0.4	85%	85%	85%	45%	0.6
0.2	70%	70%	70%	60%	0.8
0.0	75%	75%	75%	75%	1.0

Table 3.2: The percentage of each sublattice that is made up of Mn atoms depending on the order and composition of the structure.

In ordered $IrMn_3$ one sublattice is completely Ir and the other three are completely Mn. In the disordered phase the Ir is equally split (25%) between each sublattice. In a partially ordered phase the level of order will lie somewhere between the ordered and disordered phases. The level of order is defined using an order parameter (O), in a fully disordered system $O = 0$ and in a completely ordered system $O = 1$. If sublattice 4 is the sublattice that is completely Ir in ordered $IrMn_3$ then the order is varied by increasing the percentage of Mn in sublattice 4 by decreasing the percentage of Mn in sublattices 1,2 and 3. The order parameter is calculated using:

$$O = 1 - \frac{D}{D_d}, \tag{3.6}$$

It is a function of D/D_d, where (D) is the percentage of Mn in sublattice 4, and (D_d) is the percentage of Mn in sublattice 4 in the fully disordered system (75%). Therefore D/D_d is a measure of how full of Mn atoms sublattice 4 is in comparison to the "full" fully disordered case. In the fully ordered system $D/D_d = 0$ as there are no Mn atoms in Sublattice 4 and for the fully disordered system $D/D_d = 1$ as $D = D_d$. The percentages of Mn in each sublattice and the calculated order parameters are given in table 3.2. The Néel temperature was simulated for the six compositions outlined in table 3.2.

To calculate the Néel temperature, six systems were created with compositions described in Table 3.2. The system was 7nm × 7nm × 7nm with periodic boundary conditions as at this size the system will have almost bulk properties and there will be no surface effects. The temperature dependence was modelled using a Monte Carlo integrator as described in section 2.3.5. The Néel temperature of ordered $IrMn_3$ is 1005K, and adding disorder should decrease the Néel temperature. The temperature dependence was therefore investigated between 0K and 1200K as for all the compositions at 1200K they should be paramagnetic. To investigate the temperature dependence the systems were cooled from 1200K to 0K over 1,000,000 Monte Carlo steps. The Néel temperature is calculated by fitting the simulated magnetisation vs temperature curves to equation 3.2, shown in Fig. 3.6. As discussed in section 3.3, ordered $IrMn_3$ has a higher Néel temperature due to the lower frustration compared to the disordered phase. Between the two phases the Néel temperature decreases linearly from 1005 for $L1_2$-ordered $IrMn_3$ to 670K for the disordered phase.

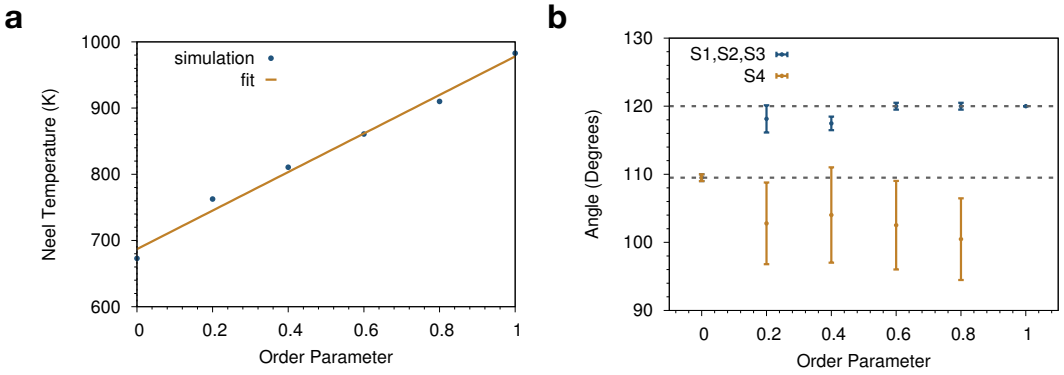

Figure 3.6: (a) The calculated Néel temperatures for different order parameters in $IrMn_3$. (b) The angle between the sublattices for different order parameters. The blue dots represent the average angle between sublattices 1,2,3. The yellow dots represent the average angle from sublattice 4 to the other three sublattices. The error bars are the standard deviation of the angles. 109.5 degrees and 120 degrees are shown as dotted lines on the diagram as these are the angles of the fully ordered and fully disordered phases.

To understand what causes the linear decrease we look at the underlying spin structure. In section 3.3 we found that the ordered phase forms a triangular structure with the sublattice magnetisation's pointing 120 degrees apart whereas the completely disordered phases forms a tetragonal structure with 109.5 degrees between the sublattices. If we calculate the angle between the sublattice magnetisation's in each phase, information about the level of frustration in the system can be obtained. The average angles are plotted in Fig. 3.6(b), for the

phases between complete order and disorder there is a large difference between the angles between sublattices 1, 2 and 3 and the angles of these three sublattice with sublattice 4. The difference occurs because sublattices 1,2 and 3 all contain the same percentage of Mn atoms whereas sublattice 4 contains a different percentage. To clarify this, two angles are calculated: the average angle between sublattices 1, 2 and 3 ($\theta_{1,2,3}$), and the average angle from sublattice 4 to the other 3 sublattices (θ_4).

($\theta_{1,2,3}$) is almost exactly 120 for all phases apart from the completely disordered phase. This suggests that the ground state has tended towards the triangular ground state of the ordered phase. (θ_4) varies a larger amount and is not between 109.5 and 120 suggesting a large amount of frustration in the structure. The frustration will have decreased the Néel temperature from the ordered $L1_2$ composition. Now we have looked into partially ordered states the completely ordered and completely disordered states with different compositions will be investigated.

3.4.2 The thermal stability of ordered Ir_xMn_{1-x} alloys

In section 3.3 we discussed the ground state and Néel temperature of ordered $IrMn_3$. These properties are well known via both experiments [53] and theory [25]. In the following section the Néel temperature and ground state structure of Ir_xMn_{1-x} alloys will be calculated from $Ir_{75}Mn_{25}$ to Mn_{100}. The compositions investigated are outlined in table 3.3 showing the percentage of Mn in each sublattice. As the percentage of Mn is increased, the sublattices fill up sequentially so each sublattice is filled with Mn atoms before the next sublattice contains any Mn atoms to preserve the ordered nature of the alloys.

The Néel temperature is calculated for a 6nm × 6nm × 6nm system using a Monte Carlo integrator using the same simulation settings as described in section 3.4.1. In these alloys, one sublattice contains a mixture of Ir/Mn atoms. It can be observed in Table 3.3 that there are three fully ordered IrMn states: $Ir_{75}Mn_{25}$, $Ir_{50}Mn_{50}$ and $Ir_{25}Mn_{75}$. In these states, every sublattice is either Ir or Mn and is no partial Ir/Mn sublattice. The properties of $Ir_{25}Mn_{75}$ otherwise known as $IrMn_3$ has already been studied in depth in section 3.3, however so far $Ir_{75}Mn_{25}$ and $Ir_{50}Mn_{50}$ - otherwise known as Ir_3Mn and IrMn respectively have not been considered.

Fig. 3.7a shows sublattice magnetisation vs temperature curves for IrMn and Ir_3Mn. IrMn has a Néel temperature of 1200K and Ir_3Mn has a Néel temperature of 590K. The Néel temperature of IrMn is very high, even higher than $IrMn_3$,

Densities	Sub. 1	Sub. 2	Sub. 3	Sub. 4
$Ir_{75}Mn_{25}$	100	0	0	0
$Ir_{70}Mn_{30}$	100	20	0	0
$Ir_{65}Mn_{35}$	100	40	0	0
...	:	:	:	:
$Ir_{50}Mn_{50}$	100	100	0	0
$Ir_{45}Mn_{55}$	100	100	20	0
$Ir_{40}Mn_{60}$	100	100	40	0
...	:	:	:	:
$Ir_{25}Mn_{75}$	100	100	100	0
$Ir_{20}Mn_{80}$	100	100	100	20
$Ir_{15}Mn_{85}$	100	100	100	40
...	:	:	:	:
Mn	100	100	100	100

Table 3.3: The percentage of Manganese was increased by maintaining as many filled sublattices as possible, these values will be used to see how increasing the percentage of Manganese changes the Néel temperature.

suggesting that there is a very low level of frustration in the structure. The Néel temperature of Ir_3Mn is also still well above room temperature. The high Néel temperature is an odd observation because of the high dilution of non magnetic Ir atoms in the system. This means that every atom should only have a small number of exchange bonds causing a low Néel temperature.

The ground state structures of Ir_3Mn and IrMn are shown in Fig. 3.7b and c respectively. The ground state of Ir_3Mn is surprisingly ferromagnetic. The FM ground state occurs because in Ir_3Mn only one sublattice contains Mn atoms and the exchange coupling between atoms in the same sublattice is FM. The FM ground state explains the high Néel temperature even though the system is very diluted. IrMn has the ground state structure of a "normal" AFM with no frustration as the sublattice magnetisation's of the two Mn sublattices point 180 degrees apart. The ground state structure explains the very high Néel temperature as the structure will have little to no frustration. The result matches the in-plane anisotropy observed experimentally[55] and the ground state matches that calculated via *ab-initio* methods[25].

Now that the properties of the completely ordered alloys have been investigated we want to know what has happened to the Néel temperature and ground state structure between these states. An example magnetisation vs temperature curve are shown in Fig. 3.8a, where the curves have been plotted separately for all three sublattices. We can notice that the Néel temperature of the diluted

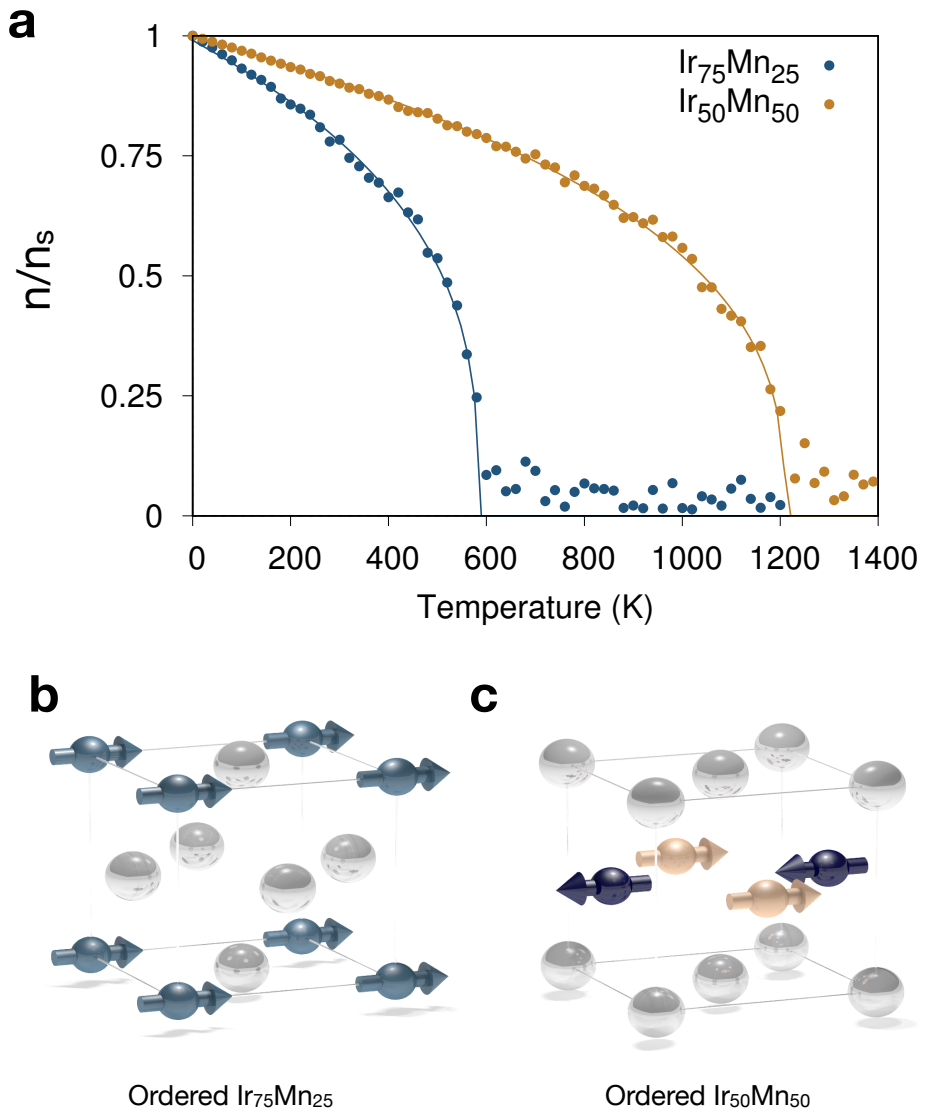

Figure 3.7: **Magnetisation vs temperature curves and visualisations of the simulated ground state spin structures for ordered IrMn and Ir_3Mn obtained from zero-field cooling.** (a) Magnetisation vs temperature curves show a Néel temperature of 584K and 1209K for IrMn and Ir_3Mn respectively. Ground state magnetic structures of (b) Ordered $Ir_{75}Mn$ and (c) Ordered $Ir_{50}Mn_{50}$. The spins show an average spin of each magnetic sublattice direction over the whole sample. IrMn has a classic AFM structure with the sublattices pointing 180° apart whereas Ir_3Mn the magnetic structure is FM.

sublattice is much lower that the other three sublattices although it does still reach saturation magnetisation. This is true for all of the compositions simulated. The lower Néel temperature for the diluted sublattice means it is hard to quantify the Néel temperature of the bulk material to a single value. The simulated Néel temperatures for all the compositions studied are shown in Fig. 3.8(b). The Néel temperatures have been plotted separately for the average of the

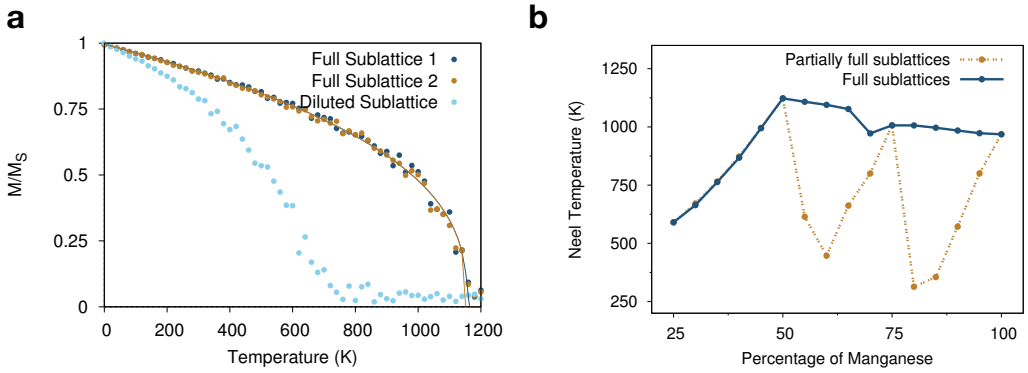

Figure 3.8: **An example magnetisation vs temperature curve for a partially ordered IrMn alloy and the simulated Néel temperatures against percentage of Manganese.** (a) Magnetisation vs temperature curve for an Mn concentration of 65%. The partially filled sublattice have a much lower Néel temperature than the full sublattices but the magnetisation length at zero Kelvin is still one. (b) The Néel temperature with percentage of Mn. The partially filled sublattices have been plotted separately as they have a much lower Néel temperature.

full sublattices and for the diluted sublattice. These values are different for Mn values about 50% however below 50% the partially full sublattice has the same Néel temperature as the full sublattices. Below 50% there is only one full sublattice, when the atoms are added in the next sublattice are added there is therefore no frustration between competing sublattices they are just anti-ferromagnetically coupled to the first sublattice, this means even if only a few atoms are added they are all strongly magnetised along the same direction. The Néel temperature of the full sublattices decreases almost linearly between the fully ordered states. The Néel temperature of the partially full sublattices increase as the percentage of Mn increases until full. The change in Néel temperature is caused by the angles between the sublattices as ($E \propto cos(\theta)$, in the only partially ordered states the angle between the sublattices (θ) must be smaller and therefore the Néel temperature decreases.

3.4.3 The thermal stability of disordered Ir_xMn_{x-1} alloys

In section 3.3 we calculated the magnetic ground state structure and Néel temperature of $IrMn_3$, the most widely theoretically studied structure of IrMn. However, in most spintronic devices the composition of IrMn used is not $IrMn_3$ but closer to $IrMn_4$ or $IrMn_5$ [56]. In the next section the composition dependence of disordered IrMn is investigated especially is the compositions between $IrMn_5$ to $IrMn_3$.

In disordered IrMn alloys the Mn atoms are randomly distributed between the four sublattices and each Mn sublattice contains approximately equal numbers of Mn and Ir atoms. Here I have varied the percentage of Mn from 25% to 100% as outlined in Table 3.4.

Composition	Sub. 1	Sub. 2	Sub. 3	Sub. 4
$Ir_{75}Mn_{25}$	25	25	25	25
$Ir_{70}Mn_{30}$	30	30	30	30
$Ir_{65}Mn_{35}$	35	35	35	35
$Ir_{60}Mn_{40}$	40	40	40	40
...	:	:	:	:
$Ir_{15}Mn_{85}$	85	85	85	85
$Ir_{10}Mn_{90}$	90	90	90	90
$Ir_{5}Mn_{95}$	95	95	95	95
Mn_{100}	100	100	100	100

Table 3.4: The percentage of magnetic Mn atoms in each sublattice for disordered IrMn as the percentage of Mn was increased from 25% to 100%.

The Néel temperatures for the simulated structures are shown in Fig.3.9. The simulations gave a T_N of 1000K for Mn. Neutron scattering measurements [57] calculate the T_N of Ir_0Mn_{100} to be much lower. The discrepancy is due to the simulations assuming the unit cell size and magnetic structure is constant for all compositions and orderings of IrMn whereas in reality, for compositions greater than 95% Mn the system has a complex anisotropic structure [48]. At compositions greater than 95% there is therefore a breakdown in the assumptions of the model and the results are no longer accurate.

The ordered compositions of IrMn have a higher Néel temperature than the disordered structures because of the frustration in the disordered systems. The frustration decreases the anisotropy causing the structures to be less stable. In fact, the simulations with a low percentage of Mn atoms have a low Néel temperature - almost zero.

To investigate why the Néel temperatures are so low for low percentages of Mn, the magnetisation length was plotted for the different simulations and is shown in Fig. 3.10(a). For atomic percentages of Mn above 75% the average sublattice magnetisation length is above 95%. For very high percentages of Mn > 0.8 the average sublattice magnetisation length is above 99%, suggesting every atom in every sublattice is nearly perfectly aligned. The compositions used in hard drives (18 - 24% Ir) have a higher magnetic ordering than $IrMn_3$. For low percentages of Mn (less than 50%) the average sublattice magnetisation length is very low

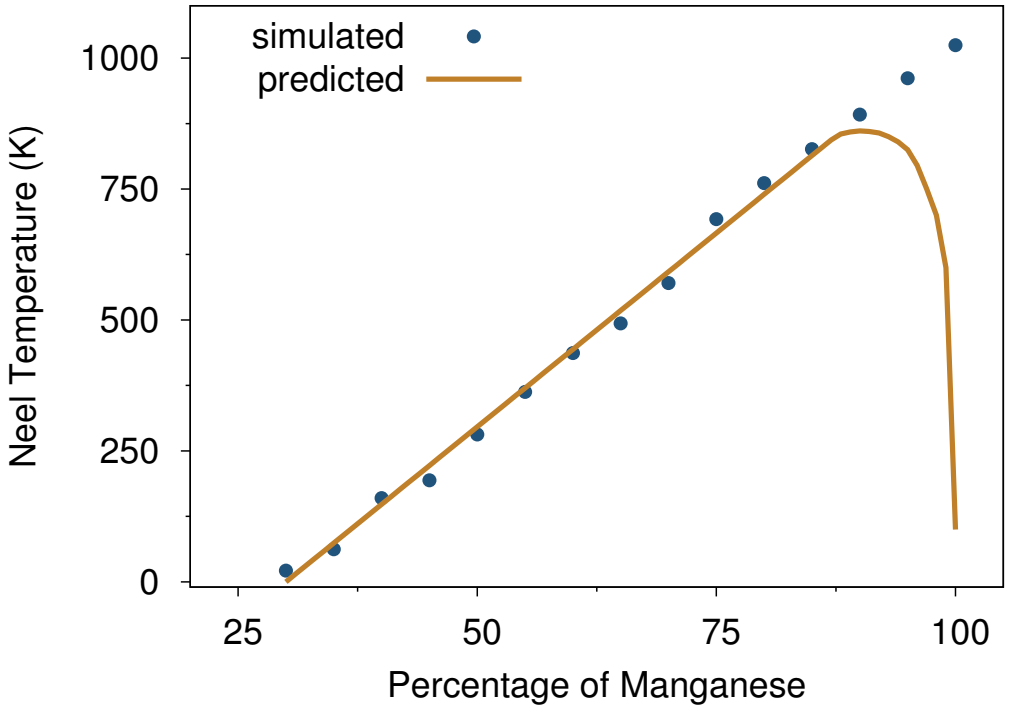

Figure 3.9: **The simulated and predicted Néel temperatures for disordered IrMn with different percentages of Mn.** The simulated Néel temperatures increase linearly with Mn concentration but the prediction from previous experimental results is for the Néel temperature to decrease as the Mn concentration approaches 100%.

as the structure forms a spin glass because concentration of Mn atoms is too low for a regular spin network to form. A cross-section of the ground state structure of IrMn and Ir_3Mn are shown in Fig 3.10b. These show that the simulation has no ground state structure explaining the low values of the Néel temperature for compositions with a low percentage of Mn atoms. Due to the spin glass, the exact values of the Néel temperature will be inaccurate for compositions less than 60%.

In disordered $IrMn_3$, the ground state structure is the Q3 tetragonal structure, characterised by an angle of 109.5 degrees between the four magnetic sublattices. The ground state structures of other compositions has so far never been theoretically studied even though in most hard drives compositions of 18 - 24% Ir are used. Usually, it is assumed that the magnetisation structure is the same and $IrMn_3$ for all these compositions. By calculating the angle between the sublattices we can see if this assumption is true. The angles between the sublattices are shown for Mn concentrations from 55 - 95% in Fig. 3.11(a). For all concentrations

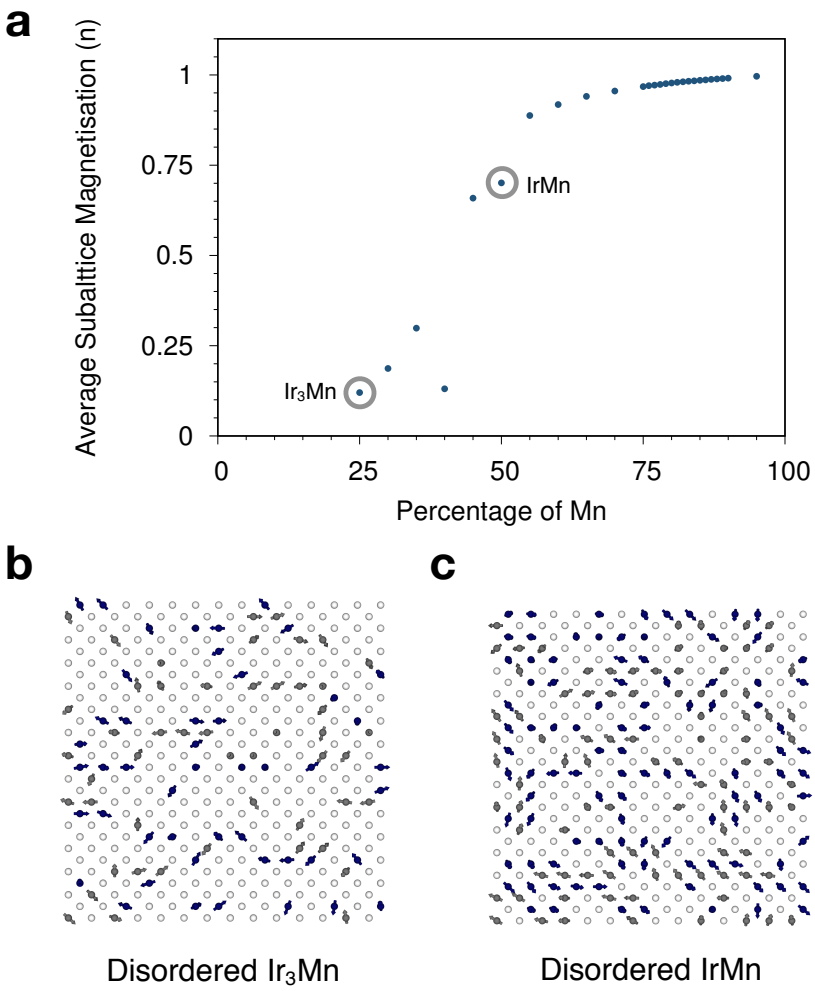

Figure 3.10: **Average sublattice magnetisation lengths (*n*) for disordered IrMn with different Mn compositions and interface magnetic structure for disordered Ir_3Mn and IrMn at T = 0K.** (a) The average sublattice magnetisation length for different Mn compositions. The magnetisation length is nearly one for all Mn percentages higher than 50% but for low concentrations the average sublattice magnetisation is less than 30%. The magnetisation structures for disordered (b) Ir_3Mn and (c) IrMn. Both compositions have almost zero net magnetisation and form spin glass structures.

the average angle between sublattices is 109.5 degrees. The error in the angle is around one degree for all compositions between 18 - 24% Ir. From the angles we can confirm that the compositions used in spintronic devices will also exhibit the Q3 structure shown in Fig. 3.11(b).

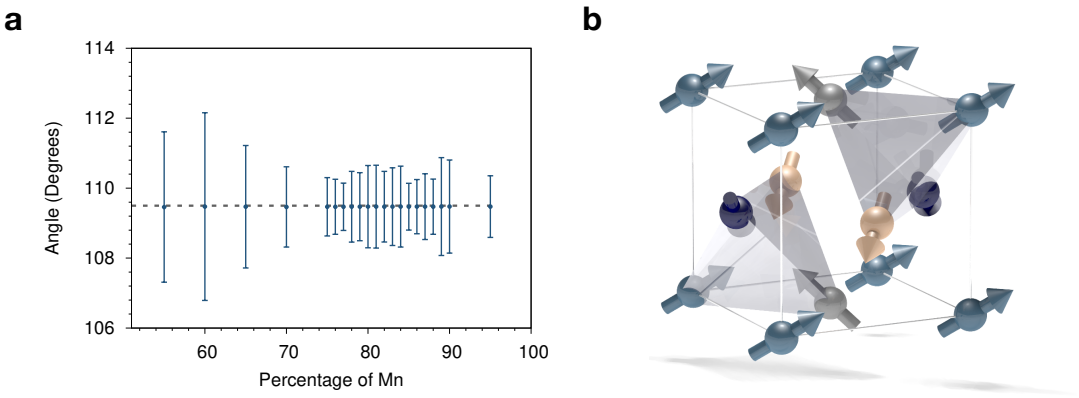

Figure 3.11: **Average angle between sublattices for disordered IrMn compositions and the ground state magnetic structure of all the compositions.** (a) The average angle between magnetic sublattices is 109.5 degrees for all percentages of Mn higher than 50%. The error is the standard deviation in the angles. (b) All the compositions higher than 50% Mn concentration have therefore formed the same magnetic structure as $IrMn_3$.

3.5 Finite size effects in ultrathin IrMn films

In practical spintronic devices the AFM layers want to be as thin as possible [19]. To minimise the size of devices it is important to maximise the interface to bulk ratio. The devices are made as thin as possible whilst still being thermally stable. Understanding the finite size effects is particularly important for spin-orbit torque driven devices which rely on interfacial properties for thermal stability and generating torques [9, 9, 58].

Finite size effects in FM materials have been extensively studied and are well understood. In AFM materials they have been little researched particularly in materials of practical importance such as IrMn. L. Frangou *et al*. found that for films less than 3 nm thick there was a linear decrease of the Néel temperature and for 0.5nm films the Néel temperature falls to only 50K [59]. They note the agreement with the work of D. Petti *et al* [60] who used nanocalorimetry to measure the Néel temperature of 2 nm thin films of IrMn. The Néel temperature of the 2nm thick film had reduced to 173K, about 20% of the bulk value they measured. The finite size properties are dependent on the film thickness and ordering and still subject to some interpretation.

In this section I will model the effects of film thickness and interfacial intermixing on the Néel temperature of different $IrMn_3$ alloys. We consider both $L1_2$ ordered and disordered (γ) phases of $IrMn_3$ which have different ordering temperatures and thermal stabilities. The work in the following section was published in

Journal of Physics D [19].

3.5.1 The system

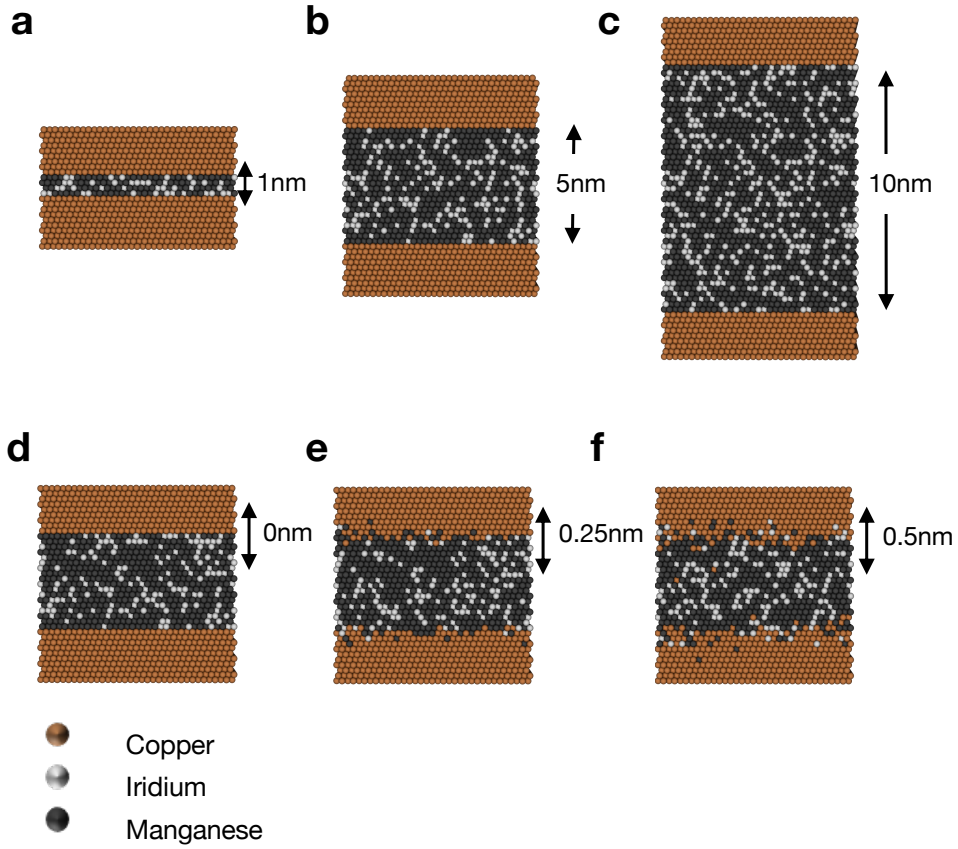

Figure 3.12: **Visualisation of the atomic structures of the system for the γ-$IrMn_3$ phase for different film thicknesses** (a) 1 nm, (b) 4 nm and (c) 10 nm. The colours represent different atomic species. The same is shown for different levels of interface mixing with interface widths of (d) 0 nm, (e) 0.25 nm and (f) 0.5 nm.

The properties of ultrathin films of $IrMn_3$ were modelled assuming the layer is sandwiched between two non-magnetic Cu layers. The non magnetic layers are introduced to the Cu layers have a low spin-orbit coupling so the Cu does not affect the properties of the Mn apart from creating missing exchange bonds at the Mn-Cu interface. The simulated system has fixed lateral dimensions of 15nm × 15nm and the thickness is varied from $0.25 - 10$ nm. A visualisation of the system is shown in Fig. 3.12. Initially the interface between the Cu and the Mn is atomically flat but then the intermixing is increased. The intermixing simulates the sputtering process which is used to create thin films experimentally. The interface mixing is generated using a probability distribution:

$$P(z) = 1 - \frac{1}{2}\tanh\left(\frac{\pi(z - z_0)}{w}\right), \tag{3.7}$$

where $P(z)$ is the probability of finding an atom of a particular type at height z, z_0 is the interface height and w is the width of the interface. Every atom in the IrMn layer is initially set as Ir or Mn and then has a probability (P) of being changed to a Cu atom depending on its height (z). The reverse process is done for the mixing of Ir and Mn into the Cu layers. The width of the interface was systematically varied between 0 and 0.5 nm as shown schematically in Fig 3.12.

3.5.2 The temperature dependent magnetisation and susceptibility in atomically flat ultrathin films

The temperature dependent sublattice magnetisation and susceptibility were calculated for varying thicknesses of $IrMn_3$. This was repeated for both $L1_2$-$IrMn_3$ and γ - $IrMn_3$ for film thicknesses between 0.25 and 10 nm. The 10 nm system has the properties close to bulk $IrMn_3$. Initially, simulations were run with an atomically flat interface between the IrMn and Cu layers.

In ultra-thin films the properties can vary massively between different simulated structures. The differences occur mostly in disordered structures or those with high levels of interface mixing. The calculated properties are averaged over 10 different simulated crystal structures with different pseudorandom number sequences in the Monte Carlo algorithm. The data is averaged to calculate the mean sublattice magnetisation and the mean susceptibility.

A typical set of data for thickness t_{IrMn} = 1 nm and atomically flat interface w = 0 nm is shown in Fig. 3.13 comparing the (a) disordered γ and (b) $L1_2$ phases. The simulations show a significant decrease in the Néel temperature for both phases due to the missing interface Mn - Mn exchange bonds. In particular the γ phase shows a Néel temperature close to room temperature. The low Néel temperature suggests that films thinner than this are unsuitable for applications in spintronics as devices will operate at room temperature.

In the disordered γ phase the zero Kelvin magnetisation is well below the saturation magnetisation. n_α/N_α is significantly less than one at only around 0.7. The low value of sublattice magnetisation suggests that the film has formed multiple domains. The small size of the system means that the spins should form a single antiferromagnetic domain. However, the random distribution of the Ir sites in the crystal means that some areas of the AFM are weakly coupled

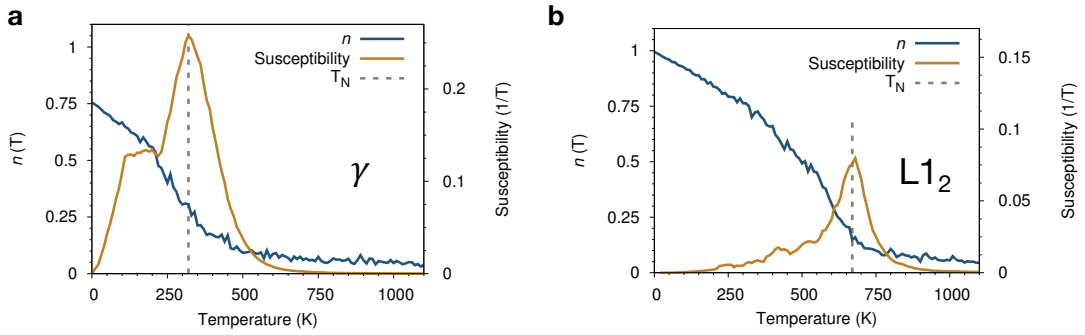

Figure 3.13: **Simulated temperature dependent sublattice magnetisation curves and isotropic susceptibility for a 1 nm thick thin film of $IrMn_3$ comparing γ (a) and $L1_2$ (b) phases for a system with a perfectly flat interface.** The data are averaged over ten statistically independent systems with different structures. Both curves show a significant reduction in the Néel temperature compared to bulk and reduced criticality near T_N due to the small finite thickness of the film.

to the rest allowing stable AFM domains to form. This effect is unique to thin films because in bulk systems there will always be a path allowing the exchange coupling of different regions together. This is even the case for areas with a high Ir concentrations where there is a very low level of exchange coupling. In thin films the exchange coupling is stopped in one dimension and this means different regions of the films can become decoupled from each other. The decoupling of different regions means that even in the absence of thermal fluctuations, full magnetic ordering of the $IrMn_3$ at nanoscale sizes may be difficult to achieve.

The presence of multiple AFM domains causes a discontinuity in the isotropic susceptibility at very low temperatures. Here, infinitesimal thermal fluctuations of the spins lead to a large variation of the sublattice magnetisation, in strong contrast to the fully ordered $L1_2$ phase which has a low susceptibility at low temperatures. This is an unusual effect and occurs due to the intrinsic instability of the AFM spin structure in the γ - phase.

3.5.3 Systematic study of the effect of intermixing and film thickness on the Néel temperature in ultra thin films

A systematic study of the effect of film thickness and intermixing on the Néel temperature is shown in Fig. 3.14 for the γ (a) and $L1_2$(b) phases. The Figure also contains simulation data for a generic FCC ferromagnet with a Curie temperature the same as the Néel temperature for both phases. The FM is presented to compare the difference in the size dependent ordering temperature between FM

and AFM materials.

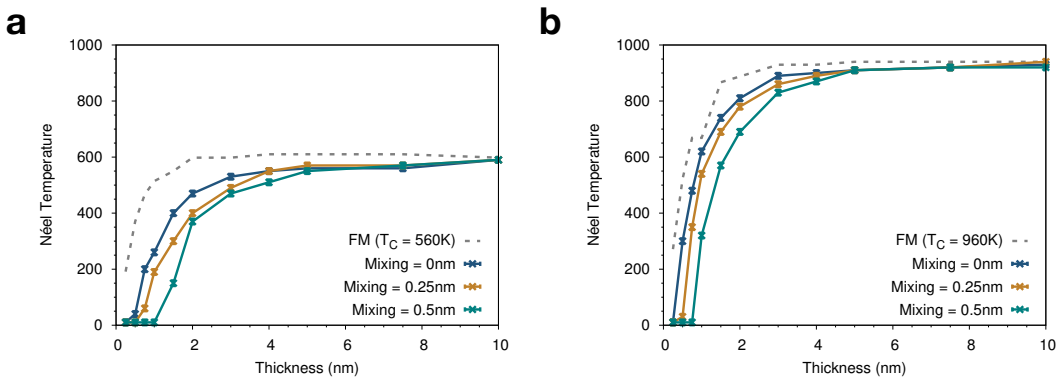

Figure 3.14: **Simulated systematic variation in the Néel temperature with varying film thickness for IrMn in both the γ (a) and $L1_2$ phases (b) for different interfacial mixing widths.** The dashed lines show comparative data for a ferromagnet with the Curie temperature T_C= T_N for each phase. The data show a systematic decrease in the Néel temperature for thinner films, and a stronger finite size effect in the γ phase compared to the $L1_2$phase. In both cases the finite size variation of the Néel temperature shows a stronger decrease than the equivalent ferromagnet (FM) due to the inherent spin disorder. Intermixing of the IrMn with a non-magnetic Cu layer shows an enhanced finite size effect for increased mixing due to a larger number of missing exchange bonds.

Both AFM phases show a stronger finite size effect than the comparable ferromagnetic film, showing a larger reduction in the Néel temperature for a given film thickness. The reduction is due to the geometric spin frustration in the AFMs. The frustration increases the influence of thermal spin fluctuations on the sublattice ordering. Comparing the two phases of $IrMn_3$, the γ phase shows a stronger finite size effect and larger reduction in the Néel temperature compared to the ordered phase. The reduction in order is due to the lower M/M_S value and the larger effect of thermal fluctuations. For the thinnest films there is an extremely large reduction in the Néel temperature to only a few degrees Kelvin in both phases of IrMn. This drop is not seen in the FM case. I argue that the origin is due to the AFM domains. The domains mean locally AFM order still exists within a domain but long range order is disrupted even over nanoscale length scales. The disruption means there is an effective low Néel temperature over the total simulated sample. These effects may be more severe for laterally larger films which would typically be used in devices

3.6 Summary

In this chapter we have discussed how to calculate the properties of an AFM material, specifically IrMn in many different compositions and orders. Our model of IrMn has been validated against previous experimental and theoretical results and we have confirmed the accuracy. The properties of never before theoretically studied compositions and orders of IrMn were modelled and it was found that all technologically relevant alloys of disordered IrMn have the same ground state spin structure. It was also found that the Néel temperature increases as you increase the Mn content making for a more stable structure.

Next the finite size effects in IrMn were investigated and it was found that IrMn films show a stronger finite size dependence of the Néel temperature than an equivalent ferromagnet due to the existence of spin frustration. Our results suggest a larger antiferromagnetic film thickness is required for spintronic devices operating at or above room temperature compared to an equivalent ferromagnet, particularly for sputtered films with a high degree of interfacial intermixing.

4

THE COMPLEX MAGNETIC ANISOTROPY OF IRMN

The anisotropy of ferromagnetic materials is in general well understood and numerous theoretical models and experimental measurements exist to explain the various observed phenomena [26, 31]. The magnetic anisotropy of antiferromagnets is a much more complicated and interesting problem, and is poorly understood because of the difficulty in experimental measurements and the complexity of the magnetic structures and materials.

The magnetic anisotropy of AFMs plays a key role in the stability of many spintronic devices. AFM materials are used in these devices to form AFM/FM bilayers where the AFM causes a shift of the hysteresis loop of the FM. The shifted hysteresis loop means the FM is effectively pinned along a fixed direction of magnetisation. A larger anisotropy in the AFM causes a stronger pinning from the AFM to the FM and therefore a larger shift in the hysteresis loop. The larger the shift in the hysteresis loop the stronger the pinning in the FM layer. The pinning is known as the exchange bias effect and is discussed in more detail in Chapter 5. Exchange bias is used in many spintronic devices such as in tunnelling magnetoresistive sensors in read heads in magnetic hard drives. The stronger the pinning the more reliable the device. The energy barrier defines the effective magnetic anisotropy energy and therefore the thermal stability.

In this chapter a constrained Monte Carlo algorithm is used to calculate the energy surfaces of IrMn and from this the energy barriers to magnetic reversal. The results are compared to previous experimental and theoretical measurements. AFMs have a bulk magnetisation of zero so as with calculating the Néel temperature we have to look at the individual sublattice properties instead of the bulk properties.

4.1 Previous calculations of the anisotropy of IrMn

The anisotropy of IrMn has previously been studied both experimentally and theoretically. The ordered phase of $IrMn_3$ was studied theoretically by L. Szunyogh *et al* [25] using *ab-initio* methods. They found an extremely large value for the second order magnetic anisotropy, leading to energy barriers of the order of 3 $\times$ 10^7J/m^3 at 0K. This is an extraordinarily large value for the anisotropy. For example, Neodymium Iron Boron is the strongest permanent magnet available today and has an anisotropy of 1.33 $\times$ 10^6J/m^3: more than an order of magnitude smaller.

Vallejo-Fernandez *et al* experimentally determined the anisotropy constant of disordered $IrMn_3$ by measuring the mean blocking temperature of a IrMn/CoFe bilayer [51, 61]. The blocking temperature was measured using a training-free measurement procedure in which hysteresis loops were repeatedly measured at the same (thermal activation free) low temperature after raising the sample to a different activation temperature. The activation reverses part of the AFM layer due to the exchange field from the FM. As the AFM reverses the exchange bias field decreases, the blocking temperature (T_B) is the point where the exchange bias field is reduced to zero and was measured to be T_B = 236K. The blocking temperature is low because of the thin films they used (3nm) and using this value the anisotropy can be determined given the measured grain volume using the equation:

$$1/\tau = f_0 \exp\left(-\frac{\Delta E}{k_B T}\right) \tag{4.1}$$

where τ is the relaxation time, ΔE is the energy barrier, k_B is the Boltzmann constant, and T is the temperature. At the blocking temperature $\Delta E = K_{AF} V$ where K_{AF} is the anisotropy constant of the AFM and V is the mean grain volume. The anisotropy constant is therefore given by:

$$K_{AF}(T_B) = \frac{\log(\tau f_0)}{V} k_B T_B. \tag{4.2}$$

Using equation 4.3 the temperature variation has the form [62]:

$$K_{AF}(T) = K_{AF}(0)\Big[\big(1 - \frac{T}{T_N}\big)^l\Big]^3 \tag{4.3}$$

The assumption is made that $l = 3$ which is only valid for a uniaxial magnetocrystalline anisotropy [52]. At 300K $K = 6.2 \times 10^5$ J/m^3 and at 0K $K = 14.8 \times 10^5$ J/m^3, the zero Kelvin value is almost two orders of magnitude lower than the theoretical calculations for ordered $IrMn_3$ [25].

The experimental measurement of the anisotropy constant is also dependent on the value of the switching attempt frequency (f_0). Originally Vallejo-Fernandez *et al* used a value of $f_0 = 10^9$ s^{-1} [51] but more recent estimates suggest values closer to $f_0 = (2.1 \pm 0.4) \times 10^{12}$ s^{-1} [62]. The attempt frequency is hard to experimentally measure, and in section 4.1.5 we calculate the range of possible attempt frequencies and compare them to the experimental result.

The symmetry of the anisotropy is also an unresolved problem. Vallejo-Fernandez [51] and Craig *et al* [63] investigated the form of the anisotropy energy surface by fitting to the temperature dependence of the magnetisation using a Callen-Callen [52] power law:

$$\frac{K_{AF}(T)}{K_{AF}(0)} = \left[\frac{n_{AF}(T)}{n_{AF}(0)}\right]^l \tag{4.4}$$

where n_{AF} is the AFM sublattice magnetisation and l is an exponent which reflects the symmetry of the anisotropy. In materials with a uniaxial anisotropy $l \sim 3$ and for a cubic anisotropy $l \sim 10$. The symmetry of the anisotropy generally reflects that of the lattice because the easy axes tend to coincide with axes of symmetry in the crystal structure [26]. This is always true in ferromagnetic materials - a cubic lattice will have a cubic anisotropy unless there is strain, shape or another form of anisotropy acting on the material. While the Callen-Callen theory [52] holds for most FM materials because the anisotropy of AFM materials is so difficult to measure it has previously been difficult to say if it will also hold for AFM materials. In section 4.1.2 the theory will be tested for a AFM with a known symmetry to see if the temperature dependence is consistent with Callen-Callen theory.

Szunyogh *et al* [25] calculated the energy surface for ordered $IrMn_3$ by rotating the triangular ground state around the (111) direction and calculating the change in energy. The same calculation was done using our IrMn model with

the Néel pair anisotropy, in Fig. 2.6, finding an exact match to the *ab-initio* results. Both experiment and theory agree that the anisotropy has a uniaxial form contradicting the predicted relationship between crystallographic symmetry and the temperature dependence of the anisotropy from the Callen-Callen [52] and Zener [64] relations. As IrMn has a cubic crystal structure, the anisotropy would be expected to have a cubic symmetry.

In this chapter we use a constrained Monte Carlo algorithm to calculate the magnitude and symmetry of the anisotropy in different degrees of order and compositions of IrMn. We aim to to resolve the differences between the experimental and theoretical calculations for the magnitude of the anisotropy constant in $IrMn_3$ by calculating the energy barrier to magnetic reversal. Then the symmetry of the anisotropy will be calculated from the temperature scaling of the anisotropy using Callen-Callen law. Results in the following chapter were published in Physical Review B [20].

4.1.1 Calculation of the energy surface

The energy barrier separating two ground states is the minimum energy path for the spins to rotate from one ground state to another. At a finite temperature the anisotropy constant is a free energy difference arising from spin fluctuations. To calculate the energy barrier, we use a constrained Monte Carlo (CMC) algorithm to determine the entire energy surface. From the energy surface we can find the ground states and calculate the minimum energy required to rotate between them.

Constrained Monte Carlo (CMC) is an extension of the metropolis Monte Carlo algorithm where the steps of the random walk are modified to conserve the average magnetisation direction ($\hat{\mathbf{M}}$) as:

$$\hat{\mathbf{M}} \equiv \frac{\sum_i (\hat{\mathbf{S}}_i)}{\sum_i \parallel \hat{\mathbf{S}}_i \parallel}, \tag{4.5}$$

where $\hat{\mathbf{S}}_i$ is the unit vector of the direction of magnetisation of a spin i. The constraint keeps the system out of equilibrium in a controlled manner but allows its microscopic degrees of freedom to thermalise [65]. In this thesis CMC is used to calculate energy surfaces of materials, and from this compute the ground states and energy barrier between them. CMC was developed by Asselin *et al* [65] and works by creating a new trial spin state which is constructed by altering the

magnetisation directions of two spins. The first follows the same move as for a Monte Carlo trial move. The second (the compensation spin) is chosen for which the magnetisation direction is left unaltered but the magnetisation length can change. The acceptance probability (P) is now:

$$P = -\frac{M_z'}{M_z}\frac{S_j}{S_j'}\exp\left(\frac{-\Delta E}{k_B T}\right) \tag{4.6}$$

where M_z' and S_j' are the magnetisation and direction of the newly proposed state, ΔE is the energy barrier to move between these states, k_B is the Boltzman constant and T is the temperature. The notation assumes that the net direction is constrained along the z direction, the extension to 3D is done by a global rotation [65].

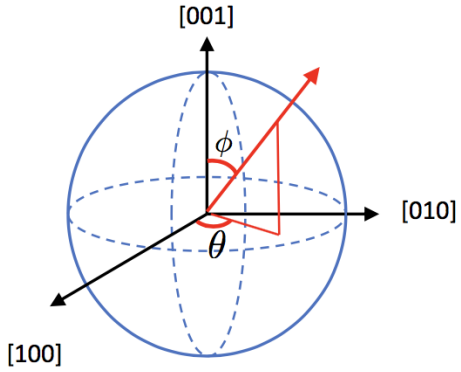

Figure 4.1: **Visualisation of the constraint directions θ, ϕ.** The red arrow represents the constraint direction and θ, ϕ are the angles to this direction.

The energy surface is calculated by constraining the direction of magnetisation of a single sublattice of the AFM along a specific (θ,ϕ) direction while allowing all other spins in the system to equilibrate to a minimum energy state. The constraint used is a weaker constraint than that used by L. Szunyogh *et al* where all of the sublattices were rigidly constrained preserving 120 degrees between each sublattice. L. Szunyogh *et al* constrained all three sublattices and rotated them simultaneously around the 111 plane whereas in the following chapter only one subalttice is constrained and a full θ, ϕ energy surface will be explored allowing for lower energy paths than only the [111] path. The constraint directions are visualised in Fig 4.1. The angles were varied in 1 degree increments from $\theta = 0$ to 360° and $\phi = 0°$ to 180°. The constrained sublattice is integrated using CMC while the other sublattices are integrated using a regular MC algorithm. For each value of θ and ϕ the system was initially heated to 1500K to thermalise the spins and

then cooled to 0K. The simulation was run over 1,000,000 MC steps to the ground state for each θ, ϕ value, using batch parallelisation for each unique angle-pair.

The CMC method determines the Helmholtz free energy ($\mathscr{F}$) for a given constraint direction. This cannot be computed directly but is related to the internal energy (E) as:

$$\mathscr{F} = E - TS; \tag{4.7}$$

where T is the temperature and S is the entropy. At zero Kelvin the internal energy equals the Helmholtz free energy ($\mathscr{F}$). The internal energy can be calculated directly as the sum of all the energies acting on the system (anisotropy, dipolar, exchange etc.) but as we cannot calculate S at $T > 0$ we cannot directly calculate the energy. Instead $\mathscr{F}$ can be indirectly calculated from the integral of the torque (τ) acting upon the system.

Magnetic torque can be defined as:

$$\tau = <\mathbf{M}> \times <\mathbf{B}>, \tag{4.8}$$

where $\mathbf{M}$ is the magnetic moment and $\mathbf{B}$ is the field acting on this moment. The torque is a measure of the force that can cause an object to rotate about an axis and in this case causes precession of the magnetic moment around the effective field. Our system is comprised of many atoms all with their own individual moment $\mathbf{S}_i$ In our system the field is defined by equation 2.23 and the total torque is given by:

$$\tau = -\frac{<\mathbf{M}>}{\mu_0 \mu_S} \times \frac{\partial \mathscr{F}}{\partial \mathbf{M}}, \tag{4.9}$$

where $\mathbf{M}$ is the magnetisation direction and $\mathbf{M} = \sum_i \mathbf{S}_i$, where $\mathbf{S}$ is the direction of spin i. $\mathbf{H}$ is the field acting on spin i. The Helmholtz free energy cannot be computed directly and so instead we can reconstruct it from the integral of the torque:

$$\mathscr{F} = \mathscr{F} + \int_{\vec{M}}^{\vec{M}'} (\mathbf{M}' \times \vec{\tau}) \cdot d\mathbf{M}', \tag{4.10}$$

where the integral of the torque is taken along the minimum energy path between two ground states ($\mathbf{M}$ and $\mathbf{M}'$) on the energy surface. From this the energy barrier to magnetic reversal can be calculated. At zero Kelvin the energy to rotate between these ground states ($\mathscr{F}$) equals the internal energy (E) but at higher temperatures this is not the case and the free energy must be calculated from the torque.

4.1.2 Anisotropy energy barrier for ordered $L1_0$-IrMn

In the following section, the anisotropy energy barrier and temperature dependence will be calculated for ordered $L1_0$ IrMn. Ordered IrMn is an easy plane AFM comprised of two magnetic sublattices, where the minimum energy occurs when the two sublattices are 180 degrees apart. Ordered IrMn has an inplane magnetic ground state as shown in Fig. 4.2. The ground states are in a plane at phi = 90 degrees, there is a magnetic energy barrier to reversing out of this ground state. In the following section we will calculate the energy barrier to magnetic reversal from the torque and then determine the symmetry of the anisotropy from the temperature dependence of the magnetisation. As IrMn is a uniaxial AFM, we expect the temperature dependence to give a uniaxial symmetry and the exponent in the Callen-Callen relation in equation 4.4 to be equal to three.

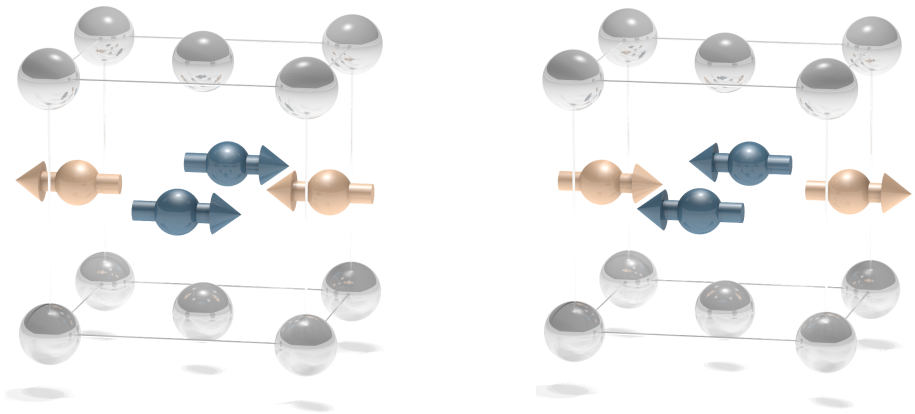

Figure 4.2: **Ordered IrMn has an inplane anisotropy and therefore the minimum energy occurs anywhere in the phi = 90 degree plane.** As IrMn is an in plane uniaxial AFM there is a minimum energy at phi = 90 degrees.

An 8nm × 8nm × 8nm system of ordered IrMn was simulated. A full energy surface was created by running a constrained Monte Carlo simulation with one of the sublattices constrained along the θ, ϕ direction as described in section 4.1.1. θ, ϕ were incremented in 1 degree steps and at each step a simulation was run for 3,000,000 Monte Carlo under no applied field. The first 1,000,000 steps of the

simulation were equilibration time steps meaning the calculated energy/torque values did not contribute to the final average energy/torque values. During the equilibration time steps the system should find its minimum energy state so the output average free energy/torque values only include the equilibrated free energy.

The energy surface is calculated from the torque as described in section 4.1.1. The energy surface produced is shown in Fig. 4.3, where the minimum energies occur when $\theta = 0\circ$ or $\theta = 180\circ$ and the maximum energy occurs when $\theta = 90\circ$.

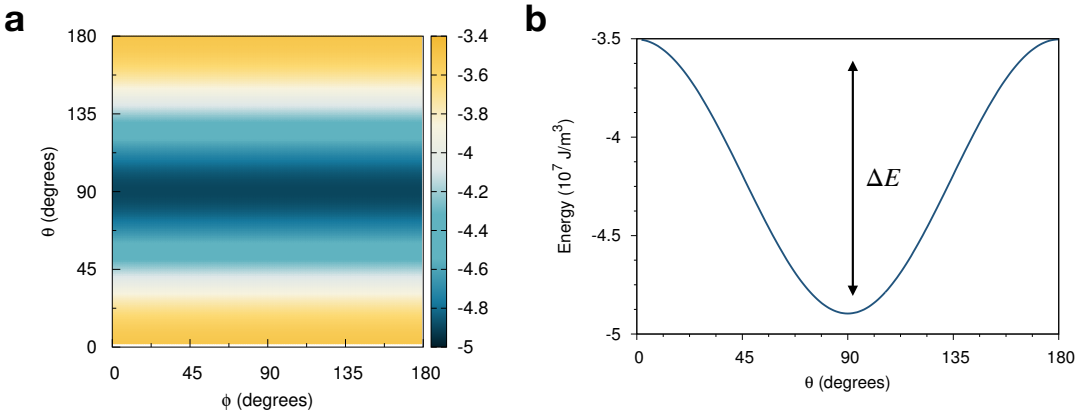

Figure 4.3: **Simulated anisotropy energy surface for IrMn and the minimum energy path between two ground states.** (a) The simulated energy surface calculated from the integral of the torque. It has the usual uniaxial symmetry. (b) the minimum energy path for a spin to rotate between these ground states. The energy barrier ΔE is shown.

The energy barrier is calculated as the difference between the maximum and minimum energies. For our simulation this gave the extraordinarily large value of $1.47\times\ 10^7$ J/m^3, approximately half the value calculated by Szunyogh *et al* for the $L1_2$ phase and an order of magnitude larger than the value calculated by Vallejo-Fernandez *et al* for the γ phase.

Looking at Fig 4.2 the system has two energy maxima, suggesting an easy plane energy barrier. The energy surface also has an easy plane shape as shown in Fig. 4.3. The temperature dependence of the anisotropy energy barrier is calculated by running the same simulation as described to create Fig. 4.3 but at increasing temperatures. Previously the simulation was run over all θ, ϕ angles however as we now know the minimum energy path only the θ, ϕ values along this path were simulated. The simulation was run through exactly the same simulation steps but repeated at increasing temperatures. The temperatures were increased in 10K intervals between 0K and 300K. The energy barrier was calculated from

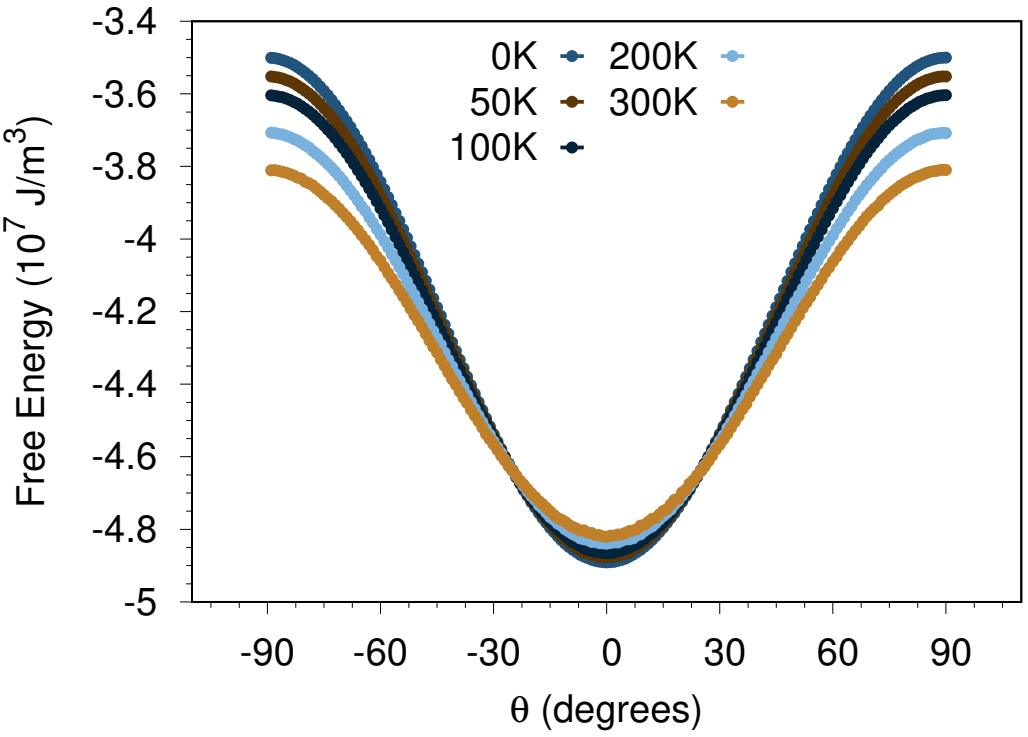

Figure 4.4: **The temperature dependence of the anisotropy in $L1_2$- IrMn**. The minimum energy path between ground states for temperatures of 0K, 10K, 100K and 300K.

the torque again and the energy barriers at 0K, 10K, 100K and 300K are shown in Fig. 4.4. The total energy of the system has increased with temperature but the energy barrier (ΔE) has decreased, due to thermal fluctuations.

The exponent (l) is calculated by plotting the scaling of the anisotropy energy barrier with sublattice magnetisation length n_{AF} on a logarithmic scale. Fig. 4.5 shows the result, giving a temperature dependence of $l = 3.0005 \pm 0.0002$. The exponent almost exactly matches a uniaxial exponent suggesting that the Callen-Callen law applies for a AFM materials as well as FM materials provided the lattice has appropriate symmetry. Previously, it has been thought that Callen Callen law does not apply to AFM's [52] and that they would have different scaling laws than FM materials. However, here it has been proven that an in-plane AFM follows the same scaling laws as an in plane FM. In the next section, the anisotropy $IrMn_3$ in both its ordered and disordered phases will be investigated. In these phases the magnitude and symmetry of the anisotropy is a mystery.

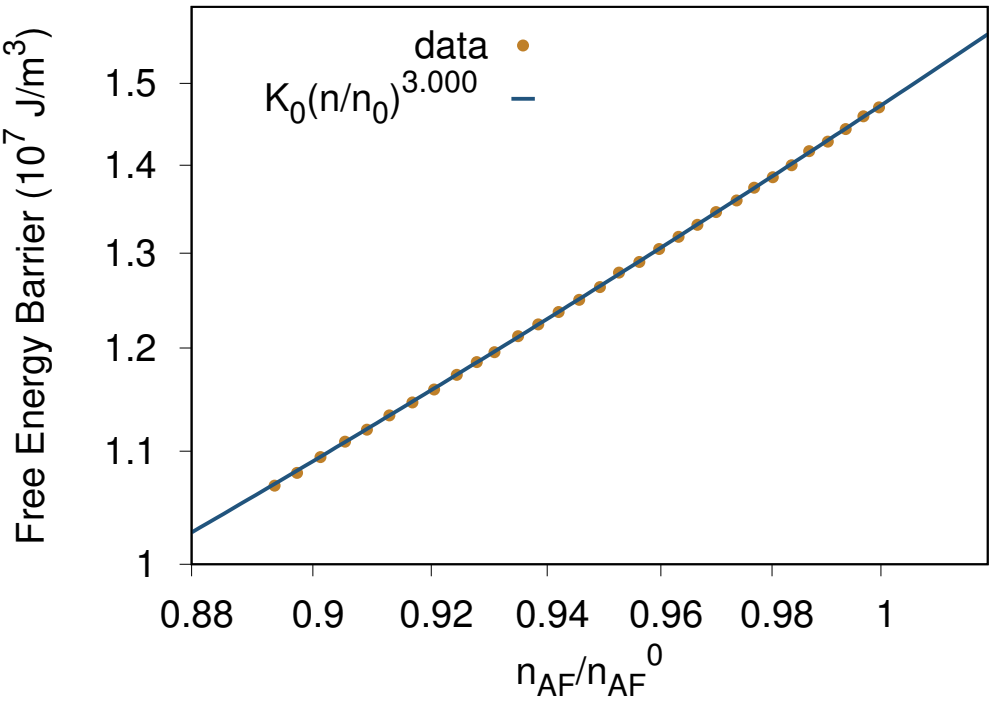

Figure 4.5: **The scaling of the effective energy barrier with sublattice magnetisation length n_{AF} fitted using $E_B(n_{\mathrm{AF}}) = E_0 n_{\mathrm{AF}}^l$.** l is calculated to be $l = 3.0005 \pm 0.0002$ suggesting a scaling similar to uniaxial anisotropy $l = 3$.

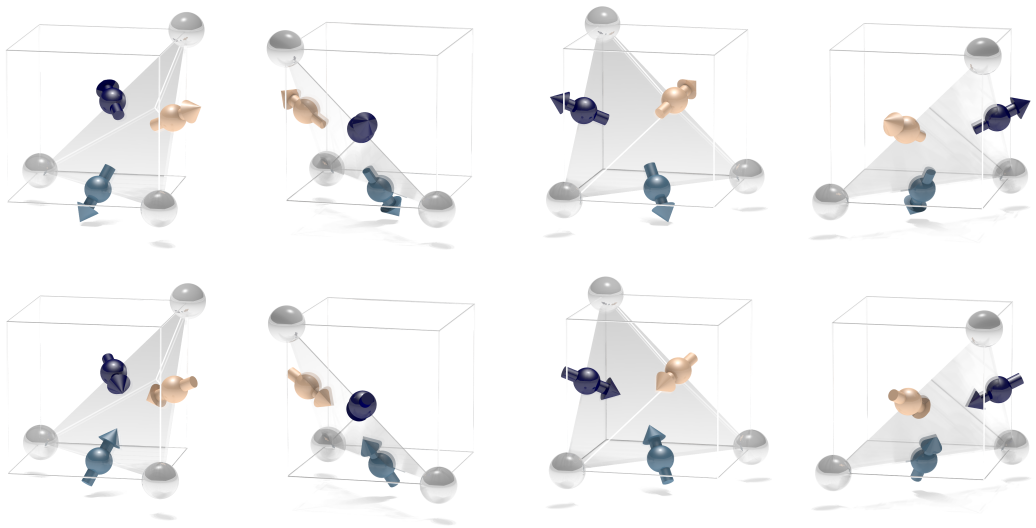

Figure 4.6: **The 8 possible ground state magnetic structures in ordered $IrMn_3$ corresponding to the 8 (111) planes.** The (111) planes are outlined via the pale grey triangles in the image.

direction	θ	ϕ
(0.83, 0.39, 0.39)	25	67
(-0.83, 0.39, 0.39)	155	67
(-0.83, -0.39, 0.39)	205	67
(0.83, -0.39, 0.39)	335	67
(0.83, 0.39, -0.39)	25	113
(-0.83, 0.39, -0.39)	155	113
(-0.83, -0.39, -0.39)	205	113
(0.83, -0.39, -0.39)	335	113

Table 4.1: The eight possible ground state magnetisation directions for one sublattice of IrMn, each of the other two sublattices will have their own eight minima.

4.1.3 The anisotropy in ordered $L1_2$-$IrMn_3$

In section 3.3 we found the ground state of $L1_2$ - ordered $IrMn_3$. In ordered $IrMn_3$ the ground state occurs when the magnetic moments lie in-plane perpendicular to the (111) crystal direction with the three sublattice magnetisation's oriented 120 degrees apart. By symmetry, a cube contains 8 different (111) planes, meaning that ordered $IrMn_3$ actually contains 8 different ground states corresponding to the 8 (111) planes. These ground states are all rotations of each other and are shown in Fig. 4.6.

The positions of the energy minima can be predicted from the ground state structures. For a single sublattice the calculated minima are outlined in table 4.1

The energy surface is computed as described in Section 4.1.1. The simulated system was 8nm × 8nm × 8nm and the simulation was run through the same simulation steps outlined in section 4.1.2. The zero Kelvin energy surface is shown in Fig. 4.7 and has a complicated structure with eight minima. The figure only shows four of the eight ground states due to symmetry. The energy minima lie at $\phi \sim 67°, 113°$ and $\theta \sim 155°, 205°$ corresponding to the expected easy directions of the constrained sublattice in Table 4.1.

To calculate the energy barrier between two adjacent minima we compute the minimum energy path between them. The minimum energy path is outlined as the white line on Fig. 4.7 and then the energy of this line is shown in Fig. 4.8. The calculated 0K energy barrier is 1.78×10^6 J/m^3, and an order of magnitude lower than that calculated by Szunyogh *et al* [25] for a rigid spin rotation around the (111) plane. This has massively reduced the disparity between the experiment and theory with this result being only 20% more than the experimental measurement.

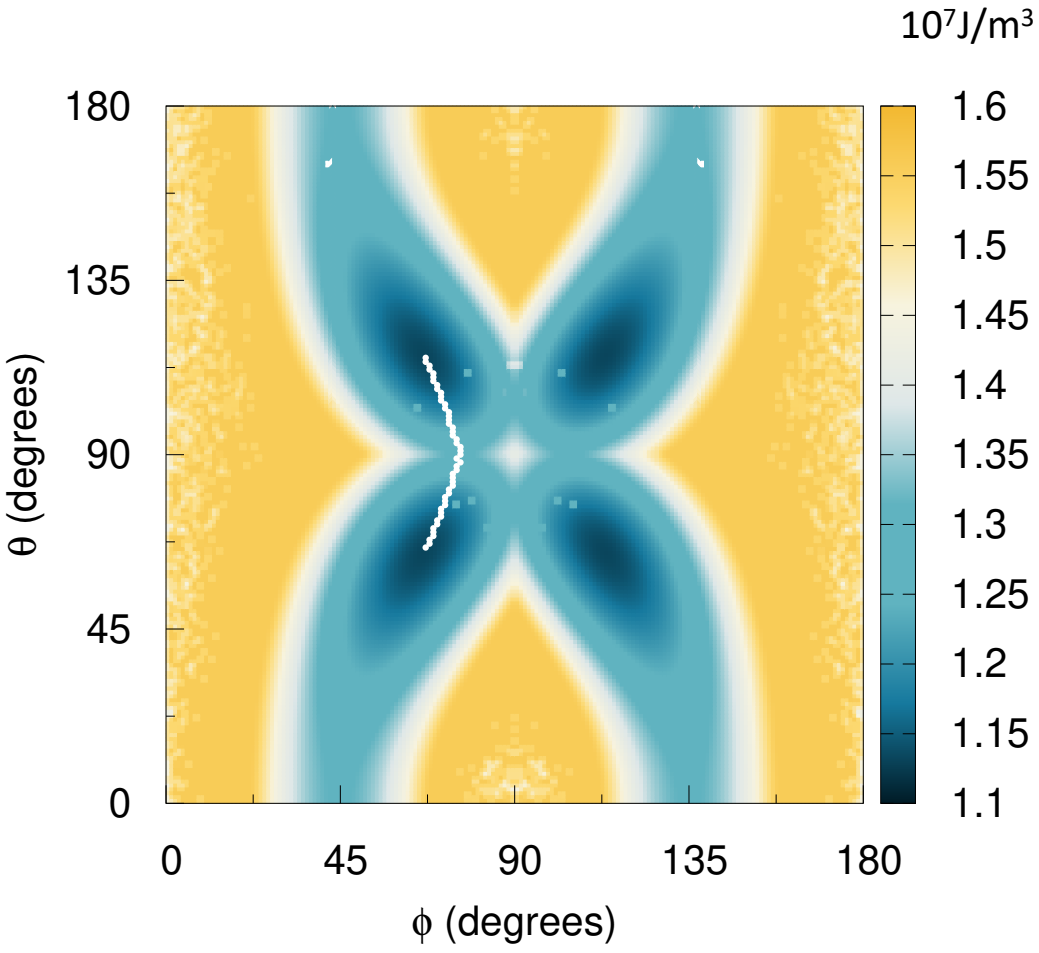

Figure 4.7: **Simulated anisotropy energy surface for ordered $L1_2$- $IrMn_3$ at zero K.** This was calculated from the integral of the total torque. The marked path shows the minimum energy route between the two energy minima.

The reduction in the energy barrier compared to the previous theoretical results arises due to a bobbing motion of the unconstrained spins. The bobbing results from the competition between the exchange and anisotropy energies leading to small deviations from the ground-state spin structure when the antiferromagnetic spins are rotated this bobbing is shown in Fig. 4.9. The reduction in energy barrier can be observed because our model has used a weaker constraint than Szunyogh *et al* [25].

This is particularly relevant to macroscopic approximations of AFM materials with Néel vectors where the sublattices are always assumed to have a fixed local spin structure. The remaining difference in the values of the effective magnetic anisotropy could be due to different ordering or defects in the experimental samples, but our results finally resolve the large disparity between the theoretically

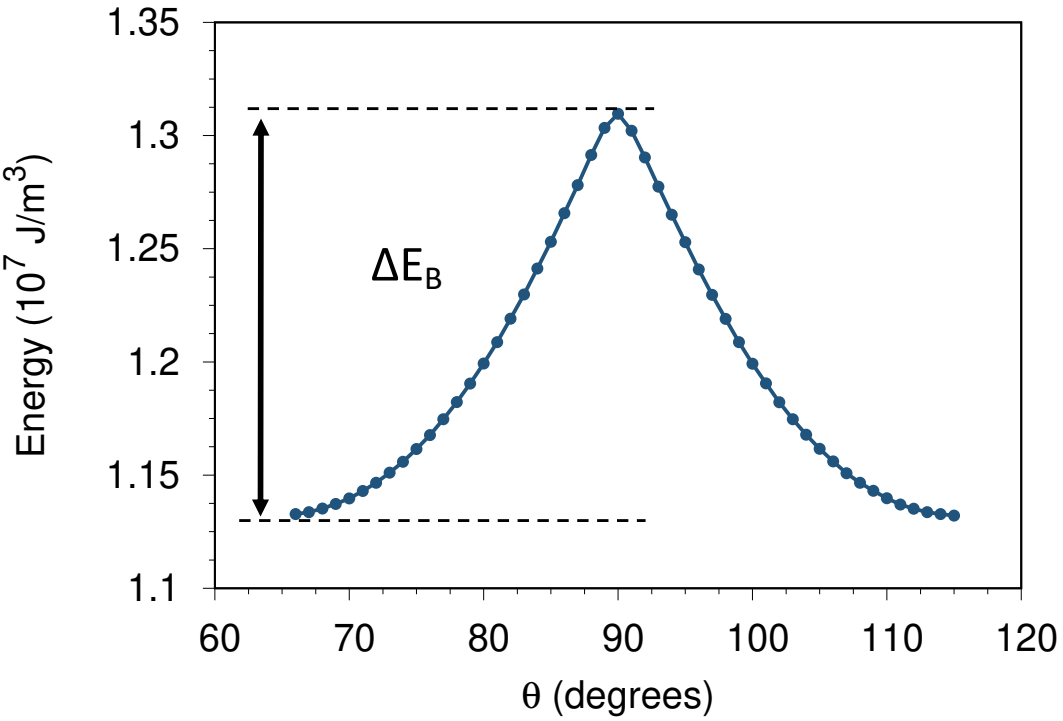

Figure 4.8: **Cross section of the anisotropy surface at $T = 0$ K showing the minimum energy path to reversal between two ground states for ordered $IrMn_3$.** The energy barrier ΔE_B to move between the minima is shown.

calculated and experimentally measured magnetic anisotropy of $IrMn_3$ [20]. We note that, although the energy surface illustrated in Fig. 4.7 has an unusually complex form, the minima themselves exhibit a four-fold symmetry, characteristic of cubic rather than uniaxial anisotropy. The question remains: how to resolve the apparent contradiction with the experimental data of Vallejo-Fernandez *et al* [51] and its requirement of a magnetisation scaling exponent consistent with uniaxial symmetry.

To resolve this discrepancy we now investigate the temperature dependence of the anisotropy constant to calculate the scaling exponent. The energy surfaces and minimum energy path were calculated for temperatures between 0K and 350K as shown in Fig. 4.10. The absolute free energy increases with temperature due to spin fluctuations but the free energy barrier between neighbouring ground state minima, i.e. the magnetic anisotropy, decreases. In Fig. 4.10 we plot the power law dependence of the effective energy barrier as a function of the magnetisation and find an unusual exponent of $l = 3.92 \pm 0.14$. The exponent is closer to a uniaxial exponent of $l = 3$ but is definitely closer to $l = 4$ which deviates from this ideal value due to the complex symmetry of the anisotropy energy surface. We also note

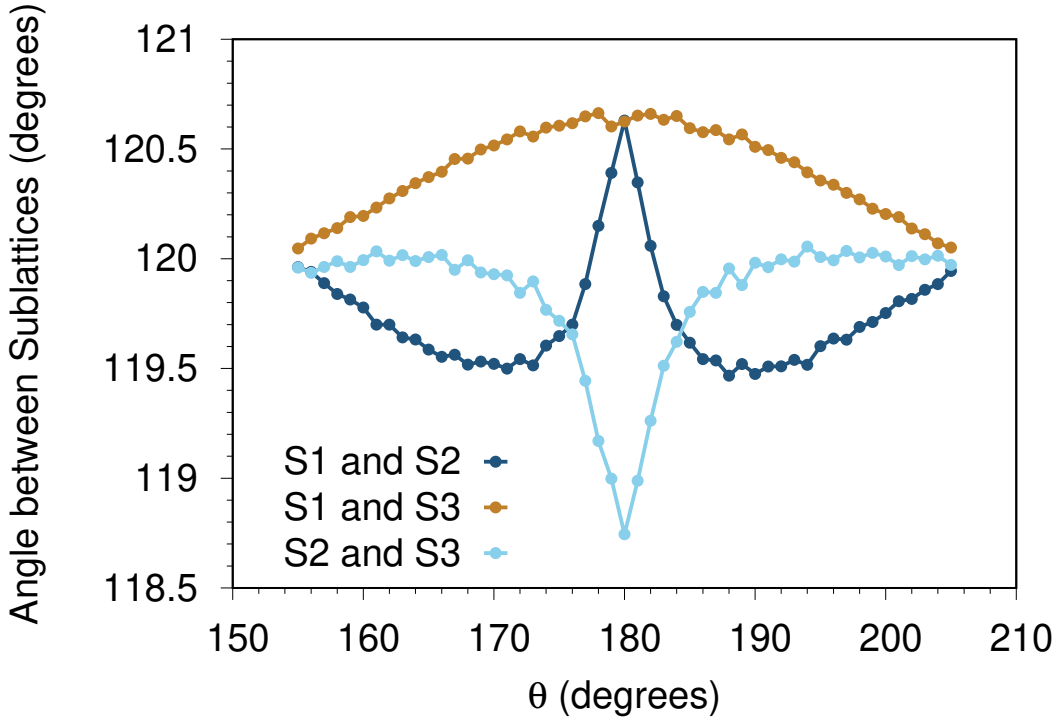

Figure 4.9: **The angle between sublattice (S) shows a bobbing motion as the system is rotated between ground states.** Where S1 is the constrained sublattice and S2 and S3 are unconstrained.

that the specific scaling exponent is dependent on the strength of the anisotropy, and for weaker anisotropy tends towards an exponent of $l = 3$, which may be seen in similar non-collinear magnets such as $PtMn_3$. We conclude that the magnetic anisotropy of $L1_2$- $IrMn_3$ possesses a close to uniaxial temperature dependence in direct contradiction with the usual Callen - Callen power laws and cubic nature of the crystal [52]. However, we do not expect Callen-Callen laws to hold necessarily for such a complex magnetic material as Callen-Callen laws were derived for simple FM materials. The uniaxial symmetry is consistent with the symmetry of the local energy surface of individual spins, as the spins have two energy minima 180 degrees apart. Therefore, the spin fluctuations are taking place in a uniaxial environment.

4.1.4 Calculation of the anisotropy in disordered γ-$IrMn_3$

In the previous section we calculated the symmetry and magnitude of the anisotropy in ordered $L1_2$ - $IrMn_3$ and compared it to the experimental energy barrier. However, the experimental measurements use a disordered alloy of IrMn close to $IrMn_3$. In the following section the energy barrier is calculated for disordered

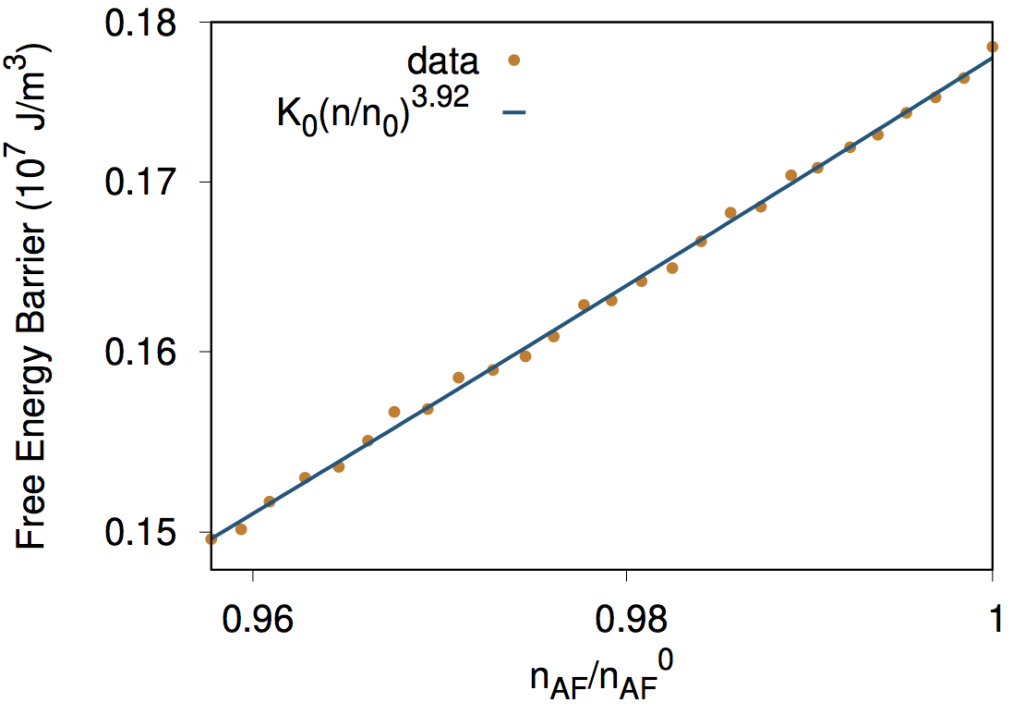

Figure 4.10: The scaling of the effective energy barrier with sublattice magnetisation length n_{AF} fitted using $E_B(n_{\mathrm{AF}}) = E_0 n_{\mathrm{AF}}^l$. l is calculated to be 3.92 ± 0.14 suggesting a scaling more similar to uniaxial anisotropy $l = 3$ than cubic $l = 10$.

$IrMn_3$ with the aim of less disparity to the experimental results.

In section 3.3 we found the ground state structures of disordered $IrMn_3$. The ground state occurs when the spins in each sublattice are oriented 109.5 degrees apart in a tetragonal structure. As with ordered $IrMn_3$ there are eight ground states corresponding to the eight (111) planes. These ground states are all rotations of each other as with ordered $IrMn_3$ shown in Fig. 4.6.

The energy surface was computed using the same method as the previous two sections using a 8nm × 8nm × 8nm system. The zero Kelvin energy surface is shown in Fig. 4.11. The energy surface has a remarkably cubic symmetry, which is a reflection of the lattice. There are four energy minima in the diagram located at $\phi \sim 55°, 125°$ and $\theta \sim 45°, 135°$. The disordered $IrMn_3$ energy surface has four clear minima however the maxima show a lot of noise which comes from the natural disorder in the structure.

The minimum energy path between two adjacent ground states is outlined on Fig. 4.11 as a white line. The line shows more noise fluctuations in comparison to that of ordered $IrMn_3$ due to the noise in the energy surface. The energy along the

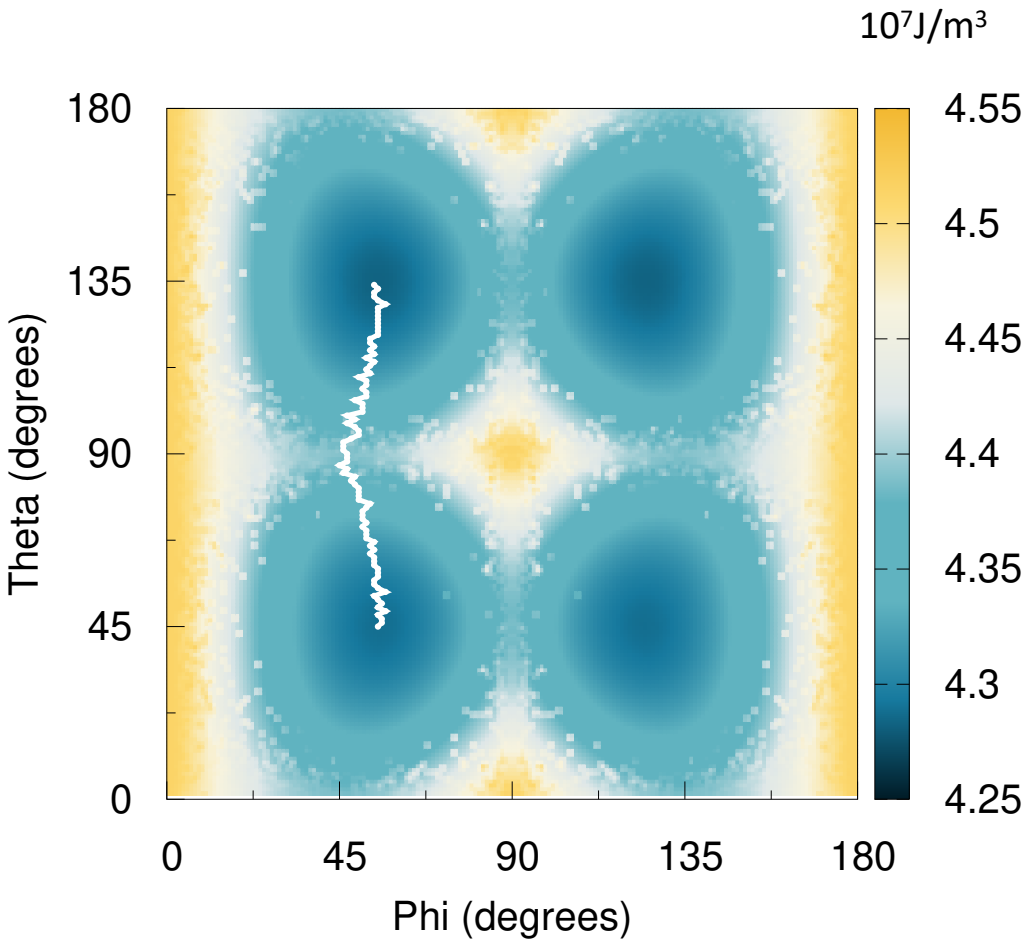

Figure 4.11: **Simulated anisotropy energy surface for disordered γ - $IrMn_3$ at zero K.** This was calculated from the integral of the total torque. The marked path shows the minimum energy route between the two energy minima.

path is shown in Fig. 4.12. The energy barrier has a much smoother transition between energy states than would be expected from the energy surface. The shape of the energy barrier is very similar to that of ordered $IrMn_3$ but the energy difference is slightly lower at only 9.96×10^5 J/m^3. The value is 40% lower than the experimentally measured value from Vallejo-Fernandez *et al* but as with ordered $IrMn_3$ the value has greatly reduced from the theoretical calculations. The remaining difference between our value and the experimental value could be due to differences in composition. We have used $IrMn_3$ however often the composition used experimentally is closer to $IrMn_4$, which may alter the total anisotropy for the material.

The energy surface shows a distinctly cubic symmetry, reflecting the cubic nature of the crystal structure. The temperature dependence of the sublattice

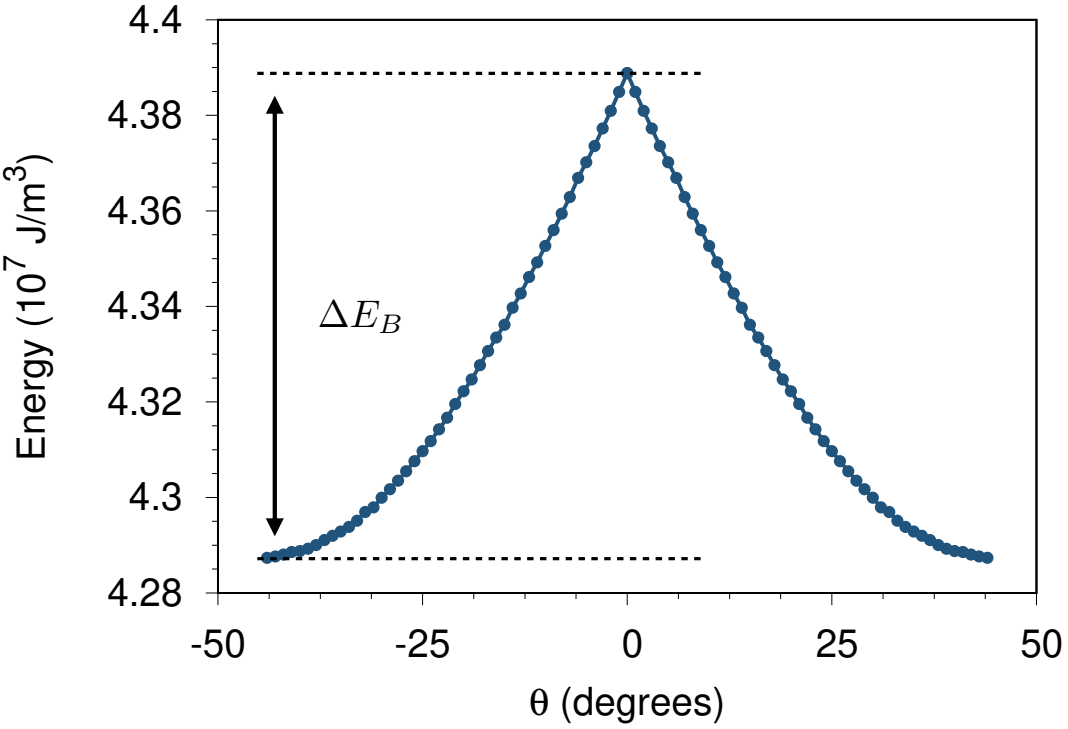

Figure 4.12: **Cross section of the anisotropy surface at T = 0 K showing the minimum energy path to reversal between two ground states.** The energy barrier ΔE_B to move between the minima is shown.

magnetisation was calculated for disordered $IrMn_3$ as in the previous two sections. The result is shown in Fig. 4.13 and the Callen-Callen exponent was calculated to be 3.12 ± 0.03. The temperature dependence is only 4% off the uniaxial exponent. The result is surprising due to the clear cubic symmetry in the energy surface. The apparent contradiction could be due to the local energy surface felt by each atom. The results suggest that although the energy surface is cubic, each individual spin sits in a uniaxial energy environment, where the local environment for each spin governs the spin fluctuations rather than the symmetry of the energy surface as a whole. The results go a long way towards understanding the large difference between the previous experimental and theoretical results.

4.1.5 Calculations of the switching attempt frequency in ordered $L1_2$-$IrMn_3$

The experimental value of the anisotropy constant calculated by Vallejo-Fernandez *et al* is dependent on the value of the attempt frequency (f_0) [51, 61]. In FM materials a value of $f_0 = 10^9$ s^{-1} is usually used. Initially Vallejo-Fernandez *et al*

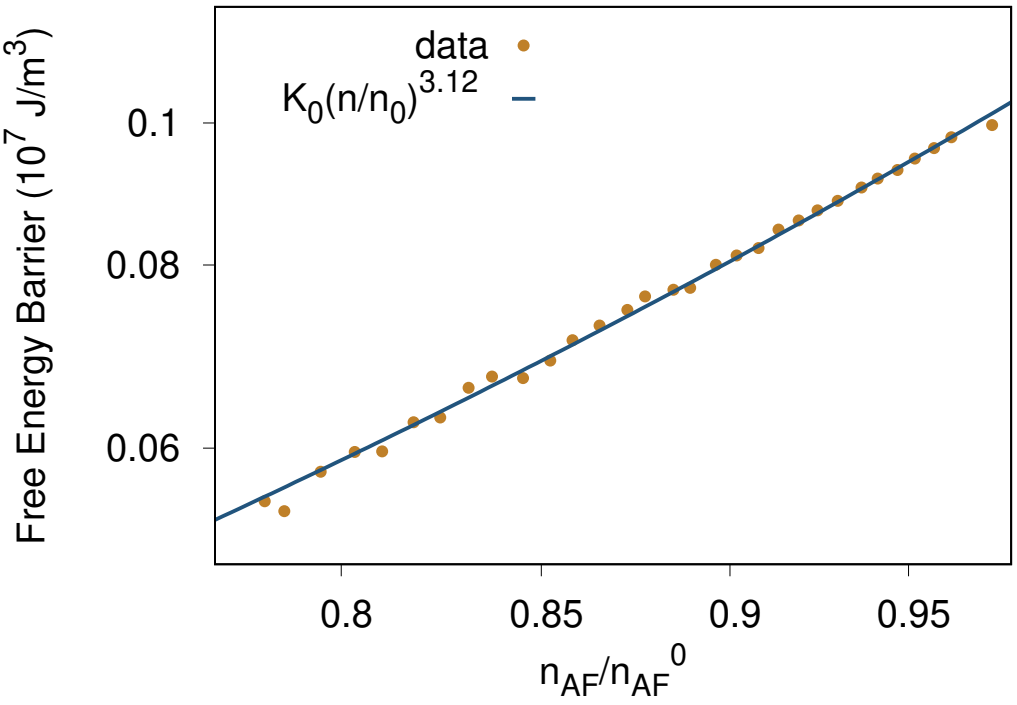

Figure 4.13: The scaling of the effective energy barrier with sublattice magnetisation length n_{AF} fitted using $E_B(n_{\mathrm{AF}}) = E_0 n_{\mathrm{AF}}^l$. l is calculated to be 3.12 ± 0.14 suggesting a scaling similar to uniaxial anisotropy $l = 3$.

used the same value for IrMn giving an overly small value for the anisotropy [62]. More recently they measured the attempt frequency of disordered - γ - IrMn to be 4×10^{12} s^{-1} from a high resolution measurement of the time dependence of the median blocking temperature. This value for IrMn is much larger than the value usually observed for FM materials [51].

In the following section we will calculate the attempt frequency (f_0) of ordered $IrMn_3$. The attempt frequency can be calculated if you know the transition rate (τ) and energy barrier (ΔE) at a given temperature from Equation 4.1. The transition rate is calculated by simulating the time dependent switching over a long time period (much greater than τ) and then taking the average time between transitions (τ). The temperature dependence of the energy barrier was calculated in section 4.1.3. However, the frequency of the transitions is dependent on the magnitude of the damping constant. In the previous simulation we used a damping constant of 0.1 but the value can typically vary from 0.01 to 1 for materials with large spin-orbit coupling. The simulation was repeated for damping constants within this range to determine how the damping constant is affected by the attempt frequency. This means that we cannot accurately calculate the damping

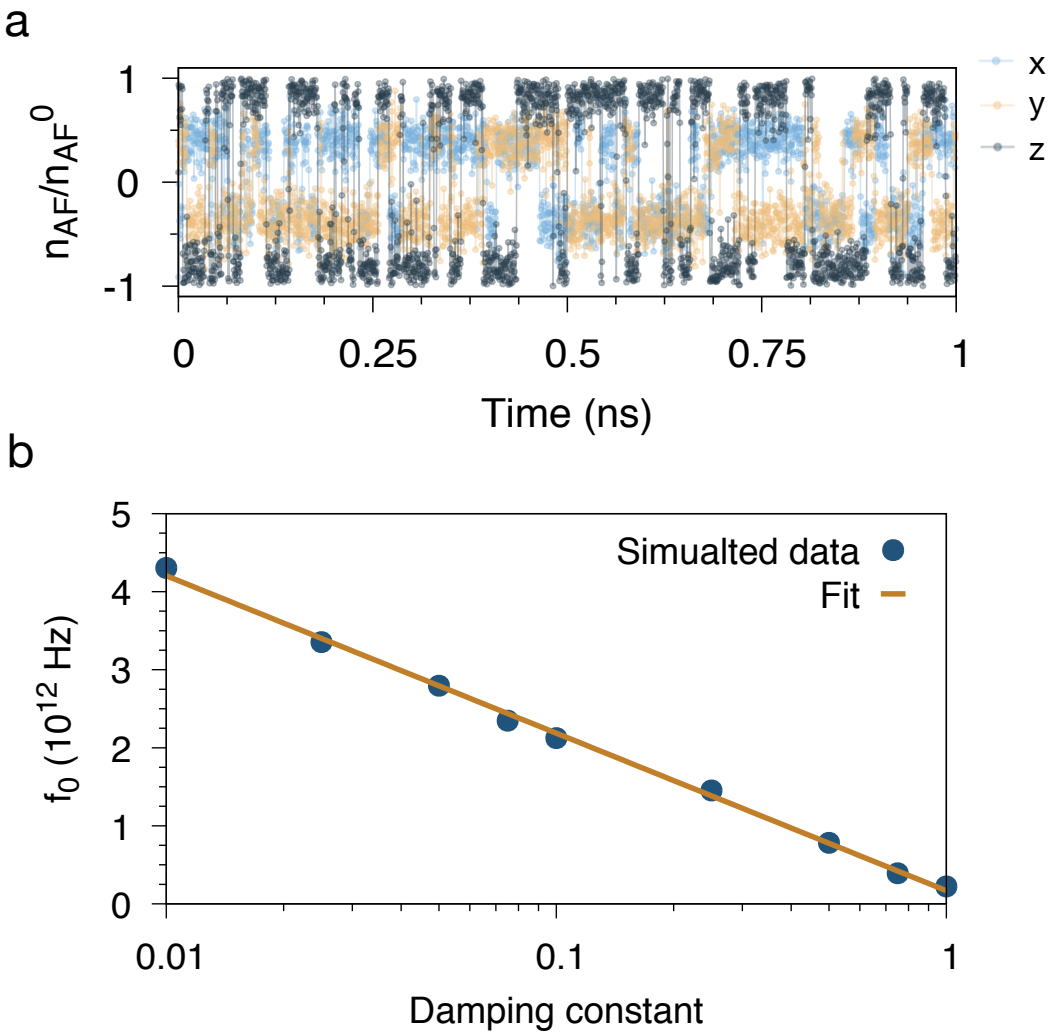

Figure 4.14: **Time-dependent magnetisation of $IrMn_3$ at 100K simulated and dependence of the switching frequency on the damping constant.** (a) The magnetisation of IrMn was simulated for 100ns for a damping constant of 0.1, where only the first 1ns is shown for clarity. The sublattice magnetisation flips superparamagnetically between different coherent ground state orientations. At this temperature the sublattice ordering is approximately 90% since the system is simulated far from the Néel temperature. (b) Dependence of the attempt frequency for reasonable values of the damping constant from 0.01-1 shows a range for the attempt frequency between $f_0 = 0.1 - 4$THz. The data is fit using an equation of the form -0.87 ln(4.30α)+1.44, to show the semilog form of the simulated points.

constant to a specific value, we can only calculate a suitable range of values.

$IrMn_3$ has a giant magnetic anisotropy meaning it takes a lot of energy or a large number of attempts to overcome the energy barriers and transition between states. Due to the limited time scales accessible by simulations we simulate a small sample (1.5 nm)^3 which has a blocking temperature of T_B = 101.5K for a

characteristic timescale of τ = 0.1 ns. As the temperature is just below the blocking temperature the IrMn switches between stable states giving a time dependent form similar to telegraph noise. At this temperature the system will undergo the largest number of transitions giving the most accurate results for the shortest timescales. The dynamic behaviour is simulated using the stochastic Landau-Lifshitz-Gilbert equation [42, 66] as shown in Equation 2.22, the time dependent dynamics of the magnetisation for a single sublattice is shown in Fig. 4.14. The system was simulated for 100 ns using a 0.1 fs time-step and the first 1 ns is shown in Fig. 4.14(a). For each value of the damping constant the transition time was calculated by counting the number of transitions that occurred divided by the total simulation time. The attempt frequency was calculated to be between 0.1 and 4×10^{12} Hz, shown in Fig. 4.14(b). The simulated values are of the same order as the experimentally determined value [62] and provide reasonable bounds for the attempt frequency for non-collinear antiferromagnets, putting these values back into equation 4.1 we can calculate that the anisotropy energy barrier will be between 1.4 - 2.5 $\times$ 10^6 J/m^3.

4.2 Summary

In this chapter a constrained Monte Carlo method was used to calculate the effective temperature dependent anisotropy and the symmetry in different compositions of IrMn. One sublattice of the IrMn was constrained along different θ, ϕ directions and a full energy surface was calculated for ordered $L1_0$ - IrMn, ordered $L1_2$ - $IrMn_3$ and disordered γ - $IrMn_3$.

It was found that AFM's follow the same power scaling laws as FM's as ordered $L1_0$ - IrMn has an exponent of almost exactly 3, as would be expected for an in-plane FM. We found that the anisotropy energy surface for ordered $L1_2$ - $IrMn_3$ is unusually complex and the scaling exponent of the effective magnetic anisotropy is fundamentally different from the expectations of Callen-Callen theory despite the presence of a cubic crystal symmetry and localised uniaxial anisotropy at atomic Mn sites [20]. We find that meta stable spin structures lower the overall energy barrier to a tenth of the energy barrier estimated the *ab-initio* values predicted by L, Szunyogh *et al* [25].

The energy surface of disordered γ - $IrMn_3$ has a cubic symmetry, however the temperature dependence was calculated to be almost exactly equal to the uniaxial exponent. This surprising result shows that the energy surface is cubic however each individual spin sits in a uniaxial energy surface and the local environment

for each spin governs the spin fluctuations rather than the symmetry of the energy surface as a whole.

Spin dynamics calculations revealed a extremely large value for the attempt frequency in ordered $L1_2$ - $IrMn_3$ with values between 0.1 and 4×10^{12}Hz, three orders of magnitude larger than the typical value chosen for FMs. Our results have gone a long way to resolving the discrepancy between previous experimental and theoretical results and represent the first detailed understanding of non-collinear anisotropy in AFM materials.

5

THE ATOMIC ORIGIN OF EXCHANGE BIAS IN SINGLE GRAIN γ-IrMn$_3$/CoFe BILAYERS

The exchange bias effect was first discovered in 1956 by Meiklejohn and Bean [67] and since then it has become one of the most fascinating and complex effects studied within the field of magnetism [26]. This is due to its wide range of applications from read heads in hard drives to more recent developments like neuromorphic computing devices [13, 58, 68]. The effect occurs when a FM is coupled to an AFM and causes a shift of the magnetic hysteresis loop in the FM as shown in Fig. 5.1.

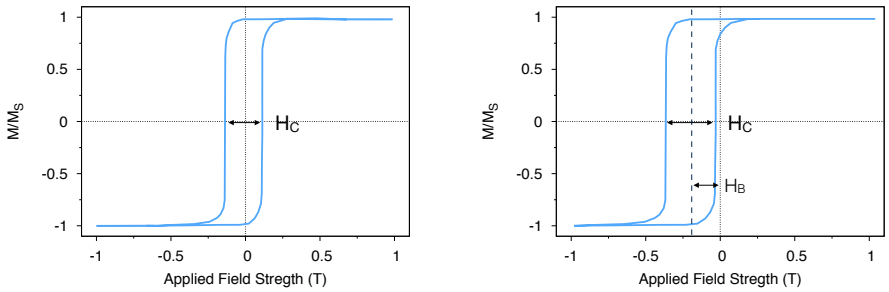

Figure 5.1: (a) The hysteresis loop of a normal FM, the hysteresis loop is symmetric around a zero field and the coercivity (H_C) is fairly small. (b) The hysteresis loop of a FM when coupled to an AFM, the coercivity has increased and the loop has been shifted a distance H_{Bias} and is no longer symmetric around the origin. This gives the FM a preferred direction of magnetisation with only this direction being stable in zero field.

A simplified schematic representation of the atomistic cause of exchange bias is shown in Fig. 5.2. The schematic shows three steps, first heating up the AFM to disorder it, second, cooling it with a field applied in one direction and third applying a large negative field.

In the first step a temperature is applied above the Néel temperature of the AFM, at this temperature the AFM spins are completely paramagnetic and show no long range order. As the Curie temperature of the FM is much higher the FM is completely aligned along the field direction. In the next step as the temperature is decreased to below the Néel temperature, the AFM spins start to align. At the interface the AFM spins are ferromagnetically coupled to the FM spins and therefore the interface of the AFM aligns with the FM. In the final step the field is reduced and then reversed, without the presence of the AFM, the FM would follow the direction of the applied field. However, there is a large field coupling the FM interface spins to the AFM. IrMn is impervious to applied fields due to its strong anisotropy, the AFM remains along the previous field direction at the interface. This causes a unidirectional field to act on the FM and therefore a larger field is required to reverse the magnetisation of the FM. This also means that if the field was to reverse again as there is already a unidirectional field along this direction the FM should reverse back to its original position at a lower applied field than it would with no AFM coupling. This gives a hysteresis loop as shown in Fig. 5.2, shifted away from the zero field point. In the simplified schematic all the interface spins are parallel to cause a unidirectional field however in real materials the cause of the unidirectional field is unknown. Exchange bias has been intensively researched over the past 50 years but despite this there is still no encompassing theory on the cause of the unidirectional field at the interface. The development of a theory has been hampered due to the difficulty in experimentally probing the interface and the complexity of the materials involved.

5.1 Previous models of exchange bias

Since the discovery of exchange bias over 60 years ago there have been many theoretical models proposed to explain the effect. The first model came from Meiklejohn and Bean themselves. The model assumed a perfectly uncompensated spin structure at the interface as in Fig. 5.2. Meiklejohn and Bean's theory predicted the exchange bias as:

$$\mathbf{H}_{EB} = \frac{cJ}{\mu_{FM} t_{FM}} \tag{5.1}$$

where J is the interface exchange coupling, μ_{FM} is the moment of the FM spins and t_{FM} is the thickness of the FM, c is the coupling fraction, the percentage of the AFM interface moment which couples to the FM to cause Exchange Bias.

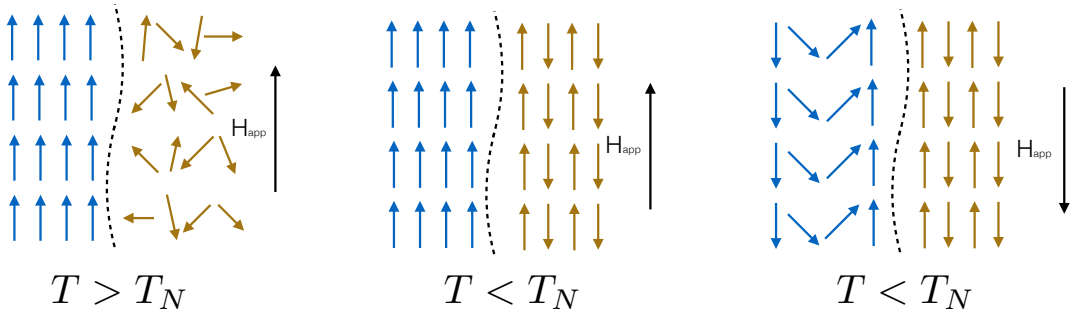

Figure 5.2: A simplified representation of the cause of exchange bias. a) At temperatures above the Néel temperature of the AFM the AFM spins are completely paramagnetic, however as the Curie temperature of the FM is much higher the FM is completely aligned along the field direction. b) As the temperature is decreased to below the Néel temperature of the AFM the AFM spins start to align. At the interface the AFM spins are ferromagnetically coupled to the FM spins. c) As the field is reduced and then reversed the FM follows the field. However, there is a large field coupling the FM interface spins to the previous field direction because the alignment of the AFM is unaffected by the applied field due to its high anisotropy. This causes a larger unidirectional field to be required to change the direction of magnetisation of the FM.

In Meiklejohn and Bean's model they assumed a fully uncompensated interface where $c = 1$. When Meiklejohn and Bean calculated the predicted exchange bias they found that the predicted values for the exchange bias field were orders of magnitude larger than those obtained from their experimental measurements [67].

Over the next 30 years there were many corrections to this model in an attempt to reduce the discrepancy between theory and experiments. The models mostly assumed that the lowest energy magnetic configuration may not be a perfectly rigid AFM and a perfectly uniform FM [69–72]. Most of these models were based on the idea of AFM domains. Domains in FM materials are caused by the demagnetising field however in AFMs the demagnetising fields are usually negligible and domains shouldn't form. Domains can form in our exchange biased bilayers due to the magnetostatic energy from the FM to the AFM [73]. The first model to utilise AFM domains came in 1987 from Mauri *et al* [70]. They assumed a perfectly flat interface and a perfectly compensated spin structure but proposed that the formation of domain walls led to a reversal of the spins at the interface causing an additional "domain wall energy" term. The extra energy reduced the predicted exchange bias by an order of magnitude to match the experimental results. The model accurately calculated the exchange bias shift but fails to predict the increase in coercivity. They attempt to explain this by imperfections pinning the domain walls in the AFM. However a key assumption of the model is that the

AF layer must be thicker than the domain wall width which is not the case in the $IrMn_3$ films used in read heads.

So far the models discussed have all been analytical calculations using energy equations. However, in the 1990's due to the sudden increase in computational power available, the field of theoretical magnetism was transformed with the invention of numerical micromagnetic modelling.

The first micromagnetic model of exchange bias came from Koon *et al* [71] where he modelled a perfectly flat uncompensated interface and predicted that exchange bias can exist through a spontaneous canting of antiferromagnetic spins. The idea is that spins in the interface region are frustrated by competing AFM exchange between the two sublattices and the FM. The competition results in a canted configuration where the spins deviate slightly from the easy axis direction in such a way as to generate a net magnetic moment. This turns out to be possible only by forming a stable domain wall in the antiferromagnet while keeping the ferromagnet mostly aligned with the canted moment. The exchange coupling must therefore be large enough to preserve the relative orientation of the ferromagnet and antiferromagnet interface moments during the entire reversal process [71].

The next micromagnetic model was created in 2002 by Nowak *et al* and is known as the domain state model [74]. They used similar theory to that of Malozemoff [75] assuming that the domains form in the AFM due to defects in the film. However, in the domain state model they assume the defects are caused by a dilution in the bulk of the AFM due to non magnetic atoms or vacancies. The domains that form have a distribution of sizes and shapes depending on the minimum energy. The model is a Monte Carlo simulation and reproduces an accurate prediction of the hysteresis loop shift. The model also accurately reproduced the dependence of loop shift on the AFM dilution. The higher the dilution, the more domains form causing a larger field at the interface, increasing the exchange bias. However, if the dilution is too strong the AFM loses its structure and the exchange bias decreases. The successes of the model meant it was the dominant model used to predict exchange bias in the early 2000's. However, there are still a number of issues with the model. The first issue is that it doesn't consider multigranular structures like those used experimentally. The second is that it doesn't include interface mixing between the AFM and the FM. The largest problem with the domain state model is that the anisotropy constant necessary to create domains in the AFM is orders of magnitude higher than measured experimentally and the model no longer works if the anisotropy is reduced, as the

domains no longer form.

O'Grady *et al* [5] predicted that the interface structure is independent of the bulk material and forms spin clusters of approximately 50 spins which are randomly distributed in shape and size. These behave in a similar way to a spin glass or paramagnetic particles. The exchange interaction between the FM and AFM grains is mediated by the degree of order in the spin cluster. These spin clusters have never been experimentally observed.

The next models of exchange bias were all based on multigranular systems, and will be discussed in Chapter 6. All the models discussed so far have assumed that the interface exchange field occurs due to domain walls in the AFM. In the following Chapter I discuss the origin of exchange bias in single grain IrMn/CoFe bilayers using an atomistic spin model and prove that exchange bias can occur without the need for AFM domains.

5.2 System setup

In this chapter I will simulate the hysteresis loop of a single grain γ - IrMn$_3$/CoFe bilayer to calculate the exchange bias effect and prove that AFM domains are not necessary for exchange bias to occur. We have previously discussed a model of γ - IrMn$_3$ in section 2.4. To calculate exchange bias the γ - IrMn$_3$ must be coupled to a thin FM layer of CoFe to form a bilayer. The following section discusses the modelling parameters for CoFe and the IrMn/CoFe interface.

5.3 Atomistic Modelling parameters

The FM modelled was an alloy of Cobalt and Iron, $Co_{40}Fe_{60}$ due to its high magnetic moment at room temperature, high saturation magnetisation, high Curie temperature and low coercivity. At this composition the CoFe alloy has an isotropic point which is useful for magnetic sensors using an exchange biased system to avoid an anisotropic bias in the magnetic orientation of the film [76]. At this point the material has an amorphous structure [76] meaning there is no long range crystallographic order. Non uniform crystallographic structures are complicated to model and therefore we have assumed the CoFe to have an FCC structure so that the same crystal structure can be used for CoFe and IrMn. The magnetic structure is much simpler in CoFe as it is just a simple FM so the change in crystal structure will not alter the properties or exchange bias greatly, the FM will be completely magnetised (M/M_S = 1) and the exchange coupling

between the FM and the AFM is an order of magnitude lower. In the following section the modelling methods used for modelling CoFe are discussed. CoFe is modelled as a generic Heisenberg ferromagnet.

5.3.1 CoFe parameters

In FM materials the value of the exchange constant can be calculated from the mean field expression:

$$J_{ij} = \frac{3k_B T_C}{z\epsilon} \tag{5.2}$$

where k_B is the Boltzmann constant, T_C is the Curie temperature, z is the number of nearest neighbours and ϵ is the correction factor from the usual mean-field expression ($\equiv$0.86) [42].

In our model, CoFe was assumed to have an FCC structure which has 12 nearest neighbour atoms. The Curie temperature of CoFe is 1300K, so this gives an exchange constant of 5.5×10^{-21} J/link.

In the composition used in this model, CoFe is an isotropic material it has almost no anisotropy[76]. In spintronic devices the CoFe would have a large shape anisotropy due to the planar shape of the thin films. This causes the CoFe to align in plane to minimise the demagnetising field. In this section only a single grain of the thin film was simulated and the demagnetising field has a weaker effect. The in plane orientation was instead approximated using a weak uniaxial anisotropy, with an anisotropy constant of k_u =1 $\times10^{-24}$ J/m^3, in the CoFe a negative anisotropy constant is used corresponding to an easy plane perpendicular to the z axis.

The uniaxial anisotropy Hamiltonian is given by equation 5.3. This calculates the change from the minimum energy configuration by summing over every atom in the crystal. This minimum energy configuration occurs when all of the atomic moments lie in the easy plane [26].

$$\mathscr{H}_{ani} = -k_u \sum_i (\mathbf{S}_i \cdot \mathbf{e})^2 \tag{5.3}$$

Cobalt is the only element which when added to Iron increases its magnetisation. CoFe has the largest saturation magnetisation of any known material

at 2.45T. This leads to a very high value for the magnetic moment ($2.5\mu_B$). The increase in magnetic moment occurs because the exchange coupling increases in CoFe compared to Co and Fe separately as measured experimentally [76] and predicted from results [77].

5.3.2 Interface parameters

Direct experimental measurements of the buried interface are not feasible, and so the interface spin structure and coupling are a continuously debated problems. To find a value for the interface exchange coupling to use in the model indirect methods must be used. O'Grady *et al* predicted that within an interfacial spin cluster the coupling would be FM [5]. L. Szunyogh calculated the magnetic moments, the exchange coupling and the magnetic anisotropy from first principles. They found the exchange integral at the interface was approximately 50% of the that of the bulk structure [78] and that the system had bulk properties within 1-2 atomic layers of the interface. The exchange constant was therefore assumed to be a nearest neighbour interaction, initially given a value of 1.5×10^{-21} J/link. The effects of the exchange coupling will be investigated parametrically in section 5.7 and the simulated exchange bias will be compared to experimental data.

5.4 Simulation steps

The disordered γ - IrMn/CoFe bilayer was created to be 8nm × 8nm × 8nm, with 5nm of IrMn$_3$ topped with 3nm of CoFe as shown in Fig. 5.3. The IrMn has a (111) out of plane orientation as this gives the largest possible exchange bias [79, 80].

Experimentally, to achieve exchange bias the AFM needs to be set by annealing under an applied field. In this step the magnetic moments of the FM will align with the applied field direction. As the AFM and the FM are coupled together at the interface, the interface of the AFM will align with the applied field as well. This means the AFM is now set along the applied field direction even though the AFM is impervious to applied fields. The same needs to be done in our simulation and the AFM is set before the exchange bias is calculated from the hysteresis loop using three simulation steps:

1. **Annealing under an applied field:** The system was heated to above the Néel temperature of the AFM then cooled in the presence of a high field.

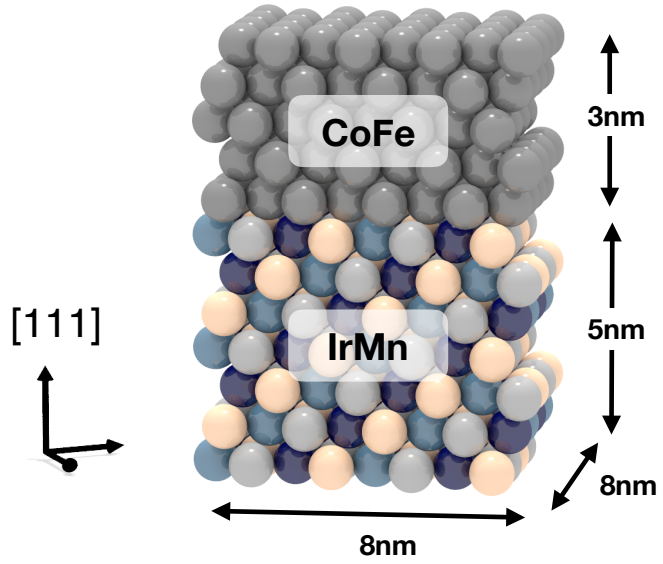

Figure 5.3: **A schematic diagram showing a section of the IrMn$_3$/CoFe bilayer**. Each sphere represents one atom, the top half is CoFe and the bottom IrMn (with the colours representing the different sublattices). This was 8nm × 8nm × 8nm with 5nm CoFe and 3nm IrMn$_3$.

2. **Equilibration:** The system was left to equilibrate at 0K under no applied field to let the system relax to its equilibrium ground state position.

3. **Hysteresis Loop:** A hysteresis loop was performed on the system to measure the strength of the exchange bias field.

5.4.1 Annealing under an applied field

Experimentally, the direction of the exchange bias is set by annealing. Annealing is the process of heating the sample up to a high temperature (above the blocking temperature of the AFM) then slowly cooling to a temperature below the blocking temperature under an applied field. The cooling takes place over a long timescale (minutes to hours). These timescales are 10^{11} times larger than our atomistic time step making simulations of this length computationally unfeasible. Experimentally, the annealing process cannot heat to the Néel temperature as this would cause damage to the structure, such as by destructive diffusion between the layers. Instead the simulation is heated to a setting temperature, which is between the blocking temperature and the Néel temperature. At this temperature the AFM has a probability of the magnetisation flipping between different AFM ground states. The time between flips (τ) is given by:

$$\frac{1}{\tau} = f_0 \exp\left(-\frac{KV}{k_B T}\right), \tag{5.4}$$

where f_0 is the attempt frequency, K is the anisotropy constant and V is the volume. As the temperature (T) decreases the thermal relaxation time (τ) increases. The simulation time must be long enough that it is greater than (τ) or the magnetisation will not change states and the AFM interface will not be correctly set. We computationally model the setting process using a similar procedure to the procedure used experimentally. In the simulations however, we can heat the sample up to a higher temperature (higher than the Néel temperature of the AFM) without destroying it and cool it all the way to 0K. The increased heating and cooling should cause the AFM to set in a shorter timescale as just below the Néel temperature the relaxation time will tend to zero.

The spin dynamics were modelled using the Landau-Lifshitz-Gilbert equation with a Heun integrator as described in section 2.3.3, the system was heated to 1500K and then cooled over 80,000,000, 0.1 fs time steps to 0K for a total of 8 ns. We note that although 8 ns is computationally very expensive and requires a lot of simulation steps it is still orders of magnitude below the experimental setting time which is often hours.

IrMn has 8 possible ground states as discussed in section 4.1.3, corresponding to the 8 (111) planes. Each of these eight possible states is a local energy minimum but the global minimum energy will occur when the interface exchange field of the AFM aligns with the FM. The global minimum energy state should have a slightly lower energy than the other local minimum energy states.

Fig. 5.4 shows the variation of the magnetisation in the system with time and temperature throughout the field cooling process. As the system cools the probability of the magnetisation changing state decreases as the relaxation time increases as given by equation 5.4. At the blocking temperature (T_B) the relaxation time is longer than the simulation time and the AFM magnetisation can no longer change state. In our simulation the blocking temperature is approximately 400-500K. The simulation must therefore have a large number of small time steps close to the blocking temperature as there is only a small energy difference between the global minimum energy and a local minimum energy. This is explained in figure 5.5

Ideally, during the field cooling step the AFM should end up in the global minimum energy state. However, because the energy of the states are so similar

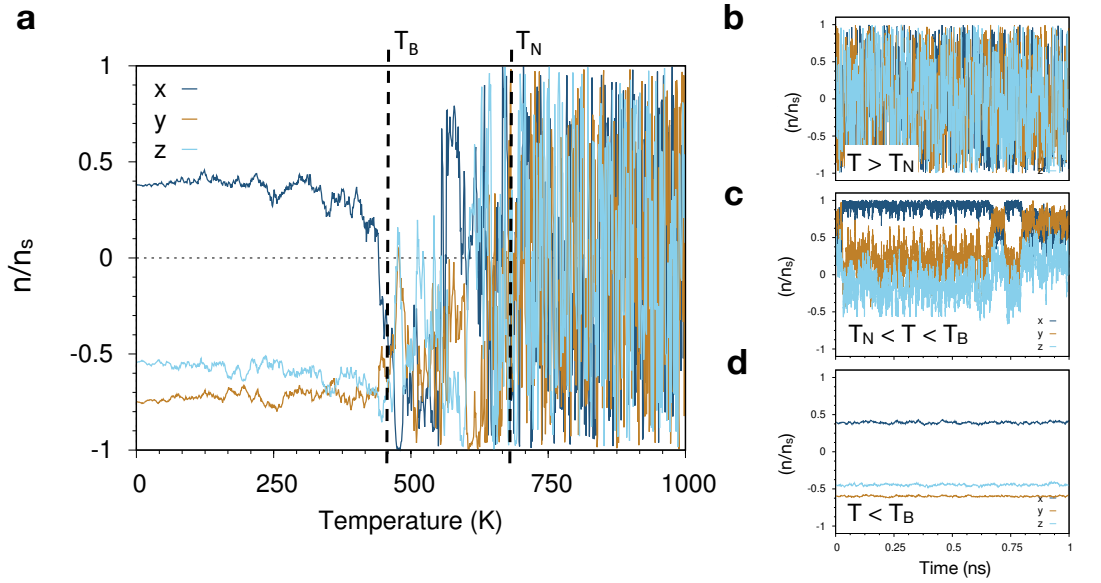

Figure 5.4: **The variation of the total magnetisation in x,y,z with temperature for a single sublattice.** (a) The temperature dependent magnetisation (b) Above the Néel temperature (T_N) the magnetisation fluctuates rapidly. (c) Once the Néel temperature is reached the system must lie in one of the ground states however it still has the energy to rapidly fluctuate between these states until the blocking temperature (T_B) is reached. (d) Below this temperature the system remains in the same state as at these timescales it no longer has enough thermal energy to change state. This shows the times and temperatures where these changes occur.

often a different energy state is found instead. If the AFM does not end up in the global minimum energy, the exchange bias of the system will be along the wrong direction (not the setting field direction). The energies are very close because there is a complex coupling between the interface and the bulk material. The ground state which causes the interface moment to be closest to the field may not be the same ground state which causes the bulk moment to be closest to the field. As the temperature (T) decreases the thermal relaxation time (τ) increases until the simulation reaches the blocking temperature and it is longer than the measurement time and it is unlikely the magnetisation will fluctuate between states. Only at T_B is the energy high enough that the system can change states but low enough that it is always stuck in one of the ground states. The simulation must have a large number of small time steps around T_B as there is only a small energy difference between the global minimum energy and a local minimum energy. If the temperature is decreased in too large a temperature step, the magnetisation may become fixed in a state that is only a local minimum. As the temperature is decreased the atomic moments lose thermal energy as

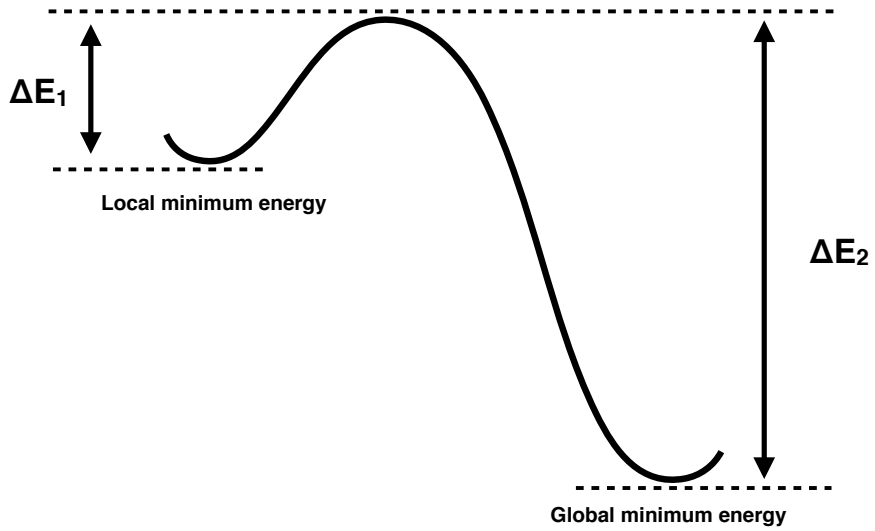

Figure 5.5: **A visualisation of the energy barriers to magnetic reversal showing the energy difference between the global and local energy minima for our bilayer.** If the temperature is decreased in too large a temperature step, the magnetisation may become fixed in a state that is only a local minimum. As the temperature is decreased the thermal energy decreases ($E \propto k_B T$). As ΔE_1 and ΔE_2 are very close in energy the sublattice magnetisation may be able to transition to the local minimum in one temperature step but as the temperature is decreased it may not be able to transition back as the thermal energy is now less than ΔE_1 and ΔE_2.

($\Delta E = k_B \Delta T$). As the global and local minima are very close in energy the spin direction may be able to transition to the local minimum in one temperature step but as the temperature is decreased it may not be able to transition back as the energy is now too small. If the change in temperature is too great the AFM has an equal probability of setting in any of its ground state positions. This problem could have been solved using a simulated annealing algorithm [81] which is a technique for energy minimisation and finding the ground state of a function or system. In the future this will be implemented and would be a better way of simualting the annealing process.

5.4.2 Equilibration

During the equilibration stage the field is removed and the atomic moments are left to equilibrate to their ground state positions at zero Kelvin. The only external field remaining on the FM layer is from the interface of the AFM. The AFM is fixed in its ground state position and the FM rotates to align along the direction of the compensated unidirectional interface field from the AFM.

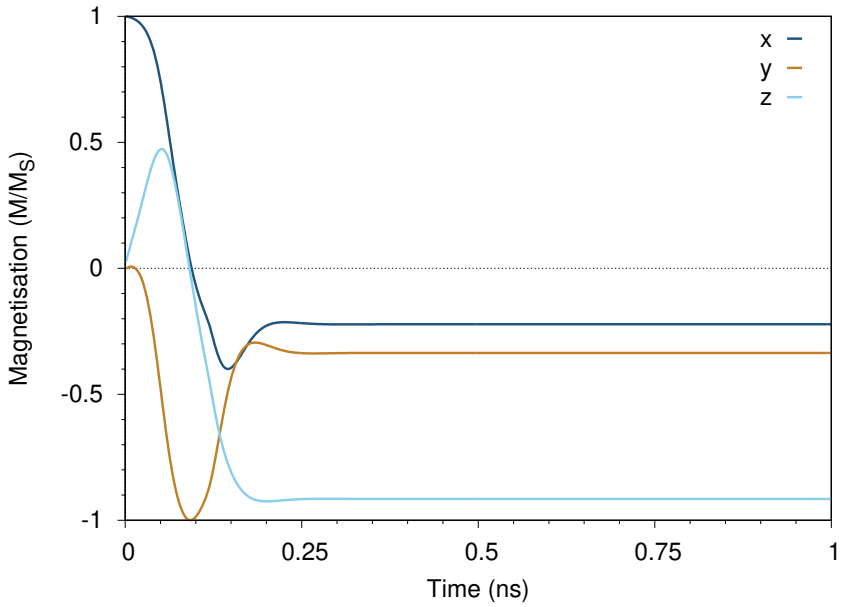

Figure 5.6: **The simulated equilibration of the magnetisation of the FM layer in x,y,z.** The system equilibrates away from the applied field direction (0,1,0) and instead to (-0.18,-0.22, -0.94) suggesting that the setting process has not worked.

The simulation used 500,000, 0.1 fs time steps and the dynamics were modelled using the LLG equation. Fig. 5.6 shows the direction of magnetisation of the FM throughout the equilibration stage. If the setting has worked correctly the magnetisation of the interface AFM and therefore the FM should be approximately along the direction of the setting field (1,0,0). Fig. 5.6 shows that the magnetisation has rotated far from the initially applied field direction meaning that the system has not been properly set by the field cool process. The field cooling failed because ΔE_1 and ΔE_2 are very similar in value and the temperature steps in the simulation are too large to account for the small change in energy. I have increased the number of time steps in the field cooling calculation and focused on cooling around T_B but unfortunately this problem occurred for all timescales that were viable on the computational resources available. In the experimental setup the field cool process occurs over a matter of hours but in our simulations we can only viably run simulations up to a few tens of nanoseconds.

To enable the continuation of the project instead of running the hysteresis loops along the setting field direction the hysteresis loops were run along the direction to which the FM equilibrates. This method is used for the rest of the current section until a new setting method is developed in section 6.3.1. The global minimum energy direction changes depending on the direction of the applied field

and every local has the potential to be the global minimum. Therefore by finding out the state the system is in and applying the field along that direction the local minimum becomes the global minimum.

5.4.3 Hysteresis loop

After equilibration a 1T field was applied to the bilayer along the direction of equilibration of the FM. The field is slowly reduced to -1T then increased to 1T in 0.01T increments. At each increment a number of 0.1 fs timesteps occur, the number of timesteps is important because at each new field point the magnetisation takes time to equilibrate. The equilibration time is due to the damped procession of the LLG equation, during which the magnetisation precesses around the minimum energy direction. If the number of timesteps is too few the sample will not have fully equilibrated between each 0.01T field step, which leads to an increase in the coercivity of the hysteresis loop as the spin direction has not yet equilibrated to the minimum energy state.

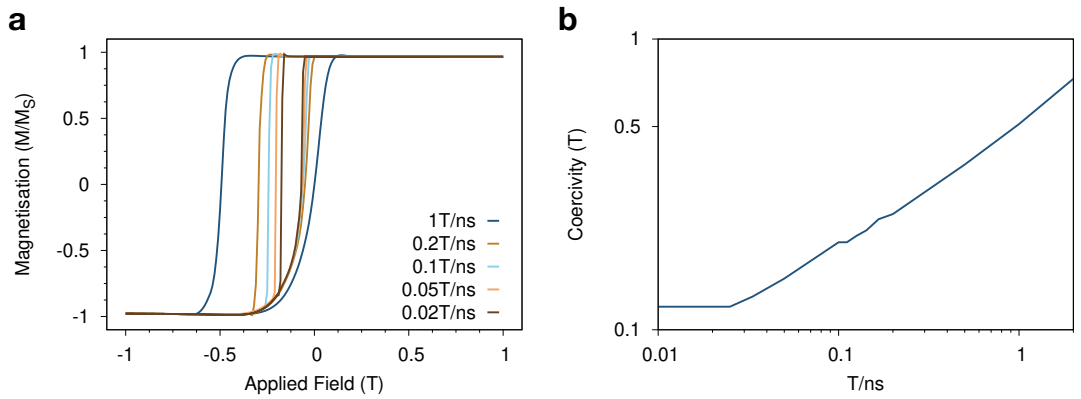

Figure 5.7: **Convergence of the coercivity for decreasing field rates** (a) Comparison of hysteresis loops for disordered IrMn$_3$/CoFe as the number of time steps per field increment is varied between 50000 and 5000000. The field increment rate is kept constant at 0.01 T. Each time step is 0.1 fs. As the number of time steps increases the coercivity decreases. The hysteresis loop converges to a minimum coercivity for time steps over 0.03 T/ns. (b) The variation of the coercivity with field rate. The minimum coercivity occurs at 0.03 T/ns as seen in the hysteresis loops.

The number of steps was varied, the resulting hysteresis loops are shown in Fig. 5.7. The coercivity converged at 0.03 T/ns which corresponds to 3,000,000 steps per 0.01 T field step increment. This number of steps was used for the remainder of the chapter.

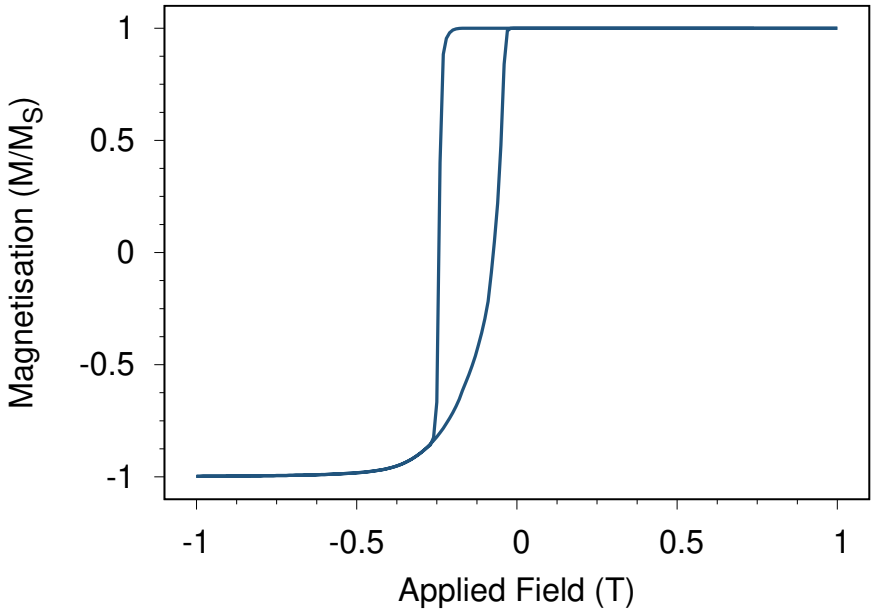

Figure 5.8: **Simulated hysteresis loops at T = 0K for the disordered IrMn$_3$/CoFe system.** The system exhibits a classic shift of the loop due to the exchange bias effect, the system shows an exchange bias of magnitude 0.14T.

The field is applied along the direction of the interface field of the AFM because this will give the highest exchange bias field. The Stoner-Wohlfarth model states that when a field is applied at an angle to the easy direction the field required for reversal decreases. Therefore, if the hysteresis loop is measured along the setting field direction the exchange bias decreases in comparison to the equilibrium direction.

The hysteresis loop for the disordered γ - IrMn$_3$/CoFe system shows an exchange bias field of 0.14 T, assuming a reduction in the exchange bias due to temperature affects this value is close to typical experimental measurements. O'Grady et al. measured an exchange bias field of 0.02 T using 10 nm of CoFe at room temperature with a rough interface. The FM in their calculations was approximately three times thicker than our simulations and from Equation 5.5 we can see this would cause a three times reduction in the exchange bias from our simulated exchange bias. The larger size will decrease the exchange bias field. The remaining discrepancy may be due to the rough interface or temperature effects. The effects of temperature and rough interfaces will be studied in sections 5.8 and 7 respectively. The current simulated bilayer has no defects or lattice imperfections and therefore the exchange bias must be attributed to the intrinsic ordering, raising the question: how does the intrinsic ordering in the

antiferromagnet determine the exchange bias?

5.5 An investigation into the atomistic origin of the exchange bias effect

To investigate the cause of exchange bias we analysed the direction and magnitude of the magnetisation of the IrMn at the interface throughout the hysteresis loop. The data shows a clear hysteresis in the net magnetic moment which follows the hysteresis of the FM and exhibits the same coercivity and exchange bias. The hysteretic behaviour is characteristic of a large reversible component of the interfacial magnetisation, in agreement with previous XMCD measurements [82]. The interface magnetisation shows a small vertical shift not present in the CoFe loop due to a change in magnitude of the magnetisation at the interface shown in Fig. 5.9(b). The change in the magnitude of the interface magnetic moment arises due to the uncompensated interface field, these spins are irreversible and do not rotate during the hysteresis cycle. We can say that our interface moment is comprised of a compensated moment which reverses (n_c) and an uncompensated moment which does not reverse (n_{un}). When the field is pointing along the positive saturation direction the interface field is equal to $n_c + n_{un}$, whereas when the field is pointing along the negative saturation direction the interface field is equal to $n_c - n_{un}$. The vertical shift in the hysteresis loop is therefore equal to two times the number of uncompensated spins at the interface. These uncompensated spins which are irreversible are the spins which contribute to the exchange bias effect. In the example in Fig. 5.9 (b) the vertical shift is 13.92 which corresponds to 6.96 uncompensated spins.

The exchange bias is proportional to the ratio of the strength of the pinning field from the AFM to the total FM magnetisation. It is quantitatively calculated from the number of uncompensated spins as:

$$B_{EB} = \frac{n_{un} J_{int}}{\mu_{FM} N_{FM}} \tag{5.5}$$

where N_{FM} is the number of ferromagnetic atoms and μ_{FM} is the magnetic moment of the FM atoms. The equation represents the strength of the pinning field from the AFM ($n_{un} J_{int}$) compared to the total moment of the FM ($\mu_{FM} N_{FM}$) and therefore the strength of the exchange bias. (Using n_{un} equals 6.96 we can

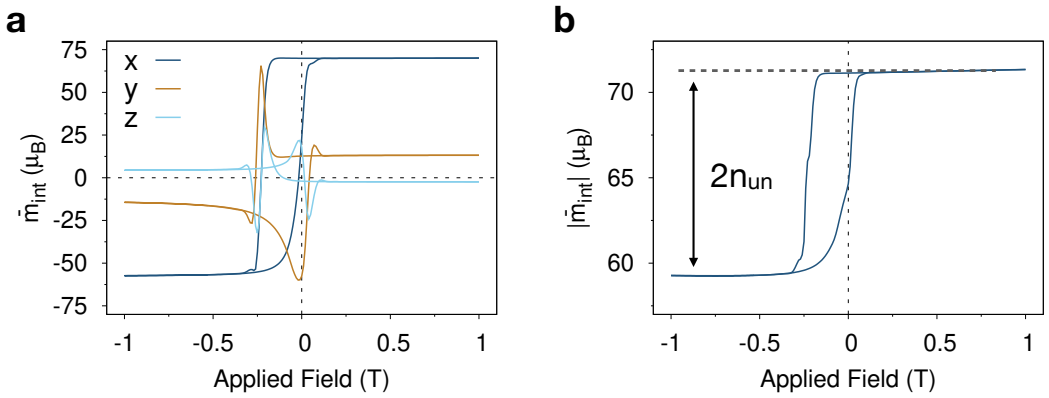

Figure 5.9: **The net magnetic moment of the IrMn interface layer throughout the hysteresis loop.**(a) Behaviour of the components of the net magnetic moment in the interfacial layer of γ $IrMn_3$ showing hysteretic behaviour of the interfacial moment which follows the CoFe magnetisation, indicating a large reversible component of the magnetisation. The loop is vertically shifted showing a change in the magnitude of the interfacial $IrMn_3$ moment during the hysteresis cycle (b), indicating the irreversible spins n_{un} contributing to the exchange bias field.

calculate the exchange bias to be (0.13 $\pm$ 0.01)T which is in agreement with the simulated value.

We have now calculated the number of uncompensated spins at the interface and know that they can occur without the need for AFM grains or interface mixing. But what is causing these spins to be uncompensated?

5.5.1 What causes the net interface moment in $IrMn_3$?

In disordered $IrMn_3$ 25% of the atoms are Ir in each sublattice, meaning 25% of the atoms are non-magnetic. The 25% which are non magnetic are chosen randomly using a probability function. The random nature of the removal means that although on average 25% are removed from each sublattice in reality a slightly different number will be removed from each sublattice. For an infinite grain the difference would balance out but as our grain is of a finite size the system can end up with large differences between the numbers in each sublattice. The difference leaves a net magnetic moment along the direction of the sublattice with the largest number of Mn atoms remaining. For the simulated hysteresis loop previously discussed the number of atoms in each sublattice is outlined in table 5.1.

From the number of atoms in each sublattice the number of uncompensated

Sublattice	N_S	($\mathbf{M}_S$)	(M_l)
1	192	(-0.45, -0.81,-0.35)	0.92
2	193	(0.92,-0.08,-0.38)	0.91
3	200	(0.66,-0.71,0.24)	0.90
4	195	(-0.016,-0.013,0.99)	0.89

Table 5.1: **How the exchange bias is predicted from the crystallography.** The number of atoms in each magnetic sublattice (N_S) and the magnetisation direction ($\mathbf{M}_S$) and length (M_l). This gives n_{un} as 6.67 uncompensated spins, as calculated from Equation 5.6. This imbalance is caused by there being an average of 6.67 atoms more in sublattice 3 than in the other 3 sublattices, while the magnitude is reduced due to sublattice disorder arising from local spin frustration.

interface spins can be calculated:

$$n_{un} = N_L - N_{av}, \tag{5.6}$$

where N_L is the number of Mn atoms in the sublattice with the largest number of atoms in and N_{av} is the average number of Mn atoms in the other three sublattices. For our interface the calculation gives $n_{un} = 6.67$ which is an almost exact match to the result calculated in Fig. 5.9(b). The discrepancy between the values is because the calculation is simplified and assumes that the bias field lies exactly along the direction of one of the AFM sublattices. In reality this will only occur when $N_L >> N_{av}$ and the direction of the bias field will be a vector combination of all four sublattice magnetisation directions dependent on the positions of the removed atoms as described in Table 5.1.

As there are 780 Mn atoms in the interface layer the number of uncompensated spins n_{un} is about 0.9% of the total interface magnetisation. The small imbalance, combined with a large exchange interaction, predicts an exchange bias field of 0.15 T using equation 5.5 which is very close to the numerical simulation of 0.14 T. Now we know what causes the uncompensated spins we want to know where they are located across the interface. There are two options for the location of these spins: a) 6.67 specific spins are pinned and the rest rotate as normal or b) a small proportion of every spin is pinned (9% pinned). For the rest of the thesis I will refer to option (a) as localised pinning and option (b) as delocalised pinning. To investigate the location of the pinned spins we visualise the interface spin structure throughout the hysteresis loop. The visualisation of a small section of interface is shown in Fig. 5.10.

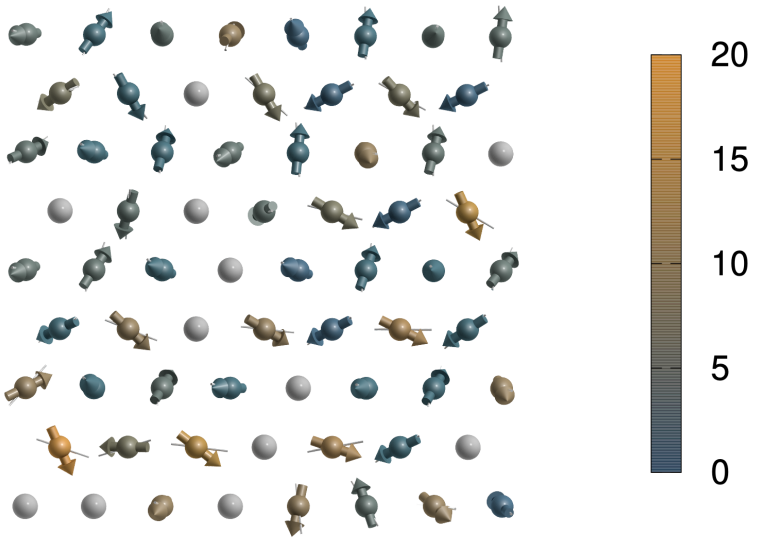

Figure 5.10: **A visualisation of the net magnetic moment of the interface layer throughout the hysteresis loop.** Arrows indicate spin positions at negative saturation, thin bars indicate the starting positions at positive saturation and the colour scale shows the angular change. The small angular deviation of individual spins demonstrates the delocalised nature of the reversible and irreversible spins.

The magnetisation direction was compared between the positive saturation and negative saturation points in the hysteresis loop. During the hysteresis loop each of the interfacial spins moves only slightly, amounting to a small distortion of the interfacial spin structure. The reversible spins come from a net change in the total interfacial moment rather than the local reversal of individual spins. The strong exchange coupling between the spins stabilises the overall spin structure preventing a large angular change for individual spins. In a similar way the pinned interface spins are not actually pinned local spins, but arise from the net irreversible interface moment in the AFM. The figure suggests a delocalised motion of the magnetic moments.

Previous models of exchange bias have focused on the uncompensated interface moment being due to localised spins. Our model suggests that, the exchange bias can also be caused by delocalised spins. We suggest that although delocalised spins do cause exchange bias, localised spins can also cause exchange bias. In real devices the localised spins would occur due to localised defects such as point defects, non magnetic impurities or grain boundaries. We have simulated a disordered - γ -IrMn$_3$ bilayer but without the delocalised interface spins instead we have created localised "defects" which will contribute to the exchange bias. This was created by removing all of the AFM interface spins apart from 6, which

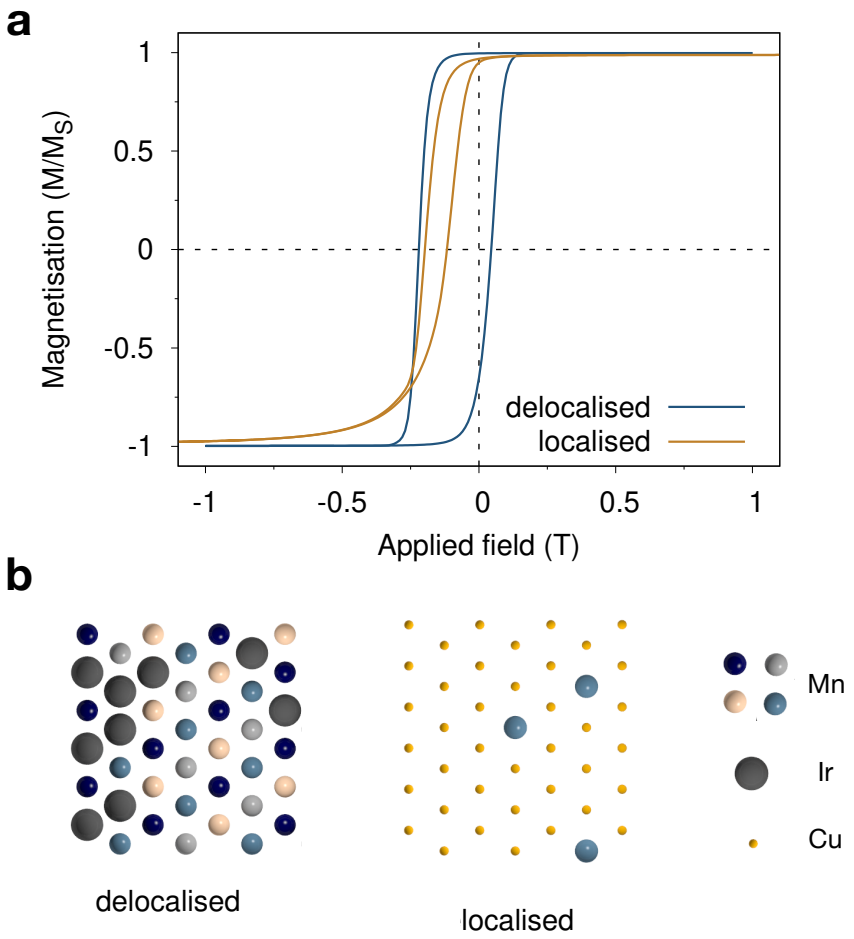

Figure 5.11: Exchange bias simulations for localised and continuously distributed uncompensated spins. (b) shows the difference between delocalised distributed and localised spins at the interface.

are still coupled to the bulk and to the FM. These are localised points and are the only points which contribute to the exchange bias field. We have simulated this by removing the rest of the interface spins and replacing them with a non magnetic material (Cu). The hysteresis loop produced is shown in Fig. 5.11 and is compared to our previous hysteresis loop which occurred due to the delocalised interface spins. Both of these simulations exhibit similar levels of exchange bias which is stable with temperature. For delocalised spins all the spins in the interface layer contribute to the exchange bias field. Both the hysteresis loops have very different shapes, the delocalised hysteresis loop has a much larger coercivity, due to a larger rearrangement of AFM spins at the interface whereas in the localised hysteresis loop only the localised atoms rotate. In real exchange bias systems the exchange bias will be a combination of these two interfaces. It is however a very

System	n_{un}	B_{pred}	B_{sim}
a	5	0.16	0.14
b	7	0.23	0.25
c	8	0.26	0.25
d	10	0.33	0.21

Table 5.2: **The predicted (B_{pred}) and simulated (B_{sim}) exchange bias for the four interfaces**. The predicted exchange bias in calculated using equation 5.5 from the number of uncompensated spins (n_{un})in each AFM interface.

interesting and never before observed result that exchange bias can exist without the need for these defects.

5.6 The influence of the net interface moment on exchange bias

Exchange bias is caused by the natural disorder in the AFM, and ideally we want the exchange bias to be as high as possible to add the most stability to devices. The disorder is due to the uneven number of Mn atoms in each sublattice, and in this section we want to investigate if the exchange bias increases as the statistical imbalance increases as predicted from Equation 5.5 or if there is a limit to the increase and what would cause this limit. To test this we will create different interface each with a different statistical imbalance and measure the exchange bias.

The number of Mn atoms in the simulated structure depends on the random number seed. By varying the random number seed different interfaces can be created which will have different numbers of uncompensated spins. In this section different interfaces were simulated and from the interface structure the exchange bias will be predicted and then compared to the simulated result.

Four bilayer systems were generated, each one 8nm × 8nm × 8nm with 4nm of CoFe and 4nm of disordered γ - IrMn as used in the previous section (Fig. 3.12). For each system the random number seed used to create the structure was changed. The number of uncompensated Mn atoms in each interface was calculated using equation 5.6 and is outlined in Table 5.2.

The number of uncompensated spins in each interface layer was used to predict the exchange bias using equation 5.5. The predicted exchange bias was then compared to the simulated exchange bias by running the same three simulation

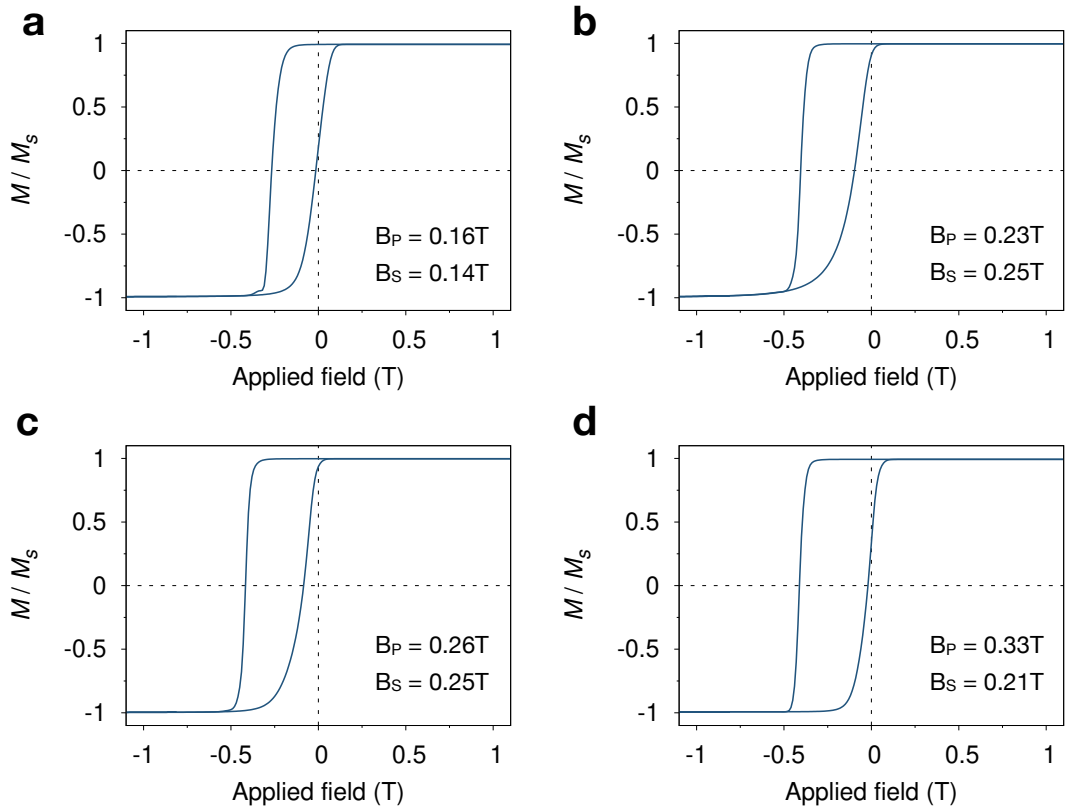

Figure 5.12: **Hysteresis loops showing the effect of the number of uncompensated spins on the simulated exchange bias field**. The interfaces have (a) 5 (b) 7 (c) 8 and (d) 10 uncompensated interface spins. B_p is the predicted exchange bias from the number of interface spins and B_S is the simulated exchange bias calculated from the hysteresis loops. The predictions increase with the number of uncompensated spins, while the simulated exchange bias saturates and then decreases due to the effects of the exchange on the interfacial spin structure of the antiferromagnet.

steps outlined in Section 5.4. The hysteresis loops produced are shown in Fig. 5.12 and the resulting simulated exchange biases are given in Table 5.2.

The simulated exchange bias field should increase linearly with the number of uncompensated interface spins. Surprisingly however we find a saturating behaviour, as seen in interface C, the number of uncompensated spins increases after a certain point this no longer leads to an increase in the simulated exchange bias field. The larger number of uncompensated interface spins increases the effective coupling between the FM and the AFM leading to a larger reversible interfacial moment. The larger moment increases the distortion of the interface spin structure during the hysteresis loop. As the pinned spins are evenly spatially distributed (delocalised) over the interface the distortions in the interface spin

structure decrease the number of irreversible spins causing the exchange bias to saturate and then decrease with increasing interfacial exchange coupling. The prediction for the uncompensated moment only holds at low numbers of uncompensated spins. Another noticeable difference between the hysteresis loops is that as the number of predicted uncompensated spins increases the coercivity also increases. The increase in coercivity is likely due to the increased distortion of the AFM, as the distortion require energy meaning a higher field is necessary to flip the FM.

5.7 The effect of the interface exchange coupling on exchange bias

The simulations in the previous sections have been run with an interface exchange constant of 1.5×10^{21} J/link. The exact value of this parameter is unknown so in the following section the strength of this parameter will be varied to see how it affects the exchange bias field. The 8 nm × by 8 nm × 8 nm system was set up as in Fig 5.4 and the exchange constant was varied from 0.5 to 5×10^{21} J/link. The interface spin structure and therefore the number of uncompensated spins was kept constant for each of the interface spin structures. The systems were run through the same three simulation steps as described in section 5.4.

The simulated hysteresis loops are shown in Fig. 5.13. From Equation 5.5, the exchange bias should increase linearly with the interface coupling strength. However, although it initially increases, as the exchange coupling strength increases more the exchange bias actually starts to decrease again. To understand why a visualisation of the magnetic configurations throughout the hysteresis loop was created and is shown on Fig. 5.14.

The figure shows that increasing the interface exchange coupling energy increases the distortion of the AFM throughout the hysteresis loop. The distortion occurs because when the exchange coupling is increased the AFM spins try to align with the FM. As the coupling between the FM and the AFM approaches the coupling in the bulk AFM the interface will start to align with the FM causing more of the atoms to be reversible than irreversible. The reversibility of these spins acts to decrease the strength of the field from the number of uncompensated spins as it distorts the interface. The same increase in coercivity can be seen in these simulations as with the net interface moment, this is again due to the distortion of the AFM interface meaning it takes more energy to rotate the FM as

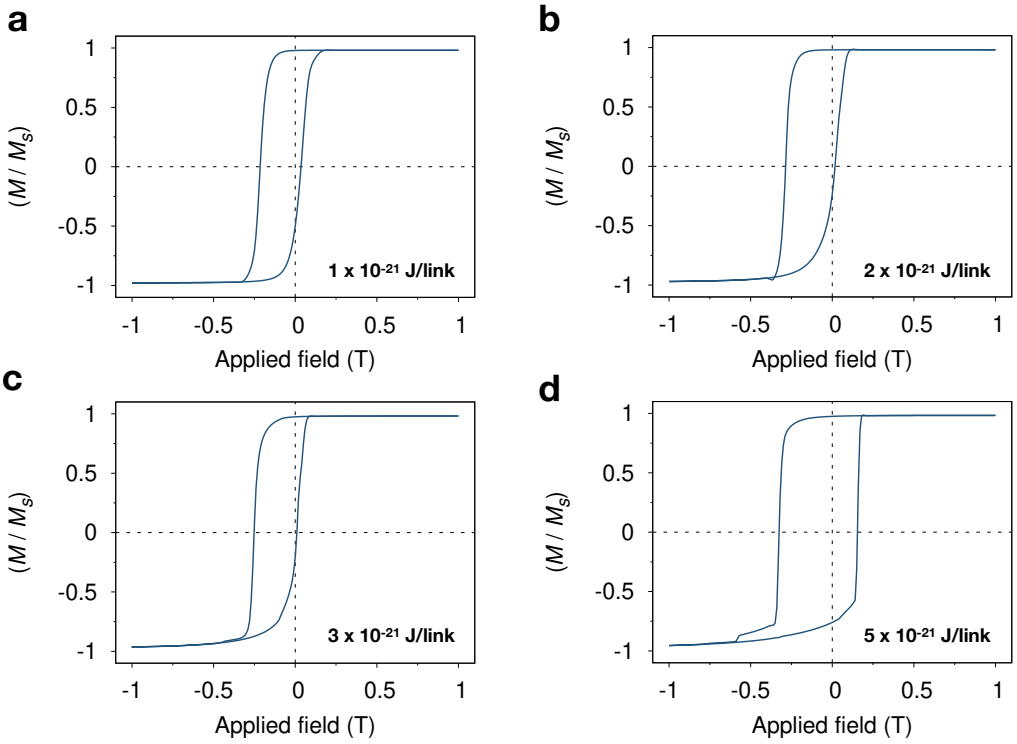

Figure 5.13: **Hysteresis loops for varying interface coupling strengths.** The increase in interface coupling from 1x10-21J/link to 5x10-21J/link causes an increase in the coercivity and an initial increase in the exchange bias field but this saturates and then decreases at higher exchange values.

more of the AFM is also reverse breaking the anisotropy. Increasing the interface coupling does increase the exchange bias field, however this is reduced for high values of interface exchange coupling (approaching the bulk values) as the AFM structure is distorted reducing the exchange bias.

5.8 The temperature dependence of the exchange bias effect in disordered $IrMn_3$

In reality any practical use of exchange bias will not occur at zero Kelvin, and hard disk drives operate at just above room temperature (approximately 300K). So far this chapter has only included zero Kelvin calculations of exchange bias. An important aspect of exchange bias in real devices is the role of thermal spin fluctuations and the stability of the pinned interfacial spins.

Hysteresis loops have been simulated at temperatures up to 500K, systematically investigating the temperature dependence of the exchange bias field. Each

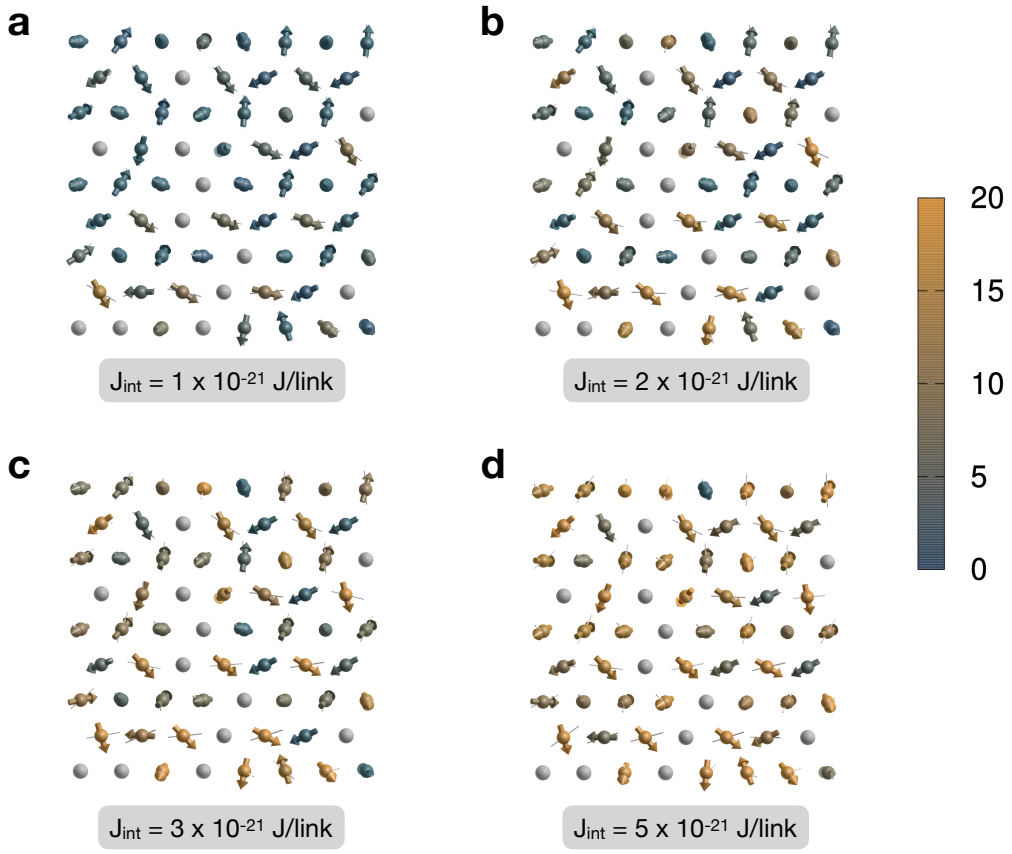

Figure 5.14: **Effect of the interface coupling on the interface spin structure.** The change in interface structure for a small cross section of the interface for different exchange coupling constants. This shows a cross section at the negative saturation point with the colour representing the change in spin angle from positive saturation. An increase in the interface exchange coupling causes the structure of the AFM at the interface to become distorted, meaning the interfacial field at the interface which causes exchange bias is destroyed causing a net decrease in the exchange bias.

simulation is of the same bilayer, the only difference is the temperature. The bilayer was created using the same dimensions and then set using the same simulation steps as described in section 5.4.

At high temperatures the simulated hysteresis loops become very noisy leading to large possible variations in the exchange bias. The average exchange bias at a given temperature is calculated by averaging over 10 simulations. The simulations were all run using the same simulated bilayer but with different integration seeds changing the simulated temperature fluctuations. The averaged hysteresis loops for temperatures of 10K,50K, 300K and 500K are shown in Fig. 5.15.

The hysteresis loops show an increase in noise due to increased spin fluctua-

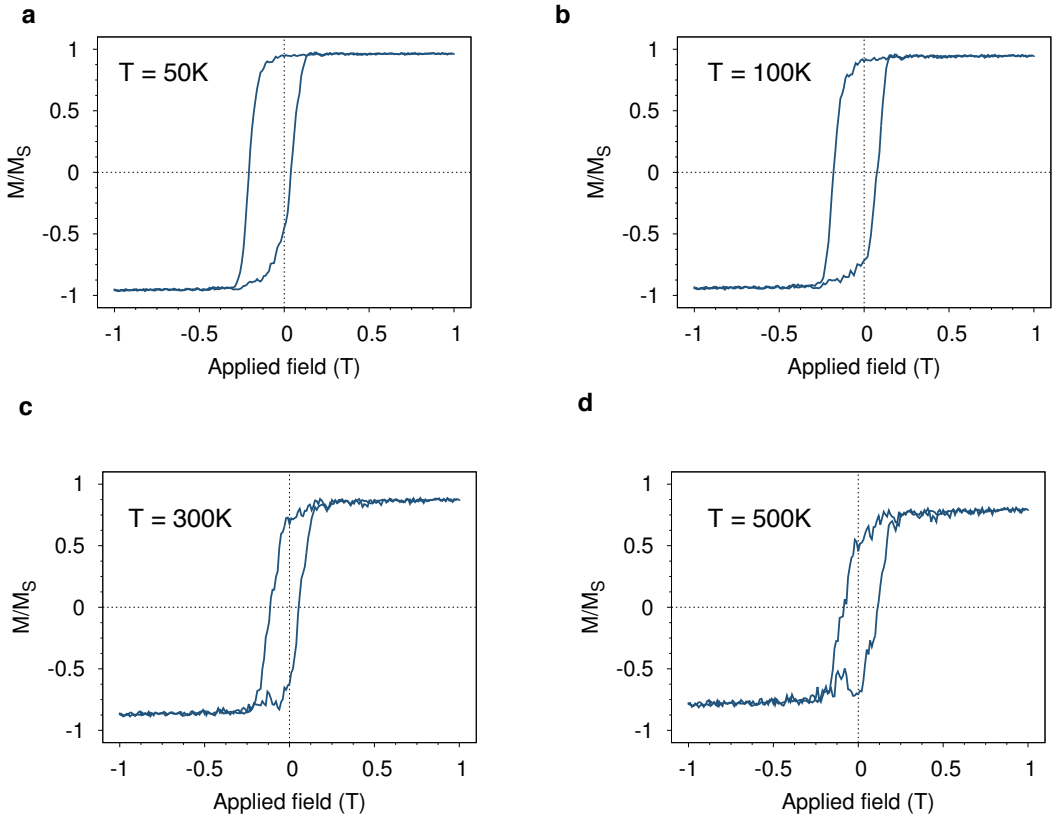

Figure 5.15: **Simulated hysteresis loops at 10K, 50K, 300K and 500K.** The hysteresis loops are averaged over ten simulations of the same system.

tions and a decrease in the exchange bias field. At 300K the loop shows a reduced exchange bias but still 40% of the 0K value. The stability demonstrates the high thermal stability of the pinned interfacial spins. The temperature dependence of the exchange bias is plotted in Fig. 5.16.

Above 450K the exchange bias is zero because the the AFM loses its directional order. For our system the blocking temperature is 450K as shown in Fig. 5.16. Above the blocking temperature the orientation of the AFM sublattice moments fluctuate randomly in space. The simultaneous loss of exchange bias and directional order in the bulk of the AFM shows that the delocalised pinned spins take the order from the bulk of the AFM. This is because the pinned spins responsible for exchange bias are delocalised and strongly coupled to the bulk AFM. This explains their remarkable stability despite the small effective size. The same phenomenon was observed for the localised spin structure described in Fig. 5.11 suggesting that it is the bulk AFM which is causing the stability.

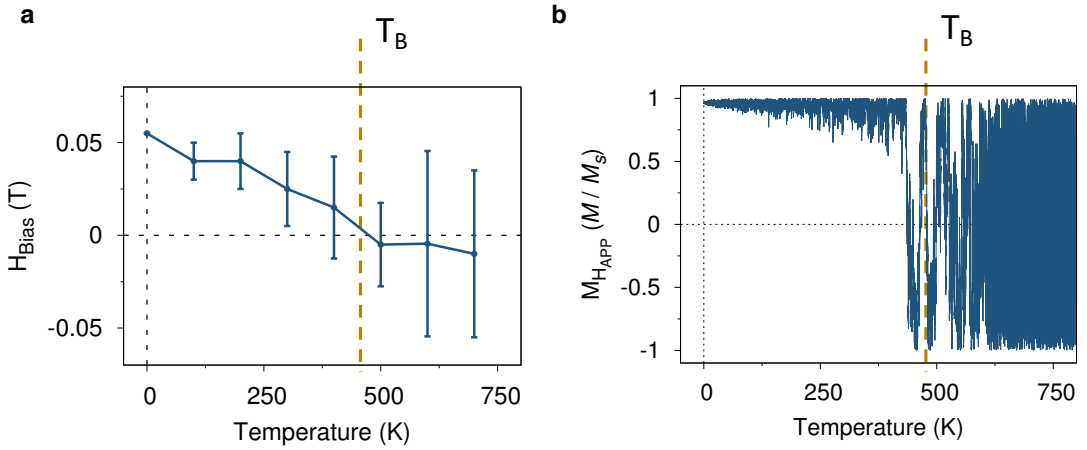

Figure 5.16: **The temperature dependence of exchange bias in single grain γ - IrMn$_3$/CoFe bilayers.** The exchange bias. decreases with temperature and is positive until 450K. (b) Shows the temperature dependence of the magnetisation showing that the Blocking temperature is also 450K. This shows that the exchange bias holds until the blocking temperature.

5.9 The dependence of Exchange Bias on the composition of IrMn

So far in this chapter we have focused on exchange bias in bilayer with disordered - IrMn$_3$ as the AFM. In real devices however compositions closer to IrMn$_4$ to IrMn$_5$ are used. In section 3.4.3 the magnetic ground states it was found that all of these compositions have the same ground state as disordered - IrMn$_3$. Therefore we expect that all of these phases will also give exchange bias. This assumption will be tested in the following section.

5.9.1 Exchange bias in disordered IrMn$_5$ to IrMn$_3$

The compositions are varied as described in section 3.4.3. Following the same simulation steps outlined in section 5.4, the resulting zero Kelvin simulated hysteresis loops are shown in Fig. 5.17 for compositions of Ir$_{15}$Mn$_{85}$, Ir$_{17}$Mn$_{83}$, Ir$_{19}$Mn$_{81}$, Ir$_{21}$Mn$_{79}$. All of the hysteresis loops have shown 0.1T of exchange bias and have a coercivity of 0.1T, very similar values to those measured for IrMn$_3$. These hysteresis loops seem to show no particular trend in either exchange bias or coercivity, in contrast to experimental observations [56]. Only one hysteresis loop was simulated for each composition and as the exchange bias is due to a random disorder this means to extract a trend repeated simulations of different

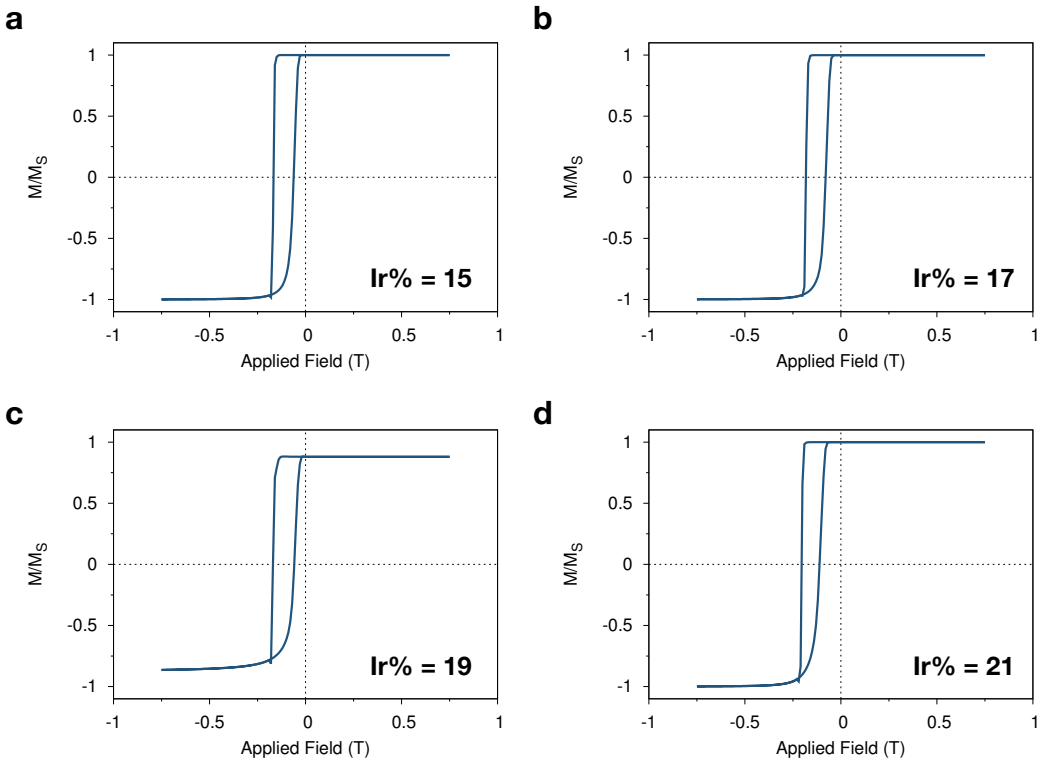

Figure 5.17: **The simulated hysteresis loop for a) $Ir_{15}Mn_{85}$ b)$Ir_{17}Mn_{83}$ c) $Ir_{19}Mn_{81}$ d) $Ir_{21}Mn_{79}$** The hysteresis loops all exhibit similar levels of exchange, which is similar to the level of exchange bias previously measured in $IrMn_3$.

structures would be required to average out this randomness. This, would be an interesting area for further work.

5.9.2 Exchange bias in ordered $L1_2$- $IrMn_3$

In this final section we will investigate what happens if the disordered γ -$IrMn_3$ is replaced by ordered $IrMn_3$. Experimental studies of ordered $IrMn_3$ systems give no exchange bias in the (111) orientation [53]. In ordered $IrMn_3$ the Ir atoms are not randomly removed, instead they are all removed from the same sublattice leaving a perfectly compensated spin structure which is shown in Fig. 5.18. As there are no uncompensated spins in the interface there is no net interface magnetisation which explains the lack of exchange bias in the simulation. The simulated system is a very simplified case due to the atomically flat interface. In reality, the interface will not be atomically flat and this disorder may cause the sample to exhibit some exchange bias.

Following the same simulation steps outlined in section 5.4, the resulting

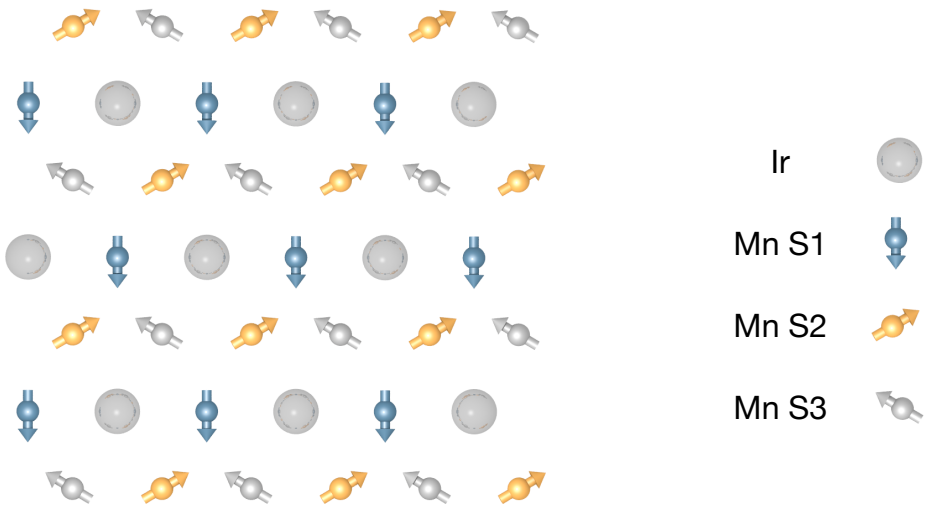

Figure 5.18: **Interface spin structure for an ordered $L1_2$- $IrMn_3$/CoFe bilayer.** where S represents the sublattice. The lack of exchange bias in ordered $IrMn_3$ is due to the completely compensated moment at the interface of the AFM causing zero net interface moment. The colours represent the three sublattices and the grey spheres are the Iridium atoms.

simulated hysteresis loop is shown in Fig. 5.19. The simulation gives no exchange bias matching the previous experimental measurements.

5.10 Summary

In this chapter, the atomistic origin of exchange bias in single grain IrMn/CoFe bilayers was discovered. Exchange bias occurs in all disordered compositions of IrMn from $IrMn_5$ to $IrMn_3$ but does not exist in perfectly ordered $IrMn_3$ due to the perfectly compensated interface structure. The pinned interface spins are distributed across the whole interface and are strongly coupled to the bulk antiferromagnet explaining their stability.

It is an interesting observation that exchange bias occurs in our perfect IrMn/CoFe system without the need for multigrain structures or grain boundaries. In the following sections exchange bias will be studied for more complex structures, initially for multigrain structures and then for structures with more complex interfaces and additional imperfections such as interface mixing.

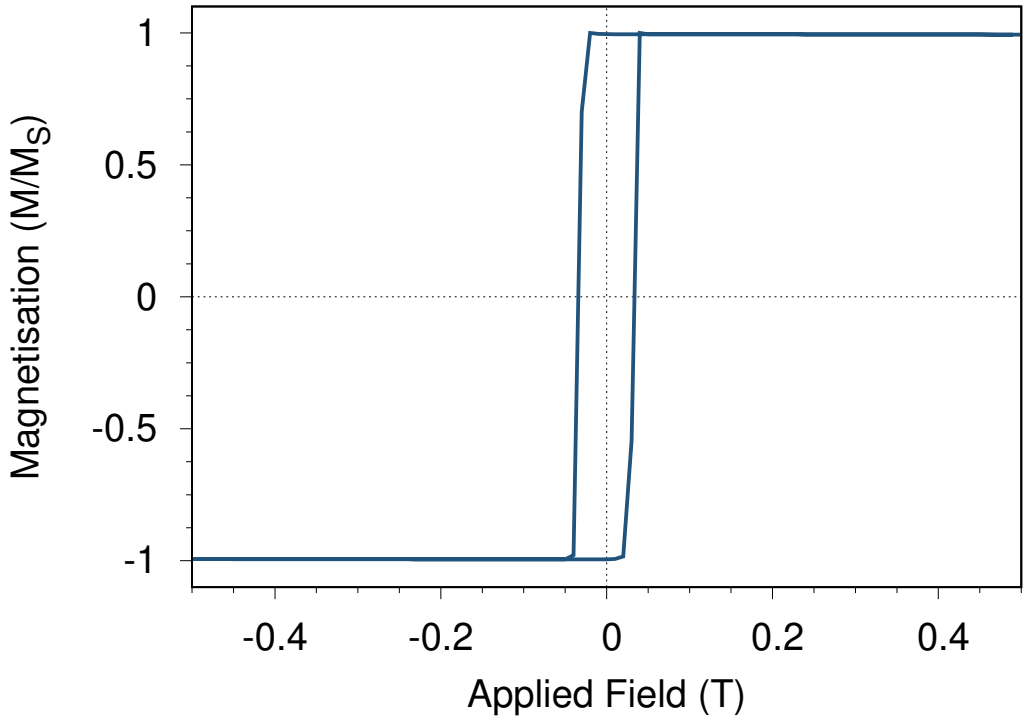

Figure 5.19: **The hysteresis loop for an ordered L1$_2$- IrMn$_3$, CoFe bilayer.** The hysteresis loop has exhibited no exchange bias and is the same as a hysteresis loop measured for just CoFe.

6

EXCHANGE BIAS IN MULTIGRANULAR γ-IRMN$_3$/COFE BILAYERS

In the previous chapter the origin of exchange bias was investigated for single grain $IrMn_3$/CoFe bilayers. The simulated single grains were 8nm × 8nm × 8nm, orders of magnitude smaller than a real device. Real devices use structures which are hundreds of nanometers in size causing the AFM to break up into grains. The deposition parameters are designed to break the device up into grains because these grains give the largest exchange bias. If the AFM was a single grain it would give almost no exchange bias as the number of uncompensated spins would be small compared to the number of atoms in the interface layer. While the single grain model showed exchange bias, the values were slightly higher than observed experimentally, the hysteresis loops show a large instability with temperature and the coercivity is much larger than those observed experimentally. In this chapter the IrMn/CoFe model will be extended to investigate multigranular structures, the effect of grain size/shape and grain boundaries and on the exchange bias field. In the next section previous models of granular exchange bias systems will be reviewed as well as any experimental results on the shape and size of the granular distribution.

6.1 Models and experiments of exchange bias in multigranular systems

In section 5, previous models of exchange bias in single grain IrMn/CoFe bilayers were discussed. All of these models assumed the interface exchange field occurs due to domain walls, imperfections in the AFM or grain boundaries. Our model of IrMn/CoFe proved that these are not necessary for exchange bias to occur. Instead, exchange bias is caused by the naturally occurring statistical imbalance

in the number of AFM spins in each sublattice at the interface. In the following chapter, we will address the question of how having a system of many grains affects the cause of exchange bias as these are much more relevant to real device sizes/structures. The larger structure will also give less thermal noise and the temperature dependence of exchange bias can be more accurately studied. We will start by looking at previous models of exchange bias and experimental results which were used as a basis to create the model.

The first polygranular model of exchange bias was created in 1972 by Fulcomer and Charap [83]. They modelled the FM as a single domain and the AFM as a system of N non-interacting grains with a distribution in size and shape. Each particle was exchange coupled to the FM layer and the anisotropy was assumed to be uniaxial with the easy axis of the FM and the AFM assumed to lie parallel, with all the AFM grains having the same easy axis. The model was the first ever model to give accurate results for the value of the exchange bias field over a wide range of temperatures. Whilst the coercivity was accurate near the blocking temperature the values were too large below the Néel temperature. Fulcomer and Charap explained the inaccuracy as being due to two problems in the model. Firstly, they used a distribution of particle volumes and deemed the shape of the distribution to be unimportant. The shape of the distribution has been experimentally proven to change the size of the exchange bias [5]. Secondly, they used the bulk values for the AFM anisotropy and the interface exchange coupling. Both of these have since been proven to be incorrect at the interface [84].

The next model of multigranular exchange bias systems came from Stiles and McMichael [85]. Their model was similar to that of Fulcomer and Charap in that it also assumed exchange decoupled AFM grains which only interact with the FM layer. The major difference between the models is that Fulcomer and Charap assumed the AFM grains to have a uniform orientation and magnetisation whereas Stiles and McMichael assume a randomly oriented AFM. The random orientation allows for the formation of domain walls. They also assume all the grains to be equally sized unlike the model of Charap which used a distribution of grain sizes. The model of Stiles and McMichael assumes the AFM grains to have a uniaxial anisotropy, each grain having a random easy axis direction. The interface exchange coupling was said to be due to interface disorder, leading to both sublattices being present at the interface giving a mixture of compensated and uncompensated moments which, when averaged over all the grains, leads to a net coupling. The FM layer is assumed to be fully saturated along the applied field direction. As the FM rotates, the AFM interface magnetisation attempts

to align with the FM leading to the formation of a partial domain wall within the AFM in an attempt to minimise the exchange energy. The model shares a similar level of success to that of the model of Fulcomer and Charap. It can predict the exchange bias however it is only applicable to systems of a size sufficient to support a domain wall.

Van der Heijden *et al* measured the dependence of the exchange bias field on AFM thickness [86]. They observed no change, disagreeing with the model of Fulcomer and Charap [83]. Van der Heijden *et al* suggested that the grains of NiO were in fact multi-domain and that the the model of Malozemoff [75] would be more applicable. For the thicker AFM samples (approximately 60 nm) multiple domains may have occurred however it is far less likely to have occurred in the thinner (10 nm) thick layers. Furthermore, the distribution of grain sizes was not measured which is far more important than grain thickness [5] as the switching probability of a grain is proportional to the volume, not the thickness. The main problem with these measurements was that they only measured two systems and therefore no real conclusions can be drawn.

The next model of multigranular exchange bias systems, an adaptation of the Fulcomer and Charap model, came from O'Grady *et al* [5]. The model is based on an ensemble of grains distributed in size. The model makes two main assumptions, the first is that the easy axis of the AFM grains are all aligned, the second is that the grains are non interacting. The model is restricted to that of single domain AF grains that reverse through coherent rotation. Aley *et al* measured the variation of the anisotropy constant in (111) oriented IrMn$_3$ [56]. They measured that in polycrystalline materials the direction of the anisotropy could vary from fully disordered in three dimensions to aligned within the plane of the film.

O'Grady *et al* assumed the the anisotropy in an AFM to be constant within each grain, meaning the energy barrier within a grain is only dictated by its volume [5]. The probability of a grain switching is therefore dependent on the volume as:

$$1/\tau = f_0 \exp\left(-\frac{K_{AF}V}{k_B T}\right), \tag{6.1}$$

where τ is the relaxation time, k_B is the Boltzmann constant, T is the temperature, k_{AF} is the anisotropy constant of the AFM and V is the mean grain volume.

If the grains are larger than the set volume ($V_{set}(T)$) the relaxation time will be too long to set the uncompensated interface moment of these grains, and they will not be aligned with the FM layer. Furthermore, if the volume is too small the grains will be superparamagnetic at room temperature and therefore also not contribute to the exchange bias. Therefore only grains with grain volume ($V_C < V < V_{set}$ will contribute to the exchange bias as shown in Fig.6.1.

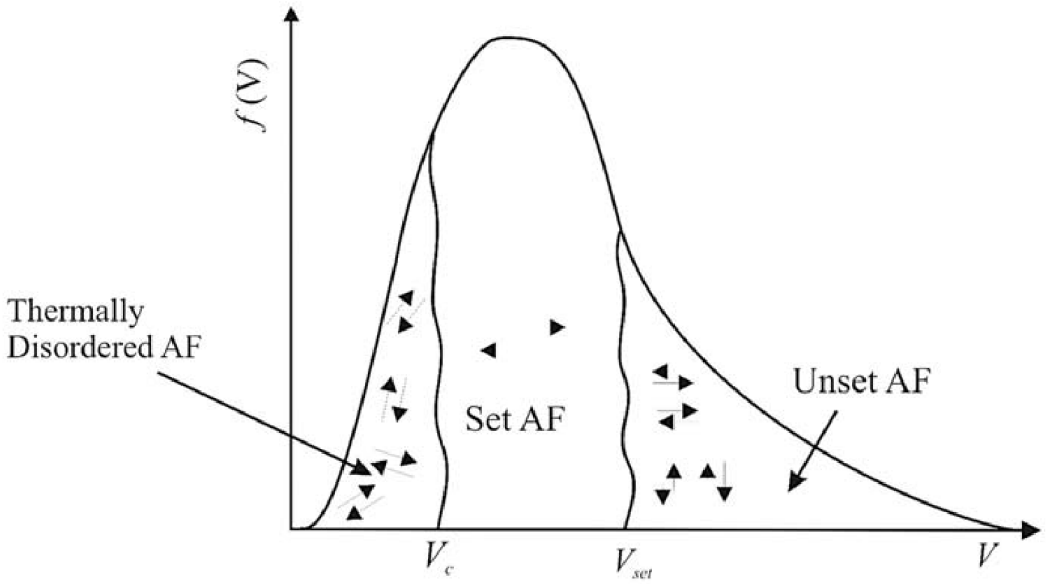

Figure 6.1: **Schematic of the grain size distribution showing the fraction that is set and thermally stable from O'Grady *et al* [5]**. They found that the small grains were thermally unstable and large grains were not set during the setting process meaning only the grains between these two volumes contribute to the exchange bias.

The exchange bias in multigranular systems can be calculated as:

$$H_{ex} \propto \int_{V_C(T)}^{V_{set}(T)} f(V)dV, \tag{6.2}$$

where the exchange bias is proportional to the grain volume between these critical volumes. The prediction was compared to experimental results by creating films with different AFM grain diameters and the thickness of the AFM to get different grain volumes. They found that the experimental results almost exactly matched their predictions [87].

They also concluded that there will be no direct exchange coupling between AFM grains because in polycrystalline FM films the intergranular exchange occurs via RKKY coupling. For RKKY coupling to occur each grain must possess a

large moment in order to polarise the conduction electrons. AFMs do not contain a large magnetic moment and therefore it is expected that there will be no RKKY coupling. This has been experimentally measured in the case of Co alloys with a CoCr boundary, where the AFM boundary reduces or even eliminates the RKKY coupling of the Co[88]. From TEM images the grain boundaries can be observed to be amorphous and as such direct exchange will not occur [5]. However, this conclusion is highly debatable because it has never been directly measured.

Choo *et al* developed a micromagnetic model of exchange bias where both the AFM and FM are both assumed to rotate coherently [89]. Their model used a Monte Carlo solver and the AFM was modelled by assuming each AFM grain has a small moment arising from the uncompensated spins. Under this assumption you can calculate the energy of the AFM grains. Craig *et al* [63] used this model to calculate the temperature dependence of exchange bias and found good agreement with experiments. Daeng-am *et al* created a micromagnetic model of granular IrMn/CoFe bilayers [90]. Their model was an adaptation of that of Choo *et al* and Craig *et al* . Their model added a Gaussian distribution of easy axis direction for the AFM grains. They found that the exchange bias increases with grain diameter due to the thermal disorder of the smaller grains as predicted by O'Grady *et al* [5]. Their model used a Voronoi tessellation to create a granular structure as did our model however their model uses the uniform generation process which gives unrealistic grain shapes at larger standard deviations. They used this model to calculate the grain volume dependence of exchange bias [91].

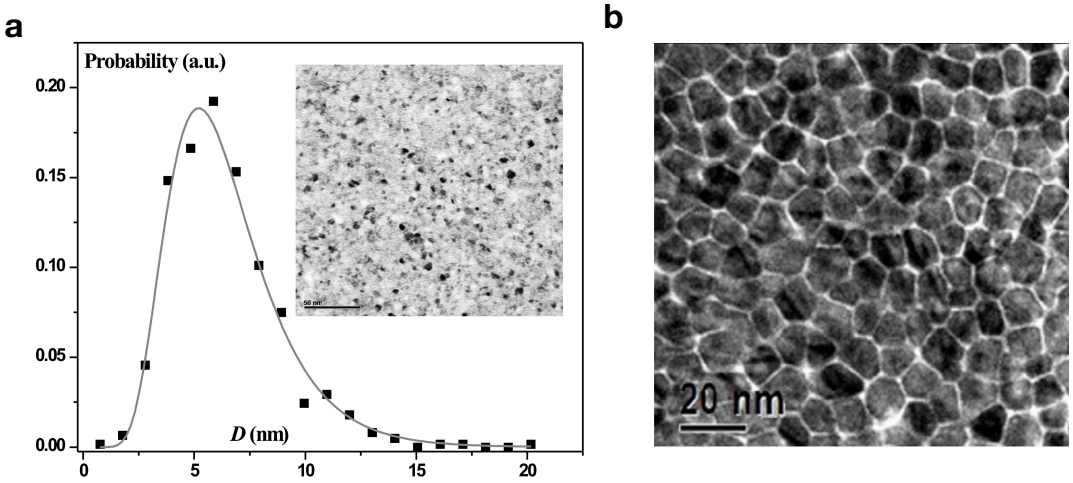

Figure 6.2: **Grain size distribution and TEM image (inset) for a IrMn/CoFe bilayer.** (a) Grain size distribution, the sample was experimentally measured by G. Vallejo-Fernandez *et al* data from [92] (b) A close up of an granular structure used in recording media taken from [91]

.

Vallejo-Fernandez *et al* [51] measured the grain size dependence in polycrystalline IrMn/CoFe thin films. They measured that in the case of sputtered thin films the grains are single crystal and usually 5-20nm in diameter. An example grain size distribution and granular structure is shown in Fig. 6.2. They observed that the growth process in granular systems creates grains which follow a lognormal volume distribution [51]. The lognormal distribution is defined as:

$$f(D)dD = \frac{1}{\sqrt{2\pi}D}\exp\Big(-\frac{(\ln(D)-\ln(\mu))^2}{2\sigma^2}\Big)dD, \tag{6.3}$$

where D is the grain diameter, μ is the median grain diameter and σ is the standard deviation. An image of the experimentally observed granular structure is shown in Fig. 6.2, showing a median grain diameter for the sample of 6.7nm with grains ranging in diameters from 2 - 20 nm. Each grain is believed to contain a single AFM domain as the domain wall size for AFMs is much larger than the grain diameter [93]. The grains are treated as non interacting as there is no experimental evidence of intergranular exchange coupling between AFM grains [5].

Although many models of exchange bias in polycrystalline thin films have been developed, every model so far has assumed some distribution for the anisotropy and easy axis directions. In this chapter we will create our own model of polycrystalline thin films and use it to model exchange bias. Our model will use a lognormal distribution of grains, matching the previous experimental results. The anisotropy of the grains will be calculated using the Néel pair anisotropy model and therefore each grain will have its own unique exchange bias direction, not input by a distribution but calculated from the crystallography of the material.

6.1.1 Simulating a realistic granular structure

The first step is to evaluate the validity of the current grain structure generation in VAMPIRE to create the same size/shape grains as those observed experimentally. An example of a grain size distribution and a TEM image of the grain structure is shown in Fig. 6.2 in Section 6.1. We know that in IrMn the grain volumes follow a lognormal distribution, have a median diameter of approximately 6 nm and a standard deviation of approximately 0.37 [56]. The current method for generating grains in VAMPIRE uses a Voronoi construction with a hexagonal grid of seed points. The method works well for low values of standard deviation but when the standard deviation is increased the grain shapes are no longer realistic shapes. A

new method for generating the granular structure was developed and the grains created were compared to the granular distributions seen experimentally. The new model was used to explore the grain size and temperature dependence of the exchange bias. From this an encompassing theory of how exchange bias emerges in realistic granular systems was created.

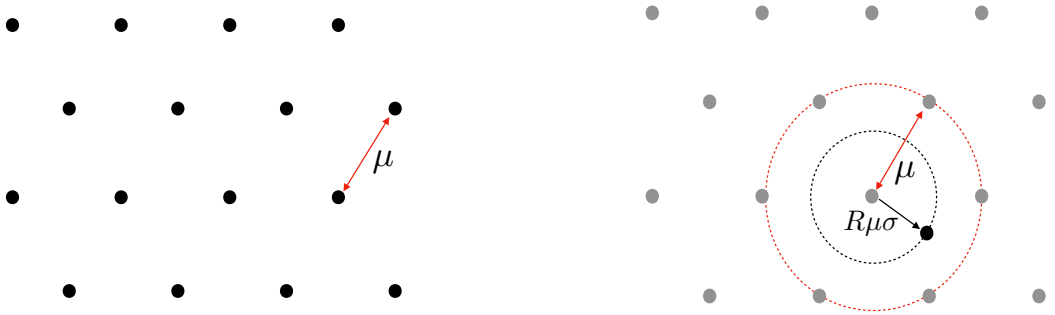

Figure 6.3: **Generated seed points for the Voronoi grain construction**. (a) The seed points are generated in a hexagonal grid, each seed point is separated by a distance equal to the median grain size. (b) The grain size distribution is input by moving each seed point a distance equal to the required standard deviation times the average grain size multiplied by a random number between zero and one.

Currently, the granular structure in VAMPIRE is created using a Voronoi construction from a list of seed points. The seed points are generated on a hexagonal grid as shown in Fig. 6.3a. The user inputs a median grain size and a standard deviation. The median grain size is the distance between seed points in the hexagonal lattice. The standard deviation is introduced by moving each of these seed points in a random direction a distance (d) defined as $d = R\sigma\mu$ where R is a random number between zero and one, σ is the standard deviation and μ is the mean grain size. The random number is generated using a uniform random number generator. Fig. 6.3b shows how the seed points are moved based on the standard deviation.

From the list of seed points the granular structure is created using a Voronoi construction. Voronoi constructions decompose the space into regions, where each region contains one seed point and all the points within that region are closer to that seed point than any other seed point in the space [94].

Initially, two granular structures were generated, both with a median grain diameter of 6 nm, one with a standard deviation of zero and one with a standard deviation of 0.37. The generated grain structures are shown in Fig. 6.4(a). The first shows a perfectly hexagonal structure as expected. The second has created

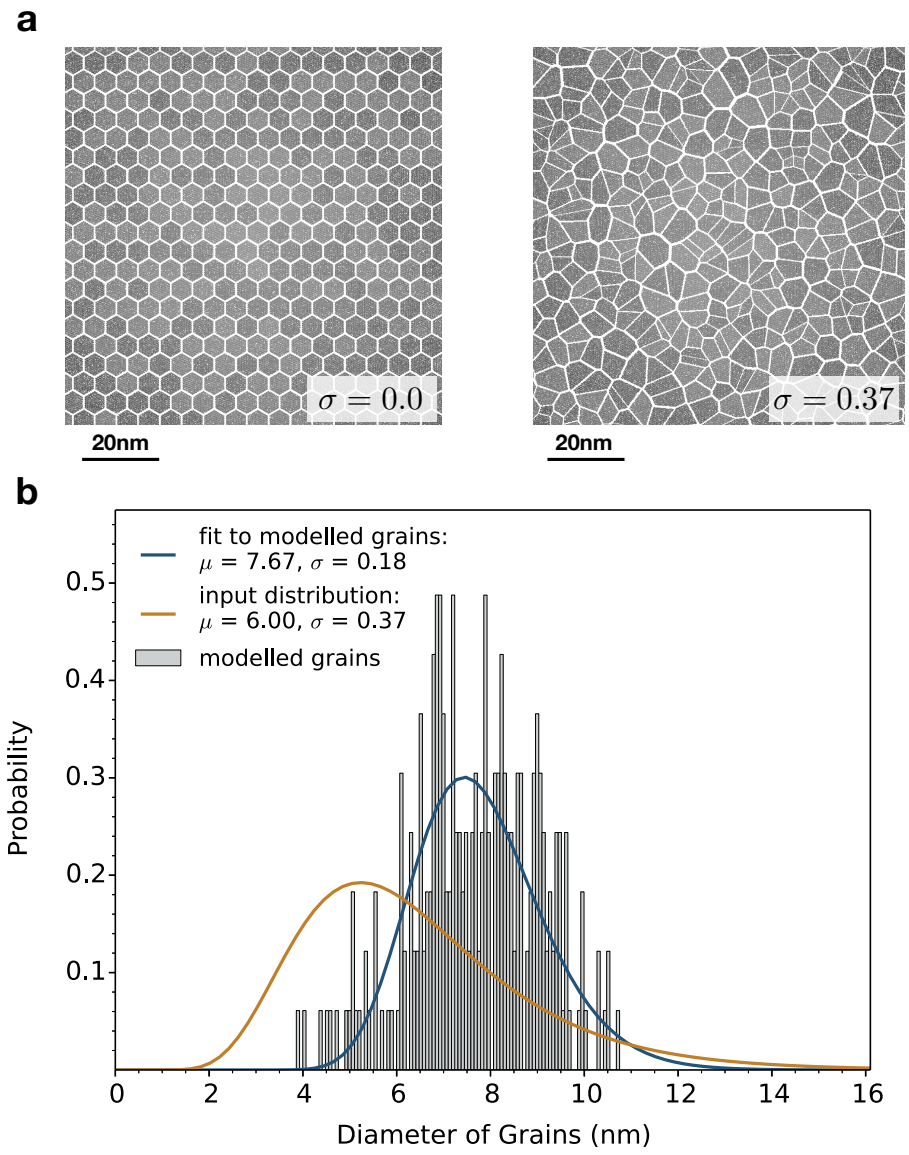

Figure 6.4: **The grain structure and size distribution for the hexagonal lattice seed points.** (a) The generated grain structure for a standard deviation of 0.0 and 0.37. For σ = 0.0 the grains are all perfect hexagons. For σ = 0.37 the grain shapes are more random and triangular. (b) The grain size distribution for the system with a standard deviation of 0.37. The lognormal distribution from the input parameters is compared to the distribution from the modelled grains.

grains which are no longer hexagonal in shape. The grain shapes do not match those imaged in the experimental results in Fig. 6.2 and instead the grains have made almost triangular pointy shapes. These shapes will have a lot of corner effects and do not create a realistic granular distribution. The distribution of grain sizes was also plotted against the expected distribution from the input parameters. For σ = 0.0 both the predicted and calculated grain distribution is

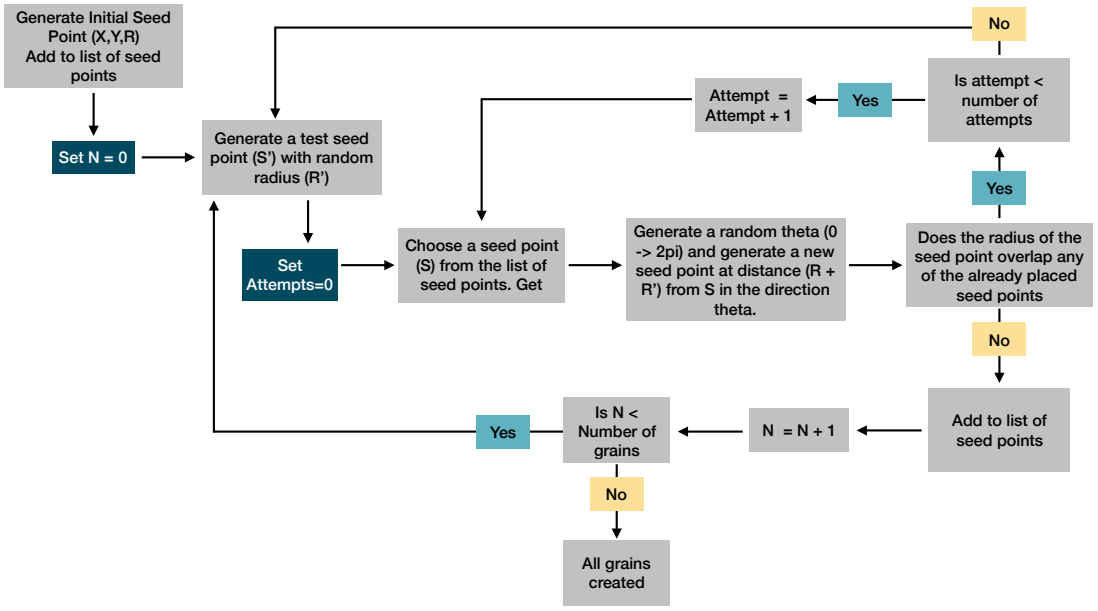

Figure 6.5: **A flow chart describing the adaption of the Poisson disk sampling algorithm for generating close packed grains.** The algorithm generates an initial seed point (S) at (X,Y). Another seed point is generated (S') the grain is positioned so it should touch one of the already generated seed points. The algorithm attempts to add the new grain to the system making sure it doesn't overlap any of the previous grains until the number of attempts is reached. This is repeated until N grains have been added.

a delta function at a diameter of 6nm. For $\sigma = 0.37$ the distribution is shown in Fig. 6.4. The radius of the grain is calculated as the average distance from the seed point at the centre of the Voronoi grain to each of the vertex points at the edges. The grey histogram is a distribution of the grain diameters simulated. The blue line is a lognormal fit to this grain distribution using equation 6.3. The grains produced have a slightly larger median grain diameter and a much smaller standard deviation than the input values. The shape of the modelled distribution is normal instead of the lognormal distribution we wanted. From both the shape of the distribution and the shape of the grains created we can say that the current method does not match the experimentally observed granular structure. A new method was therefore created to generate seed points which improve the match to the experimental granular structure.

6.1.1.1 A new method for generating seed points

The algorithm chosen to replace the old method was an adaptation of the Poisson-disc sampling algorithm. Poisson-disc sampling produces points that are tightly-packed, but no closer to each other than a specified minimum distance, resulting

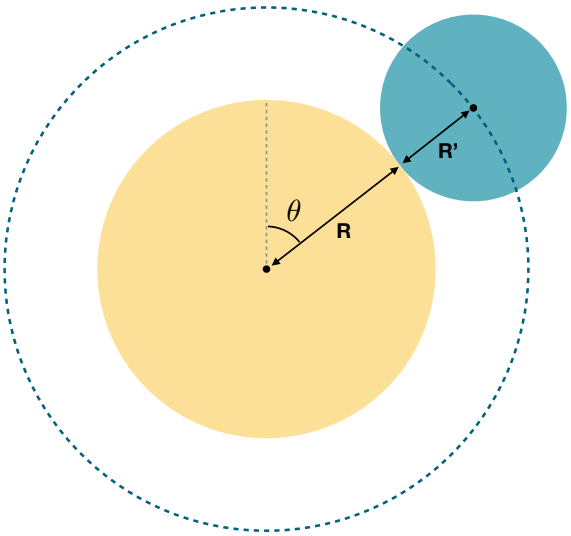

Figure 6.6: **The generation of new seed points in the Poisson distribution.** The new seed point is placed a distance $R + R'$ away from an existing seed point, where R is the radius of the existing seed point and R' is the radius of the new seed point. The new seed point could be generated anywhere on the blue dotted circle. The position of the seed point on this line is chosen at random by choosing a random angle (θ) between 0 and 2π.

in a more natural looking pattern. This algorithm is usually used in computer graphics as sampling for graphics applications or mesh algorithms [95].

The algorithm creates a close packed structure by generating seed points which touch the existing seed points. An outline of the algorithm is shown in the flow chart in Fig. 6.5. The initial seed point is generated at point (X,Y) using a uniform random number, this seed point has a radius (R) generated using a lognormal random number using the median grain size and standard deviation input by the user. A test seed point is then generated with a lognormal random radius (R'). The new grain will be placed next to one of the preexisting grains. The grain it is placed next to is chosen at random. The randomly chosen grain has radius (R) the new grain will be placed at a distance $R + R'$ away from the old grain at a random angle θ. The process of placing the new grain is described in Fig. 6.6. Now the grain has a position it is tested against every other grain already added to the system to make sure it doesn't overlap with any of them. If it doesn't overlap it is added to the list of grains. If it does overlap the same grain radius (R') is kept and tested to see if it fits anywhere else in the system using a new grain with radius (R) and a new angle (θ). This process is repeated until the grain fits in the system or it has been attempted a large number of times (10,000). Grains are continuously generated until the number of seed points equals the

number of desired grains (N).

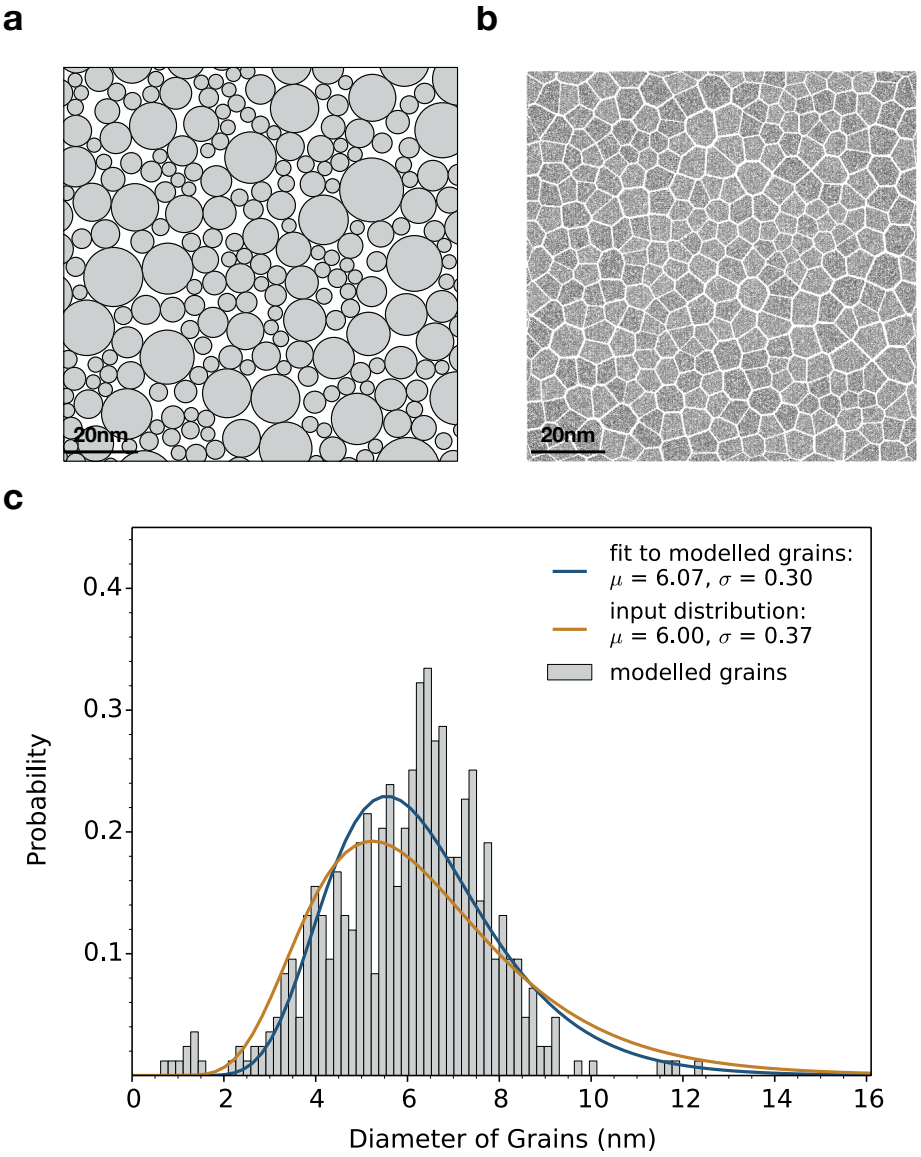

Figure 6.7: **The granular structure generated from the Poisson distribution.** (a) The generated seed points using the Poisson distribution. The grains are much more tightly packed than either of the previous methods. (b) The granular structure generated. The grain shapes look realistic as do the distribution of grain sizes. (c) The grain size distribution, the input median and standard deviation nearly match the output distribution.

The seed points and granular structure are shown in Fig.6.7 (a) and (b) respectively. The grains have realistic shape, matching the experimental images of granular structures. The grain size distribution is shown in Fig.6.7(c). The distribution almost exactly matches the input values for median and standard deviation. The median grain size is correct to 1% and the standard deviation is within 20%. The new distribution is a massive improvement compared to the dis-

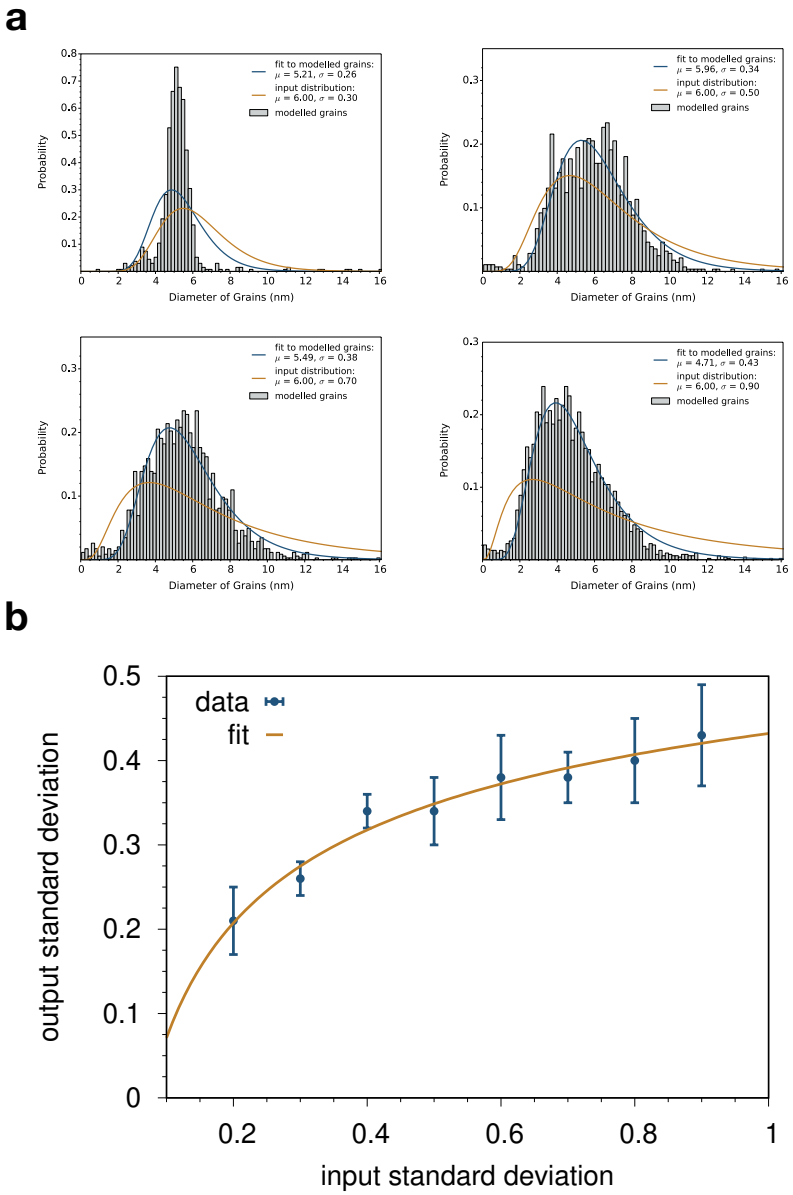

Figure 6.8: **The effect of input standard deviation on the computed standard deviation**. For low values of the standard deviation the input (σ_{in}) and output (σ_{out}) match however as the input standard deviation increases the output plateaus at about 0.4. The curve is fit as σ_{out} = -0.356$\sigma_{in}^{-0.304}$ + 0.787

tributions created using the old grain generation method. The method now needs further testing to see how it holds up to very high and low standard deviation values.

The output standard deviation value was calculated for values of input standard deviation between 0.2 and 0.9. The standard deviation was not reduced any lower because the method does not work for low standard deviations as the

grains are not tightly packed enough. For low standard deviations the previously implemented hexagonal method creates much better granular structures. For each input standard deviation a probability distribution was created and from this the standard deviation was calculated using a lognormal fit. This was repeated twenty times for each each value of input standard deviation and then the output standard deviation was calculated as the average of the twenty repeats. Fig. 6.8(a). shows four grain size distributions for input standard deviation values of 0.3, 0.5, 0.7 and 0.9. In each of the four distributions the output mean grain size matches the input to within 15%. The output standard deviation is between 0.2 and 0.45. The standard deviation does increase with increasing input standard deviation however it does not match the input value. Fig. 6.8(b) shows the average output standard deviation calculated from the twenty repeats for each value of the input standard deviation. It shows that the maximum value calculated is never higher than 0.5. The error in the figure is calculated as the standard deviation of the twenty repeats. The output standard deviations do not equal the input because of the Voronoi construction. When the seed points are created they are all given a radius which fits the required grain size distribution. However when the Voronoi construction is created it acts to average all of the grains towards the mean value. This means that even if a large grain is generated if there are small grains near it some of the space of the large grain will be included into the small grain instead averaging the distribution.

The input to output standard deviation can be fit using $\sigma_{out} = -0.356\sigma_{in}^{-0.304} + 0.787$ where σ_{out} and σ_{in} are the output and input standard deviations respectively. As shown in Fig. 6.8, however the fit is strongly grain size dependent and becomes a very complex function very quickly. For simulations of IrMn the standard deviation is approximately 0.2-0.4 [56] and therefore we can use this grain generation technique as it creates good granular structures in the range that we require. The input standard deviation does not necessarily match the output however we can calculate the output standard deviation and therefore this value can be used for any analysis performed.

Now a more accurate model of the granular structure in IrMn has been created the model can be used to explore the origin of exchange bias and how the grains effect the exchange bias in comparison to a single grain system.

6.2 Computational Details

The IrMn/CoFe bilayer was created in the same way as a single grain system but this time the dimensions were 50nm × 50nm × 8nm, with 5nm of $IrMn_3$ topped with 3nm of CoFe in the z direction. The IrMn is modelled as a granular structure with no exchange across the grain boundaries, and the CoFe is modelled as a continuous film. The grain boundaries are modelled as Ir atoms, as they have to be either Mn or Ir, and Ir are non-magnetic so will stop the exchange between grains. The Ir in the grain boundaries does not contribute to the composition of the IrMn. A visualisation of this structure is shown in Fig. 6.10. The structure contains over 1.5 million atoms, meaning the simulations are very computationally expensive. This is especially true for hysteresis simulations which take nanoseconds to complete so the system can fully equilibrate at each time-step. Running this code in serial would take years to run even a single hysteresis loop simulation. However, VAMPIRE is a highly scalable parallel code and for large scale systems obeys almost ideal scaling.

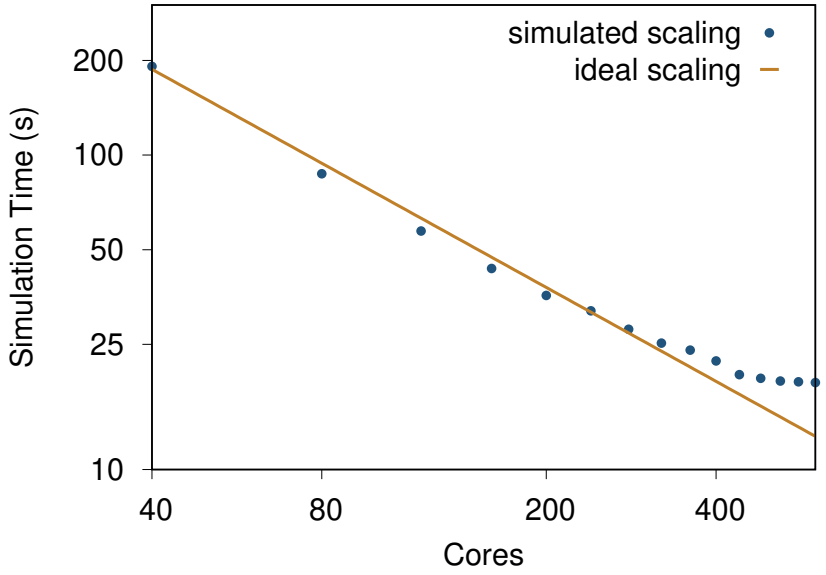

Figure 6.9: **The scaling with number of cores on viking the super computer located at the University of York.** In VIKING each node contains 40 cores. The system scales almost ideally until 200 cores or 5 nodes.

To run the simulations VIKING was used, the cluster located at the University of York which has 173 nodes and a total 42TB of memory, connected by a high-speed 100Gb Infiniband network. The nodes each contain 40 cores. To test the scaling of the multigranular system simulations were run for 10,000 steps on up to 15 nodes and the time taken for the simulation to run was measured. On one

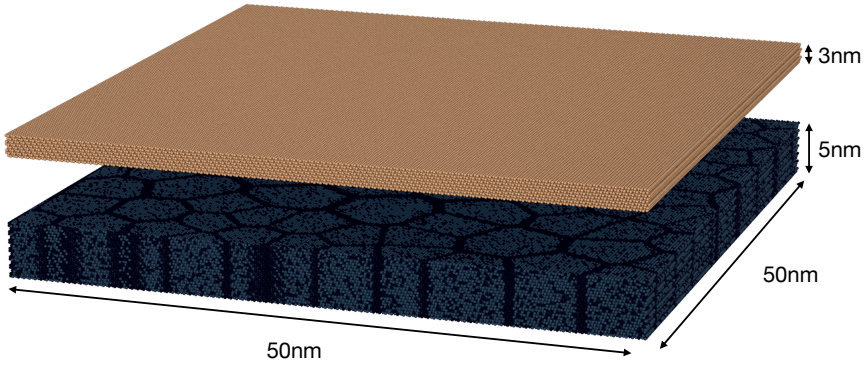

Figure 6.10: **Visualisation of the multigranular IrMn/CoFe bilayer structure.** The CoFe is represented by gold spheres and lifted 5nm above the IrMn to show the multigranular structure below. The Ir is represented as black spheres and the Mn is dark blue. The system is 50nm by 50nm in size

node the simulation took 191 seconds. For ideal scaling doubling the number of nodes should halve the run-time. However, as the number of nodes increases the time taken for the processors to transfer information between each other also increases and each processor stores less information and has to receive/send more information from the other processors, this increases the run time from the ideal run-time.

The scaling data is shown in Fig. 6.9 and is compared to the ideal scaling. The simulations show almost ideal scaling until 5 nodes, after this point although the simulation time still decreases it is no longer ideal and the increase in computational resources is not worth the speed up. For the rest of this chapter and the next chapter all simulations on multigranular systems will use be run on 5 nodes (200 cores).

6.3 Simulation Steps

The simulation follows the same three simulation steps outlined in section 5.4. The first step is field cooling which sets the magnetisation of the sample along the setting field direction. In section 5.4 it was concluded that due to computational time constraints it was not possible to set the magnetic structure of the AFM by following the experimental procedure. Instead the AFM grains were not set along the setting field direction but randomly set. The hysteresis loop could then be measured along the bias field direction. In single grain systems the method worked as the hysteresis loop could be run along any direction however in multigranular systems if all the grains are randomly set the system will have no

Sublattice	N_S	($\mathbf{M}_S$)	(M_l)
1	189	(-0.45, -0.81,-0.35)	0.92
2	191	(0.92,-0.08,-0.38)	0.91
3	204	(0.66,-0.71,0.24)	0.90
4	197	(-0.016,-0.013,0.99)	0.89

Table 6.1: **How the exchange bias is predicted from the crystallography.** The number of atoms in each magnetic sublattice (N_S) and the magnetisation direction ($\mathbf{M}_S$and length (M_l). The number of uncompensated spins is calculated as the vector summation of the number of atoms in each sublattice with the direction of each sublattice . In this case this gives the vector (6.15, 2.45, -0.19) with a magnitude. This imbalance is caused by there being an average of 10 atoms more in sublattice 3 than in the other 3 sublattices, while the magnitude is reduced due to sublattice disorder arising from local spin frustration.

net bias direction as the exchange bias of all the grains will cancel out. Before hysteresis loops can be measured for multi-granular systems the setting procedure must be adapted.

6.3.1 The setting process

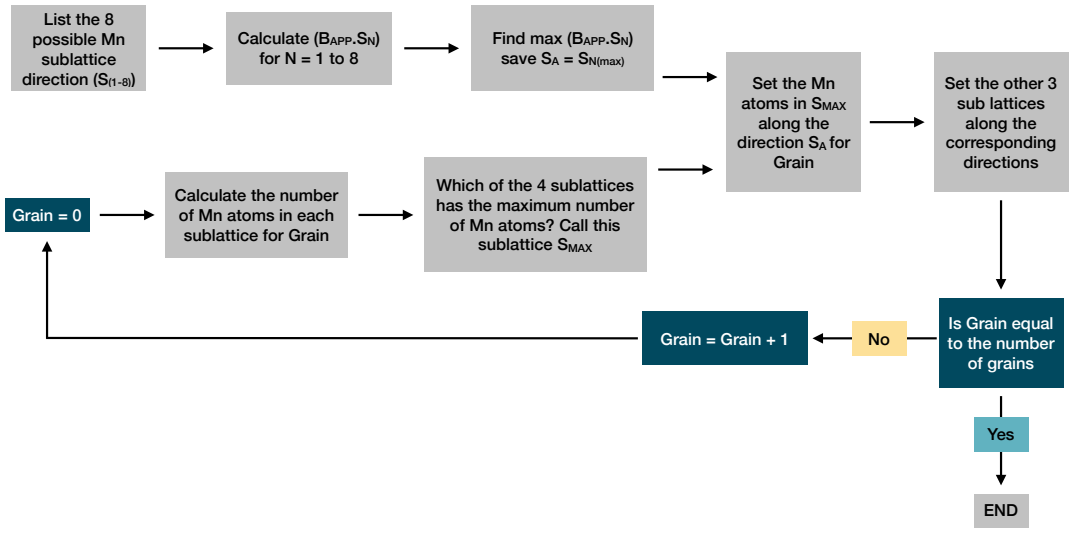

Figure 6.11: **Flowchart describing the setting procedure to set the interface spin direction of the AFM along the direction of an applied field.** B_{APP} is the direction of the applied field and N is the sublattice from 1-8.

A new setting procedure was created to replace the field-cooling step. The setting procedure will force the AFM to set with the direction of the net interface magnetisation along the direction of the setting field. In chapter 5 the mechanism for exchange bias in a single grain was discovered, and using this knowledge we

can create a setting procedure which will set the direction of the uncompensated interface moment of each grain along the setting field direction. In each grain the magnetisation of the AFM sublattices can lie along four possible directions. Table 6.1 shows these four directions for the incorrectly set grain used in chapter 5. In this example sublattice 3 has the largest number of Mn atoms and therefore you would expect sublattice 3 to be along the direction closest to the setting field direction (1,0,0) in this case (0.92, -0.08, -0.38) however instead sublattice 2 is along that direction. A setting procedure was created which sets the magnetisation of the sublattice with the largest number of Mn atoms along the AFM magnetisation direction closest to the setting field direction. The other three sublattices are then set along the remaining three possible sublattice magnetisation directions, which sublattice is set along each direction was calculated from the geometry, and the magnetisation of the CoFe is set along the applied field direction. The exact mechanism for the setting procedure is outlined in Fig. 6.11.

The new setting process was initially tested for the same single grain system used in section 5. The system was run through the setting procedure program and then to test whether the AFM was correctly set, an equilibration simulation was run. In the equilibration there are no external fields acting on the FM apart from the interface field from the AFM and therefore the FM aligns along this direction. The simulation parameters were the same as the parameters used in section 5.4.

Fig. 6.12 shows the movement of the CoFe magnetisation through the first 0.5 ns of the equilibration simulation. The CoFe magnetisation tilts around 19 degrees from the applied field direction. The rotation occurs because although the AFM is now set in the direction closest to the applied field, there are only 8 possible directions this direction might not necessarily be equal to the applied field direction. In this case the FM has rotated to the direction of sublattice 3 in 5.1 as shown in Fig. 6.12.

Next, the setting procedure was tested for a multigranular system. In multigranular systems the setting procedure runs separately for each grain as described in Fig. 6.11. To test the setting process a 100nm × 100nm × 8nm bilayer was created. Usually, the FM will be modelled as a continuous thin film. However, for this test simulation the FM was given the same granular structure as the AFM. This was done as way of measuring the direction of the interface field the FM feels from the AFM. The bilayer was run through the setting procedure simulation. After the setting procedure an equilibration simulation was run. During this simulation there are no fields acting on the FM and as the FM grains are now

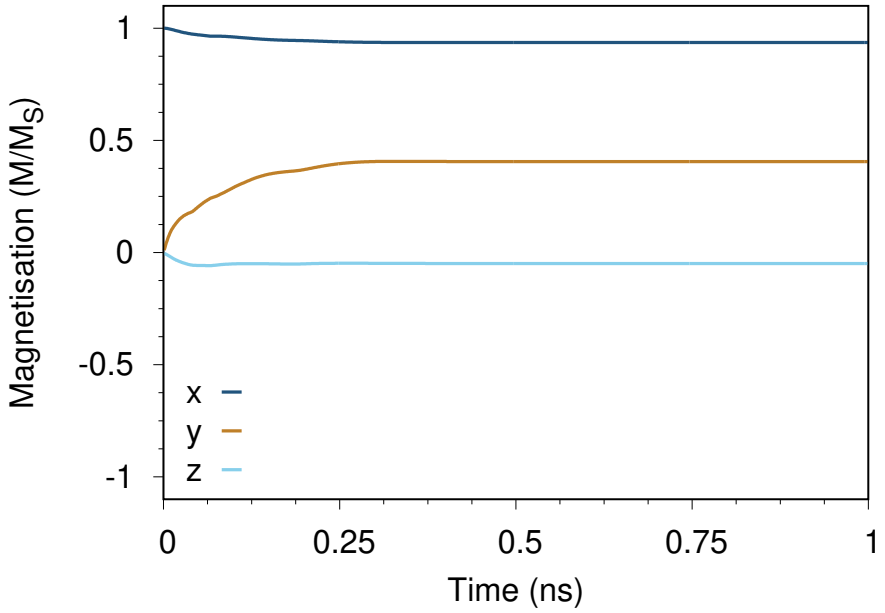

Figure 6.12: **The magnetisation direction throughout the equilibration stage of the simulation**. During the equilibration step the FM relaxes to its minimum energy position, as there is no applied field, the minimum energy occurs when the FM aligns with the interface moment of the AFM. This causes the FM to cant away from the applied field direction, in this case canting about 19 degrees. Initially the interface moment is aligned along the direction of the applied field as it is coupled to the FM but when the field is removed the magnetisation cants towards the minimum energy direction caused by the underlying structure of the AFM.

decoupled, each FM grain will align with the interface field from the AFM grain below it. The resulting magnetic structure of the FM is shown in Fig. 6.13(b). The Figure shows that whilst most of the grains have been correctly set along the setting field direction a small proportion have not been and some of the grains have even rotated almost 150^o away from the setting direction. However the net direction of the FM is along the setting field direction as shown in Fig. 6.13(a).

The incorrectly set grains are due to the more complicated grain shapes in the multigranular structure than a single grain. The strength and direction of the interface exchange field is a vector combination of the uncompensated interface spins, and in these more complicated structures the placement of the spins in the interface becomes more important and the simple summation we created becomes less accurate. However, as the setting procedure has worked for the majority of grains this method is used for the remainder of the chapter.

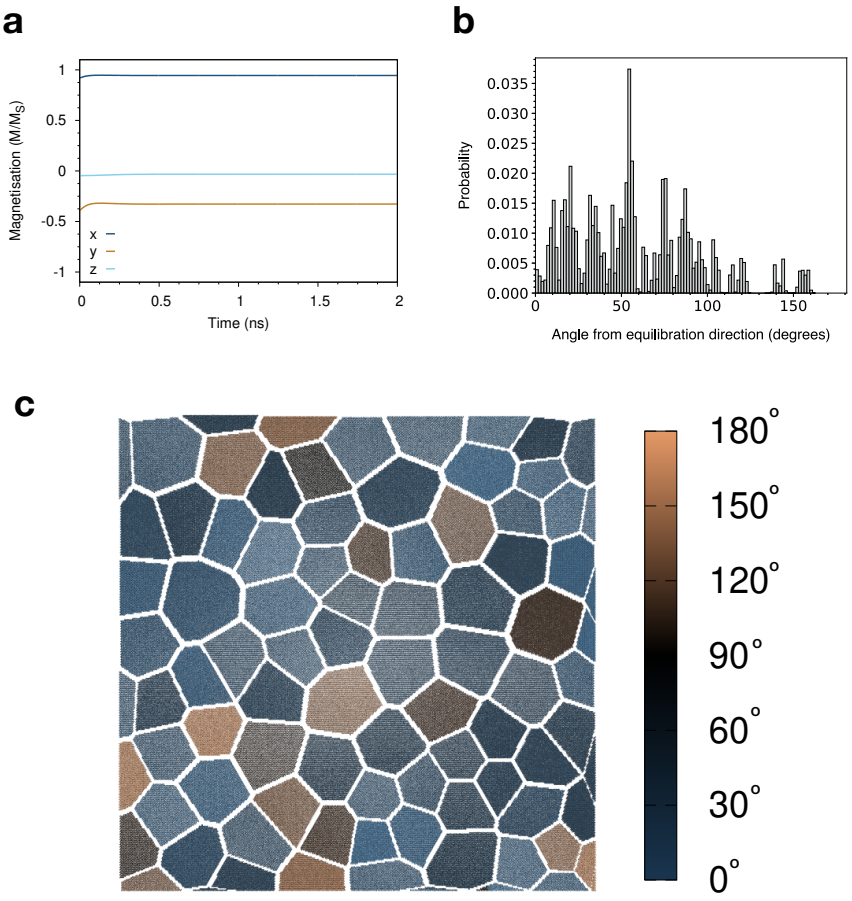

Figure 6.13: **The magnetisation direction throughout the equilibration stage of the simulation and direction of the net interface exchange field**. (a) The direction of the net magnetisation of the FM throughout the equilibration stage. The simulated magnetisation has remained along the [1,0,0] direction. (b) During the equilibration step the FM relaxes to its minimum energy position, as there is no applied field, the minimum energy occurs when the FM aligns with the interface moment of the AFM. In this simulation the FM also has a granular structure so each FM grain will follow the magnetisation of the interface field of the AFM below it. The angle of rotation away from the setting field direction is plotted on the histogram in (b) and shown schematically in (c). In (c) the colour in the diagram represents the angle to the setting field direction at the end of the equilibration simulation. Whilst most of the grains are have only canted 10 - 60^o away from the setting field direction some of the grains are almost 150^o away.

6.4 Hysteresis loop simulations

The setting procedure and equilibration stages of the simulation were repeated but replacing the granular FM with a continuous FM. This means that each of the FM grains are now coupled together, but the AFM grains are still uncoupled. The simulated structure was 50 nm × 50 nm × 8 nm with an input average grain size

of 5nm and a standard deviation of 0.37. The granular structure created in the AFM is shown in Fig. 6.14(a). The grain size distribution not including the edge grains is shown in Fig. 6.14(b). The median grain size in the system was 5.16 nm and the standard deviation was 0.30. This median grain size is very close to the input size but the standard deviation is quite a lot smaller than the input value.

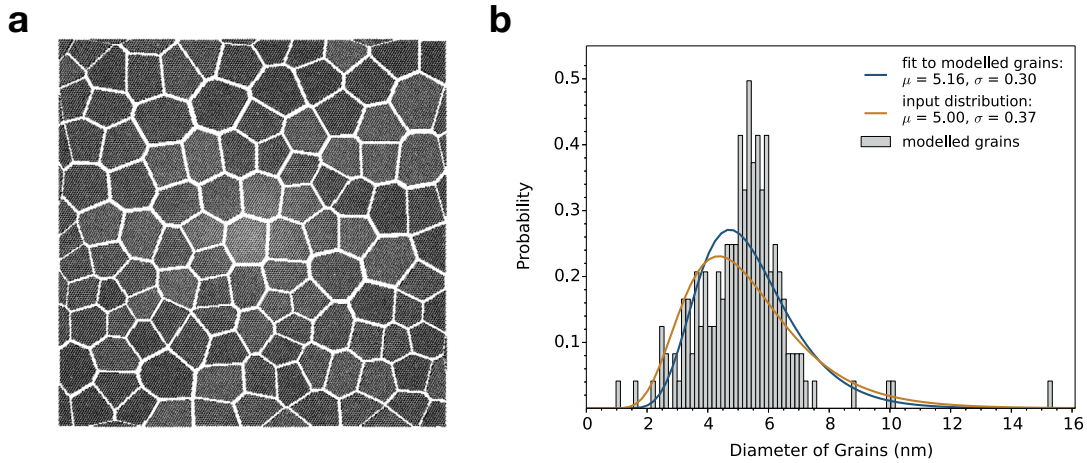

Figure 6.14: **Grain size distribution for the multigranular test system.** (a) A visualisation of the simulated granular structure. (b) A histogram of the simulated grains, this is fit to a lognormal distribution and compared to the input lognormal distribution.

The equilibration was then run on this system, the simulation used the LLG equation with a Heun integrator as described in section 2.3.3. The simulation was run for 1.5 ns using a 0.1 fs timestep. During the simulation the FM cants slightly away from the setting field direction (1,0,0) to (0.895,-0.440,0.001). This is because the system is still relatively small and only contains 100 grains, each with their own set direction. This is not enough grains to average out all of the directions accurately to exactly the setting direction especially if you take into account the unset grains seen in Fig. 6.13. The set direction is still at an angle to the setting field direction. It is predicted that in a larger system the FM would cant to almost exactly the setting field direction.

It was proposed by Barker *et al* [96] that at the interface of the FM the magnetic structure of the FM would show an imprint of the granular AFM magnetisation below. In this imprint above each AFM grain the FM magnetisation would align with the interface field of the AFM. The imprint would cause the magnetisation of the FM to not be 100% aligned. They used a micromagnetic model to simulate the bilayer with a granular AFM and a continuous FM. The uncompensated moment was modelled as a set field from the AFM onto the FM.

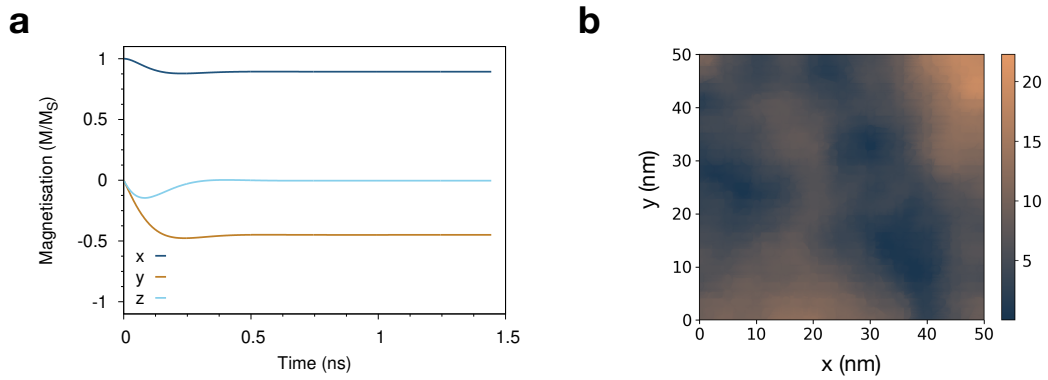

Figure 6.15: **The motion of the FM throughout the equilibration stage of the simulation.** During the equilibration stage all external fields are removed and the only force the FM feels is from the AFM below. (a) The motion of the FM throughout the simulation. The FM cants slightly away from the setting field direction and into the direction of the interface moment from the AFM below. The direction of the interface field is only slightly away from the setting field direction. (b) The interface layer of the FM shows canting of up to 20 degrees and imprinting from the grains below.

The FM rotation was modelled as a Stoner - Wohlfarth coherent rotation. To test if our model also observes this imprint we have visualised the FM spin structure at the interface. The spin structure is shown in Fig. 6.15b, the colour of the spins represents the angle from the average FM direction. It shows the same imprinting pattern seen by Barker *et al* . Although individual grains cannot be seen the FM spins can be seen to rotate up to 20% and the total FM M/M_S has reduced from 1 to 0.992.

A hysteresis loop simulation was run along the equilibrated bias direction, between ± 0.3T in steps of 0.01T and at each step the system was time evolved for 200,000 1 fs time-steps. The hysteresis loop produced is shown in Fig. 6.16, having an exchange bias of 0.12T, almost the same as the single grain hysteresis loop in Fig. 5.8. The exchange bias hasn't changed because in the multigrain system the total number of uncompensated spins is an average of the individual grains so will be similar to a single grain system. The coercivity was measured to be 0.07T, much smaller than the single grain coercivity of 0.13T. There are two possible reasons for this decrease in coercivity. Firstly, there is now an angular dependence to the grains, the grains have a distribution of angles to the applied field. From Stoner-Wohlfarth [97], an increase in the angle between the field and the easy axis reduced the coercivity. Secondly, the larger FM system now rotates with non coherent rotation reducing the coercivity.

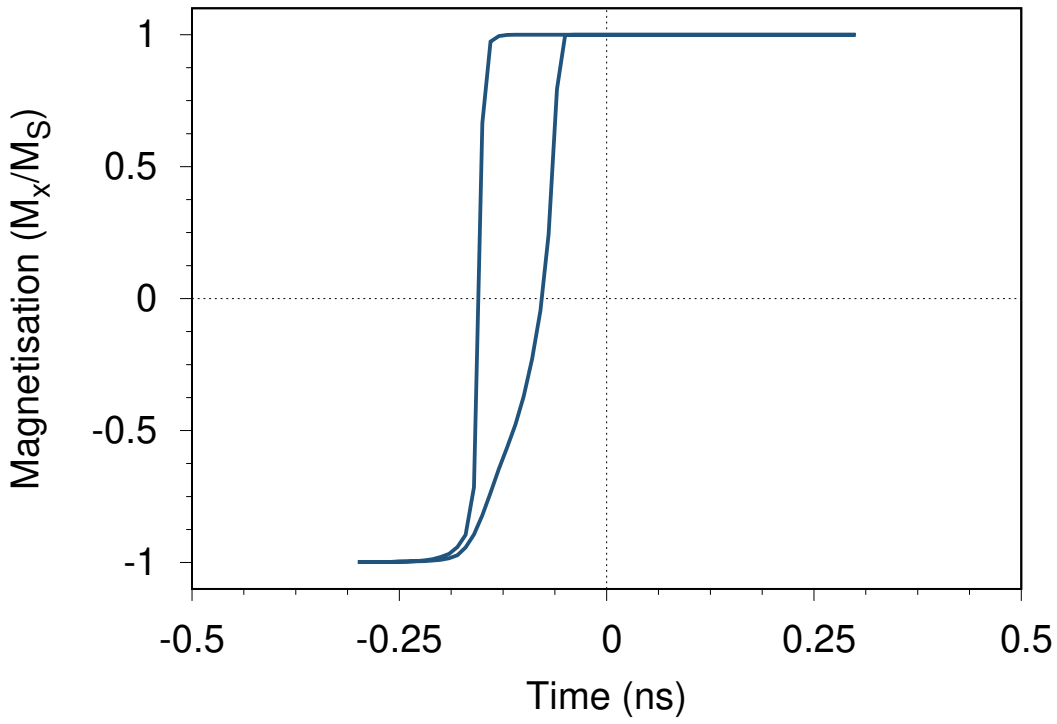

Figure 6.16: **Simulated hysteresis loop for a granular AFM.** The hysteresis loop exhibits 0.12T of exchange bias.

The exchange bias of the system is defined as the integral of all the grains between V_C and V_{set}. However, as this hysteresis loop was run at 0K, even the smallest grains will be stable and as we have forced the grains to correctly set, the exchange bias should be the integral over all grains. As the exchange coupling of the FM layer is much stronger than the interface exchange coupling the FM will only rotate when the field is higher than the net field from the AFM. It can be observed that every AFM grain flips at the same time slightly after the FM has rotated as shown in Fig. 6.16. The FM-AFM reversible moment in all grains can therefore be said to rotate coherently with the FM.

6.5 The temperature dependence of exchange bias in granular IrMn/CoFe bilayers

In section 5.8 we discussed the temperature dependence of exchange bias in single grain IrMn/CoFe bilayers. It was found that the exchange bias was positive until the blocking temperature which in our system was around 450K. The exchange bias at 300K was 40% of the 0K value. In the following section we simulate the temperature dependence of exchange bias in our multigranular system to see

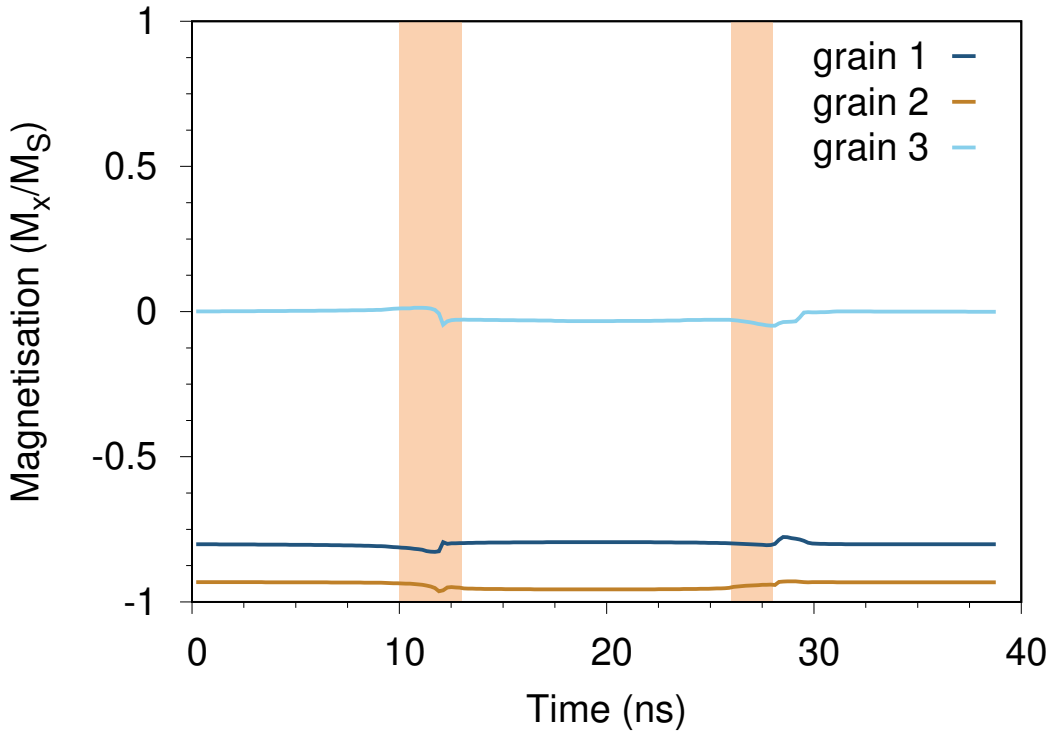

Figure 6.17: **Magnetisation along the x direction for sublattice 1 throughout the hysteresis loop for 3 different grains.** Every grain of the AFM rotates at the same time, and the shaded rectangles show the points where the FM reverses magnetisation.

how it varies from the single grain model and if our model will match previous experimental measurements. The system used has a grain size distribution with a standard deviation of 0.37. This means that although the average grain size is 6nm there will be some grains which are much smaller and some grains which are much larger. The grain size distribution in Fig. 6.14 shows that some grains only have a 1nm diameter. These small grains will have a very low blocking temperature and above the blocking temperature will not contribute to the exchange bias.

Fig. 6.16 shows the 0K hysteresis loop for the system shown in Fig. 6.15. A hysteresis loop simulation was run for temperatures between 0K and 700K, where each simulation was started from the spin configuration after the equilibration step, so all grains had the same initial starting configuration. In the single grain system we had to repeat each hysteresis loop ten times to get an average value because the small grains display large temperature fluctuations. However, in the multigranular system the system is much larger and more thermally stable (until the blocking temperature) meaning the hysteresis loops do not need to be repeated.

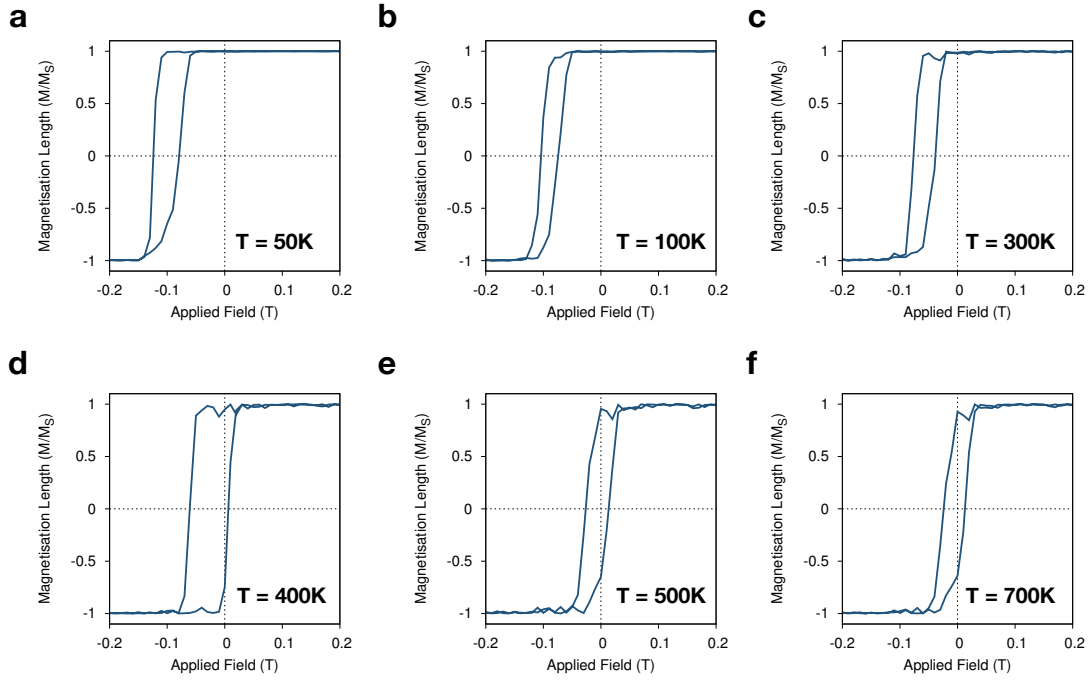

Figure 6.18: **Simulated hysteresis loop for a granular AFM at 50K,100K, 300K, 400K, 500K and 700K.**

The simulated hysteresis loops for 50, 100K, 300K, 400K, 500K and 700K are shown in Fig. 6.18. The hysteresis loops show that as the temperature increases the exchange bias decreases. The hysteresis loops show an initial decrease in the coercivity from 0K to 100K, but then an increase at 300K - 400K after which the coercivity continues to decrease. At 300K the exchange bias is 0.06T, 50% of the 0K value. The exchange bias has decreased more than for the single grain model, this is because our single grain was 8 nm × 8 nm × 5 nm, whereas our multigranular system has an average grain diameter of 6 nm and a thickness of 5 nm. The smaller grains will have a lower blocking temperature causing more thermal instability and therefore a larger drop in exchange bias. Our multigranular system also contains a few very small grains. At 300K these small grains will be completely thermally unstable as the temperature is already larger than the blocking temperature for these grains.

The temperature of the hysteresis loop simulation was systematically varied from 0K to 700K, and the computed exchange bias and coercivity are plotted in Fig. 6.19 (a) and (b) respectively. The exchange bias was found to decrease with temperature and the coercivity initially decreases but as the temperature continues to increase the coercivity also increases to a peak at about 400K - 450K. The peak in the coercivity matches the temperature that the exchange bias

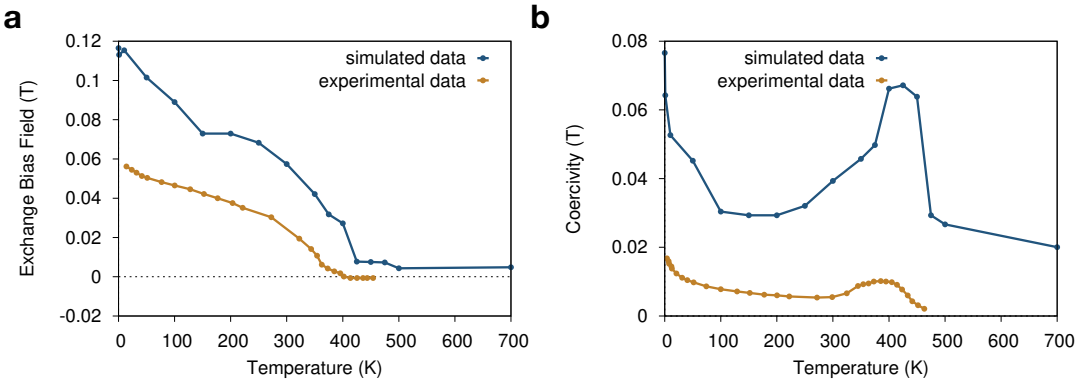

Figure 6.19: **Simulated and experimental dependence of the exchange bias and coercivity with temperature.** (a) The simulated temperature dependence of the exchange bias and (b) the coercivity, compared with the experimental results of Ali *et al* [98]. The simulated exchange bias decreases with temperature as does the experimental result.

decreases to zero given by the blocking temperature of the AFM. The temperature dependence of the exchange bias and the coercivity was experimentally measured in IrMn/CoFe systems for varying thicknesses of CoFe by Ali *et al* [98]. Their results are plotted on Fig. 6.19 (a) and (b) as well. The experimental data shows exactly the same trend as the simulated results with the exchange bias decreasing and the coercivity having a peak at 400K - 450K. Ali *et al* also calculated the coercivity for a system of just CoFe with temperature. In this system the coercivity decreased linearly with temperature, and from this we can assume that the peak in the coercivity at 400K comes from the AFM below. At 400K the exchange bias disappears because the system has reached the blocking temperature and the grains now have enough thermal energy to rotate between ground states. But why does this cause a large increase in the coercivity if there is no exchange bias? To investigate this, the change in magnetisation of the AFM in each grain was observed throughout the hysteresis loop at the blocking temperature (400K). The magnetisation along x of one AFM sublattices in one grain is shown in Fig. 6.20(a), and the magnetisation of the AFM can be seen to reverse after the FM reverses. The magnetisation then remains along this new direction. The magnetisation length is shown in Fig. 6.20(b), showing that the magnetisation length remains constant at approximately 0.6 - which is the value of M/M_s at 400K for bulk IrMn$_3$. This suggests that the IrMn$_3$ is rotating coherently and not breaking up into domains. This behaviour is observed in a large proportion of the grains.

The flipping of the AFM means that instead of the AFM adding a unidirectional anisotropy now it adds a uniaxial anisotropy. This means it gives exchange bias in

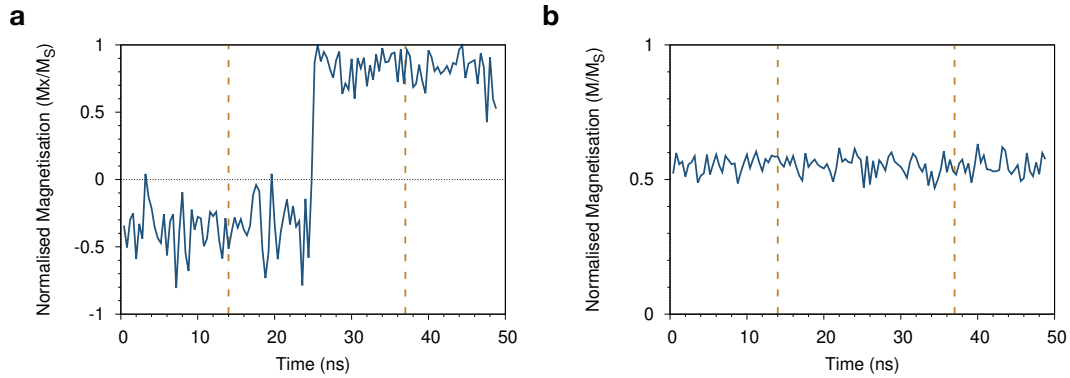

Figure 6.20: **Magnetisation along x of one AFM sublattice in one grain, it can be seen to rotate at negative saturation of the FM.** (a) The magnetisation rotates between the positive and negative exchange bias directions. The points the FM flips are outlined by the gold dashed lines. (b) The magnetisation length remains constant suggesting the grain flips coherently and does not form domains.

both directions, as after flipping the exchange bias is now in the opposite direction and has been thermally reset during the hysteresis loop. This thermal resetting therefore causes the increase in coercivity even with no exchange bias.

The experimental results have a slightly smaller amplitude than the simulated data. The experimental calculations used a thickness of 3.9 nm whereas our simulation was only 3 nm, decreasing our simulated values by 3/3.9. Here we have taken a measurement from only the first hysteresis loop, however, it is well known from Sharrock's law that the coercivity is time-dependent [99] and the experimental results are done over seconds whereas ours are done over ns so more grains will flip earlier in the experimental measurements than in our simulations. The remaining difference in magnitude could be due to the fact our system has an atomically flat interface - increasing the exchange bias value or the experimental calculations may have had a different grain size distribution which is not stated in the paper but affects the exchange bias.

6.6 The dependence of the exchange bias on the grain size distribution in IrMn/CoFe bilayers

So far we have only used one grain size distribution, assuming a median grain size of 5 nm and a standard deviation of σ =0.37. Real devices will have a distribution of grain sizes depending on the growth techniques. The grain size dependence of exchange bias was discussed in the introduction to this chapter. O'Grady *et al*

[5] found that under a certain grain volume (V_C) the AFM grains are thermally unstable and grains larger than the grain volume (V_{SET}) will not be set during the exchange bias procedure. Therefore the only grains that contribute to the exchange bias are grains with a volume $V_C < V < V_{SET}$. Using this assumption the exchange bias can be predicted from the grain volume distribution [5]. They found that a lognormal volume distribution gave a good fit to the experimental data. These results were matched using a micromagnetic simulation by Daeng-am *et al* [91].

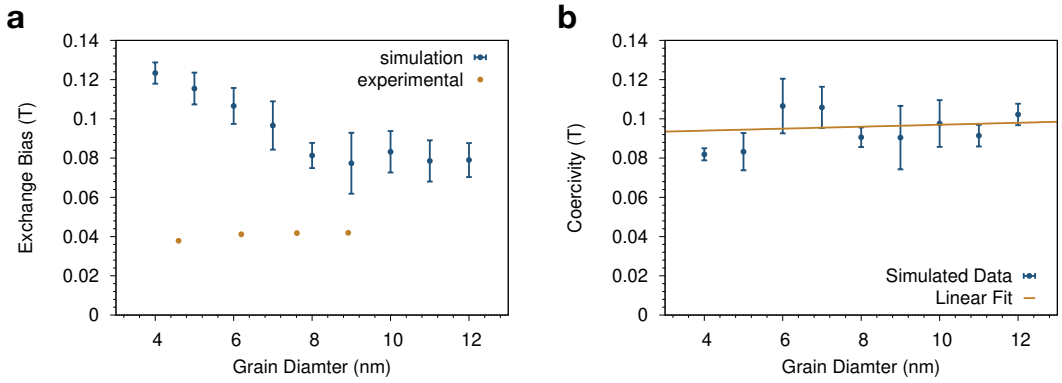

Figure 6.21: **The simulated grain size dependence of the exchange bias and coercivity at 0K compared to experimental results [5].** (a) The exchange bias has a maximum value in 4 nm grains in contradiction with the experiments. The experimental results were measured at 300K, explaining the difference in magnitude between the two datasets. The fit to the experimental data is taken from [5](b). The coercivity of the hysteresis loop seems to be unrelated to the grain diameter, as shown by the linear fit with a gradient of only 0.0005T.

The next step was the model the grain size dependence of exchange bias using our atomistic model and see if it matches the previous experimental results. The system dimensions were kept the same at 50 × 50 × 8nm but the median grain size was varied from 4nm - 12nm. The standard deviation of the grain size distribution was kept constant at 0.37. The thickness of the AFM was kept constant at 5nm. The simulations were run through the exact same simulation steps as has been used throughout this chapter. The output standard deviations were checked to make sure they approximately matched the inputs.

Five simulations were run for each grain diameter each with different random numbers used to generate the granular structure so an average exchange bias could be calculated. The five granular structures all have approximately the same median grain size and standard distribution but different structures.

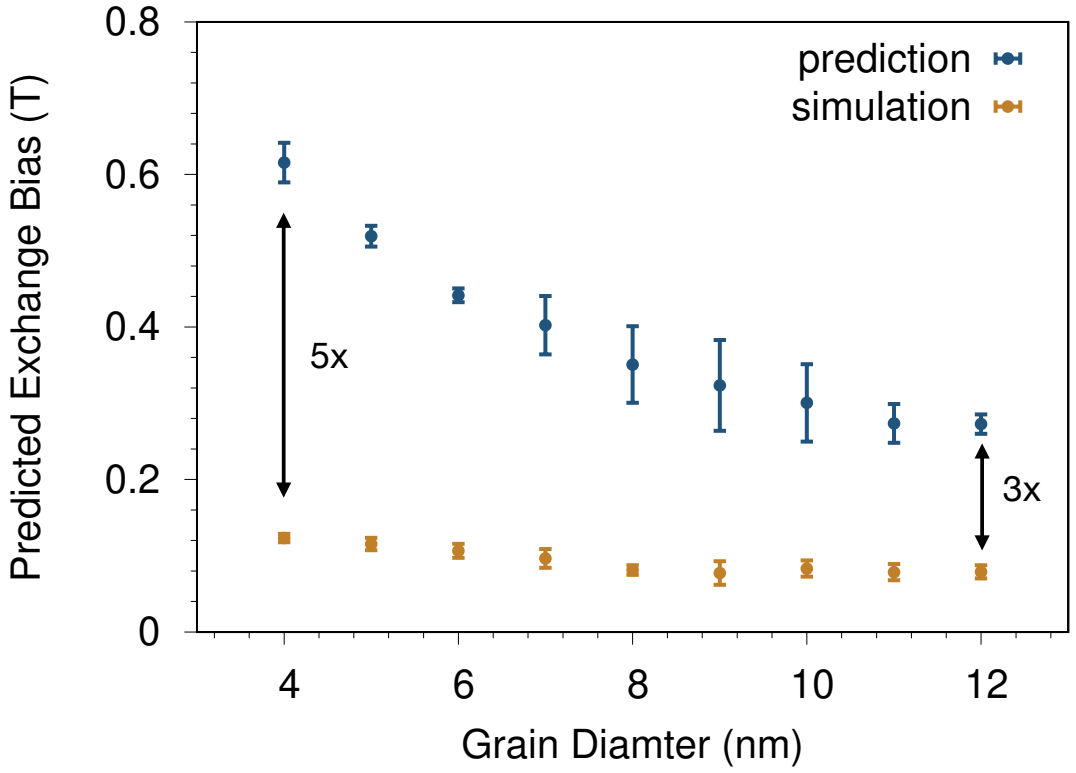

Figure 6.22: **Predicted exchange bias in the multi-granular system for different grain sizes**. The exchange bias decreases with the grain diameter as observed in our simulations.

The hysteresis loop simulations were initially run at 0K and the average exchange bias was calculated from the five simulations, as plotted in Fig. 6.21 with the experimental results from O'Grady *et al*. The exchange bias has a maximum for smaller grain sizes, because the smaller the grain size the bigger the statistical imbalance between the number of spins in each sublattice, therefore causing a larger uncompensated interface field and therefore a larger exchange bias. In reality, with temperature the small grains would because superparamgnetic, decreasing the exchange bias. The number of uncompensated spins in each grain (n_{un}) can be predicted using the same method as used in the single grain model described in chapter 5. The number of uncompensated spins can be calculated for each grain, then summed to calculate the number of uncompensated spins for the entire system. From the number of uncompensated spins the exchange bias can be predicted as:

$$H_{EB} = \frac{n_{un} J_{int}}{\mu_{FM} N_{FM} \mu_0}, \tag{6.4}$$

where N_{FM} is the number of ferromagnetic atoms and μ_{FM} is the magnetic moment of the FM atoms, J_{int} is the interface exchange constant and n_{un} is the

number of uncompensated spins. The predicted exchange bias for each grain size averaged over the five systems is plotted in Fig. 6.22. It shows the same pattern as shown in Fig. 6.21a but the predictions are about five times higher than the simulated values for low values of the grain diameter and about three times higher for high values. The reduction from the predictions is likely due to the unset grains as shown in Fig. 6.13, arising from the presence of spins at the edges of the grains. This effect is larger for smaller grain sizes, due to the increased edge to volume ratio, explaining the larger difference from the prediction for smaller grains than larger grains.

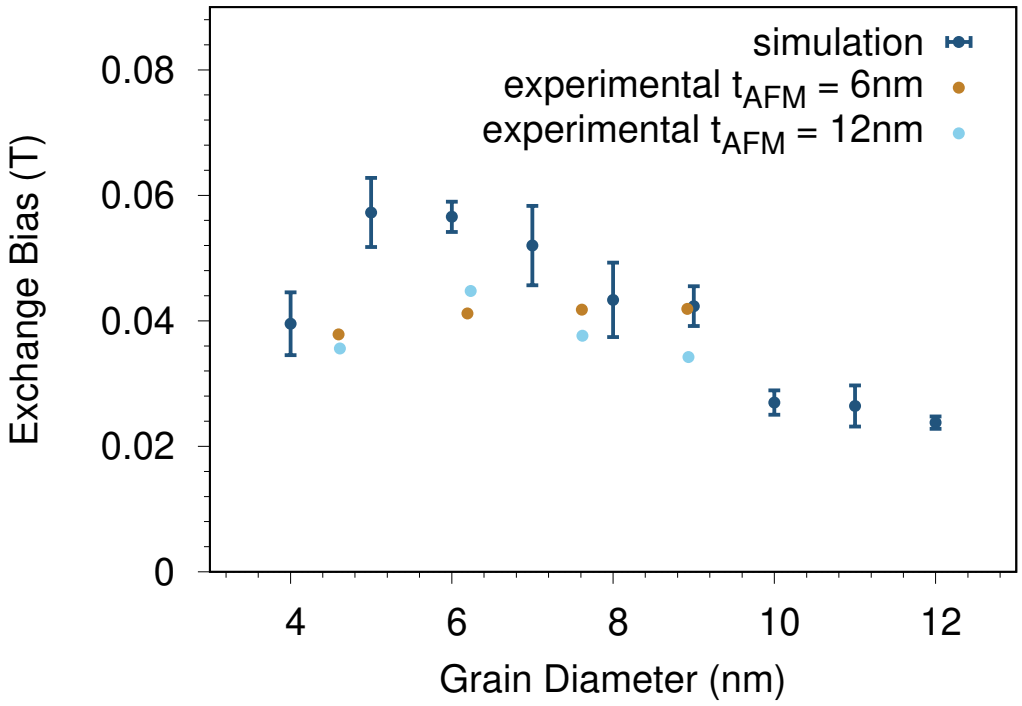

Figure 6.23: **The simulated grain size dependence of the exchange bias and coercivity at 300K compared to experimental results [5]**. The dependence of the exchange bias with grain size at 300K. The experimental results for a AFM thickness of 6nm and 12nm are shown, our simulation behaves more like a 12nm system than a 6nm system even though our AFM thickness was only 5nm.

The exchange bias is also about five times higher than the experimental results, because our simulations were run at 0K. We expect that at room temperature the exchange bias of the small grain sizes will decrease because the smaller grains will become thermally unstable. The coercivity is plotted in Fig. 6.21(b) and it seems to be unrelated to the grain size.

The average exchange bias at 300K for our different grain diameter systems is

shown in Fig. 6.23. The exchange bias for low diameter grains has decreased due to the thermal fluctuations making the small grains unstable and therefore they don't contribute to the exchange bias. The results are plotted against experimental data for film thicknesses of 6 nm and 12 nm [5], the thickness of the FM shifts the peak in the exchange bias as the peak is proportional to KV/k_BT. The simulated data has a maximum at a 6nm diameter as does the experimental data for a 12nm thick AFM. At 300K the exchange bias has dramatically reduced the exchange bias for large grain sizes to 25% of the 0K value whereas for a 6nm grain diameter the reduction is only about 50%. The 300K trend matches the trend seen experimentally but it was predicted to be due to the fact that the large grains are not set correctly during the setting process. This cannot explain the reduction in exchange bias seen here from 0K to 300K as the grains were set exactly the same in both simulations. One reason might be that there are too few grains in the simulations as for 12 nm grains a 50 nm × 50 nm system will only fit in about 20 grains meaning any unset grains will drastically reduce the exchange bias.

6.7 Summary

In this chapter I have developed the first atomistic model of a multigranular IrMn/CoFe bilayer. The size of the bilayer is comparable to realistic devices. A granular structure was created to match the granular structures used experimentally by creating a new Poisson distribution from seed point generation in the Voronoi structure. Next a new setting procedure was created which fixes the exchange bias setting problem that was found in chapter 5. These were used to calculate the exchange bias in a multigranular IrMn/CoFe system.

This is the first model of exchange bias bilayers to model a realistic granular structure in atomic level detail. The model gave exchange bias of a similar value to the single grain system and those found experimentally but with a slightly smaller coercivity. The model gives exchange bias without the need for imperfections or defects in the AFM and matched experimental results such as the temperature dependence and the grain size distribution. The temperature dependence had the same form and held until the blocking temperature of the AFM as observed experimentally. For the grain size distribution at 0K the simulated exchange bias values were found to be much larger for smaller grains due to the increased statistical imbalance between the different AFM sublattices. Whereas, at 300K, the exchange bias matched the experimental observations, the exchange bias for small grain sizes has decreased due to the increased thermal instabilities.

The model goes a long way to understanding exchange bias in multigranular systems. It can understand and predict the cause of experimentally observed phenomena without relying on imperfections or domain walls in the AFM in a way no previous model has.

7

THE ORIGIN OF THE TRAINING EFFECT IN EXCHANGE BIASED IRMN/COFE BILAYERS

The stability of many conventional spintronic devices is dependent on the size of the exchange bias field, the larger the exchange bias the more stable the device. A problem in increasing the exchange bias is the training effect. The training effect causes a large drop in the measured exchange bias after the first hysteresis loop [100], which continues with continuing hysteresis loops. Fernandez-Outen *et al* [101] postulated that the training effect could be split into two types of training: thermal training and athermal training. Thermal training is due to thermally activated depinning of the uncompensated AFM spins, usually causing a small change in the exchange bias and coercivity between every hysteresis loop [102]. Athermal training is characterised by an abrupt decrease of coercivity and exchange bias between the first and second measured hysteresis loops. A schematic diagram of the athermal training effect is shown in Fig. 7.1. It shows a reduction in both the exchange bias and the coercivity of the second hysteresis loop with respect to the first. The switching fields H_{C1} and H_{C2} are also shown, the first switching field (H_{C1}) is the point at which the magnetisation of the FM first switches to the negative saturation direction. This point is important in real devices as it is the point where the magnetisation reverses direction and represents the maximum field you can apply to the FM before it is no longer stable.

Thermal training is due to well understood thermal instabilities in the AFM [103]. The origin of athermal training however is still a widely disputed problem due to the difficulty in experimentally probing the rearrangement of AFM spins at the interface. It has been proposed to be due to the degree of order of the AFM at the interface. The initial cooling produces an AFM spin structure which may be a meta stable state. The athermal training effect can then be considered to

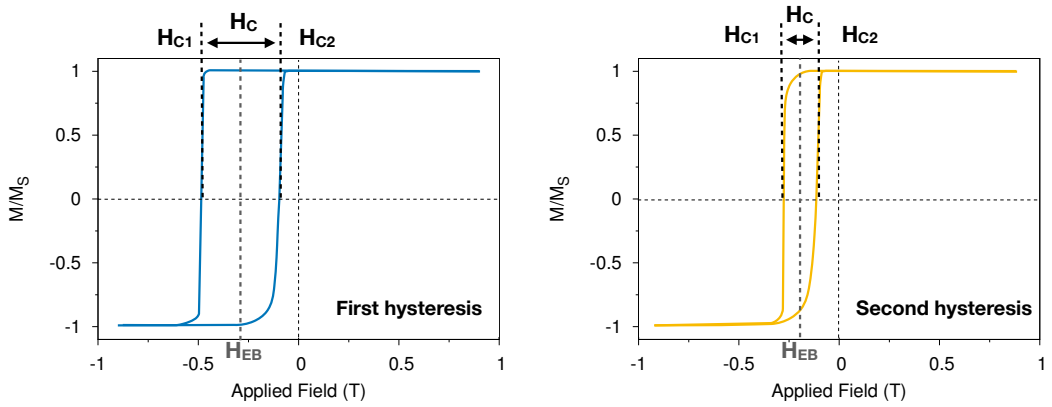

Figure 7.1: **Schematic representation of the training effect.** It shows a decrease in the exchange bias field and the loop coercivity between the first and second measured hysteresis loops. The loops have also changed shape between the first and second measured loop. The switching field (H_{C1}) is marked on the graphs, this is the field at which the magnetisation of the FM first reverses.

be the rearrangement of the spin structure towards the minimum energy state during the first hysteresis loop. Biternas *et al* predicted that training occurs due to Meta-Stable Spins, "These spins are in a meta-stable state created during the setting process. During the first reversal, they reverse only once and they are pinned to a new easy direction" [104]. This can be seen by the change in shape of the hysteresis loops in Fig. 7.1. The first branch of the first hysteresis loop is very square whereas the first branch of the second hysteresis loop is more rounded. The change in shape of these first branches suggests that the AFM layer is in a higher energy meta stable state after setting and transitions to a lower energy state during the hysteresis loop [104]. The return branch of both the first and second hysteresis loops are very similar suggesting that the transition actually occurs either after or during the first branch but before the second branch.

The first model of exchange bias which included the training effect was the Fulcomer and Charap model described in Chapter 6. Using their model, they predicted that the training effect occurred due to a misalignment between the FM magnetisation and the uncompensated magnetisation of the AFM. The next model was the Hoffman model [105]. The model used two independent magnetic sublattices for the AFM, both of which rotated with the Stoner-Wohlfarth motion. Hoffman concluded that the large drop in the first measured hysteresis loop occurs due to inherent frustration of the AFM interface magnetic moments. Suess *et al* [106] used a granular model for exchange bias similar to those described in Section 6 where the AFM grains are exchange coupled and perfectly compensated. The

easy axis for every grain was set randomly. These models were used to investigate the training effect. They found the same result as Fulcomer and Charap that training occurred due to misalignment of the FM and the AFM interface. So far all of these models have assumed an a FM and an AFM with no defects or impurities.

The next class of models are those that no longer assume ideal FM's and AFM's, including non magnetic impurities or interface effects. The first such model was that of Malozemoff [75] as described in section 6. They modelled roughness between the FM and the AFM, where the interface roughness produces a random field which leads to the creation of domains in the AFM. It was predicted that these domains are the cause of uncompensated interface spins, and therefore the cause of training. However, we now know that domain walls are unnecessary for exchange bias to occur. One of the first models of exchange bias to include a rough interface came from Biternas *et al*. [104] Their model was an extension of the domain state model and they found that for flat interface systems there was little training and as the roughness of the interface was increased the training increased. They attributed the increase in athermal training to meta-stable spins which are created due to the interface roughness in the cooling process and during the first hysteresis loop reverse only once and they are pinned to a new easy direction. Whilst this model included interface roughness it only modelled one grain and not an entire granular structure.

In the current chapter the origin of the athermal training effect in IrMn/CoFe exchange biased bilayers is investigated. We will start by looking at IrMn/CoFe bilayer with an atomically flat interface structure and as it is predicted that training is due to the degree of order of the AFM we expect this system to give no training effects. If our prediction holds true the interface between the AFM and the FM will be intermixed to investigate whether this intermixing is enough disorder to cause the training effect.

7.1 Simulating the athermal training effect

In section 5 it was discovered that exchange bias can occur in IrMn/CoFe systems without the need for domain walls or interface effects. It has been predicted that training occurs due to disorder at the interface. The first step in proving this is to run a simulation with an atomically flat interface and prove that it does not exhibit training. In the following section only the athermal training effect is investigated, meaning that all the simulations are run at zero Kelvin, so that no thermal training occurs.

The system used in this flat interface simulation was exactly the same system as the one shown in Fig. 6.16. The system was 50 nm × 50 nm × 8 nm bilayer with 5nm of disordered γ - IrMn and 3 nm of CoFe. The system has a granular structure as described in section 6.1.1, the median grain size was 5 nm and the standard deviation was 0.37. The simulation was run through the same 3 simulation steps as described in section 5.4, once these three simulation steps were completed the system was then run through another hysteresis loop simulation using exactly the same parameters as the first hysteresis loop.

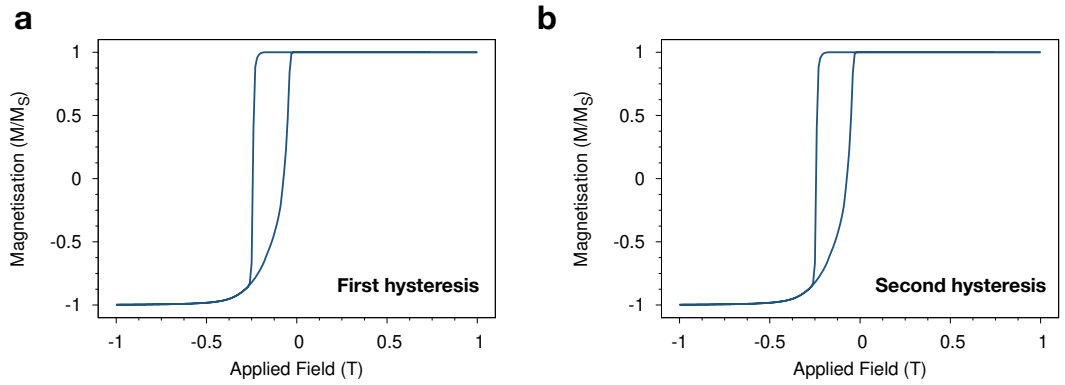

Figure 7.2: **First and second simulated hysteresis loops for a multigranular grain IrMn\CoFe system in section 5**. The system has not shown the training effect with both hysteresis loops have a exchange bias of 0.12 T and coercivity of 0.08 T.

The first and second simulated hysteresis loops are shown in Fig. 7.2. Both hysteresis loops have an exchange bias of 0.12 T and a coercivity of 0.08 T. There is also no change in the shape of the loop between the first and second measured hysteresis loops. The lack of training is not surprising as Kaeswurm *et al* [102] predicted the training effect to be due to disorder of the Mn at the interface and the interface simulated here is completely atomically flat. To test her theory we will add some disorder to the interface. The disorder will be added by mixing the atoms at the interfaces. The first step is to create a bilayer system with a mixed interface. The procedure for creating a mixed interface bilayer system is outlined below.

7.2 Simulating the interface mixing

Experimentally, the interface mixing in IrMn/CoFe systems has been measured to be in the region of 0.1nm - 1nm in width [103, 107]. To create a disordered interface, the material type (CoFe or Mn) was randomly swapped (CoFe to Mn

and Mn to CoFe) around the interface. The swapping was generated using a probability distribution defined by:

$$P(z) = 1 - \frac{1}{2}\tanh\left(\frac{\pi(z - z_0)}{w}\right), \tag{7.1}$$

where $P(z)$ is the probability of finding an atom of a particular type at height z, z_0 is the interface height and w is the width of the tanh function, corresponding to the width of the interface mixing in nanometers. Every atom in the IrMn layer has a probability (P) of being changed to a CoFe atom depending on its height (z) above the interface. The mixing can also occur the other way around mixing the CoFe into the IrMn or both types of mixing can occur simultaneously. We will refer to these three types of mixing as mixing types a,b and c respectively and they are shown in Fig. 7.3.

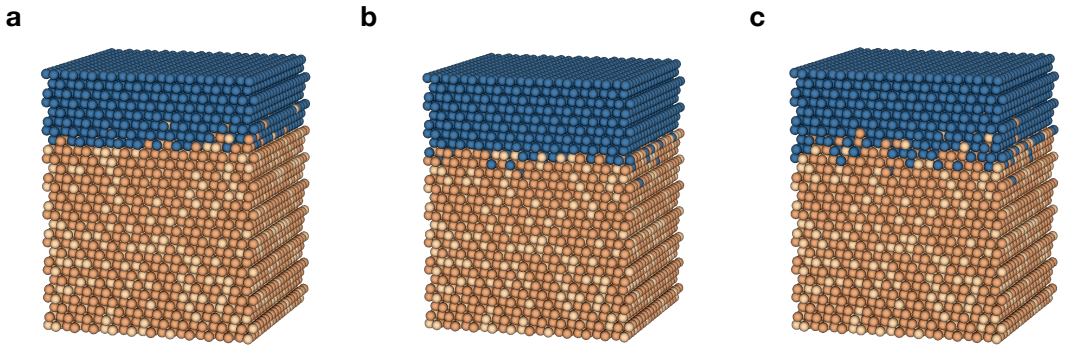

Figure 7.3: **Visualisation of the different types of interface mixing used in the simulations.** (a) The IrMn is mixed upwards into the CoFe, (b) The CoFe is mixed downwards into the IrMn and (c) Both type of mixing occur. All three figures have an intermixing width of 0.1nm

Iridium has a very high atomic weight in comparison to CoFe therefore it is expected that the CoFe will not be able to penetrate into the IrMn instead the IrMn will penetrate into the CoFe and therefore the interface mixing will mainly occur in the case shown in (a) in this case only the Mn is mixed into the Cofe and not the Ir due to its high atomic weight. The choice of diffusion type matches previous experimental measurements of the difusion [108]. We will use this type of intermixing for the remainder of the chapter. The first step is to confirm that the exchange bias still exists when the interface is mixed.

7.3 Setting the Exchange Bias in multigranular exchange biased systems with a mixed interface

The first challenge in running a hysteresis loop with a mixed interface comes from the setting process. In section 6.3.1 a setting procedure was developed which calculated the number of Mn atoms in each sublattice of the interface layer of the IrMn and then used this to set the exchange bias along the minimum energy direction. In a mixed interface system this becomes a lot more complicated as there is no longer only one interface layer and instead the interface is spread over many atomic layers. Therefore, the setting procedure cannot be used as it is no longer a simple calculation to work out the setting direction. Instead it was found that in a system with a mixed interface after the equilibration stage the direction of the CoFe magnetisation remained approximately along the setting field direction. The first two steps of the simulation steps outlined in Section 5.4, with the setting procedure being a field-cool simulation were run with interface mixing widths varying from 0.1nm to 1nm, a total of 50 simulated structures were created. The resulting angle from the setting field direction after the second step - the equilibration stage is plotted in Fig. 7.4. The figure shows that the maximum rotation from the setting field direction was 35 degrees, but the majority of the simulations remained within 20 degrees of the setting field direction. An angle of 35 degrees means that the magnetisation is still 80% along the setting field direction. The small rotation from the setting field direction is expected and observed experimentally [5].

The interface mixing causes the CoFe and IrMn to have more neighbours of the opposite type, meaning the number of interface exchange interactions is higher. This will increase the coupling between the CoFe and the Mn meaning the field between the CoFe and the IrMn is higher, which could be why the setting procedure works in mixed interface systems but not flat systems.

7.4 Simulating exchange bias in mixed interface multigranular systems

Now, the setting procedure has been proven to work in our mixed interface systems the exchange bias can be simulated. The first step in our simulation is to calculate the dependence of the exchange bias and the coercivity on a system with a mixed

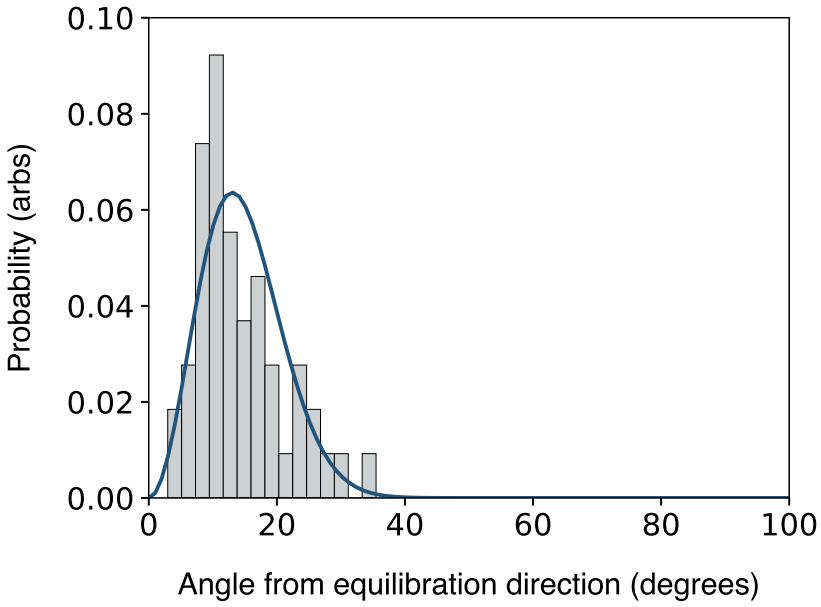

Figure 7.4: **Rotation of the CoFe from the setting field direction after the equilibration simulation.** The CoFe has rotated to a maximum of 35 degrees from the setting field direction and on average the CoFe has only rotated about 20 degrees. The histogram has been fit using a Boltzman distribution shown by the blue line. The interface mixing was varied from 0.1 nm - 1 nm in steps of 0.1 nm, with five simulation being run at each value, totalling fifty simulations.

interface and then from this determine the training.

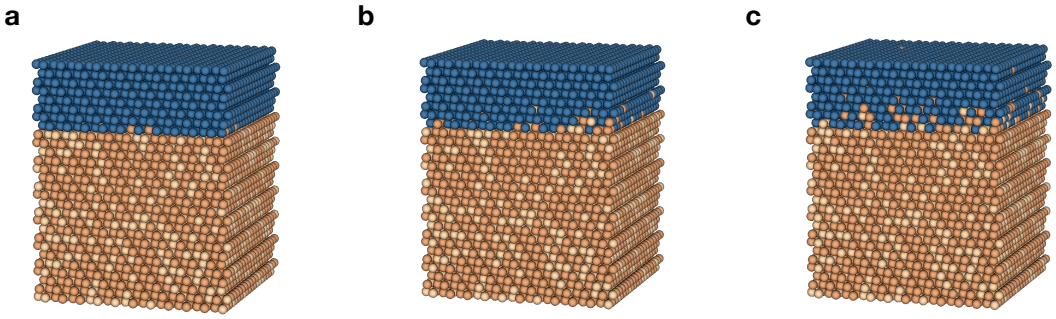

Figure 7.5: **Visualisation of different interface mixing widths in an IrMn/CoFe bilayer.** Interface mixing of (a) 0.1nm, (b) 0.5nm and (c) 1nm.

The multigranular structure used for the flat interface exchange bias simulations from Fig. 7.2 was used for these simulations so the exchange bias can be compared to the flat interface case. The simulation was a zero Kelvin simulation, so only the athermal training effect is accounted for. The simulation was 50nm × 50nm × 8nm and had a median grain size of 5nm and a standard deviation of 0.37. The flat interface had a simulated exchange bias of 0.12 T and a coercivity

of 0.08 T. The width of the interface mixing distribution was varied from 0.1nm to 1nm in 0.1nm intervals totalling 10 different values for interface mixing width. For each value five simulations were run. The five simulations all had exactly the same granular structure, however, the random number seed which defines the interface mixing was changed which varies which CoFe atoms were swapped to be Mn. A visualisation of a subsection of one grain of the bilayer in x,y is shown for interface mixing widths of 0.1 nm, 0.5 nm and 1 nm in Fig. 7.5 (a), (b) and (c) respectively.

The simulated systems are run through the same three simulation steps defined in section 5.4, with the setting field along the x direction. The systems are each cooled from above the Néel temperature under the presence of an applied field, then the system is left to equilibriate under no field at zero Kelvin, and finally a hysteresis loop is simulated.

7.4.1 Equilibration stage

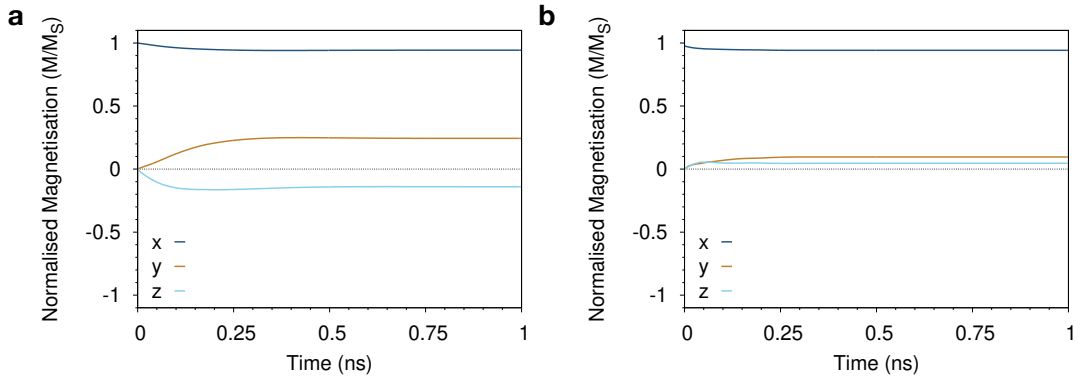

Figure 7.6: **Magnetisation vs time data for the CoFe layer during the equilibration simulation.** For interface mixing widths of (a) 0.1nm, (b) 1nm.

A plot of magnetisation vs time for the CoFe during the equilibration stage is shown in Fig. 7.6, comparing the interface mixing widths of (a) 0.1 nm (b) 1 nm. The simulation with an interface mixing of 0.1 nm has canted to almost 30 degrees away from the setting field direction whereas the 1 nm simulation has remained almost perfectly aligned along the setting field direction.

The average magnetisation directions for the CoFe at the end of the equilibration simulation was calculated for each of the 50 simulations and the trend is shown in Fig. 7.7a. The figure shows that as the interface mixing increases the angle from the setting field decreases and the system is more strongly set along the setting field direction. It can also be observed that as the interface mixing is

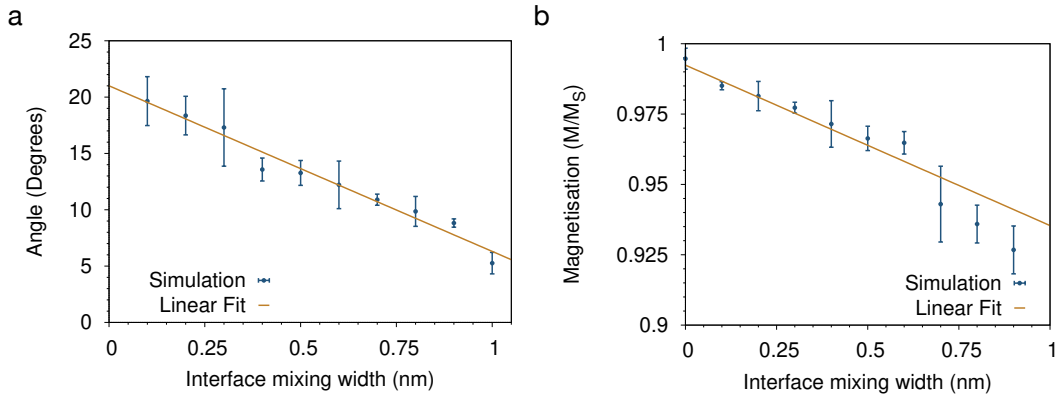

Figure 7.7: **The mean angle between the magnetisation at the end of the equilibration and the setting field direction of the CoFe after the equilibration stage and the length of the magnetisation.** (a) The angle between the CoFe magnetisation at the end of the equilibration simulation and the setting field direction. There is a linear fit to guide the eye. (b) The magnetisation length at the end of the equilibration simulation.

increased the magnetisation length of the CoFe decreases as shown in 7.7b. The decrease in magnetisation length suggests that the CoFe spin directions become disordered at the interface.

To investigate the cause of the decrease in magnetisation length the interface spin structure for the simulation with an interface mixing width of 1 nm was visualised and is shown in Fig. 7.8 (a). The interface spin structure for the CoFe is no longer completely magnetised along the same direction. Instead at the interface the CoFe has canted up to 10 degrees away from the average magnetisation direction of the CoFe. The canting can be seen to be more prevalent in areas where there are more Mn atoms nearby. In these areas the CoFe is less coupled to the bulk CoFe and is instead coupled to the Mn causing the CoFe to cant towards to Mn spin directions.

The magnitude of this disorder was measured by summing the magnetisation of the CoFe atoms in each atomic layer. From this the magnetisation length is calculated as shown in Fig. 7.8 (b). For an interface mixing width of 1 nm, far from the interface the CoFe has a magnetisation length of one, but near the interface the magnetisation length has decreased to only 89%. The decrease in magnetisation is most prominent in the interface layer and only occurs for atomic planes up to 1 nm, after 1 nm there will only be a small amount of mixing between the CoFe and the Mn and every CoFe atom will be strongly coupled to the bulk CoFe. For an interface mixing of 0.1 nm, the CoFe is completely magnetised at all

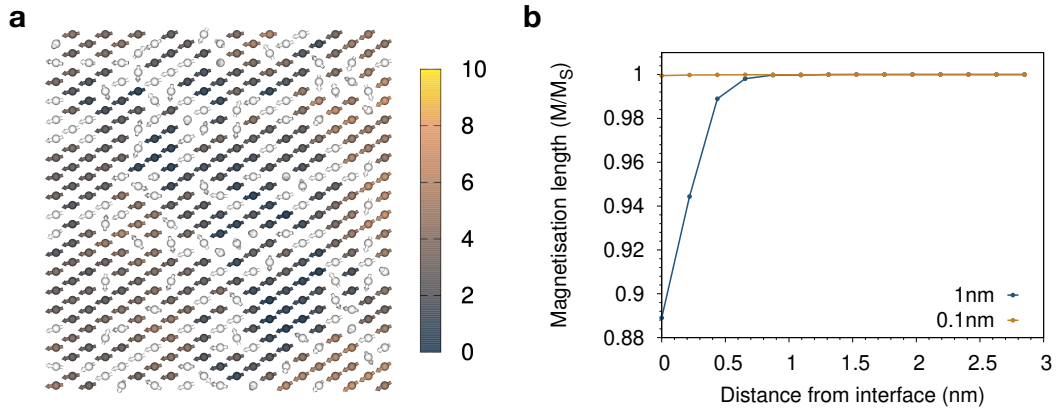

Figure 7.8: **The interface structure of the CoFe for an interface mixing of 1nm and the magnetisation length for each CoFe layer for interface mixing widths of 0.1nm and 1nm** (a) The magnetisation direction of the CoFe at the end of the equilibration simulation for a 8 nm × 8nm section of the bilayer. The white arrows represent the Mn spins and the coloured atoms represent the CoFe spins. The colour of the CoFe spin correspond to the angle in degrees from the average direction of the CoFe. Some of the CoFe spins have rotated up to about 10 degrees from the average field direction. (b) The magnetisation length of each CoFe layer, for the simulation with 0.1 nm of interface mixing the CoFe is perfectly aligned at each atomic layer. For the simulation with 1 nm of interface mixing the CoFe is disordered for about 1 nm, then is completely ordered, the magnetisation length of the interface layer is approximately 89%.

atomic planes as in all layers the CoFe atoms can couple to the bulk CoFe.

7.4.2 Simulations of the first hysteresis loop

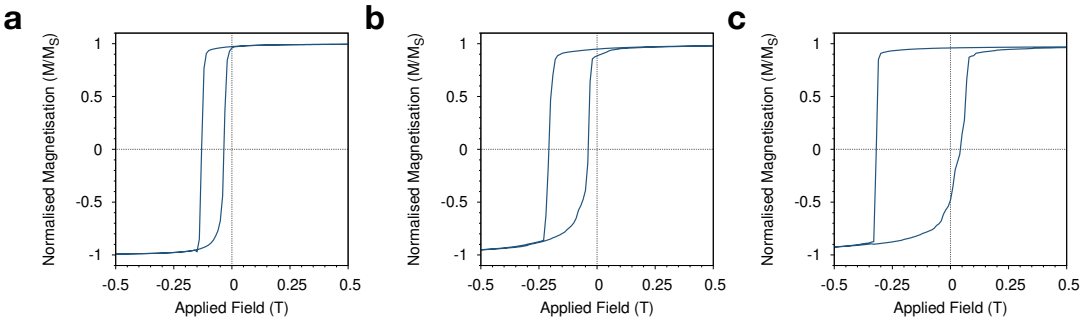

Figure 7.9: **First hysteresis loops for multigranular simulations with interface mixing**. Hysteresis loops for interface mixing widths of (a) 0.1 nm, (b) 0.5 nm and (c) 1 nm.

The hysteresis loop simulations were run along the magnetisation direction of the CoFe after the equilibration simulation to give the maximum possible exchange bias in each system. The simulations were again run at zero Kelvin

to remove any thermal training effects. Simulated hysteresis loops for interface mixing widths of 0.1 nm, 0.5 nm and 1 nm are shown in Fig. 7.9. The most noticeable difference between the three hysteresis loops is the massive increase in coercivity as the interface mixing width becomes larger. The coercivity has increased from 0.082 T for the 0.1 nm simulation to 0.32 T for the 1 nm simulation. The exchange bias has also increased between the three simulations from 0.09 T for 0.1 nm to 0.15 T for the 1 nm simulations.

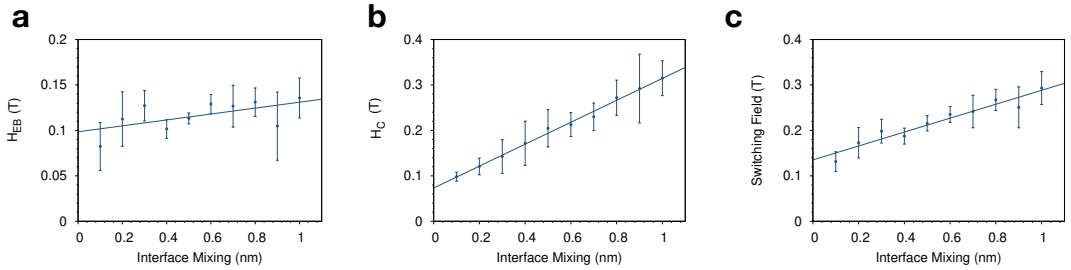

Figure 7.10: **The dependence of the exchange bias and coercivity on the interface mixing for the first simulated hysteresis loops** (a) Shows the dependence of the exchange bias on the interface mixing. (b) Shows the dependence of the coercivity on the interface mixing. (c) The dependence of the switching field on the interface mixing. In all of the figures, the error is the standard deviation in the points from five simulations. All of the figures have been fit with straight lines to help guide the eye.

For each hysteresis loop the exchange bias and coercivity were calculated, the five repeats were averaged and a mean value and standard deviation was found for each level of interface mixing. The average exchange bias for each interface mixing width is plotted in Fig. 7.10(a) showing that there is a large range of exchange bias values, and that the exchange bias can be seen to slightly increase with interface mixing, but the standard deviation sizes means that there isn't much of a trend. The coercivity is plotted in Fig. 7.10(b) The coercivity has massively increased to almost 0.3T for simulations with a high level of interface mixing. The increase in coercivity is due to the fact that with interface mixing a larger proportion of the bulk Mn is incorporated into the interface causing an increase in the interface anisotropy. Fig. 7.10(c) shows the change in the switching field, the switching field represents the stability of the CoFe to an applied field in the opposite direction. The first switching field (H_{C1}) has increased with an increased interface mixing width. There is a noticeable correlation between the coercivity and the first switching field value, suggesting that the second switching field (H_{C2}) is not affected by the interface mixing. The interface mixing instead only affects the first switching field.

The experimental dependence of exchange bias on interface roughness is still not quantified [103]. There have been many experimental measurements but as IrMn is naturally disordered and the interface mixing will have an effect on the interface spin configurations it is hard to quantify. Qi *et al* [103] experimentally measured that there was no correlation between interface mixing and exchange bias value, for interface roughness of 0.678 nm, 0.823 nm and 1.259 nm whereas, Parkala *et al* [89] measured a decrease in exchange bias with an increase in interfacial roughness comparing interface roughness values of 0.1 nm and 1.1 nm. Our measurements do not agree with either of these results, however, both of these measurements were done at non-zero temperature and therefore this may cause a large decrease in the exchange bias in the structures with more disorder.

7.5 Simulations of the second and third hysteresis loops

Now we have proven that exchange bias still exists in systems with mixed interfaces we can see if the mixing has caused the hysteresis loops to exhibit the training effect. To investigate this two more hysteresis loops have been run on the simulated system, both at zero Kelvin. These hysteresis loops are shown in Fig. 7.11, the first, second and third simulated hysteresis loops are shown for interface mixing widths of 0.1 nm, 0.5 nm and 1 nm.

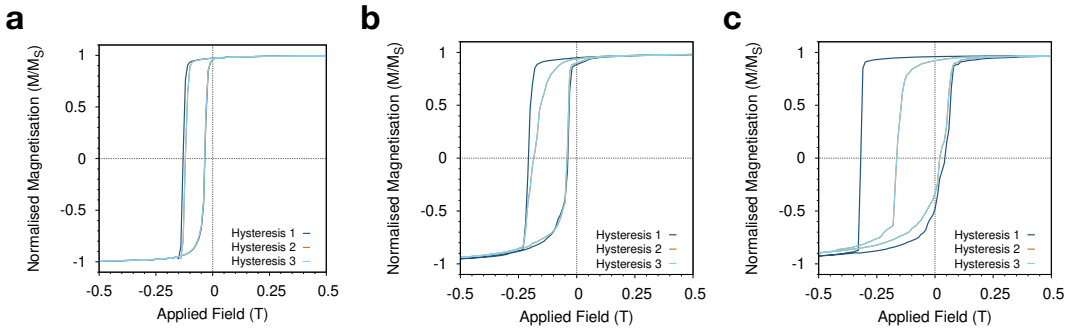

Figure 7.11: **The first three simulated hysteresis loops for different intermixing widths** The interface mixing widths were (a) 0.1nm, (b) 0.5nm and (c) 1nm.

All of the hysteresis loops exhibit a decrease in the exchange bias and the coercivity between the first and second measured hysteresis loops analogous with the training effect. The size of the decrease in both the coercivity and the exchange bias is observed to increase with the width of interface mixing. The change in

the exchange bias between the first and second simulated hysteresis loops for an interface mixing width of 0.1 nm is almost negligible. Whereas, the exchange bias in the 1 nm simulation has decreased dramatically between the first and second simulated hysteresis loops. In all three systems there is approximately no change in either the coercivity or the exchange bias between the second and third simulated hysteresis loops and no change in the coercivity. This agrees with previous experimental measurements of low temperature systems, where a large decrease in the exchange bias is found between the first and second measured hysteresis loops only [102].

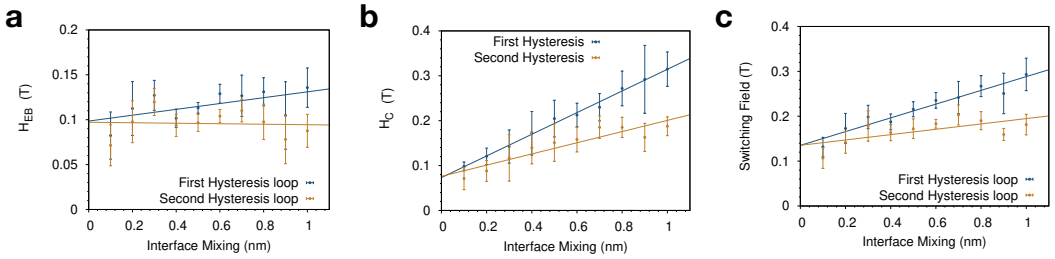

Figure 7.12: **The dependence of the exchange bias and coercivity on the interface mixing for the first and second simulated hysteresis loops** (a) Shows the dependence of the exchange bias on the interface mixing. (b) Shows the dependence of the coercivity on the interface mixing. (c) The dependence of the switching field on the interface mixing. For all of the figures the first and second hysteresis loops are shown and the error is the standard deviation in the points. All of the figures have been fit with straight lines to help guide the eye.

The second and third hysteresis loops were measured for all of the fifty simulated systems. Fig. 7.12 shows that for all interface mixing widths the exchange bias and the coercivity has decreased between the first and second simulated hysteresis loop. The most noticeable change is that for the second hysteresis loops the larger the interface mixing the larger the decrease in exchange bias between the first and second loops. For the second hysteresis loop all of the simulations gave very similar values for the exchange bias field, meaning that there is no correlation between exchange bias and interface mixing width, as experimentally predicted by Qi *et al* [103]. For the coercivity, the higher the interface mixing the higher the drop in coercivity between the first and second simulated hysteresis loops. This leads to a plateau in the coercivity values at about 0.18 T for high levels of interface mixing. Fig. 7.12(c) shows that the first switching field increases with increased interface mixing, but plateaus at about 0.18T again showing a similar form the the coercivity. The initial increase with interface mixing, increases the stability of the CoFe. However, this plateaus because only Mn atoms which are still coupled to the bulk Mn will increase the coercivity, once the interface

mixing it too high the Mn atoms are no longer coupled to the bulk and therefore don't contribute As there is no difference between the second and third simulated hysteresis loops these graphs for the third hysteresis loops match the data for the second hysteresis loops.

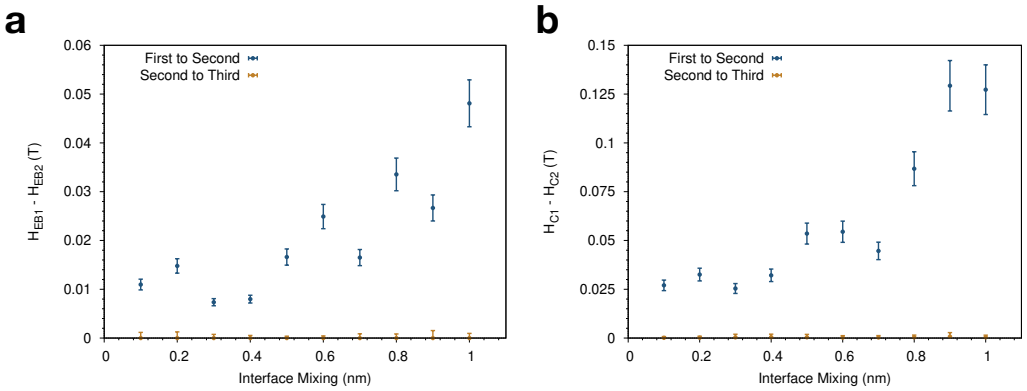

Figure 7.13: **The change in exchange bias and coercivity between the first and second and second and third simulated hysteresis loops** (a) The change in the exchange bias between consecutive hysteresis loops. (b) The change in the coercivity between consecutive hysteresis loops. There is a large change in both the coercivity and the exchange bias between the first and second simulated hysteresis loops but almost no change between the second and third.

The mean change in exchange bias and coercivity between the first and second and second and third hysteresis loops is shown in Fig. 7.13. The error is the standard deviation in the values. The simulations have shown there is a large decrease in both the exchange bias and the coercivity between the first and second hysteresis loops, but almost no change between the second and third simulated hysteresis loops. The change in both the coercivity and the exchange bias is proportional to the width of the interface mixing. The more mixed the interface the higher the change between the first and second hysteresis loops. Experimentally, a continuous decrease is measured due to the thermal training effect. The athermal training effect is a large decrease in training and coercivity between the first and second measured hysteresis loops.

7.6 The interface structure throughout the hysteresis loops

To understand what is causing the training effect, the magnetisation in the interface layer was observed throughout the hysteresis loop for the simulated systems with intermixing of 0.1 nm and 1 nm shown in Fig. 7.9 and Fig. 7.11. The

direction and magnitude of the interface magnetisation of the Mn is shown in Fig. 7.14, the direction of the magnetisation can be seen to follow the direction of the CoFe magnetisation as they are ferromagnetically coupled together.

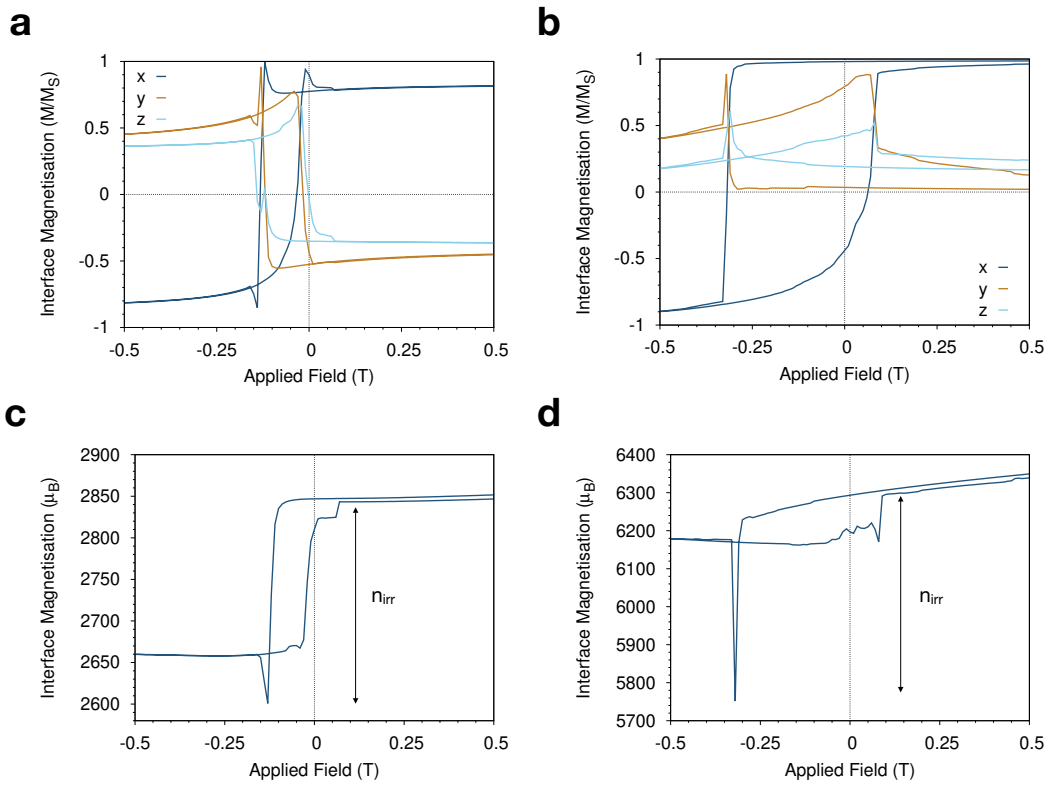

Figure 7.14: **The magnitude and direction of the interface moment of the Mn throughout the hysteresis loop.** The direction of the Mn moment in the interface layer (in direct contact with the CoFe) throughout the hysteresis loops for interface mixing widths of (a) 0.1 nm and (b) 1 nm respectively. In both cases the interface moment has followed the interface moment of the CoFe (shown in Fig. 7.13). (c) and (d) The magnitude of the net interface moment throughout the hysteresis loops for interface mixing widths of 0.1 nm and 1 nm respectively.

The interface magnetisation can be observed to decrease between positive and negative saturation as was observed in section 5. The decrease in saturation magnetisation is due to the number of irreversible Mn spins (n_{irr}) in the interface layer.

Both interfaces have a pronounced minima in the interface moment just after the first switch has occurred, suggesting a large reordering of the interface at this point. This reordering is analogous to the meta stable spins described by Biternas *et al* [104]. At the start of the first hysteresis loop the interface magnetisation of the Mn is in a meta-stable state, which arose during the setting procedure. It takes a large field to evolve the interface magnetisation from this meta stable

state into the ground state - causing the pronounced minima in the interface moment. As the change in spin structure occurs just after the first switching point of the hysteresis loop by the time the system has reached the negative saturation point it is already in the ground state configuration and no longer in a meta stable state. This explains why the returning loops of the first and second hysteresis loops are always experimentally observed to have a similar shapes whereas there is a large change in the first arms of the hysteresis loops [104].

For the 0.1 nm interface, the pronounced minima in the interface magnetisation ($2603\mu_B$) is about 20% lower than the negative saturation value for the interface magnetisation ($2662\mu_B$). We therefore expect the exchange bias to be about 20% lower in the second hysteresis loop simulation as it no longer has to overcome this larger energy barrier. For the 1 nm simulation the pronounced minima ($5765\mu_B$) is about 70% lower than the interface magnetisation at negative saturation ($6183\mu_B$). It is therefore expected that the exchange bias will decrease by about 70% between the first and second hysteresis loops. Both of these predictions approximately match the change in exchange bias shown in the hysteresis loops shown in Fig. 7.9.

Looking at Fig. 7.14 you can see that in both the 0.1 nm and 1 nm of interface mixing hysteresis loop simulations there is a change in magnitude of the Mn interface magnetisation between the start and the end of the first hysteresis loop. In Fig. 7.14(b) the direction of the interface moment has also changed from (a). This is because the interface configuration has changed from a meta-stable state to the ground state. The change in spin configuration means that the first and second hysteresis loops will start from different interface spin structures. To quantify this change, a subsection of the interface spin structure was visualised and the change in angle from start to end of the hysteresis loop was calculated. The angles between the initial and final positions of the spins are shown in Fig. 7.15. From this image it can be seen that for low levels of interface mixing there is almost no rotation between the initial and final states of the hysteresis loop. However, for the larger interface mixing widths it can be seen that there has been a large level of distortion between the initial and final states. The change in the interface spin structure means that the interface will have a different number of reversible and irreversible spins from the initial hysteresis loop. After this the interface has reordered. Fig. 7.15 also shows that there is no large changes in angle for either the 1 nm or 0.1 nm simulated system between the start and end of the second hysteresis loop. This shows that the spin configuration has returned to the ground state and the spin configuration has become stable.

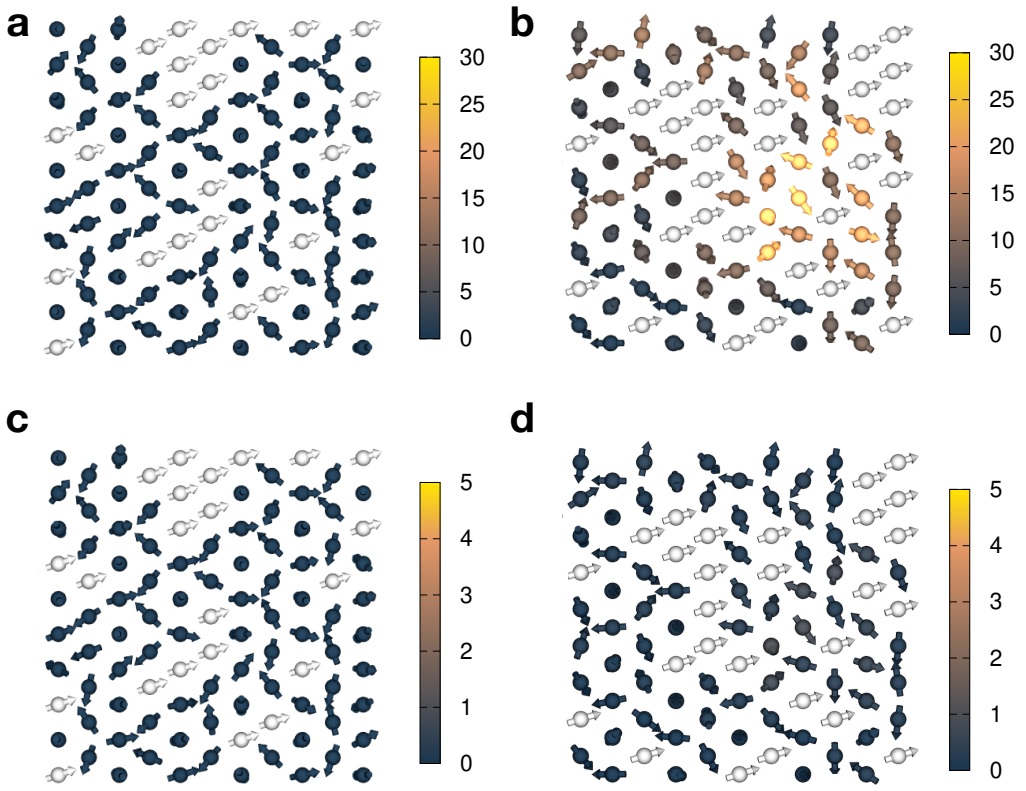

Figure 7.15: **The change in the interface spin structures between the start and the end of the hysteresis loops.** (a) and (b) show the change in interface spin structure between the start and end of the first hysteresis for interface mixing widths of 0.1 nm and 1 nm respectively. (c) and (d) show the change in interface spin structure between the start and end of the second hysteresis for interface mixing widths of 0.1nm and 1nm respectively. The change in colour shows the change in angle in degrees as shown by the scale bar on the side.

To work out whether this reordering is due to a movement of the entire bulk structure or just an interface effect the average angle between initial and final hysteresis loop was plotted as a function of distance from the interface. The interface used had an interface mixing width of 1nm, to show the largest changes in angle as it is assumed this will have the largest effect on the bulk Mn. The angles are shown in Fig. 7.16, the plot shows the average angle the atoms in each layer have moved. The interface spins have moved an average of approximately 6 degrees at the interface but far away from the interface the spins have only rotated about 2 degrees. This suggests that the movement is an interface effect and not a bulk effect, this is to be expected due to the large anisotropy in IrMn.

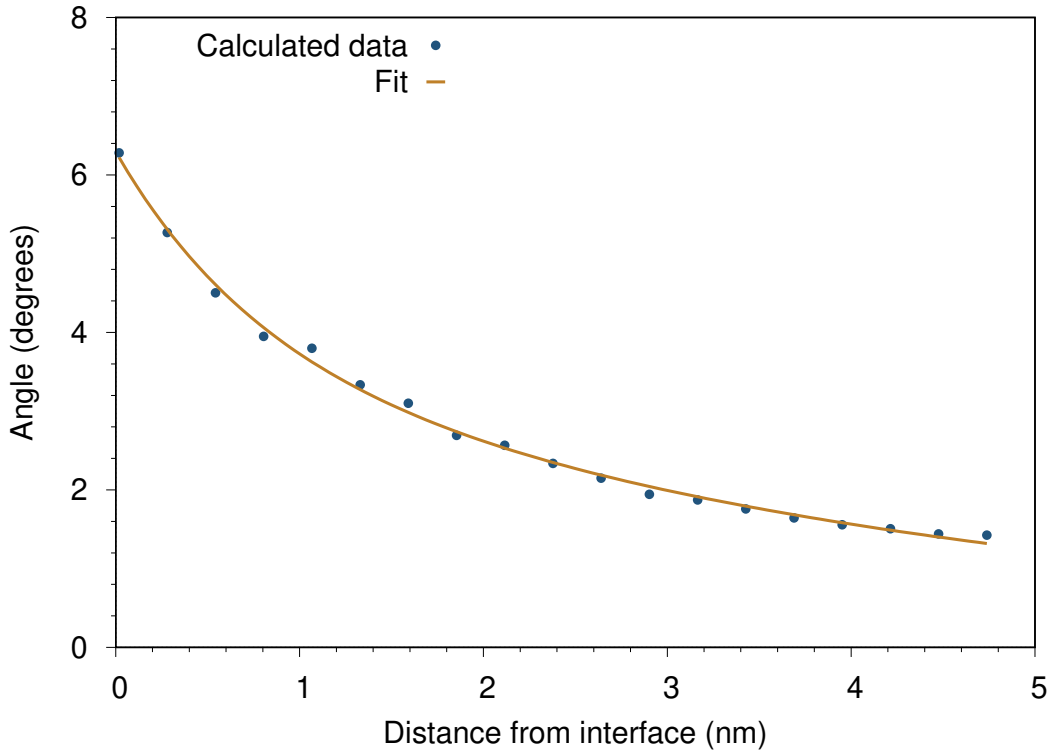

Figure 7.16: **The average rotation of each layer of the Mn between the start and end of the first hysteresis loop.** The angle between the start and end magnetisation of each Mn spin during the first hysteresis loop. These were averaged across every Mn layer. The interface spins have a much higher change in magnetisation that the bulk Mn.

7.7 Summary

In this chapter the origin of the athermal training effect was investigated. The athermal training effect is a large drop in exchange bias after the first measured hysteresis loop. The drop in exchange bias is caused by meta stable spin states occurring during the the setting process, which have a higher interface moment than the ground state. During the first hysteresis loop these spin states are reversed and the interface falls into its minimum energy state, reducing the interface moment and therefore the exchange bias of further hysteresis loops.

The meta-stable spin states were found to be due to roughness at the interface as no training was found for a perfectly flat interface. The interface can be seen to reorder between the first and second hysteresis loop where the angle between this reordering increases with the amount of interface roughness therefore increasing the training. This shows that training is purely an interface effect, in agreement with the model of Biternas *et al* [104].

8

CONCLUSIONS

AFM materials could hold the key to the creation of novel AFM spintronic devices which will give smaller, faster, devices with lower power consumption to keep up with Moore's law. This thesis focused on increasing the understanding of the technologically relevant AFM, IrMn, using an atomistic spin model. In the following conclusion, the main results of each chapter are summarised and the central conclusions are drawn.

The aim of Chapter 3 was to calculate the properties of IrMn in different compositions, orders and finite-sizes. The first step was to validate our model against previous experimental and theoretical results to confirm its accuracy. Once confirmed, the properties of different compositions and orders were simulated. IrMn has the highest exchange bias values between 17% - 25% Ir, and it was found that in all of these compositions disordered IrMn had the same ground state but increasing the Mn concentration caused a more thermally stable structure. In real devices the IrMn is used in thin film form. These thin films will cause finite-size effects in the properties of the IrMn. It was found that IrMn films show a stronger finite size dependence of the Néel temperature than an equivalent ferromagnet due to the existence of spin frustration. Our results suggest a larger antiferromagnetic film thickness is required for spintronic devices operating at or above room temperature compared to an equivalent ferromagnet, particularly for sputtered films with a high degree of interfacial intermixing.

In Chapter 4 the effective temperature dependent anisotropy and the symmetry was calculated for different compositions of IrMn. Modelling $L1_0$ - IrMn, which has an in-plane anisotropy, it was found that AFM's follow the same power scaling laws as FM's. In $IrMn_3$ both ordered and disordered structures have very different anisotropy surfaces. For ordered $L1_2$ - $IrMn_3$ it was found that the energy surface

is unusually complex and the scaling exponent of the effective magnetic anisotropy differs from the expectations of Callen-Callen theory. The energy surface of disordered γ - $IrMn_3$ has a cubic symmetry, however the temperature scaling was calculated to be almost exactly equal to the uniaxial exponent. This surprising result shows that the energy surface is cubic however each individual spin sits in a uniaxial energy surface and the local environment for each spin governs the spin fluctuations rather than the symmetry of the energy surface as a whole. We find that in both ordered and disordered $IrMn_3$ meta stable spin structures lower the overall energy barrier to a tenth of the energy barrier estimated the *ab-initio* values predicted by L, Szunyogh *et al* [25]. Our results have resolved the discrepancy between previous experimental and theoretical results and have contributed massively to the understanding of anisotropy in AFM materials.

Chapters 5, 6 and 7 focus on the Exchange Bias effect. Exchange bias occurs when you couple our AFM to a FM and it used in a wide range of technological applications such as hard disk drives. Chapter 5 focused on the origin of exchange bias in a single grain $\gamma-$ $IrMn_3$/ CoFe bilayer. Our model is the first model of exchange bias in these bilayers to not rely on grain boundaries or interface defects to be the cause of exchange bias. Instead, it was found that exchange bias is caused by a small statistical imbalance in the number of Mn atoms in each AFM sublattice. The imbalance causes a net field at the interface which pins the FM, causing exchange bias. Exchange Bias occurs in all disordered compositions of IrMn from $IrMn_5$ to $IrMn_3$. Although exchange bias can occur due to point defects as found in previous models it was also found that the pinned interface spins can be delocalised across the interface.

In Chapter 6, our single grain model of IrMn/CoFe bilayers was extended to a multigranular system, more representative of real devices. These simulations are the first atomistic simulations of exchange bias on this scale, and are only possible due to the highly scalable, parallel nature of VAMPIRE. At 0K the simulated exchange bias values were much larger for smaller grains than the experimental trends would suggest. At 300K, the exchange bias matched the trend in the experimental measurements as the exchange bias for small grain sizes has decreased due to the decreased thermal instabilities [5].

In Chapter 7, the athermal training effect was investigated. The athermal training effect is a large drop in exchange bias after the first measured hysteresis loop. We found that the drop in exchange bias is caused by meta stable spin states occurring during the the setting process. These meta-stable spin states were found

to be due to intermixing at the interface as no training was found for a perfectly flat interface. The meta stable spin states have a higher energy to rotation than the ground state. During the first hysteresis loop these spin states are reversed and the interface falls into its minimum energy state, reducing the exchange bias simulated in the following hysteresis loops. We found that training is purely an interface effect and only the interface spins reorder in agreement with the model of Biternas *et al* [104].

In conclusion, this is the first comprehensive atomistic investigation into IrMn alloys, simulated with details which are not possible using micromagnetic or current *ab-initio* approaches. The model gives results which match experimental measurements and from this more complex structures such as finite size systems and different material alloys can be studied. It is the first model of an exchange biased bilayer which does not rely on grain boundaries, impurities or AFM domains to create the exchange bias field. The highly parallel, scalable nature of VAMPIRE means that exchange bias can be simulated in systems of comparable size to those in real devices such as hard drive read heads. Details such as interface mixing and the effect of composition can be simulated and the model can be used to determine the atomistic cause of macroscopically observable effects such as exchange bias and the athermal training effect.

8.1 Further Work

The work described in this thesis only touches the surface of the interesting magnetic effects and properties still to be explored in IrMn. With this model a complete understanding of the material is now possible which will pave the way for the next generation magnetic memory devices.

In this thesis we have modelled many interesting effects specifically in exchange bias. However, there is still a lot left to discover, such as the thermal training effect or a more in depth study into the composition effect of exchange bias in multigranular systems. In the longer term there are some interesting projects relating to spin transport and spin wave resonances for novel AFM spintronic devices which might be interesting to model. These are described in more detail below:

8.1.1 Spin current effects in IrMn

The next generation of anti-ferromagnetic spintronic devices will use the anti-ferromagnet to store the information. For the information to be written to an anti-ferromagnet you need a way to change the magnetic configuration. Recently there has been significant progress in this area by using spin-orbit torque or spin transfer torques to change the magnetic configurations of the AFM [58]. So far this has been experimentally measured in disordered γ - $IrMn_3$ but never theoretically modelled. There are many models of spin transfer torque and spin orbit torque including the Slonczewski spin torque model [109] which is implemented in VAMPIRE.

8.1.2 Anti-ferromagnetic resonance simulations in IrMn

Anti-ferromagnetic resonance was first predicted by Kittel in 1951 [110]. He calculated that unlike FM materials even without an external field, the presence of the internal fields can results in a dynamic response from the AFM. Spin waves can be used to probe the properties of a material, via spin-wave resonance. The frequency with which the spin waves precess is an important property of that material and depends on the orientation of the material, the strength of the magnetic field, as well as the magnetic properties of the sample. If we know the orientation of the material and the strength of the magnetic field, the resonance frequency can be used to calculate the material properties such as the exchange, the anisotropy and the gyromagnetic ratio. Since the discovery of anti-ferromagnetic resonance there have been many experimental measurements of anti-ferromagnetic resonance spectrum's, a lot of which show contradictory data [111–114]. This is because in anti-ferromagnets the resonance modes are much more complex than ferromagnets as the magnetic structure of tends to be much more complicated. Atomistic modelling could be the key to understanding this phenomenon, especially in complex non-collinear anti-ferromagnets such as IrMn.

8.1.3 Spin-wave propagation in IrMn and in IrMn/CoFe bilayers

Spin wave propagation could potentially be used in the next generation of spintronic devices to transport and process information [115]. These new technologies could massively outperform current devices using electric currents as spin wave propagation occurs at very high frequencies and has a very low energy dissipation. One of the most important issues stopping the development of such devices is

tuning the ferromagnetic resonance (FMR) frequency [116]. The FMR frequencies necessary in such devices are beyond 5GHz, meaning that the FMR has to be increased from the natural resonance state of a material. It has also observed experimentally that coupling a FM to an AFM increases the anisotropy via the exchange bias effect causing the FMR frequency to increase by up to 10GHz [117]. Although this shift in resonance frequency has been well known for a number of years, the underlying physical causes and effect on the FM are still poorly understood [118]. Atomistic modelling could be the key to understanding this complex phenomena and lead to the next generation of spintronic devices.

BIBLIOGRAPHY

[1] Louis Néel. Magnetism and the local molecular field. *Nobel Lecture*, 1970.

[2] B. Dieny. Giant magnetoresistance in spin-valve multilayers. *Journal of Magnetism and Magnetic Materials*, 136(3):335–359, 9 1994.

[3] M N Baibich, J M Broto, A Fert, F Nguyen, Van Dau, F Petroff, P Eitenne, G Creuzet, A Friederich, and J Chazelas. Giant Magnetoresistance of (001)Fel(001) Cr Magnetic Superlattices. *Physical Review Letters*, 61, 1988.

[4] G. Binasch, P. Grünberg, F. Saurenbach, and W. Zinn. Enhanced magnetoresistance in layered magnetic structures with antiferromagnetic interlayer exchange. *Physical Review B*, 39(7):4828–4830, 3 1989.

[5] K. O'Grady, L. E. Fernandez-Outon, and G. Vallejo-Fernandez. A new paradigm for exchange bias in polycrystalline thin films. *Journal of Magnetism and Magnetic Materials*, 322(8):883–899, 2010.

[6] Gordon E. Moore. Cramming more components onto integrated circuits. *Electronics*, 38, 1965.

[7] Scott E. Thompson and Srivatsan Parthasarathy. Moore's law: the future of Si microelectronics. *Materials Today*, 9(6):20–25, 6 2006.

[8] John M. Shalf and Robert Leland. Computing beyond moore's law. *Computer*, 48(12):14–23, 12 2015.

[9] T. Jungwirth, X. Marti, P. Wadley, and J. Wunderlich. Antiferromagnetic spintronics. *Nature Nanotechnology*, 11(3):231–241, 3 2016.

[10] T. Jungwirth, J. Sinova, A. Manchon, X. Marti, J. Wunderlich, and C. Felser. The multiple directions of antiferromagnetic spintronics. *Nature Physics*, 14(3):200–203, 3 2018.

[11] Rembert Duine. Spintronics: An alternating alternative. *Nature Materials*, 10(5):344–345, 4 2011.

[12] Y. Y. Wang, C. Song, B. Cui, G. Y. Wang, F. Zeng, and F. Pan. Room-temperature perpendicular exchange coupling and tunneling anisotropic magnetoresistance in an antiferromagnet-based tunnel junction. *Physical Review Letters*, 109(13):137201, 9 2012.

[13] Matthias B. Jungfleisch, Wei Zhang, and Axel Hoffmann. Perspectives of antiferromagnetic spintronics. *Physics Review Letters A*, 382(13):865–871, 2018.

[14] Allan A. Mills. The Lodestone: History, Physics, and Formation. *Annals of Science*, 61(3):273–319, 7 2004.

[15] Sarah Jenkins, Andrea Meo, Luke E Elliott, Stephan K Piotrowski, Mukund Bapna, Roy W Chantrell, Sara A Majetich, and Richard F L Evans. Magnetic stray fields in nanoscale magnetic tunnel junctions. *Journal of Physics D: Applied Physics*, 53(4):044001, 11 2020.

[16] V Saidl, P Nemec, Peter Wadley, V Hills, Richard Campion, Vit Novak, Kevin Edmonds, F Maccherozzi, S Dhesi, B L Gallagher, F Trojanek, Jan Kunes, Jakub Zelezny, Petr Maly, and T Jungwirth. Optical determination of the Neel vector in a CuMnAs thin-film antiferromagnet. *Nature Photonics*, 11, 5 2016.

[17] L. Baldrati, A. Ross, T. Niizeki, C. Schneider, R. Ramos, J. Cramer, O. Gomonay, M. Filianina, T. Savchenko, D. Heinze, A. Kleibert, E. Saitoh, J. Sinova, and M. Kläui. Full angular dependence of the spin Hall and ordinary magnetoresistance in epitaxial antiferromagnetic NiO(001)/Pt thin films. *Physical Review B*, 98(2):024422, 7 2018.

[18] Geert R. Hoogeboom, Aisha Aqeel, Timo Kuschel, Thomas T.M. Palstra, and Bart J. Van Wees. Negative spin Hall magnetoresistance of Pt on the bulk easy-plane antiferromagnet NiO. *Applied Physics Letters*, 111(5):052409, 7 2017.

[19] Sarah Jenkins and Richard F. L. Evans. Enhanced finite size and interface mixing effects in iridium manganese ultra thin films. *Journal of Applied Physics*, 124(15):152105, 10 2018.

[20] Sarah Jenkins, Roy W. Chantrell, Timothy J. Klemmer, and Richard F.L. Evans. Magnetic anisotropy of the noncollinear antiferromagnet IrMn3. *Physical Review B*, 100(22), 12 2019.

[21] Takayuki Shiino, Se Hyeok Oh, Paul M. Haney, Seo Won Lee, Gyungchoon Go, Byong Guk Park, and Kyung Jin Lee. Antiferromagnetic Domain Wall Motion Driven by Spin-Orbit Torques. *Physical Review Letters*, 117(8):087203, 8 2016.

[22] S. Wienholdt, D. Hinzke, and U. Nowak. THz switching of antiferromagnets and ferrimagnets. *Physical Review Letters*, 108(24):247207, 6 2012.

[23] Ernst Ising. Beitrag zur Theorie des Ferromagnetismus. *Zeitschrift für Physik*, 31(1):253–258, 2 1925.

[24] R. E. Watson, M. Blume, and G. H. Vineyard. Spin motions in a classical ferromagnet. *Physical Review*, 181(2):811–823, 1969.

[25] L. Szunyogh, B. Lazarovits, L. Udvardi, J. Jackson, and U. Nowak. Giant magnetic anisotropy of the bulk antiferromagnets IrMn and IrMn3 from first principles. *Physical Review B*, 79(2):1–4, 2009.

[26] David Jiles. *Introduction to magnetism and magnetic materials*. CRC Press, 2 edition, 1998.

[27] R.F.L. Evans. https://vampire.york.ac.uk/.

[28] Alastair I. M. Rae. *Quantum mechanics*. Taylor & Francis, 2008.

[29] N W Ashcroft and N D Mermin. *Solid State Physics*. Holt-Saunders, 1976.

[30] R Skomski, A Kashyap, A Solanki, A Enders, and D J Sellmyer. Magnetic anisotropy in itinerant magnets. *J. Appl. Phys*, 107:9–735, 2010.

[31] Ralph Skomski. *Simple Models of Magnetism*. OUP Oxford, 2008.

[32] D. A. Garanin, R. Schilling, and A. Scala. Saddle index properties, singular topology, and its relation to thermodynamical singularities for a phiˆ4 mean field model. *Physical Review E - Statistical Physics, Plasmas, Fluids, and Related Interdisciplinary Topics*, 70(3):9, 5 2004.

[33] L Landau and E Lifshitz. On the theory of the dispersion of magnetic permeability in ferromagnetic bodies. *Phys. Zeitsch. der Sow*, 8:153–169, 1935.

[34] T.L. Gilbert. A Lagrangian Formulation of the Gyromagnetic Equation of the Magnetization Field. *Physical Review*, 100:1243, 1955.

[35] M. O.A. Ellis, R. F.L. Evans, T. A. Ostler, J. Barker, U. Atxitia, O. Chubykalo-Fesenko, and R. W. Chantrell. The Landau-Lifshitz equation in atomistic models. *Low Temperature Physics*, 41(9):705–712, 9 2015.

[36] L. Landau and E. Lifschitz. On the theory of the dispersion of magnetic permeability in ferromagnetic bodies. In *Perspectives in Theoretical Physics*, pages 51–65. Elsevier, 1992.

[37] W. Brown. Thermal fluctuation of fine ferromagnetic particles. *IEEE Transactions on Magnetics*, 15(5):1196–1208, 9 1979.

[38] U. Atxitia, O. Chubykalo-Fesenko, R. W. Chantrell, U. Nowak, and A. Rebei. Ultrafast spin dynamics: The effect of colored noise. *Physical Review Letters*, 102(5):057203, 2 2009.

[39] Ulrich Nowak. *Thermally activated reversal in magnetic nanostructures*. PhD thesis, 2001.

[40] D V Berkov and N L Gorn. Thermally activated processes in magnetic systems consisting of rigid dipoles: equivalence of the Ito and Stratonovich stochastic calculus. *Journal of Physics: Condensed Matter*, 14(13):L281–L287, 4 2002.

[41] Jose Luis Garcia-Palacios and Francisco J. Lazaro. Langevin-dynamics study of the dynamical properties of small magnetic particles. *Physical Review B*, 58(22):14937–14958, 12 1998.

[42] R. F.L. Evans, W. J. Fan, P. Chureemart, T. A. Ostler, M. O.A. Ellis, and R. W. Chantrell. Atomistic spin model simulations of magnetic nanomaterials. *Journal of Physics Condensed Matter*, 26(10), 2014.

[43] Nicholas Metropolis, Arianna W. Rosenbluth, Marshall N. Rosenbluth, Augusta H. Teller, and Edward Teller. Equation of state calculations by fast computing machines. *The Journal of Chemical Physics*, 21(6):1087–1092, 6 1953.

[44] John S. Thomsen. Logical Relations among the Principles of Statistical Mechanics and Thermodynamics. *Physical Review*, 91(5):1263–1266, 9 1953.

[45] George Marsaglia. Choosing a Point from the Surface of a Sphere. *The Annals of Mathematical Statistics*, 43(2):645–646, 4 1972.

[46] J D Alzate-Cardona, D Sabogal-Suárez, R F L Evans, and E Restrepo-Parra. Optimal phase space sampling for Monte Carlo simulations of Heisenberg spin systems. *Journal of Physics: Condensed Matter*, 31(9):095802, 3 2019.

[47] U. Nowak and D. Hinzke. Magnetization switching in small ferromagnetic particles: Nucleation and coherent rotation. *Journal of Applied Physics*, 85(8):4337, 4 1999.

[48] The crystal structure of α-manganese. *Proceedings of the Royal Society of London. Series A, Containing Papers of a Mathematical and Physical Character*, 115(771):456–471, 7 1927.

[49] Louis Neel. L'approche à la saturation de la magnétostriction. *J. Phys. Radium*, 15(5), 1954.

[50] Sam C. Westmoreland, Connor Skelland, Tetsuya Shoji, Masao Yano, Akira Kato, Masaaki Ito, Gino Hrkac, Thomas Schrefl, Richard F.L. Evans, and Roy W. Chantrell. Atomistic simulations of α - Fe /Nd2Fe14B magnetic core/shell nanocomposites with enhanced energy product for high temperature permanent magnet applications. *Journal of Applied Physics*, 127(13):133901, 4 2020.

[51] G. Vallejo-Fernandez, L. E. Fernandez-Outon, and K. O'Grady. Measurement of the anisotropy constant of antiferromagnets in metallic polycrystalline exchange biased systems. *Applied Physics Letters*, 91(21):212503, 11 2007.

[52] H.B. Callen and E. Callen. The present status of the temperature dependence of magnetocrystalline anisotropy, and the l(l+1)2 power law. *Journal of Physics and Chemistry of Solids*, 27(8):1271–1285, 8 1966.

[53] A Kohn, A Kovács, R Fan, G J McIntyre, R C C Ward, and J P Goff. The antiferromagnetic structures of IrMn3 and their influence on exchange-bias. *Scientific reports*, 3:2412, 2013.

[54] $\sqrt{\text{Å}}$ *Buruzs*, *P. Weinberger*, *L. Szunyogh*, *L. Udvardi*, *P. I.Chleboun*, *A. M.Fischer*, *a*

[55] Kari Selte, A. Kjekshus, A. F. Andresen, and W. B. Pearson. Equiatomic Transition Metal Alloys of Manganese. VII. A Neutron Diffraction Study of Magnetic Ordering in the IrMn Phase. *Acta Chemica Scandinavica*, 22:3039–3042, 1968.

[56] N. P. Aley and K. O'Grady. Compositional dependence of antiferromagnetic anisotropy in IrMn/CoFe exchange bias systems. *Journal of Applied Physics*, 109(7):07D719, 4 2011.

[57] Izumi Tomeno, Hiromi N. Fuke, Hitoshi Iwasaki, Masashi Sahashi, and Yorihiko Tsunoda. Magnetic neutron scattering study of ordered Mn3Ir. *Journal of Applied Physics*, 86(7):3853, 9 1999.

[58] O Gomonay, T Jungwirth, and J Sinova. Concepts of antiferromagnetic spintronics. *Rapid Research Letters*, 11, 2017.

[59] L. Frangou, S. Oyarzún, S. Auffret, L. Vila, S. Gambarelli, and V. Baltz. Enhanced Spin Pumping Efficiency in Antiferromagnetic IrMn Thin Films around the Magnetic Phase Transition. *Physical Review Letters*, 116(7):077203, 2 2016.

[60] D. Petti, E. Albisetti, H. Reichlová, J. Gazquez, M. Varela, M. Molina-Ruiz, A. F. Lopeandía, K. Olejník, V. Novák, I. Fina, B. Dkhil, J. Hayakawa, X. Marti, J. Wunderlich, T. Jungwirth, and R. Bertacco. Storing magnetic information in IrMn/MgO/Ta tunnel junctions via field-cooling. *Applied Physics Letters*, 102(19):192404, 5 2013.

[61] R Carpenter, A J Vick, A Hirohata, G Vallejo-Fernandez, and K O'grady. Effect of grain cutting in exchange biased nanostructures. *Journal of Applied Physics*, 115:17–905, 2014.

[62] G. Vallejo-Fernandez, N. P. Aley, J. N. Chapman, and K. O'Grady. Measurement of the attempt frequency in antiferromagnets. *Applied Physics Letters*, 97(22):222505, 11 2010.

[63] B. Craig, R. Lamberton, A. Johnston, U. Nowak, R. W. Chantrell, and K. O'Grady. A model of the temperature dependence of exchange bias in coupled ferromagnetic/antiferromagnetic bilayers. *Journal of Applied Physics*, 103(7), 2008.

[64] Clarence Zener. *Elasticity and anelasticity of metals.* University of Chicago Press, Chicago,, 1948.

[65] P. Asselin, R. F. L. Evans, J. Barker, R. W. Chantrell, R. Yanes, O. Chubykalo-Fesenko, D. Hinzke, and U. Nowak. Constrained Monte Carlo method and calculation of the temperature dependence of magnetic anisotropy. *Physical Review B*, 82(5):054415, 8 2010.

[66] Matthew Ellis. *Simulations of magnetic reversal properties in granular recording media*. PhD thesis, 2015.

[67] W. H. Meiklejohn and C. P. Bean. New Magnetic Anisotropy. *Physical Review*, 105(3):904–913, 2 1957.

[68] Daniele Ielmini. Brain-inspired computing with resistive switching memory (RRAM): Devices, synapses and neural networks. *Microelectronic Engineering*, 190:44–53, 4 2018.

[69] Louis Néel. Étude théorique du couplage ferro-antiferromagnétique dans les couches minces. *Annales de Physique*, 14(2):61–80, 4 1967.

[70] D. Mauri, H. C. Siegmann, P. S. Bagus, and E. Kay. Simple model for thin ferromagnetic films exchange coupled to an antiferromagnetic substrate. *Journal of Applied Physics*, 62(7):3047–3049, 10 1987.

[71] N. C. Koon. Calculations of Exchange Bias in Thin Films with Ferromagnetic/Antiferromagnetic Interfaces. *Physical Review Letters*, 78(25):4865–4868, 6 1997.

[72] Miguel Kiwi, Jose Mejia-Lopez, Ruben D. Portugal, and Ricardo Ramirez. Exchange-bias systems with compensated interfaces. *Applied Physics Letters*, 75(25):3995, 12 1999.

[73] R. D. Shull, A. J. Shapiro, V. S. Gornakov, V. I. Nikitenko, and Hong-Wu Zhao. Stationary antiferromagnetic domains during magnetization reversal in an exchange-biased FeMn/Fe76Mn6C18 bilayer. *Journal of Applied Physics*, 93(10):8603–8605, 5 2003.

[74] U Nowak, K D Usadel, J Keller, P Milté, B Beschoten, and G Gü. Domain state model for exchange bias. I. Theory. *Journal of Applied Physics*, 11, 2000.

[75] A. P. Malozemoff. Random-field model of exchange anisotropy at rough ferromagnetic-antiferromagnetic interfaces. *Physical Review B*, 35(7):3679–3682, 3 1987.

[76] R. S. Sundar and S. C. Deevi. Soft magnetic FeCo alloys: Alloy development, processing, and properties. *International Materials Reviews*, 50(3):157–192, 6 2005.

[77] S Blizak, G Bihlmayer, and S Blügel. Ab initio investigations of magnetic properties of FeCo monolayer alloy films on Rh(001). *Physics Review B*, 86:94436, 2012.

[78] L. Szunyogh, L. Udvardi, J. Jackson, U. Nowak, and R. Chantrell. Atomistic spin model based on a spin-cluster expansion technique: Application to the IrMn 3 /Co interface. *Physical Review B*, 83(2):024401, 1 2011.

[79] I. L. Castro, V. P. Nascimento, E. C. Passamani, A. Y. Takeuchi, C. Larica, M. Tafur, and F. Pelegrini. The role of the (111) texture on the exchange bias and interlayer coupling effects observed in sputtered NiFe/IrMn/Co trilayers. *Journal of Applied Physics*, 113(20):203903, 5 2013.

[80] Marian Fecioru-Morariu, Gernot Güntherodt, Manfred Rührig, Alessio Lamperti, and Brian Tanner. Exchange coupling between an amorphous ferromagnet and a crystalline antiferromagnet. *Journal of Applied Physics*, 102(5), 2007.

[81] Peter J. M. van Laarhoven and Emile H. L. Aarts. *Simulated Annealing: Theory and Applications*. Springer, 1987.

[82] H. Ohldag, A. Scholl, F. Nolting, E. Arenholz, S. Maat, A. T. Young, M. Carey, and J. Stöhr. Correlation between Exchange Bias and Pinned Interfacial Spins. *Physical Review Letters*, 91(1):017203, 7 2003.

[83] E. Fulcomer and S. H. Charap. Thermal fluctuation aftereffect model for some systems with ferromagnetic-antiferromagnetic coupling. *Journal of Applied Physics*, 43(10):4190–4199, 1972.

[84] L. Szunyogh, L. Udvardi, J. Jackson, U. Nowak, and R. Chantrell. Atomistic spin model based on a spin-cluster expansion technique: Application to the IrMn 3 /Co interface. *Physical Review B*, 83(2):024401, 1 2011.

[85] M. D. Stiles and R. D. McMichael. Model for exchange bias in polycrystalline ferromagnet-antiferromagnet bilayers. *Physical Review B*, 59(5):3722–3733, 2 1999.

[86] P. A.A. Van Der Heijden, T. F.M.M. Maas, J. C.S. Kools, F. Roozeboom, P. J. Van Der Zaag, and W. J.M. De Jonge. Influences on relaxation of exchange biasing in NiO/Ni66Co 18Fe16 bilayers. *Journal of Applied Physics*, 83(11):7207–7209, 6 1998.

[87] G Vallejo-Fernandez, L E Fernandez-Outon, and K O'grady. Antiferromagnetic grain volume effects in metallic polycrystalline exchange bias systems Related content Antiferromagnetic grain volume effects in metallic polycrystalline exchange bias systems. *Journal of Physics D: Applied Physics*, 41:5, 2008.

[88] M. Futamoto, N. Inaba, Y. Hirayama, K. Ito, and Y. Honda. Compositional microstructure and micromagnetics of Co-based thin film media. In *Materials Research Society Symposium*, volume 517, pages 243–254. MRS, 1998.

[89] D. Choo, R. W. Chantrell, R. Lamberton, A. Johnston, and K. O'Grady. A model of the magnetic properties of coupled ferromagnetic/antiferromagnetic bilayers. In *Journal of Applied Physics*, volume 101, 2007.

[90] W Daeng-am, P Chureemart, A Rittidech, L J Atkinson, R W Chantrell, and J Chureemart. Micromagnetic model of exchange bias: effects of structure and AF easy axis dispersion for IrMn/CoFe bilayers. *Journal of Physics D*, 53, 2019.

[91] W Daeng-am, P Chureemart, R W Chantrell, and J Chureemart. Granular micromagnetic model for perpendicular recording media: quasi-static properties and media characterisation. *Journal of Physics D*, 52, 2019.

[92] G. Vallejo-Fernandez, N. P. Aley, L. E. Fernandez-Outon, and K. O'Grady. Control of the setting process in CoFe/IrMn exchange bias systems. *Journal of Applied Physics*, 104(3):033906, 8 2008.

[93] Risalat A Khan, Hans T Nembach, Mannan Ali, Justin M Shaw, Christopher H Marrows, and Thomas A Moore. Magnetic domain texture and the Dzyaloshinskii-Moriya interaction in Pt/Co/IrMn and Pt/Co/FeMn thin films with perpendicular exchange bias. *Physical Review B*, 98, 2018.

[94] F. Preparata and M. Shamos. *Computational Geometry*. Springer-Verlag, 1 edition, 1985.

[95] Guanghui Liang, Lin Lu, Zhonggui Chen, and Chenglei Yang. Computational Visual Media Poisson disk sampling through disk packing. *Computational Visual Media*, 1(1):17–26, 2015.

[96] J. Barker, B. Craig, R. Lamberton, A. Johnston, R. W. Chantrell, and O. Heinonen. A model of the exchange bias setting process in magnetic read sensors. *Applied Physics Letters*, 95(2):022504, 7 2009.

[97] E. C. Stoner and E. P. Wohlfarth. Interpretation of high coercivity in ferromagnetic materials. *Nature*, 160(4071):650–651, 1947.

[98] M. Ali, C. H. Marrows, M. Al-Jawad, B. J. Hickey, A. Misra, U. Nowak, and K. D. Usadel. Antiferromagnetic layer thickness dependence of the IrMn/Co exchange-bias system. *Physical Review B*, 68(21), 12 2003.

[99] M. P. Sharrock. Time dependence of switching fields in magnetic recording media. *Journal of Applied Physics*, 76(10):6413–6418, 11 1994.

[100] X. P. Qiu, D. Z. Yang, S. M. Zhou, R. Chantrell, K. O'Grady, U. Nowak, J. Du, X. J. Bai, and L. Sun. Rotation of the pinning direction in the exchange bias training effect in polycrystalline NiFe/FeMn bilayers. *Physical Review Letters*, 101(14):147207, 10 2008.

[101] L. E. Fernández-Outón, K. O'Grady, and M. J. Carey. Thermal phenomena in IrMn exchange biased systems. In *Journal of Applied Physics*, volume 95, pages 6852–6854, 6 2004.

[102] B. Kaeswurm and K. O'Grady. The origin of athermal training in polycrystalline metallic exchange bias thin films. *Applied Physics Letters*, 99(22), 11 2011.

[103] Xianjin Qi, Fengyan Hao, Xuezhu Li, Yongkui Li, and Zhixu Lu. Influence of temperature on the texture and magnetic properties of IrMn-based spin-valve multilayers. *AIP Advances*, 9:105008, 2019.

[104] Andreas Biternas. *Study of the training effect in exchange bias using the domain state model*. PhD thesis, 2009.

[105] A Hoffmann. Symmetry Driven Irreversibilities at Ferromagnetic-Antiferromagnetic Interfaces. *Physics Review Letters*, 93, 2004.

[106] D Suess, M. Kirschner, T. Schrefl, J Fidler, R L Stamps, and J.-V Kim. Exchange bias of polycrystalline antiferromagnets with perfectly compensated interfaces. *Physical Review B*, 67, 2003.

[107] Jaroslaw Kanak, Tomasz Stobiecki, and Sebastiaan Van Dijken. Influence of interface roughness, film texture, and magnetic anisotropy on exchange

bias in [Pt/Co]3/IrMn and IrMn/[CoZPt]3 multilayers. *IEEE Transactions on Magnetics*, 44(2):238–245, 2 2008.

[108] J. H. Lee, H. D. Jeong, C. S. Yoon, C. K. Kim, B. G. Park, and T. D. Lee. Interdiffusion in antiferromagnetic/ferromagnetic exchange coupled NiFe/IrMn/CoFe multilayer. *Journal of Applied Physics*, 91(3):1431–1435, 2 2002.

[109] J. C. Slonczewski. Current-driven excitation of magnetic multilayers. *Journal of Magnetism and Magnetic Materials*, 159(1-2):L1–L7, 6 1996.

[110] Takeo Nagamiya. Theory of Antiferromagnetism and Antiferromagnetic Resonance Absorption, II. *Progress of Theoretical Physics*, 6(3):350–355, 6 1951.

[111] E. P. Trounson, D. F. Bleil, R. K. Wangsness, and L. R. Maxwell. Magnetic resonance in antiferromagnetic materials near the curie temperature. *Physical Review*, 79(3):542–543, 8 1950.

[112] Tosihiko Okamura, Yosiharu Torizuka, and Yuzo Kojima. Magnetic resonance absorption in antiferromagnetic materials. *Physical Review*, 82(2):285–286, 1951.

[113] P L Richards. Infrared Lattice-Vibration Spectra in NiF2, CoF2 and FeF2. *YbIG Journal of Applied Physics*, 35:252404, 1964.

[114] F. M. JohnsoN and A. H Nethercot. Antiferromagnetic Resonance in MnF. *Physical Review*, 1959.

[115] A. V. Chumak, V. I. Vasyuchka, A. A. Serga, and B. Hillebrands. Magnon spintronics, 6 2015.

[116] Jamileh Beik Mohammadi, Joshua Michael Jones, Soumalya Paul, Behrouz Khodadadi, Claudia K A Mewes, Tim Mewes, and Christian Kaiser. Broadband ferromagnetic resonance characterization of anisotropies and relaxation in exchange-biased IrMn/CoFe bilayers. *Physical Review B*, 95:64414, 2017.

[117] Nguyen Nguyen Phuoc, Le Thanh Hung, and C. K. Ong. Ultra-high ferromagnetic resonance frequency in exchange-biased system. *Journal of Alloys and Compounds*, 506(2), 2010.

[118] Jing-Guo Hu, Guo-Jun Jin, and Yu-Qiang Ma. Ferromagnetic resonance and exchange anisotropy in ferromagnetic/ antiferromagnetic bilayers. *Journal of Applied Physics*, 91:2180, 2002.